Quantum Dots Based Superluminescent Diodes and Photonic Crystal Surface Emitting Lasers

Aye Su Mon Kyaw

James Watt School of Engineering

College of Science and Engineering

University of Glasgow

Submitted in fulfilment of the requirements for the Degree of Doctor of Philosophy (Ph.D.)

January 2023

Abstract

This thesis reports the design, fabrication, and electrical and optical characterisations of GaAs-based quantum dot (QD) photonic devices, specifically focusing on superluminescent diodes (SLDs) and photonic crystal surface-emitting lasers (PCSELs). The integration of QD active regions in these devices is advantageous due to their characteristics such as temperature insensitivity, feedback insensitivity, and ability to utilise the ground state (GS) and excited state (ES) of the dots.

In an initial study concerning the fabrication of QD-SLDs, the influence of ridge waveguide etch depth on the electrical and optical properties of the devices are investigated. It is shown that the output power and modal gain from shallow etched ridge waveguide is higher than those of deep etched waveguides. Subsequently, the thermal performance of the devices is analysed. With increased temperature over 170 ºC, the spectral bandwidth is dramatically increased by thermally excited carrier transition in excited states of the dots.

Following this, an investigation of a high dot density hybrid quantum well/ quantum dot (QW/QD) active structure for broadband, high-modal gain SLDs is presented. The influence of the number of QD layers on the modal gain of hybrid QW/QD structures is analysed. It is shown that higher number of dot layer provides higher modal gain value, however, there is lack of emission from QW due to the requirement of large number of carriers to saturate the QD. Additionally, a comparison is made between “unchirped QD” and “ chirped QD” of hybrid QW/QD structure in terms of modal gain and spectral bandwidth. It is showed that “chirped” of the QD can improve the “flatness” of the spectral bandwidth.

Lastly, the use of self-assembled InAs QD as the active material in epitaxially regrown GaAs-based PCSELs is explored for the first time. Initially, it is shown that both GS and ES lasing can be achieved for QD-PCSELs by changing the grating period of the photonic crystal (PC). The careful design of these grating periods allows lasing from neighbouring devices at GS (~1230 nm) and ES (~1140 nm), 90 nm apart in wavelength. Following this, the effect of device area, PC etch depth, PC atom shape (circle or triangle or orientation) on lasing performance is presented. It is shown that lower threshold current density and higher slope efficiencies is achieved with increasing the device size. The deeper PC height device has higher output power due to more suitable height and minimal distance to active region. The triangular atom shape has slightly higher slope efficiency compared to triangular atom shape which is attributed to breaking in-plane symmetry and increase out-of-plane emission.

Declaration

I declare that, except where explicit reference is made to the contribution of others, this thesis is the result of my own work and has not been submitted for any other degree at the University of Glasgow or any other institution.

Publications

[1] A. F. McKenzie, A. S. M. Kyaw, N. D. Gerrard, D. A. MacLaren, and R. A. Hogg., "Kinetic influences on void formation in epitaxially regrown GaAs-based PCSELs," *Journal of Crystal Growth* , vol. 602, p. 126969, 2023.

[2] A. S. M. Kyaw, D. Kim, I. M. Butler, K. Nishi, M. Sugawara, D. T. D. Childs, and R. A. Hogg., "Extreme temperature operation for broad bandwidth quantum-dot based superluminescent diodes," *Applied Physics Letter,* vol.122, no.3, p. 031104, 2023.

[3] A. S. M. Kyaw, D. Kim, K. Nishi, M. Sugawara, D. T. D. Childs, and R. A. Hogg., "Ultrabroad bandwidth and high modal gain by using hybrid QW/QDs based superluminescent diodes," Submitted to Applied Physics Letter.

[4] A. S. M. Kyaw, B. C. King, A. F. McKenzie, N. D. Gerrard, Z. Bian, D. Kim, K. Nishi, K. Takemasa, M. Sugawara, D. T. D. Childs, C. H. Hills, R. J. E. Taylor, and R. A. Hogg., "Epitaxially Regrown Quantum Dot Photonic Crystal Surface Emitting Lasers,", In preparation, targeted for IEEE Journal of Selected Topics in Quantum Electronics.

Conference Presentations

[1] A. S. M. Kyaw, B. C. King, A. F. McKenzie, N. D. Gerrard, Z. Bian, D. Kim, J. Liu, X. Zhao, K. Nishi, K. Takemasa, M. Sugawara, D. T. D. Childs, C. H. Hills, R. J. E. Taylor, and R. A. Hogg., "Epitaxially Regrown Quantum Dot Photonic Crystal Surface Emitting Lasers,", IEEE International Semiconductor Laser Conference (Japan) [2022].

[2] Z. Bian, X. Zhao, K. J. Rae, A. S. M. Kyaw, D. Kim, A. F. McKenzie, B. C. King, J. Liu, S. Thoms, P. Reynolds, N. D. Gerrard, J. R. Orchard, C. H. Hills, C. W. Munro, P. Ivanov, D. T. D. Childs, R. J. E. Taylor, and R. A. Hogg., " Resonator Embedded Crystal Surface Emitting Lasers," IEEE International Semiconductor Laser Conference (Japan) [2022].

[3] A. S. M. Kyaw, B. C. King, A. F. McKenzie, N. D. Gerrard, Z. Bian, D. Kim, K. Nishi, K. Takemasa, M. Sugawara, D. T. D. Childs, C. H. Hills, R. J. E. Taylor, and R. A. Hogg., "Epitaxially Re-grown Quantum Dot Photonic Crystal Surface Emitting Lasers,", Photonic West (San Francisco) [2023].

Acknowledgment

I am deeply grateful for the guidance and support of my supervisors, Prof. Richard Hogg and Dr. David Childs. Their patience, understanding, and encouragement have been a constant source of motivation throughout this journey.

I also would like to express my sincere gratitude to my colleagues, who have always been willing to engage in discussions with me about my work and provide their valuable opinions and advice. I am forever grateful for their kindness and support. In particular, thanks go to Zijun, Daehyun, Alex, Iain, Katie, Olesya, Danqi, Adam M, Adam A, Ben, Mauro, Connor, Jingzhao, Xingyu, and Jousha.

I also would like to acknowledge QD Laser (Japan) for providing high-quality materials that were used in the experiments. Their contribution was crucial to the success of the research. Additionally, I would like to express my gratitude to III-V Epi ltd. for their technical expertise and support in the regrowth process for PCSEL.

I am also deeply grateful to my family and friends for their support and encouragement. Their love and support have been a constant source of strength throughout my journey.

Contents

List of Figures

List of Tables

List of Abbreviation

Throughout the thesis technical abbreviations are used, while they follow natural conventions this is a useful list for most common. The first time each abbreviation is used in a chapter it will be declared.

DOS	Density of States
QW	Quantum Well
QD	Quantum Dot
GS	Ground State
$ES_{\#}$	Excited State # (e.g., ES_1= Excited State 1)
S-K	Stranski-Krastanov
FWHM	Full Width Half Maximum
T_0	Characteristic Temperature
2D	Two-dimensional
PC	Photonic Crystal
EBL	Electron Beam Lithography
SEM	Scanning Electron Microscope
TEM	Transmission Electron Microscope
AFM	Atomic Force Microscopy
ASE	Amplified Spontaneous Emission
SE	Spontaneous Emission
EL	Electroluminescence

Chapter 1: Introduction

1.1 Introduction

This thesis details research on GaAs quantum dot (QD) based photonics devices with specific attention to superluminescent diodes (SLDs) and photonic crystal surface-emitting lasers (PCSELs) for biomedical imaging and telecommunications applications, respectively. In this chapter, a brief history and the working principles of semiconductor lasers are introduced. The evolution of low-dimensional QD material is then described, followed by the application areas for QD-based photonic devices.

1.2 Semiconductor Light-Emitting Devices

Semiconductor lasers have been extensively studied and continue to advance in terms of performance and reliability. Their small size, high-volume manufacturability, and electrical efficiency make lasers well suited for use in a large variety of applications from consumer communications and entertainment to medicine and defense [1], [2]. The first demonstration of the semiconductor laser was the direct bandgap GaAs homojunction (*p*-*n* junction) where the gain was provided by carrier recombination in the depletion region [3]. The small changes in refractive index in the cladding layers above and below the depletion region provide the waveguiding effect, whilst optical feedback was provided by cleaving facets at the edges of the devices. These lasers exhibited very high threshold current densities and required operation at low temperatures due to poor carrier and photon confinement. Most of these limitations were addressed by the introduction of double heterostructure (DHS) lasers [4]. An intrinsic (active) layer of lower band gap material (high refractive index) is sandwiched between doped cladding layers of higher band gap materials (low refractive index). By using a high refractive index intrinsic layer between the cladding layers, the optical mode was confined more to the active region. Additionally, carriers are also more effectively confined to the active region due to the band-gap variation. The advantage of DHS was demonstrated with the achievement of room temperature continuous wave (CW) operation [5], [6].

Figure 1.1 shows a schematic illustration of the operation of a semiconductor laser with a DHS. The basic operating principles of semiconductor lasers are briefly described in this section. A more comprehensive discussion on the subject can be found in the reference [7]. The carrier injection into the active region is achieved by fabricating *p* and *n* metal contacts above and below the semiconductor wafer. Under forward bias operation, electrons are

injected from the *n*-type layer and holes are injected from the *p*-type layer and various scenarios unfold depending on carrier density.

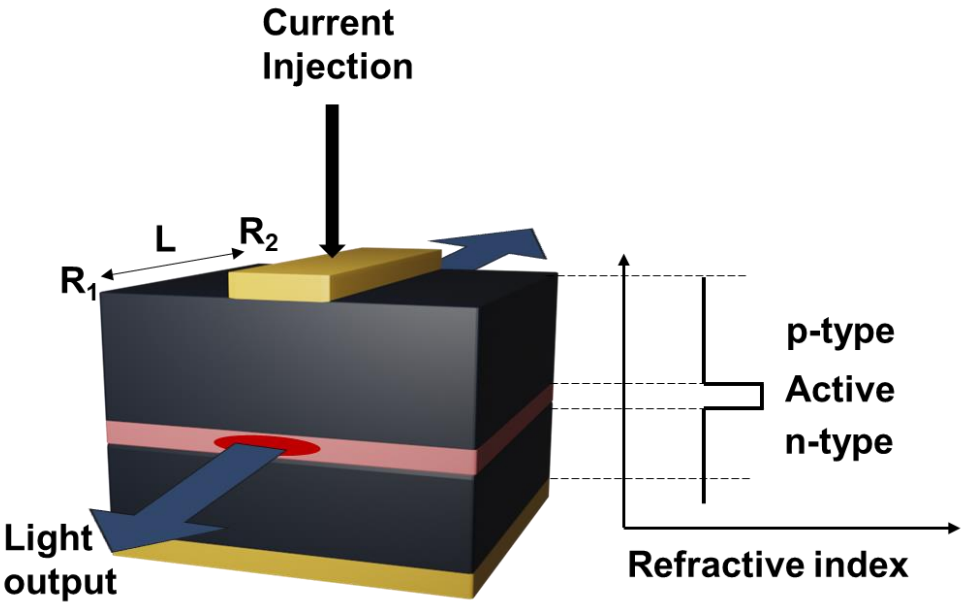

Figure 1.1: Schematic illustration for the operation of a FP laser with double-heterostructure.

Firstly, under low levels of carrier injection into the lowest energy states of the conduction and valence band, carriers recombine radiatively and the emitted light travels along the waveguide before being re-absorbed by the active region, as the number of carriers in the conduction band is low. If the carrier concentration in the conduction band increases, more photons are emitted which may undergo stimulated emission but if the conduction band occupancy remains low, absorption again dominates, attenuating the light. By increasing the carrier density, the system reaches its transparency point where the carrier density is sufficient to make absorption and stimulated emission rates equal. If the carrier density in the conduction band is increased above that required for transparency, a population inversion is reached, and amplification of stimulated photons dominates over absorption. Although the primary mechanism of light radiation in lasers is stimulated emission, the phase of the emitted light must be fixed, and this is achieved by utilising some form of optical feedback. There are different ways to provide optical feedback in laser diodes. The simplest way to achieve optical feedback is to create a resonant cavity between two parallel cleaved crystal facets, which act as mirrors, as in the Fabry-Pérot (FP) laser. In this case, light reflects between the two mirrors whilst traversing the gain medium, and laser operation occurs when the round-trip gain is equal to the total loss in the device, i.e., the sum of the internal losses (α_i) and mirror losses (α_m). The internal losses are optical losses due to parasitic effects

(absorption, scattering, etc.) in the cavity and the mirror loss is the emitted light from the facets. The threshold gain (g_{th}) can be defined as:

$$g_{th} = \alpha_i + \alpha_m = \alpha_i + \frac{1}{2L} ln \frac{1}{R_1 R_2} \tag{1.1}$$

where L is the length of the cavity and R_1 and R_2 are the facets with reflectivity.

1.3 Evolution of Low-Dimensional Structures

In the early DHS lasers [4], bulk materials were used as the active region where there is zero-dimensional (0D) confinement and continuous density of states (DOS). The carriers are free to move in all directions leading to only a small fraction of injected carriers contribution to power in the lasing mode. The improvements in wafer-growth technologies enable the control of the epitaxial layer thickness to sub-nanometre ranges and led to the development of quantum well (QW) and QD.

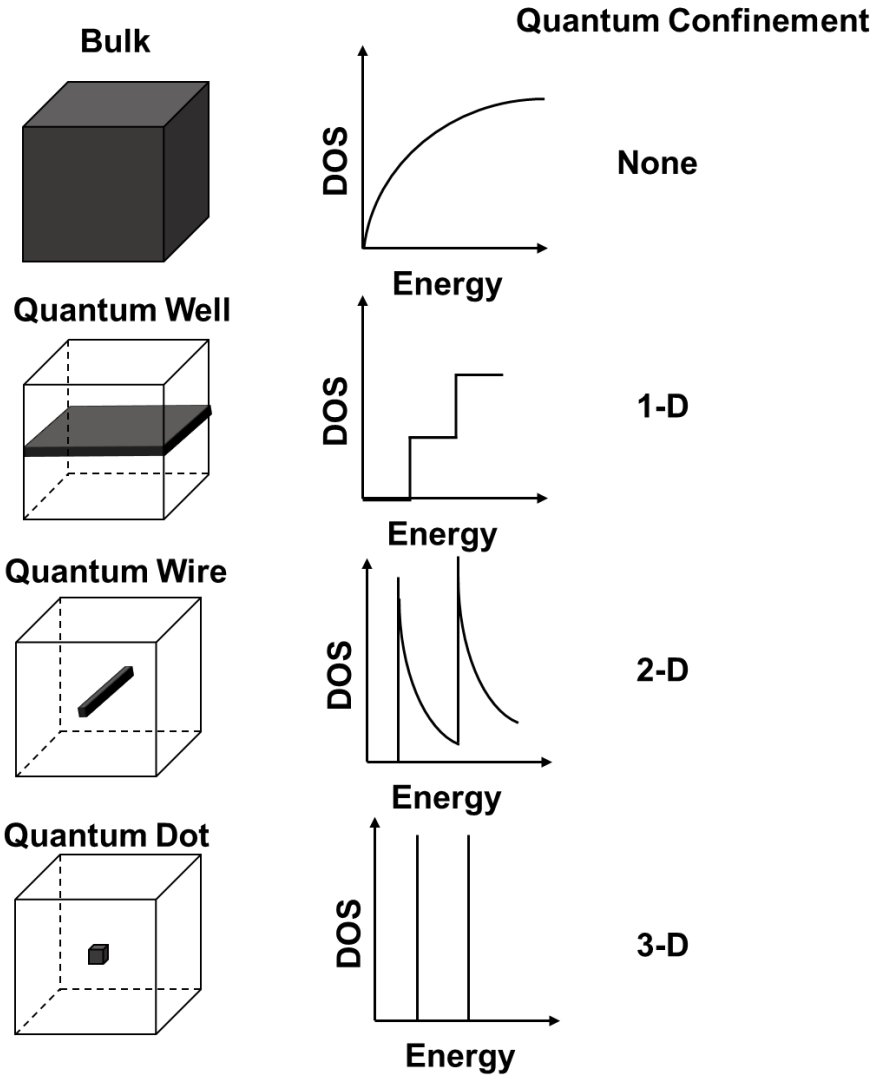

Figure 1.2 Schematic comparison of the density of states for different confinement degrees.

In 1974, Dingle *et al.* proposed a new kind of ultra-thin QW layer as the active region where there is one-dimensional (1D) confinement and a step-like DOS [8]. These lasers have lower threshold current density compared to bulk material-based lasers [9]-[11]. However, the characteristics temperature (T_0) of these devices are lower than desired because of the small energy gap between the conduction and valence-bands of the confined levels and the barrier layers [12], which restricts uncooled operation of the device in high-temperature environments. In 1982, Arakawa and Sakaki proposed a material with three-dimensional (3D) quantum confinement and delta-like DOS. They modelled the threshold current density of lasers as a function of temperature for devices with increasing quantization from 3D to 0D confinement and the results showed considerable improvement in the characteristic temperature [13]. Initial QD structures were fabricated by using electron beam lithography and focused ion beam milling or a wet etch [14]. Those attempts all suffered from large QD size, high defect densities, and a low dot density. Thanks to considerable advances in epitaxial growth techniques for QD, self-assembled QD ensembles with high uniformity, and high density have been successfully manufactured avoiding etch damage [15]-[17]. The Stranski-Krastanov (S-K) growth technique relies on a mismatched lattice constant of the deposited material compared to the substrate [18]. The first few monolayers grown will share the same lattice constant as the substrate and is known as the wetting layer. When the critical thickness has been exceeded, the accumulated strain is relaxed through the formation of randomly distributed islands. The lateral sizes of these islands are within the order of 10's nm, with vertical height typically less than 10 nm, therefore 3D quantum confinement has been achieved [19],[20]. As they are self-assembled, QD grown using this method exhibit a large variation in size, a phenomenon that is reflected in the inhomogeneous line-width of the QD emission. The lowest energy state of QD is called ground state (GS) and the second lowest energy state is known as the 1st excited state (ES_1).

As shown in Figure 1.3, the energy state density of an ideal QD system, where all dots have a uniform distribution of size shape and composition, is a set of discrete levels separated by regions of forbidden states. The line-width of the individual QD is described by a homogeneous line-width and is determined by the finite lifetime of the e-h pair due to radiative and non-radiative recombination. This homogeneous line-width is therefore a function of temperature and carrier density. Even though inhomogeneous broadening cannot be completely avoided, several unique features of QD lasers compared to QW have attracted considerable attention and have been demonstrated. These include low threshold current density [21], [22], decreased line-width enhancement factor [23], ultra-broad bandwidth [24], [25], the possibility of two-state lasing [26], [27], improved high-speed modulation

[28] and high T_0 value (temperature insensitive threshold current) [29]-[31] due to strong quantum confinement effect.

Alongside attempts to achieve the theoretical predictions of QD in terms of threshold and temperature insensitivity for laser by working to minimise the inhomogeneous line-width, there were many researchers seeking to use the inhomogeneity of the QD ensembles as an advantage to achieve broad spectral bandwidth sources such as SLDs [32]-[34]. As a result, use of SLDs has been demonstrated for a number of applications, such as optical fibre-based sensors [35], biomedical imaging [36], wavelength division multiplexing system testing [37], and other optoelectronic systems. Since the first demonstration of QD-based SLD, several tens of nanometre bandwidth were achieved by utilising the natural broadening due to size and composition fluctuations in addition to state filling [38]-[41].

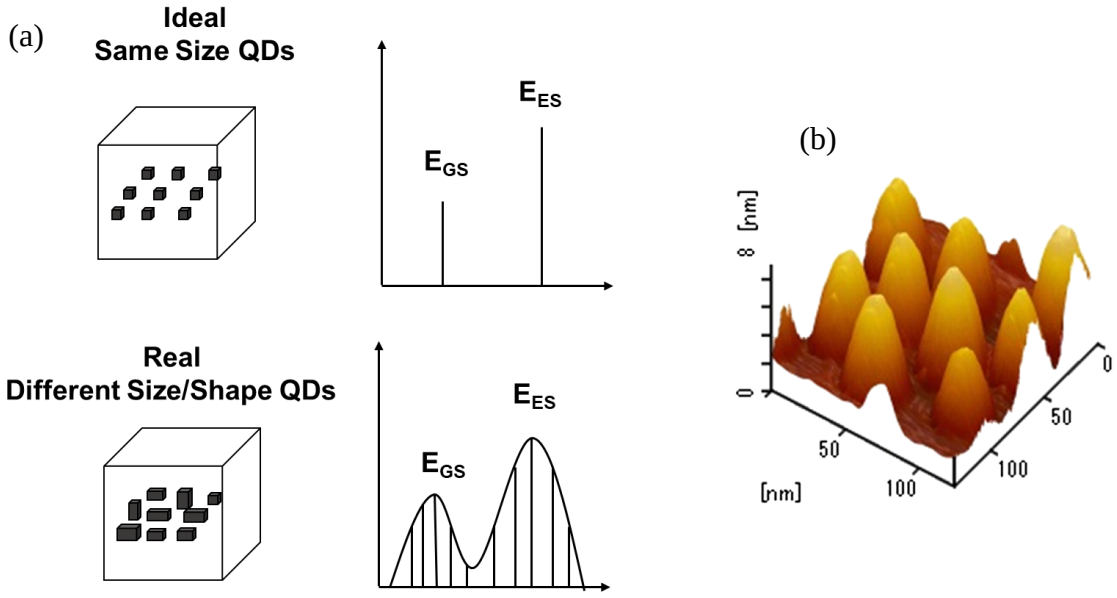

Figure 1.3 (a) Ideal and Real Size QD and resultant density of states (b) real QD grown by S-K method [42].

1.4 Self-Assembled Quantum Dot Superluminescent Diodes

SLDs, which combine a high brightness of semiconductor lasers and a broadband emission spectrum of semiconductor light-emitting diodes, have emerged as ideal low-coherence light sources for medical imaging such as optical coherence tomography (OCT) [33], [43]. OCT is a low-coherence technique based on a Michelson interferometer, where the axial resolution (l_c) is governed by the spectral bandwidth ($\Delta\lambda$) and central wavelength (λ_0) of the light source with a Gaussian spectral shape and l_c given by [44]

$$l_c = \frac{2\ln(2)}{\pi}\frac{{\lambda_0}^2}{\Delta\lambda} \tag{1.2}$$

SLD emission in the near-infrared (NIR) region is important for applications like OCT since the deepest penetration into tissue can be achieved in this wavelength range, owing to low scattering and absorption in biological tissues [45]. The emission wavelength of QD in the NIR region (1-1.3 μm) meets this requirement. Moreover, SLDs using S-K grown QD as their active region have naturally broad emission bandwidth due to size and composition fluctuations and state filling of the QD. QD-SLDs have been intensively investigated to achieve a broad spectral bandwidth together with high output power [46]-[50]. To increase the spectral bandwidth, a deliberate increase of the dot size dispersion is a straightforward method [51]-[53]. In addition, the bandwidth can be widened by incorporating the InAs QD layers in InGaAs QW of different indium compositions [54]. Another method used to broaden the bandwidth of QD-SLDs is by inserting an Al-GaAs layer beneath the In(Ga)As QD layers [55], increasing the growth rate [40], or decreasing the growth temperature [56] to decrease the indium migration length and increase the number of nucleation centres on the growth surface. Flatter and wider emission spectra from InAs/GaAs QD SLDs was achieved by optimization and control of growth parameters such as the variation of the thickness of layers [57]-[58].

To further broaden the emission bandwidth of QD-based SLDs, various methods have been pursued by manipulating the structure of the active region. For instance, by using “chirped” InAs QD multi-layers (varying peak GS and ES emission of different layers) as well as involving GS and ES transition simultaneously, a spectral bandwidth of 121 nm was achieved [59]. In the chirped quantum dot approach, InAs can be used to grow quantum dots with different sizes and emission wavelengths, which can be combined with GaAs barriers to achieve a broad range of emission wavelengths. However, because of the differences in the bandgap and other material properties between GaAs and InAs, strain can become a significant factor in the growth of quantum dots using these materials. Careful control of the growth conditions and strain is necessary to ensure that the quantum dots are stable and have the desired properties. Utilising a rapid thermal-annealing process on an InAs multiple QD layer structure, QD SLDs with 146 nm bandwidth were also demonstrated [60]. The application of post-growth annealing and modulation *p*-doping in addition to chirped QD multilayers have been used to improve spectral width [61]. The use of hybrid QW/QD for the active region has also been demonstrated to tailor the emission bandwidth and gain spectrum of the SLD [62]. OCT heavily relies on broad emission to achieve high axial resolution for clear images. According to Eq. 1.2, the axial resolution is inversely proportional to bandwidth. For skin imaging, the central wavelength is fixed to the biological

window of 1200-1350 nm. The bandwidth of 290 nm in this region provides a theoretical OCT resolution of 2.9 μm [63].

1.5 Self-Assembled Quantum Dot Lasers

In 1994, the first current injection laser based on self-assembled QD with emission at 1.3 μm was demonstrated [64] which is an important wavelength for telecommunications that is currently met by InP QW lasers. Due to the lower carrier confinement and poor temperature stability [65]-[66], InP QW lasers often require an active cooling system to maintain device performance over the temperature ranges for data-centres, leading to high costs. A high T_0 removes the requirement for the incorporation of costly Peltier packaging in devices. This goes alongside the associated complexity of feedback isolation circuitry to inhibit external feedback to the laser. On the other hand, GaAs based lasers can be grown on larger wafers (6" c.f. 4" for InP) leading to lower manufacturing costs and also have higher T_0 values due to larger band offset. The appearance of self-assembled QD on GaAs substrate opened opportunities for near-infrared semiconductor lasers [64]. There has been continued research on producing high-quality InGaAs/GaAs QD lasers since they reach 1.3 μm and beyond. Improved performance has been realized for 1.3 μm QD lasers with a low threshold current density of 19 A/cm^2 demonstrated for oxide confined InGaAs/GaAs QD lasers [21]. Other advances include the demonstration of devices with a high characteristic temperature of 161K between 0 and 80 ºC [67] and enhanced small-signal modulation bandwidth of 15 GHz and T_0 of 237K [68], as well as 10 Gb/s 1.3 μm lasers at high operating temperatures up to 100 ºC [69].

For the telecoms market, a cooler-free laser with temperature insensitivity would reduce cost and improve environmental impact. The most common types of QD-based lasers are edge-emitting lasers such as FP [70] or DFB lasers [71] due to their simplicity in fabrication, and ability to provide high power. However, longer chip lengths are required to provide high output power which may lead to multimode operation and may not be able to offer an ideal beam quality. In addition, they often require complex manufacturing and testing processes due to the requirement of cleaving facets to create optical feedback. An attractive alternative to the standard laser diode is a vertical cavity surface emitting lasers (VCSELs) [72], [73] which have DBR mirrors above and below the active region of the laser. Since the light output is normal to wafer surface, they can be tested on wafer, and this reduces manufacturing costs. They also offer symmetric beams but are limited to low (sub 10 mW) single mode power levels due to their structure, with area scaling resulting in higher-power multi-mode lasers. A high power, narrow divergence, symmetric single lobe beam is desired

to achieve high optical coupling to single mode fibre and long-distance communication. The limitation of single mode operation of VCSEL poses limitations for some applications.

PCSELs have emerged as new class of semiconductor lasers that incorporate a two-dimensional (2D) photonic crystal into a semiconductor laser structure [74]. They have drawn significant attention due to the high-power single-mode vertical emission with narrow divergence, beam steering [75], control of the wavelength, and polarization [76]. As the gain medium in epitaxially regrown PCSELs, QW has so far been used universally [74], [77]. QD active media offer a number of advantages which have been mentioned above such as temperature-insensitive operation [78], low threshold current density [79], and feedback insensitivity [80], and are especially interesting for silicon photonics applications [81]. Additionally, the ability to utilise both the GS and ES of the QD allows multiple emission wavelengths from one heterostructure [82], with the ES offering both higher saturated gain and direct modulation rates [83].

QDs can be integrated with passive waveguides in several ways. One approach is to use grating couplers, which are devices that use a periodic structure of grooves or ridges on the surface of a waveguide to couple light into or out of the waveguide. By placing the QDs close to the grating coupler, the emitted light can be directed into the waveguide through the periodic structure of the grating, allowing for efficient coupling of the light emitted by the QDs into the waveguide. Another approach is to use a hybrid integration scheme, in which the QDs are grown separately and then bonded onto the silicon waveguide. This approach allows for greater control over the QD properties and can result in higher coupling efficiency between the QDs and the waveguide.

As compared to QW active elements, QD laser material has demonstrated a 30 dB reduction in sensitivity to external feedback [84]. The insensitivity of PCSELs to external feedback has not yet been discussed in the literature. However, it is possible to make the following estimate to provide a ballpark figure for the PCSEL. Typical values of out-of-plane loss of in-plane lasing power are 20-40 cm^{-1} [85], where the out-of-plane loss represents the probability of the light scattering out of the plane of the PCSEL. A value of $25cm^{-1}$ corresponds to a characteristic length of ~400 μm to give a 37% (1/e) chance of scattering out. Given a period of ~1/3 μm, this corresponds to a ~1/1000 probability of in-plane light scattering out at each period of the PC. If we assume that the coupling of incident light to in-plane light has the same probability of coupling in-plane light to surface emission, and the light only makes one pass of the PC (this is not the case as typically a mirror will be positioned to reflect light back to the PC with identical phase to maximise output power,

providing two chances to be coupled), then we may expect a 1000-fold (30 dB) reduction in the coupling of light in-plane, as compared to an edge-emitting DFB. This drops to 27 dB if we consider the light has a second pass of the PC due to a mirror integrated within the device structure. The combination of PCSELs and QD active elements, therefore, suggests a possible ~60 dB reduction in sensitivity to external feedback.

1.6 Thesis Outline

This chapter has provided a brief background on semiconductor lasers and materials. 1.3 μm QD based photonic devices have introduced. The applications of QD-based light emitting devices specifically telecommunication and medical imaging (OCT) have been highlighted and the reasoning behind why QD lasers are beneficials have been established.

Chapter 2 provides an overview of the fabrication and experimental methods carried out in this research. This includes a general description of fabrication process flow for making SLDs and PCSELs developed in my PhD, together with details of those technological steps that were developed or optimised in my research.

Chapter 3 presents an analysis of the effect of ridge etch depth on QD-based SLD performance. The influence of thermal effects on SLDs was also studied for both etch depths. The effect of extremely high temperature operation on the optical performance of GaAs-based QD SLDs for a broad spectral bandwidth light source is also investigated.

Chapter 4 provides an analysis of hybrid QW/QD actives for SLD applications utilising high density QD layers to achieve high modal gain while maintaining broad bandwidth. Three hybrid QW/QD SLD devices are compared. All these structures have higher modal gain compared to previous works hybrid QW/QD structures due to the high dot density and the gain spectrum is wider due to the spectral positioning of the QW to shorter wavelength. Future designs are then described and discussed.

Chapter 5 presents epitaxially regrown QD-based PCSELs. The ability to utilise both the GS and ES of the QD allows multiple emission wavelengths from one heterostructure. The epitaxial re-growth processes developed is discussed, and the effect of PCSEL device area, PC atom shape (etch depth, feature size, and corresponding re-grown feature), and crystallographic orientation of the PC on device performance are explored.

Bibliography

[1] G. P. A. Agrawal, N. K. Dutta, and D. Renner., "Long-Wavelength Semiconductor Lasers," *IEEE journal of quantum electronics,* vol. 23, no. 5, p. 641, 1987.

[2] N. Holonyak., "The Semiconductor Laser: A Thirty-Five-Year Perspective Invited Paper," *Proceedings of the IEEE,* vol. 85, no. 11, p. 1678-1693, 1997.

[3] R. N. Hall, G. E. Fenner, J. D. Kingsley, T. J. Soltys, and R. O. Carlson., "Coherent Light Emission from GaAs Junctions," *Physical Review Letter,* vol. 9, no. 9, p. 366-368, 1962.

[4] H. Kroemer., "A Proposed Class of Hetero-junction Injection Lasers," *Proceedings of the IEEE,* vol. 51, no. 12, pp. 1782–1783, 1963.

[5] I. Hayashi, M. B. Panish, P. W. Foy, and S. Sumski., "Junction lasers which operate continuously at room temperature," *Applied Physics Letter,* vol. 17, no. 3, p. 109-111, 1970.

[6] Z. I. Alferov., "The history and future of semiconductor heterostructures," *Semiconductors,* vol. 32, no. 1, p. 1-14, 1998.

[7] L. A. Coldren, S. W. Corzine, and M. L. Masanovic., "*Diode lasers and photonic integrated circuits,*" John *Wiley & Sons,* 2012.

[8] R. Dingle, W. Wiegmann, and C. H. Henry., "Quantum States of Confined Carriers in very Thin $Al_xGa_{1-x}As$-GaAs- $Al_xGa_{1-x}As$ Heterostructures," *Physical Review Letters,* vol. 33, no. 14, p. 827-828, 1974.

[9] J. P. van der Ziel, R. Dingle, R. C. Miller, W. Wiegmann, and W. A. Nordland., "Laser oscillation from quantum states in very thin GaAs-$Al_{0.2}Ga_{0.8}As$ multilayer structures," *Applied Physics Letters,* vol. 26, no. 8, p. 463-465, 1975.

[10] W. T. Tsang., "Extremely low threshold (AlGa)As graded-index waveguide separate-confinement heterostructure lasers grown by molecular beam epitaxy," *Applied Physics Letters,* vol. 40, no. 3, p. 217-219, 1982.

[11] R. D. Dupuis, P. D. Dapkus, N. Holonyak, E. A. Rezek, and R. Chin., "Room-temperature laser operation of quantum-well $Ga_{(1-x)}Al_xAs$-GaAs laser diodes grown by metalorganic chemical vapor deposition," *Applied Physics Letters,* vol. 32, no. 5, p. 295-297, 1978.

[12] R. Chin, N. Holonyak, B. A. Vojak, K. Hess, R. D. Dupuis, and P. D. Dapkus., "Temperature dependence of threshold current for quantum-well $Al_xGa_{1-x}As$-GaAs heterostructure laser diodes," *Applied Physics Letters*, vol. 36, no. 1, p. 19-21, 1980.

[13] Y. Arakawa and H. Sakaki., "Multidimensional quantum well laser and temperature dependence of its threshold current," *Applied Physics Letters*, vol. 40, no. 11, p. 939-941, 1982.

[14] H. Temkin, G. J. Dolan, M. B. Panish, and S. N. G. Chu., "Low-temperature photoluminescence from InGaAs/InP quantum wires and boxes," *Applied Physics Letters*, vol. 50, no. 7, p. 413-415, 1987.

[15] Y. Miyamoto, Y. Miyake, M. Asada, and Y. Suematsu., "Threshold Current Density of GalnAsP/InP Quantum-Box Lasers," *IEEE journal of quantum electronics*, vol. 25, no. 9, p. 2001-2006, 1989.

[16] D. J. Eaglesham and M. Cerullo., "Dislocation-Free Stranski-Krastanow Growth of Ge on Si (100)," *Physical review letters*, vol. 64, no. 16, p. 1943, 1990.

[17] P. B. Joyce, T. J. Krzyzewski, G. R. Bell, B. A. Joyce, and T. S. Jones., "Composition of InAs quantum dots on GaAs (001): Direct evidence for (In, Ga) As alloying," *Physical Review B*, vol. 58, no. 24, p. R15981, 1998.

[18] W. Seifert, N. Carlsson, M. Miller, M.-E. Pistol, L. Samuelson, and L. R. Wallenberg., "In-situ growth of quantum dot structures by the Stranski-Krastanow growth mode," *Progress in Crystal Growth and Characterization of Materials*, vol. 33, no. 4, p 423-471, 1996.

[19] V. A. Shchukin, N N Ledentsov, P. S. Kop'eV, and D. Bimberg., "Spontaneous Ordering of Arrays of Coherent Strained Islands," *Physical Review Letters*, vol.75, no. 16 , p. 2968, 1995.

[20] V. A. Shchukin, N. N. Ledentsov, M. Grundmann, P. S. Kop'eV, and D. Bimberg., "Strain-induced formation and tuning of ordered nanostructures on crystal surfaces," S*urface Science*, vol. 352, p. 117-122, 1996.

[21] G. Park, O. B. Shchekin, D. L. Huffaker, and D. G. Deppe., "Low-threshold oxide-confined 1.3-μm quantum-dot laser," *IEEE Photonics Technology Letters*, vol. 12, no. 3, p. 230-232, 2000.

[22] D. G. Deppe, K. Shavritranuruk, G. Ozgur, H. Chen, and S. Freisem., "Quantum dot laser diode with low threshold and low internal loss," *Electronics Letters*, vol. 45, no. 1, p. 54-56, 2009.

[23] R. R. Alexander, D. T. D. Childs, K. M. Groom, and H. Y. Liu., "Zero and controllable Linewidth Enhamcement Factor in p-Doped 1.3um Quantum Dot Laser," *Japanese journal of applied physics*, vol. 46, no. 4S, p. 2421, 2007.

[24] Z. Y. Zhang, Z. G. Wang, B. Xu, P. Jin, Z. Z. Sun, and F. Q. Liu., "High-Performance Quantum-Dot Superluminescent Diodes," *EEE Photonics Technology Letters*, vol. 16, no. 1, p. 27–29, 2004.

[25] Z. Y. Zhang, R. A. Hogg, X. Q. Lv, and Z. G. Wang., "Self-assembled quantum-dot superluminescent light-emitting diodes," *Advances in Optics and Photonics*, vol. 2, no. 2, p. 201-228, 2010.

[26] A. Markus, J. X. Chen, C. Paranthoen, A. Fiore, C. Platz, and O. Gauthier-Lafaye., "Simultaneous two-state lasing in quantum-dot lasers," *Applied Physics Letters*, vol. 82, no. 12, p. 1818-1820, 2003.

[27] C. Liu, H. Wang, Q. Meng, B. Gao, and K. S. Ang., "Modal gain and photoluminescence investigation of two-state lasing in GaAs-based 1.3 μm InAs/InGaAs quantum dot lasers," *Applied Physics Express*, vol. 6, no. 10, p. 10702, 2013.

[28] Z. Yao, C. Jiang, X. Wang, H. Chen, H. Wang, L. Qin, and Z. Zhang., "Recent Developments of Quantum Dot Materials for High Speed and Ultrafast Lasers," *Nanomaterials*, vol. 12, no. 7, p. 1058, 2002.

[29] O. B. Shchekin and D. G. Deppe., "Low-threshold high-T_0 1.3-μm InAs quantum-dot lasers due to p-type modulation doping of the active region," *EEE Photonics Technology Letters*, vol. 14, no. 9, p. 1231–1233, 2002.

[30] C. Y. Liu, S. F. Yoon, Q. Cao, C. Z. Tong, and H. F. Li., "Low transparency current density and high temperature operation from ten-layer p -doped 1.3 μm InAs/InGaAs/GaAs quantum dot lasers," *Applied physics letters*, vol. 90, no. 4, p. 041103, 2007.

[31] K. Otsubo, N. Hatori, M. Ishida, S. Okamura, T. Akiyama, Y. Naka, H. Ebe, M. Sugawara, and Y. Arakwa "Temperature-Insensitive Eye-Opening under 10-Gb/s Modulation of 1.3μm p-doped Quantum-Dot Lasers without Current Adjustments," *Japanese Journal of Applied Physics*, vol. 43, no. 8B, p. 1124, 2004.

[32] C. F. Lin and B. L. Lee., “Extremely Broadband AlGaAs/GaAs Superluminescent diodes,” *Applied Physics Letters*, vol. 71, p. 1598-1600, 1997.

[33] V. R. Shidlovski and J. Wei., “Superluminescent diodes for optical coherence tomography,” In *Test and Measurement Applications of Optoelectronic Devices SPIE*, vol. 4648, p. 139-147, 2002.

[34] G. A. Alphonse, D. B. Gilbert, M. G. Harvey, and M. Ettenberg., “High-Power Superluminescent Diodes,” *IEEE Journal of Quantum Electronics*, vol. 24, no. 12, p. 2454-2457, 1988.

[35] N. S. K. Kwong, K. Y. Lau, N. Bar-Chaim, I. Ury, and K. Lee, "High Power GaAlAs Superluminescent Diode For Fiber Sensor Applications," in *Optical Fiber Sensors*, p.FDD2, 1988.

[36] V. R. Shidlovski, and J. Wei., “Superluminescent diodes for optical coherence tomography.” In *Test and Measurement Applications of Optoelectronic Devices SPIE*, vol. 4648, pp. 139-147. 2002.

[37] Z. Y. Zhang, Z. G. Wang, B. Xu, P. Jin, Z. Z. Sun, and F. Q. Liu., “High-Performance Quantum-Dot Superluminescent Diodes,” *IEEE Photonics Technology Letters*, vol. 16, no. 1, p. 27-29, 2004.

[38] Z. Sun, D. Ding, Q. Gong, W. Zhou, B. Xu, and Z. G. Wang., “Quantum-dot superluminescent diode: A proposal for an ultra-wide output spectrum,” *Optical and quantum Electronics*, vol. 31, no. 12, p. 1235-1246, 1999.

[39] Z. Y. Zhang, Z. G. Wang, B. Xu, P. Jin, Z. Z. Sun, and F. Q. Liu., “High-Performance Quantum-Dot Superluminescent Diodes,” *IEEE Photonics Technology Letters*, vol. 16, no. 1, p. 27-29, 2004.

[40] N. Liu, P. Jin, and Z. G. Wang., “InAs/GaAs quantum-dot superluminescent diodes with 110 nm bandwidth,” *Electronics Letters*, vol. 41, no. 25, p. 55-56, 2005.

[41] H. S. Dijie, C. E. Dimas, D. N. Wang, B. S. Ooi, J. C. M. Hwang, G. T. Dang, and W. H. Chang., “InGaAs/GaAs Quantum-Dot Superluminescent Diode for Optical Sensor and Imaging,” *IEEE Sensors Journal*, vol. 7, no. 2, pp. 251–257, 2007.

[42] K. Nishi, T. Kageyama, M. Yamaguchi, Y. Maeda, K. Takemasa, T. Yamamoto, M. Sugawara, Y. Arakawa, “Molecular beam epitaxial growths of high-optical-gain InAs quantum dots on GaAs for long-wavelength emission”, Journal of Crystal Growth, 378, p. 459-462, 2013.

[43] R.A. Hogg, P. D. L. Greenwood, D. T. D. Childs, N. Krstajić, K. Kennedy, K. M. Groom, M. Hugues, M. Hopkinson, L.E. Smith, S.J. Matcher, M. Bonesi, S. Macneil and R. Smallwood "GaAs based quantum dot superluminescent diodes for optical coherence tomography of skin tissue," In *International Conference on Computers and Devices for Communication (CODEC)*, p. 1-6. 2009.

[44] D. Huang, E. A. Swanson, C. P. Lin, J. S. Schuman, W. G. Sitnson, W. Chang, M. R. Hee, T. Flotte, K. Gregory, C. A. Puliafito, J. G. Fujimoto., "Optical coherence tomography.," *Science*, vol. 254, no. 5035, p. 1178-1181, 1991.

[45] D. Childs, S. Matcher, and R. Hogg., "Lasers and SLEDs for optical coherence tomography," *17th International Conference on Transparent Optical Networks (ICTON)*, p. 2-5, 2015.

[46] J. H. Liang, T. Maruyama, Y. Ogawa, S. Kobayashi, J. Sonoda, H. Urae, S. Tomita, Y. Tomioka, and S. Kon., "High-power high-efficiency superluminescent diodes with J-shaped ridge waveguide structure," *Conference Proceedings. 14th Indium Phosphide and Related Materials Conference*, p. 119–122, 2002.

[47] M. Z. M. Khan, H. H. Alhashim, T. K. Ng, and B. S. Ooi., "High-power and high-efficiency 1.3-μm superluminescent diode with flat-top and ultrawide emission bandwidth," *IEEE Photonics Journal*, vol. 7, no. 1, p. 1600308, 2015.

[48] A. Kafar, S. Stanczyk, G. Targowski, T. Oto, I. Makarowa, P. Wisniewski, T. Suski and P. Perlin., "High-optical-power InGaN superluminescent diodes with 'j-shape' waveguide," *Applied Physics Express*, vol. 6, no. 9, p. 092102, 2013.

[49] A. F. Forrest, M. Krakowski, P. Bardella, and M. A. Cataluna., "High-power quantum-dot superluminescent tapered diode under CW operation," *Optics Express*, vol. 27, no. 8, p. 10981-10990, 2019.

[50] I. K. Han, H. C. Bae, W. J. Cho, J. I. Lee, H. L. Park, T. G. Kim, J. I. Lee., "Study of chirped quantum dot superluminescent diodes," *Japanese journal of applied physics*, vol. 44, no. 7 S, p. 5692-5695, 2005.

[51] Z. Z. Sun, D. Ding, Q. Gong, W. Zhou, B. Xu, and Z. G. Wang., " Quantum dot superluminescent diode: A proposal for an ultra-wide output spectrum," *Optical and quantum Electronic*, vol. 31, no. 12, p- 1235-1246, 1999.

[52] C. Y. Ngo, S. F. Yoon, and W. J. Fan., " Tuning InAs quantum dot for high areal density and wideband emission," *Journal of Applied Physics*, vol. 90, no.11, p. 113103, 2007.

[53] S. Haffouz, P. J. Barrios, R. Normandin, D. Poitras, and Z. Lu., "Ultrawide-bandwidth, superluminescent light-emitting diodes using InAs quantum dots of tuned height," *Optics letters*, vol. 37, no. 6, p. 1103-1105, 2012.

[54] S. K. Ray, K. M. Groom, M. D. Beattie, H. Y. Liu, M. Hopkinson, and R. A. Hogg., "Broad-Band Superluminescent Light-Emitting Diodes Incorporating Quantum Dots in Compositionally Modulated Quantum Wells," *IEEE photonics technology letters*, vol. 18, no. 1, p. 58-60, 2006.

[55] X. Q. Lv, N. Liu, P. Jin, and Z. G. Wang., "Broadband emitting superluminescent diodes with InAs quantum dots in AlGaAs matrix," *IEEE Photonics Technology Letters*, vol. 20, no. 20, p. 1742-1744, 2008.

[56] C. Y. Ngo, S. F. Yoon, W. J. Fan, and S. J. Chua., "Origins of high radiative efficiency and wideband emission from InAs quantum dots," *Applied Physics Letters*, vol. 91, no. 19, p. 191901, 2007.

[57] S. K. Ray, H. Y. Liu, T. L. Choi, K. M. Groom, S. L. Liew, M. Hopkinson and R. A. Hogg., "Molecular beam epitaxial growth of high-power quantum dot super-luminescent diodes," *Japanese journal of applied physics*, vol. 46, no. 4S, p. 2418-2420, 2007.

[58] M. A. Majid, M. Hugues, S. Vézian, D. T. D. Childs, and R. A. Hogg., "Optimization of quantum-dot molecular beam epitaxy for broad spectral bandwidth devices," *EEE Photonics Journal*, vol. 4, no. 6, p. 2066-2073, 2012.

[59] L. H. Li, M. Rossetti, A. Fiore, L. Occhi, and C. Velez., "Wide emission spectrum from superluminescent diodes with chirped quantum dot multilayers," *Electron Letter*, vol. 41, no. 1, p. 41-43, 2005.

[60] Z. Y. Zhang, R. A. Hogg, B. Xu, P. Jin, and Z. G. Wang., "Realization of extremely broadband quantum-dot superluminescent light-emitting diodes by rapid thermal-annealing process," *Optics letters*, vol. 33, no. 11, p. 1210-1212, 2008.

[61] Q. L. Liu, C. C. Hou, H. M. Chen, J. Q. Ning, Q. Z. Li, Y. Q. Huang, Z. Y. Zhao, Z. G. Wang, P. Jin, Z. Y. Zhang., "Effects of Modulation P-Doping on Thermal Stability of InAs/GaAs Quantum Dot Superluminescent Diodes," *Journal of Nanoscience and Nanotechnology*, vol. 18, no. 11, p. 7536-7541, 2018.

[62] S. Chen, K. Zhou, Z. Zhang, J. R. Orchard, D. T. D. Childs, M. Hugues, O. Wada and R. A. Hoggs., "Hybrid quantum well/quantum dot structure for broad spectral bandwidth emitters," *IEEE Journal of Selected Topics in Quantum Electronics*, vol. 19, no. 4, p. 1900209-1900209, 2013.

[63] S. Chen, W. Li, Z. Y. Zhang, D. T. D. Childs, K. Zhou, J. Orchard, K. Kennedy, M. Hugues, E. Clarke, I. Ross, O. Wada and R. A. Hogg., "GaAs-Based Superluminescent Light-Emitting Diodes with 290-nm Emission Bandwidth by Using Hybrid Quantum Well/Quantum Dot Structures," *Nanoscale Research Letters* 1, vol. 10, no. 1, p. 1-8, 2015.

[64] N. Kirstatedter, N.N. Ledentsov, M. Grundmann, D. Bimberg, V. M. Ustinov, S. S. Ruvimov, M. V. Maximov, P. S. Kop'ev, Zh. I. Alferov, U. Richter, P. Werner, U. Gosele and J. Heydenreich., "Low threshold, large T_0 injection laser emission from (InGa) As quantum dots," *Electronics Letters* 30, no. 17, p. 1416-1417, 1994.

[65] K. Takemasa, T. Munakata, M. Kobayashi, H. Wada, and T. Kamijoh., "High-temperature operation of 1.3 μ m AlGaInAs strained multiple quantum well lasers," *Electronics Letters*, vol. 34, no. 12, p. 1231-1233, 1998.

[66] H. Temkin, D. Coblentz, R. A. Logan, J. P. vanderzeil, T. T. Ek, R. D. Yadvish and A. M Sergent., "High temperature characteristics of InGaAsP/InP laser structures," *Applied physics letters*, vol. 62, no. 19, p. 2402-2404, 1993.

[67] O. B. Shchekin and D. G. Deppe., "1.3um InAs quantum dot laser with T_0=161 K from 0 to 80 °C," *Applied physics letters*, vol. 80, no. 18, p. 3277-3279, 2002.

[68] P. Bhattacharya and S. Ghosh., "Tunnel injection $In_{0.4}Ga_{0.6}As$/GaAs quantum dot lasers with 15 GHz modulation bandwidth at room temperature," *Applied physics letters*, vol. 80, no. 19, p. 3482-3484, 2002.

[69] M. Sugawara, and M. Usami., "Handling the heat," *Nature Photon* 3, p. 30–3, 2009.

[70] Y. Tanaka, M. Ishida, K. Takada, Y. Maeda, T. Akiyama, T. Yamamoto, H. Z. Song, M. Yamaguchi, Y. Nakata, K. Nishi, M. Sugawara and Y. Arakawa., "1.3 μm InAs/GaAs High-Density Quantum Dot Lasers," In *IEEE LEOS Annual Meeting Conference Proceedings*, p. 668-669, 2009.

[71] K. Takada, Y. Tanaka, T. Matsumoto, M. Ekawa, H. Z. Song, Y. Nakata, M. Yamaguchi, K. Nishi, T. Yamamoto, M. Sugawara, and Y. Arakawa, "10.3-Gb/s Operation over a Wide Temperature Range in 1.3-μm Quantum-dot DFB Lasers with High Modal Gain," in *Optical Fiber Communication Conference*, p. OThK2, 2010.

[72] H. Saito, K. Nishi, I. Ogura, S. Sugou, and Y. Sugimoto., "Room-temperature lasing operation of a quantum-dot vertical-cavity surface-emitting laser," *Applied physics letters*, vol. 69, no. 21, p. 3140-3142, 1996.

[73] N. Ledentsov Jr., M. Agustin, J. R. Kropp, V. A. Shchukin, V. P. Kalosha, K. L. Chi, Z. Khan, J. W. Shi, N. N. Ledentsov., "Temperature stable oxide-confined 850-nm VCSELs operating at bit rates up to 25 Gbit/s at 150ºC," In *Vertical-Cavity Surface-Emitting Lasers XXII SPIE*, vol. 10552, p. 136-142, 2018.

[74] M. Imada, S. Noda, A. Chutinan, T. Tokuda, M. Murata, and G. Sasaki., "Coherent two-dimensional lasing action in surface-emitting laser with triangular-lattice photonic crystal structure," *Applied physics letters*, vol. 75, no. 3, p. 316-318, 1999,

[75] Y. Kurosaka, S. Iwahashi, Y. Liang, K. Sakaki. E. Miyai, W. Kunishi, D. Ohnishi, S. Noda., "On-chip beam-steering photonic-crystal lasers," *Nature Photonics*, vol. 4, no. 7, pp. 447–450, 2010,

[76] M. Imada, A. Chutinan, S. Noda, and M. Mochizuki., "Multidirectionally distributed feedback photonic crystal lasers," *Physical Review B*, vol. 65, no. 19, p. 1–8, 2002.

[77] B. C. King, R. J. Taylor, P. Ivanov, I. Butler, T. S. Roberts, D. T. D. Childs and R. A. Hogg., "In-Line Non-Destructive Characterisation Method for PCSELs," In IEEE *International Semiconductor Laser Conference (ISLC)*, p. 1-2, 2018.

[78] K. Otsubo, N. Hatori, M. Ishida, S. Okamura, T. Akiyama, Y. Naka, H. Ebe, M. Sugawara, and Y. Arakwa "Temperature-Insensitive Eye-Opening under 10-Gb/s Modulation of 1.3μm p-doped Quantum-Dot Lasers without Current Adjustments," Japanese Journal of Applied Physics, vol. 43, no. 8B, p. 1124, 2004

[79] R. R. Alexander, D. Childs, and H. Agarwal, "Growth, Fabrication, and Operating Characteristics of Ultra-Low Threshold Current Density 1.3 Quantum Dot Lasers," *Japanese Journal of Applied Physics To*, vol. 44, p. 2520, 2005,

[80] D. O'Brien, S. P. Hegarty, G. Huyet, J. G. McInerney, T. Kettler, M. Laemmlin, D. Bimberg, V. M. Ustinov, A. E. Zhukov, S. S. Mikhrin and A. R. Kovsh., "Feedback sensitivity of 1.3 μm InAs/GaAs quantum dot lasers," *Electron Letter*, vol. 39, no. 25, p. 1819-1820, 2003.

[81] C. Shang, Y. Wan, J. Selvidge, E. Hughes, R. Herrick, K. Mukherjee, J. Duan, F. Grillot, W. W. Chow, and J. E. Bowers., "Perspectives on advances in quantum dot lasers

and integration with Si photonic integrated circuits," *ACS photonics,* vol. 8, no. 9. p. 2555-2566, 2021.

[82] A. Markus, J. X. Chen, C. Paranthoen, A. Fiore, C. Platz, and O. Gauthier-Lafaye., "Simultaneous two-state lasing in quantum-dot lasers," *Applied Physics Letters,* vol. 82, no. 12, p. 1818-1820, 2003.

[83] B. J. Stephens, D. T. D. Childs, H. Shahid and R. A. Hogg., "Direct modulation of excited state quantum dot lasers," *Applied Physics Letters,* vol. 95, no. 6, p. 061101, 2009.

[84] S. A. Sobhani, R. A. Hogg, K. Takemasa, K. Nishi, M. Sugawara, and D. T. D. Childs., "Systematic study of external optical feedback tolerance in 1300 nm quantum dot lasers," *IEEE Journal of Quantum Electronics,* vol. 59, no. 1, p. 1-8, 2023.

[85] K. Hirose, Y. Liang, Y. Kurosaka, A. Watanabe, T. Sugiyama, and S. Noda, "Watt-class high-power, high-beam-quality photonic-crystal lasers," *Nature photonics,* vol. 8, no. 5, p. 406–411, 2014.

Chapter 2: Fabrication and Experimental Method

2.1 Introduction

This chapter describes the process flow, designs and process modules involved in the fabrication of the GaAs-based quantum dot (QD) photonic devices, specifically, superluminescent diodes (SLDs) and photonic crystal surface-emitting lasers (PCSELs). The experimental techniques used in this thesis for characterising SLDs and PCSELs are then outlined.

2.2 Superluminescent Diodes Designs

SLDs are edge-emitting semiconductor light sources that combine the benefits of the high output power of laser diodes (LDs) and the broad emission spectrum of light-emitting diodes (LEDs). Although the primary mechanism of light radiation in lasers is stimulated emission, optical feedback is required. One way of establishing optical feedback is to create a resonant cavity by cleaving facets. When photons are incident on one of the facets a large percentage are reflected and propagate in the opposite direction within the waveguide. To achieve lasing, the gain must be greater than the total optical loss (mirror loss plus the internal loss). The threshold gain coefficient g_{th} can be calculated by considering the resonant cavity length L and facets with reflectivity R_1 and R_2. Lasers require both optical feedback and gain to lase. SLDs have waveguide structures that are very similar to LDs but have insufficient optical feedback to achieve lasing. In SLDs, the light is generated via spontaneous emission at all points in the waveguide and then experiences amplification during propagation along its length i.e., generating further photons through stimulated emission. The suppression of feedback makes this amplified spontaneous emission (ASE) have all possible phases, and hence be incoherent. The suppression of lasing can be achieved by increasing the mirror or waveguide loss. However, we require a high gain within the cavity, so the increase in mirror loss is an ideal manner to achieve high optical powers. A number of methods have been used to reduce facet reflectivity (increasing mirror loss) in SLDs such as (a) tilted waveguide [1] (b) curved (J-shaped) waveguide [2]-[4] (c) multi-section [5]-[7] (d) absorber section [8]-[10] (e) applying anti-reflective (AR) coatings to facets [11] (f) etched facets [12]. AR coating requires a complex deposition method which greatly increases the difficulty of the manufacturing process and the cost of the device. Although the design is not complicated processing for adding absorber sections, the addition of absorber sections to the device

results in an increase in the length of the resonator. An alternative approach is the modification of the waveguide shape from a straight line to a curved (J-shaped), the fabrication of this device is difficult, especially in achieving a smooth side wall at the bend region. The common structure to reduce the facet reflectivity is the single contact tilted waveguide [13]-[15]. The effect of the tilting angle on the facet reflection is studied by Zhang *et al.* [16]. However, the single contact of the tilted waveguide is unable to control to current separately, and therefore the separate control of the bandwidth and output power is not possible. Recently, the segmented contact devices known as multi-sections SLD have become popular as they allow for more flexibility in tailoring the emission spectrum and permitting control of power and bandwidth [17], [18]. The broad bandwidth is desired for OCT applications.

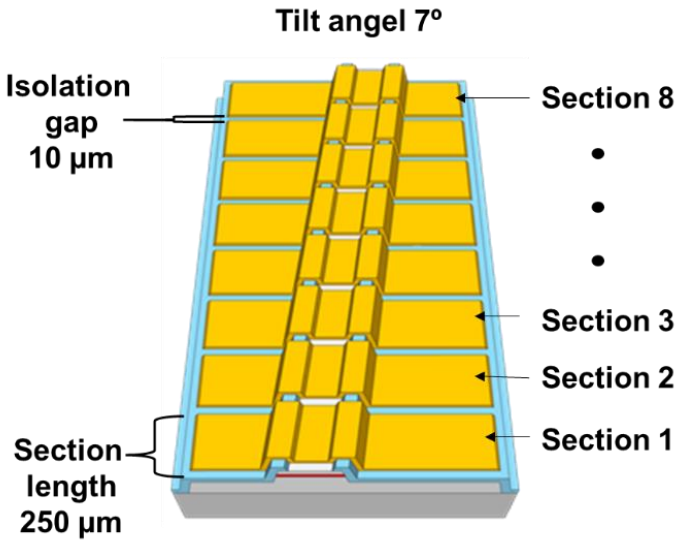

Figure 2.1: Schematic diagram of a tilted segmented contact device.

The tilted waveguide structure developed for SLDs in this thesis, which is shown in Figure 2.1, utilises a segmented contacted with eight 250 µm sections separated by 10 µm wide isolation gaps. The tilted waveguide is utilised for further suppression of the feedback due to the angled facet. The combination of multi-sections contacts with a tilted waveguide offers the advantage of increased output power as well as greater control of the spectral shape [7], [19].

2.3 Fabrication Flow of the superluminescent diodes

The fabrication process of the SLDs includes four main lithography steps. The process flow diagram is shown in Figure 2.2. Before fabrication, the wafer was cleaved using a diamond-tip scriber tool. Samples are then cleaned with acetone and isopropyl alcohol (IPA) in an ultrasonic bath. After solvent-based cleaning, oxygen (O_2) plasma ash is performed.

Cleaning is important before each step of the fabrication process to remove all organic and inorganic contaminants. The first lithography step for mesa etching is used to define the waveguide (mesa etch) after the initial cleaning process. The whole wafer is covered by a dielectric layer (SiO_2) to provide electrical isolation. The second lithography step is carried out to open the window area for metal contact deposition. This was followed by third and fourth lithography steps for *n*-metal contact and bond pad deposition for electrical injection to the top of the devices. Then final lithography step is performed to electrically isolate the sections of the multi-contacts SLD device. The three-dimensional views of the fabrication steps of the ridge waveguide are illustrated in Figure 2.3. Lithography, dry etch process for mesa etching, window opening, dielectric deposition, and metal deposition will be discussed in detail in the following sections.

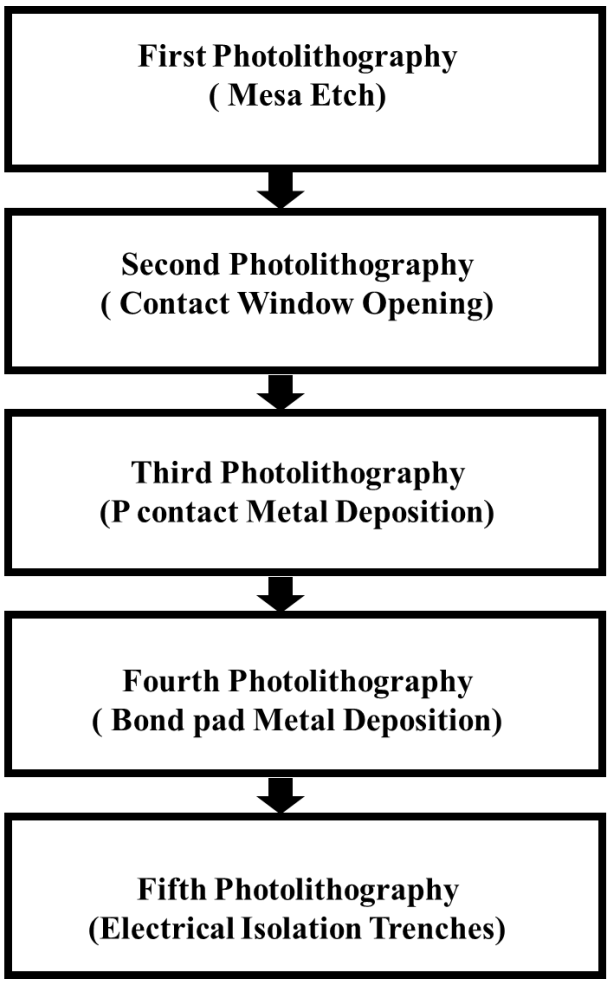

Figure 2.2: Fabrication of SLD flow diagram.

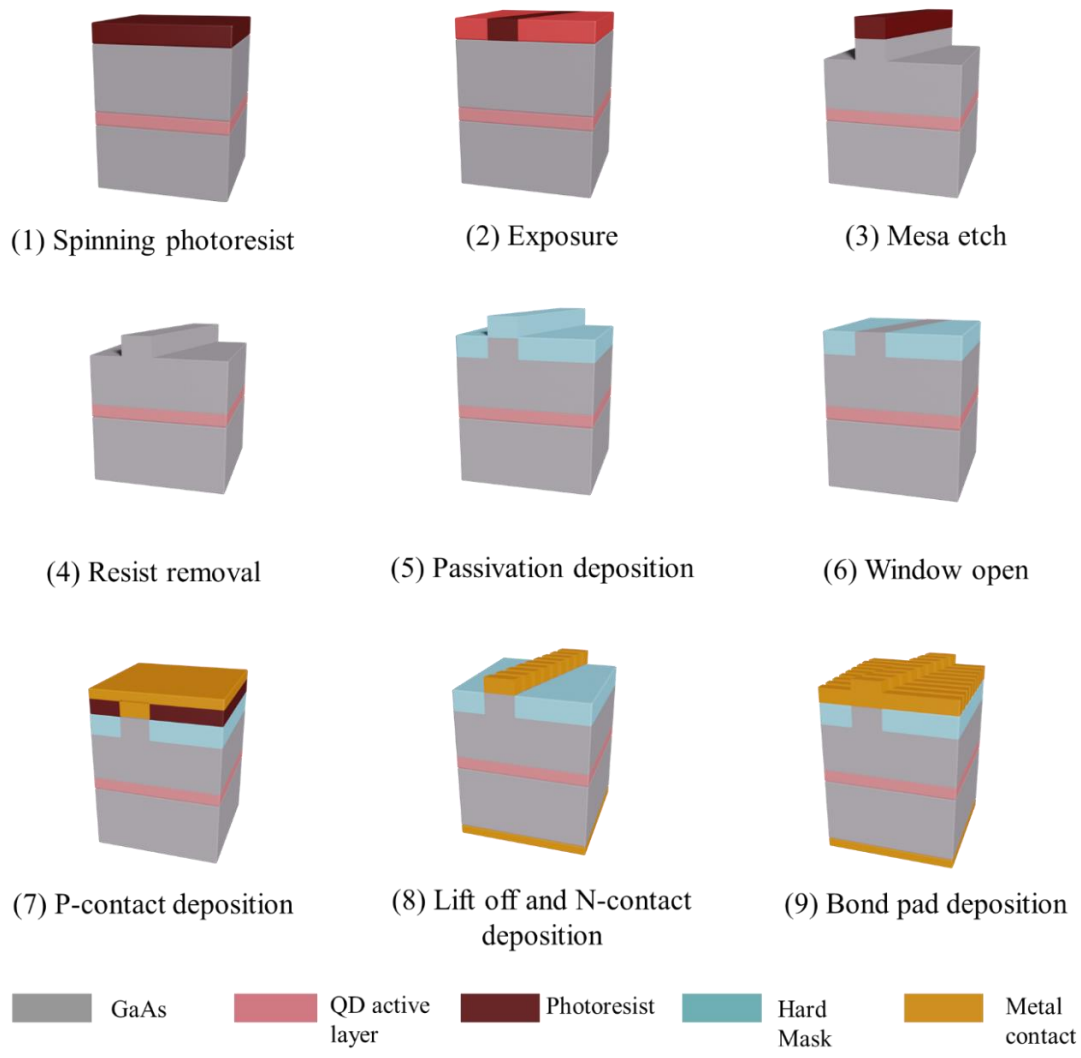

Figure 2.3: The schematic drawings for the process steps involved in the fabrication of SLD.

2.3.1 Lithography

Lithography is used to transfer desired patterns onto the surface of the semiconductor substrate [20]. Pattern transfer is often achieved by optical, or electron beam lithography (EBL) depending on the radiation sources used in the lithography techniques. Optical lithography is used to transfer a pattern from a mask to the sample by taking advantage of a light-sensitive material (photoresist). The mask contains dark and transparent regions. The dark area is coated with chrome to prevent the ultraviolet (UV) light from exposing the photoresist, while the transparent region defines the area to be patterned. EBL is direct writing technique that uses an accelerated electron beam on substrate that have been coated with an electron beam sensitive resist. EBL used computer accessed transcript program to define the features to be generated. The pattern is defined using layout generator software such as L-Edit and converted in a GDSII-type file format. The Belle software was used to

submit the pattern to the e-beam tool and the desired beam current, spot size, and necessary exposure dose settings to expose the resist are defined in that software. Depending on the desired pattern size, photolithography or EBL can be used. In general, features < 1 μm are patterned using EBL, and features > 1 μm are patterned using photolithography.

The lithography steps generally consist of three steps: coating of the resist, exposure by light or electron beam, and development. A radiation sensitive polymer called resist is deposited on the semiconductor sample surface which is then exposed to the specific wavelength of radiation to transfer the desired pattern. There are two kinds of resists: positive and negative. The positive resists can be dissolved in developer after it is exposed, forming a pattern the same as the opaque region of the mask. Negative photoresist becomes cross-linked after exposure and, the pattern formed by it is the same as the transparent region of the mask upon development. Figure 2.4 illustrates the developed results of employing positive and negative photoresists. The most commonly used positive resists in photolithography are microposit S1800 series photoresists such as S1818, S1828, lift-off resist such as LOR 5A, LOR 10A and AZ photoresists such as AZ4562. For EBL lithography, PMMA (positive resist) and HSQ (negative resist) are generally used.

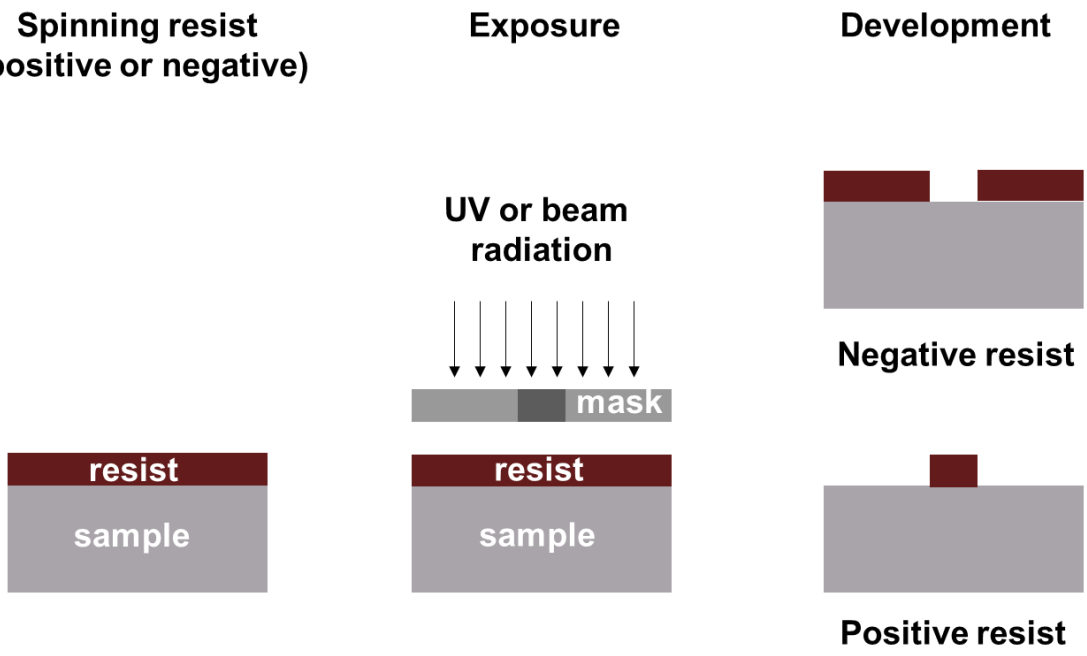

Figure 2.4: Schematic showing positive and negative resist exposure.

For the fabrication of the SLDs, the patterns are > 1 μm and therefore optical lithography is used. For the waveguide definition lithography step, AZ4562 is used as a thick photoresist and is essential as the selectivity between the photoresist mask and semiconductor is 10:1 during the semiconductor etching process. Hard baking is required to reduce the sensitivity

of the resist to etch damage. For the window opening lithography step, S1818 is acceptable to use because the selectivity to photoresist and dielectric film is 3:1 during the RIE dry etch process. For the contact lithography step, a bilayer resists (S1818 and LOR 5A) is used to achieve better lift-off after the metal deposition. Table 2-1 shows the standard process steps of resist for lithography.

Table 2-1: Parameters for photolithography.

Step	AZ4562	S1818	LOR
Spin Resist	4000 rpm for 30 secs	4000 rpm for 30 secs	3000 rpm for 30secs
Soft Bake	100 C for 3 mins	110 C for 2 mins	180 C for 2 mins
Exposure	18 secs	10 secs	
Development	4 mins	4 mins	
Hard Bake	120 C for 2 mins	-	

2.3.2 Mesa Etch Process

Waveguide definition by creating a mesa in the semiconductor is a critical step in the fabrication of SLDs as it defines the physical structures to generate and guide the optical signal as well as to define the current injection area. Any imperfections such as roughness in the sidewall in the mesa etch process would affect the performance of the final device. The waveguide patterns are defined on the sample by lithography and are followed by the removal of the unmasked area of the semiconductor materials (such as GaAs, InP) by etching. The etching of semiconductors can be performed through either wet etching or dry etching. The wet etching technique employs liquid-based etchants (acids or alkalis) to remove the material on the sample. The dry etching technique uses chemically and physically reactive plasmas to remove the desired material. It allows for better control over the direction and depth of material removal, which can result in smaller features with less critical damage compared to wet etching. Moreover, dry etching is usually preferable in waveguide definition due to its repeatability, strong anisotropy, and strongly vertical sidewalls.

The plasma dry etch process is a crucial step in the fabrication of both superluminescent diodes (SLDs) and photonic crystal surface emitting lasers (PCSELs). To optimize this process, various factors need to be considered, including the plasma chemistry, the etching power, and the etching time. The goal of optimization is to achieve precise and reproducible

patterns with high aspect ratios and low sidewall roughness. For SLDs, the plasma dry etch process is typically used to define the ridge structure that confines the lasing mode. To achieve a high-quality ridge structure, the etching process needs to be carefully controlled to avoid damage to the underlying layers and maintain a smooth sidewall profile. This can be achieved by adjusting the process parameters to optimize the ion bombardment and chemical reactions during the etching process.

2.3.2.1 Dry Etching of GaAs Materials

The dry etching processes are widely used in the fabrication of optoelectronic devices. An inductively coupled plasma (ICP) is one of the most suitable etching systems for the etching of the III-V-based material. Dry etching (known as the plasma etching) is carried out in a sealed reactor where the reactants are dissociated by RF power. The direction of incident ions is controlled by the applied voltage. Thus, the dry etch process has high anisotropic etching properties. In addition, the etch rate can be modified by adjusting applied power, pressure, gas flow rate, and other parameters.

2.3.2.2 Initial Dry Etch Process

A soft mask such as AZ4562 or a hard mask such as SiO_2 is usually desirable as the etch mask in the dry etching process. A hard mask is advantageous for the dry etching of small features as they require an initial EBL step to define the pattern and the e-beam resists are generally very thin to achieve high lateral resolution. However, dry-etching using the hard mask results in extra steps in the process such as deposition of the oxide layer, dry etching of the hard mask, and removal of hard mask after the semiconductor etch, as shown schematically in Figure 2.5 (a). This double-step method may enhance the roughness in the waveguide sidewall after etching, as shown in the SEM pictures in Figure 2.6 (a). The performance of a ridge waveguide device is typically limited by the propagation losses, whose main source in high index contrast waveguides is often scattering due to the sidewall roughness. To reduce the process steps and minimise roughness, an alternative single-step technique using a thick photoresist (AZ4562) was applied for the mesa etch of SLD. It was found that the photoresist layer must be thick enough to compensate for the rapid mask erosion during the dry etching process. Hard baking is also essential while using the soft mask to reduce the sensitivity of the resist to etch damage. By using a soft mask, it is also beneficial that the fabrication steps can be reduced which is shown in Figure 2.5 (b).

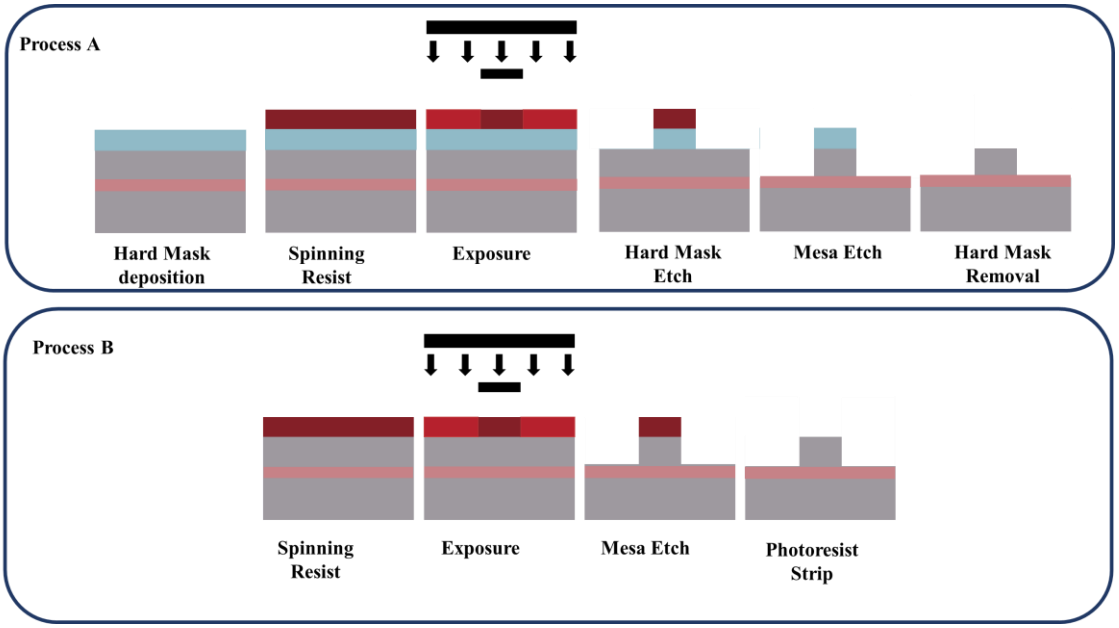

Figure 2.5: Schematic of the process steps for the mesa etching with (a) hard mask (b) soft mask.

Table 2-2 : ICP180 process parameters for etching GaAs/AlGaAs.

Parameter	**Value**
Gas Flow: $SiCl_4$/Ar	7.5/15 sccm
RF Power (ICP/Platen)	350/60 W
Pressure	2.5 mT
Temperature	20 C
Etching Rate	650 nm/mins

For the initial dry etch testing, the mesa etch was performed by ICP with $SiCl_4$/Ar chemistry [21]. The recipe of the ICP etch processes are illustrated in Table 2-2. The etch depth is monitored by the interferometer. After etching, the etch depth is also checked with a Dektak surface profilometer before stripping the mask. To check the sidewall roughness and profile, the test sample was cleaved and checked in an SEM. Even though there is an improvement in sidewall roughness, dry etching using $SiCl_4$/Ar chemistry was found to cause an undercut in the sidewall profile as shown in the SEM picture in Figure 2.6 (b). Sidewall undercutting is undesirable as it can lead to metal discontinuity during later metal deposition steps. Therefore, it is preferable to have positive sidewall to avoid this issue.

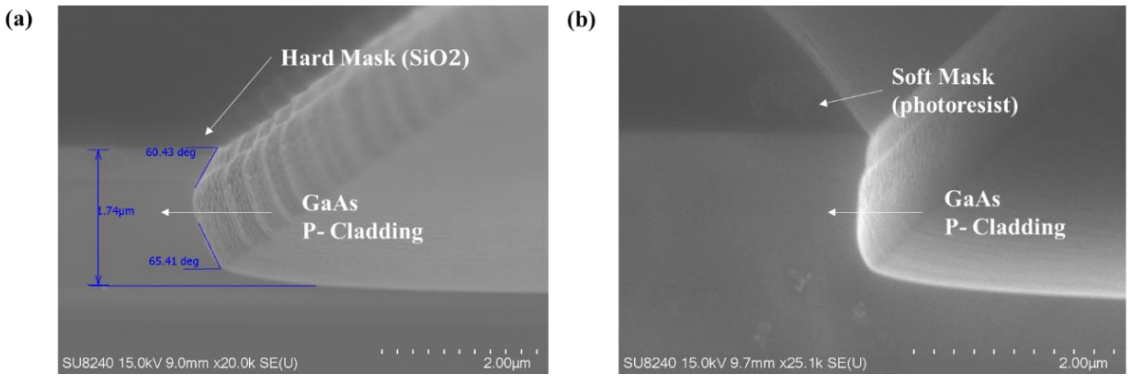

Figure 2.6: Cross-Sectional SEM images of test results of ICP 180 etching by using (a) hard mask (b) soft mask.

2.3.2.3 Improved Dry Etch Process

For the dry etching of III-V compound semiconductors, it has been shown that the use of BCl_3 and Cl_2 chemistry can minimise roughness and produces smooth sidewalls [22],[23]. Another mesa etch test was carried out using this chemistry. The parameters of the recipe are presented in Table 2-3. AZ4562 was used as the soft mask. The test sample was then cleaved and checked in an SEM. The SEM picture shown in Figure 2.7 indicates the straight and relatively smooth sidewall after ICP etching. This slight roughness in the sidewall can further be improved by optimizing the ICP conditions such as reducing the RF chuck power and increasing the ICP source power and so on.

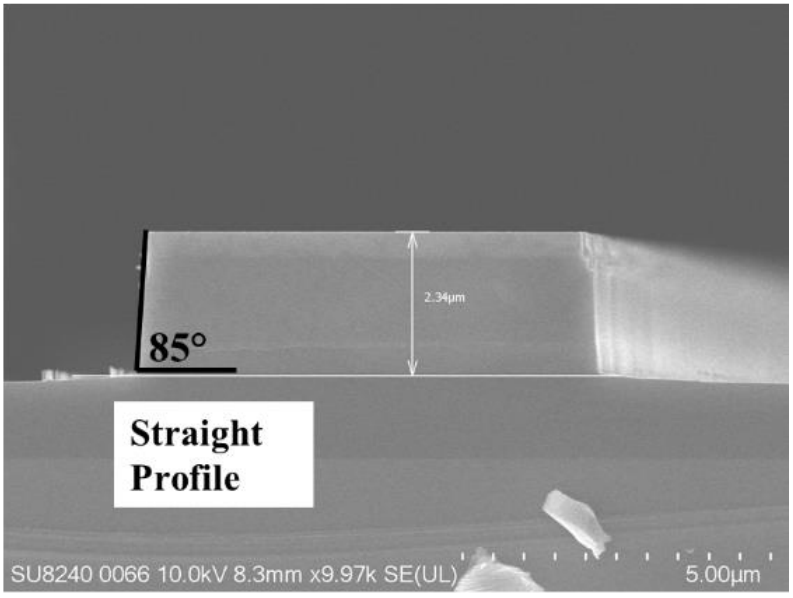

Figure 2.7: Cross-Sectional SEM image of test results of ICP 180 etching. A straight profile with 85º slope is achieved.

Table 2-3: Optimised etch recipe for GaAs/AlGaAs materials in ICP180.

Parameter	Value
Gas Flow: $Cl_2/BCl_3/Ar/N_2$	10/10/10/7 sccm
RF Power (ICP/Platen)	500/50 W
Pressure	5 mT
Temperature	10 C
Etching Rate	1600 nm/mins

2.3.3 Dielectric Deposition

Dielectric films can be used for different applications such as hard mask to protect the unexposed area during mesa etching or an electrical insulator. For SLD fabrication, a 400 nm SiO_2 film was deposited after mesa etch and soft mask removal. This silica film was deposited by an Oxford Instruments plasma-enhanced chemical vapour deposition (PECVD) 80+ which dissociates the reactants ($SiH_4/N_2O/N_2$) and delivers a uniform deposition by injecting the gases evenly through a showerhead inlet. After the deposition of the silica film, the thickness was checked by an ellipsometer. This layer passivates the sidewall acting as electrical isolation such that the injected electrons are confined within the ohmic contact region. The refractive index step also helps to confine the light within the waveguide.

Table 2-4: PECVD 80+ parameters for SiO_2 film deposition.

Parameter	Value
Gas Flow: $SiH_4/N_2O/N_2$	7/146/85 sccm
RF Power	15 W
Pressure	1000 mT
Temperature	300 ºC

2.3.4 Dry Etching of the Dielectric Layer

An Oxford Instrument reactive ion etching (RIE 80+), with CHF_3 and O_2 gases were used to etch the dielectric films for the contact window opening. The etch recipe is shown in Table 2-5. The etch depth is monitored in-situ by the interferometer. After etching, the etch depth is also checked with a Dektak before stripping the resist mask. If contact windows in the SiO_2 films are not properly opened/etched, current cannot flow across the device and leads to non-functional devices.

Table 2-5: Process parameters for the etching of dielectric layer composed of SiO_2 in RIE 80+.

Parameter	Value
Gas Flow: CHF_3/O_2	50/5 sccm
RF Power	150 W
Pressure	55 mT
Temperature	20 ºC
Etching Rate	32 nm/min

2.3.5 Device Metal Contacts

The contact resistance at the interface between the metal contact and the semiconductor material is a critical parameter because a high contact resistance results in excessive heating and may lead to the electrical breakdown of the device. For metal deposition lithography, bi-layer resists were used to achieve an undercut for ease of lift-off process shown in Figure 2.8.

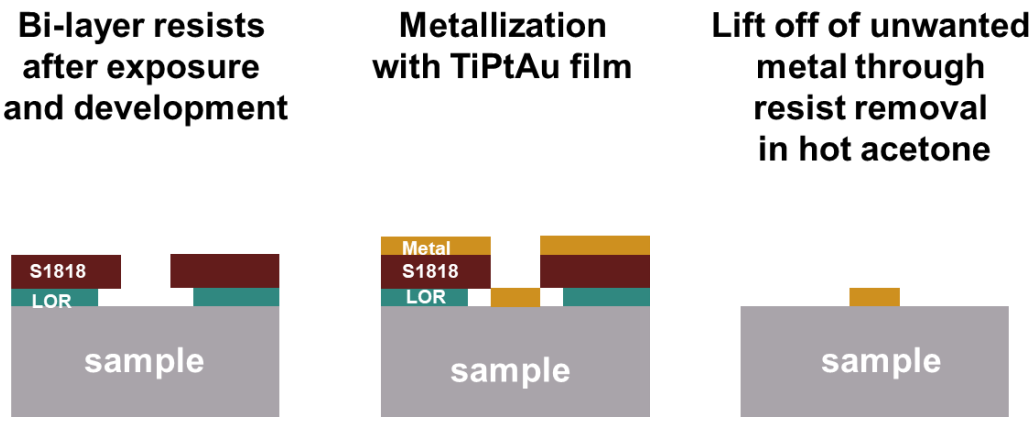

Figure 2.8: Illustration of different steps involved in the lift-off process.

A metal evaporator (Plassys MEB400S) was used for the metallization, which deposits the metal on the substrate in a high vacuum environment. Layers of Ti/Pt/Au (50/20/200 nm) are deposited on top of the waveguide for the *p*-electrode. Ti is used to promote adhesion of the contact with the SiO_2 dielectric layer. The Pt layer is used to provide a diffusion barrier and prevent the penetration of Au into the semiconductor material. The Au layer is to enhance the electrical conductivity, allowing the device to be tested reliably. The top 400 nm of the wafer is highly doped by Be ($2\times 10^{19}cm^{-3}$), enabling a good *p*-type contact with Ti/Pt/Au layers. The lift-off is performed in a hot acetone bath. For the *n-type* contact, layers of Au/Ge/Au/Ni/Au were deposited with a thickness of 14/14/14/11/240 nm by metal

evaporation. The contacts were then annealed using a rapid thermal annealer (RTA) for 60 seconds at 400ºC. Then a further Ti/Au 20/400 nm was deposited as bond pad for the probing or wire bonding during the characterization of the devices.

2.3.6 Isolation of Devices

The last lithography step is performed to electrically isolated the contacts of the device. In multi-section SLD devices, the sections need to be electrically isolated to avoid significant current leakage from one section of the device to the other. The isolation between the contacts is obtained by leaving a 10 μm gap and etching the highly doped GaAs cap and waveguide layers (to a depth of ~ 400 nm). This produces good isolation between the contacts. A wet etch process was used to remove the highly doped GaAs cap and AlGaAs waveguide layers. H_2SO_4: H_2O_2: H_2O with the ratio of 1:8:40 was used. After etching, the resist mask was stripped, and the sample was cleaned by using acetone and IPA. The devices are then ready for characterization.

2.4 SLDs Measurement Technique

2.4.1 Electrical and Spectral Characterisation

The experimental setup used to characterise SLDs electrically and spectrally in this thesis is shown schematically in Figure 2.9. To measure the electrical properties of the devices, current needs to be applied to the test devices by source measurement unit (SMU) which can supply and measure current and voltage. The SMU is connected by direct probing or via wire-bonding to the contact of the devices. The current-voltage (IV) characteristic were measured by direct probing the devices. The device was placed on a temperature-controlled, Au-coated, Cu-stage. A white light LED and CCD camera was used to align the devices and to probe the *p*-contact bond pad of the individual devices. The devices were electrically driven by a continuous wave (CW) source, Keithley 2400, for IV measurement.

For light output-current (LI) measurements, the devices are cleaved, mounted on a ceramic tile, and wire-bonded. The current is supplied by a multi-channel pulse source which was custom-built (courtesy Alexander Boldin) and allows time synchronous pulses to be delivered to individual sections of the multi-section SLD. The multichannel pulse source consists of an external modulation applied to an 8 channel CW current source, using an oscilloscope to measure and monitor pulse width, duty cycle and supplied current of each channel. The quasi-CW conditions are 1% duty cycle and 10 μs pulse width to extract heat as much as possible. The devices were measured at room temperature unless otherwise stated. For high-temperature measurements, the temperature was controlled using a variable 3A/20V power supply. The light output from the device was collected by a photodetector

and the detector was placed as close to the light source as possible to ensure all the emitted light was collected. LabVIEW software was used to communicate between the instruments and record the results.

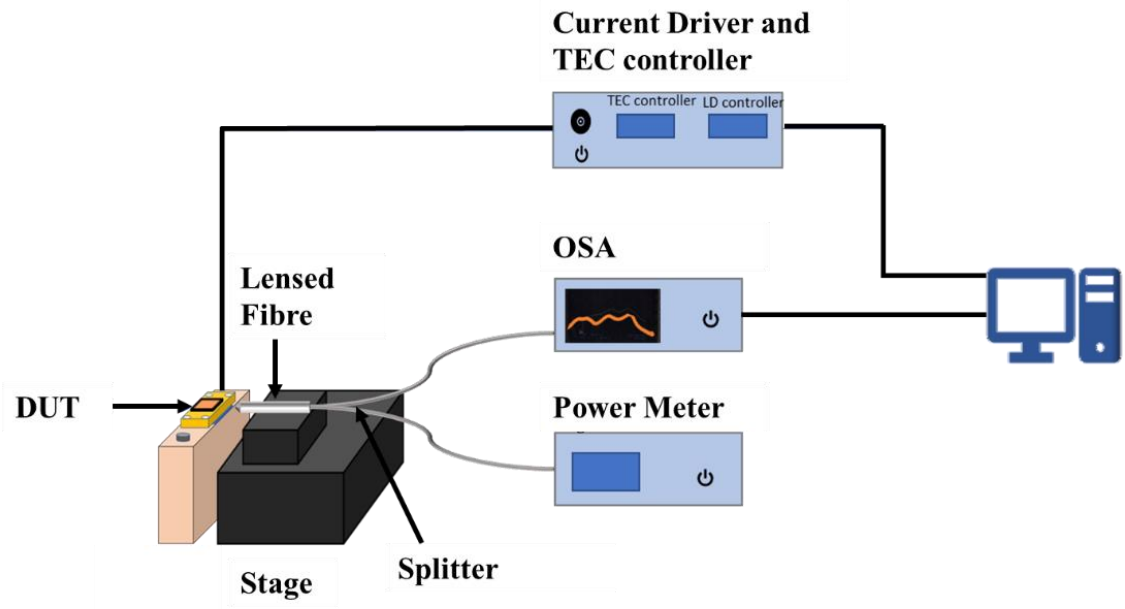

Figure 2.9: Schematic of experimental setup for light output and spectrum measurements of SLD.

For electroluminescence (EL) spectra measurements, the optical spectra of the devices were recorded by coupling the output light into an optical spectrum analyser (OSA) through a single-mode tapered lensed fibre. The fibre is placed close to the edge of the SLD to achieve maximum output power. The alignment is done by adjusting the x-y-z stage to achieve the maximum power while recording the data. The net modal gain and bandwidth can then be extracted from these EL spectra.

The bandwidth of the SLD emission for the QD devices in my thesis is defined in two terms, shown in Figure 2.10 and Figure 2.11. As is known, for state-of-the-art QD laser materials (like the materials from QD Laser Inc), the state separations of the QD may be large with a strong dip in intensity due to the narrow inhomogeneous line-width of the QD ensemble. Figure 2.10 shows the case where the spectral line-width of the QD GS and ES emission is large as compared to the energy separation of the states, where "strong" may be defined as $\frac{\Delta E_{GS}}{2} + \frac{\Delta E_{GS}}{2} \sim E_{ES} - E_{GS}$. However, if this is not the case, a different case occurs which is shown schematically in Figure 2.11. Here, whilst strong GS and ES emission is simultaneously obtained (less than 3dB difference of each other), a "strong dip" between the states is observed (greater than 3dB). In this case, the FWHM may be quoted for the

dominant state, rather than the weaker, yet significant other state. The techniques like "chirped" QD layers in a multi-layer stack (by for example reducing the indium composition in the SRL [15] or "dot in well" [27] capping layer) may be readily employed at a later date, a useful term to consider is the "FWHM of SLD emission". In the development of broadband-sources [24]-[27] , an emission spectrum like that shown in Figure 2.10 may be problematic for applications like OCT, as it will introduce a ghost image, and have poor depth resolution, but it is a promising result for future engineering of broadband active elements. Future iterations of device designs could introduce "chirping" of the QD to fill such spectral gaps. In the case where two states dominate the emission, the "FWHM of SLD emission" sum of the FWHM of the individual emission states.

To conclude, if there is strong "dip" between state, it is defined as " spectral coverage of SLD emission". If there is no strong "dip" between states, it is defined as "FWHM of SLD emission. This "strong dip" can cause coherence degradation and the formation of ghost images, which can compromise the accuracy of the OCT imaging.

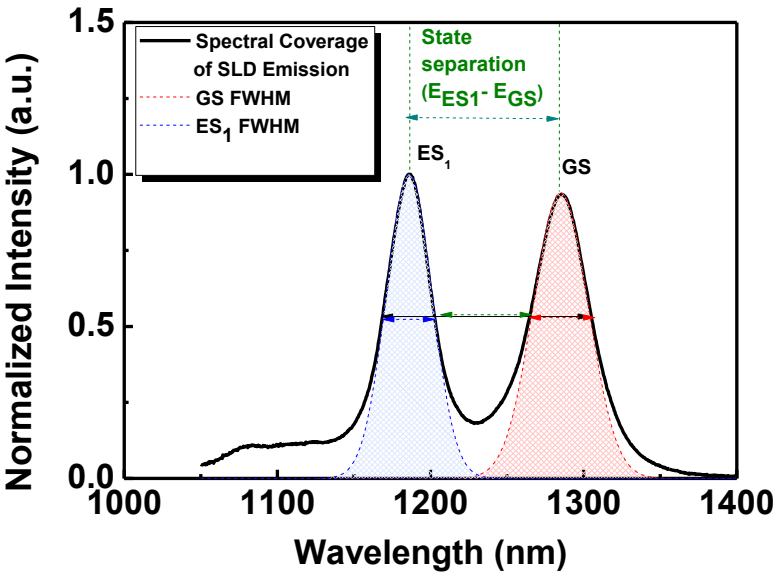

Figure 2.10: Spectral coverage of SLD emissoin (combination of FWHM of inidvidual state and large state separation at half maximum).

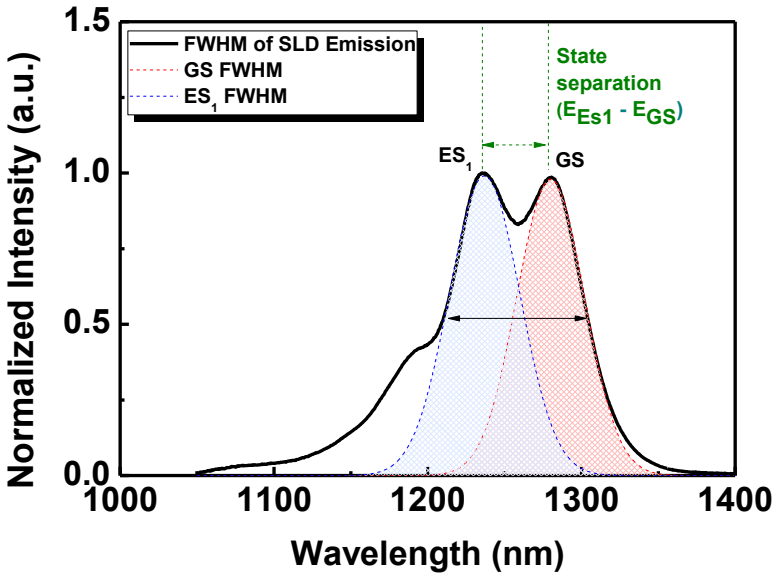

Figure 2.11: FWHM of SLD emission (the width of the spectrum at half maximum as there is no dip due to state separation).

2.4.2 Segmented Contact Gain Measurement

Optical gain measurement of semiconductor laser active elements is a critical characterization procedure to assess the performance of the device. The optical gain can be determined by either analysing longitudinal modal peaks and troughs in the stimulated emission known as Hakki-Paoli technique [28], or by analysing ASE corresponding to different path lengths known as variable stripe length method (segmented contact gain method [29]). The Hakki-Paoli method is based on high resolution spectroscopy which requires the length of the cavity to be small enough to allow the full resolution of the electroluminescence spectrum in terms of individual longitudinal modes. The net modal gain is determined from the modulation depth of the resolved peaks and valleys of the EL spectrum. Due to the high resolution required, accessing low carrier densities is difficult for this method. For the segmented contact gain method, the net modal gain can be obtained by measuring the ASE spectra corresponding to different pumped lengths. The benefits of the segmented contact gain method are that the un-pumped segments act as absorber elements to further suppress the lasing and by applying different currents to each of the segments can further increase the bandwidth of the SLD emission. Net modal gain using the segmented contact method can be calculated using the following formula.

$$G = \frac{1}{L} \ln\left(\frac{P(J, 2L)}{P(J, L)} - 1\right) \tag{2.1}$$

where *L* is the length of the single section of the multi section device, P *(J, L)* and P *(J, 2L)* are EL intensity obtained from waveguide length *L* and *2L* under the same current density. The schematic example is shown in Figure 2.12.

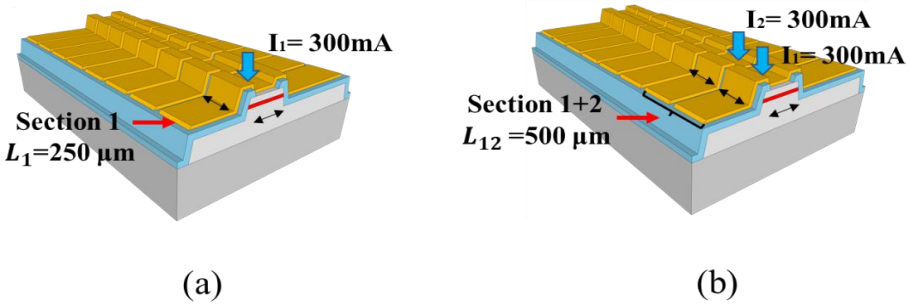

(a) (b)

Figure 2.12 : Schematic diagram of SLD showing injection of same current to each section to achieve same current density for the net modal gain calculation. (a) one section of length L injection current I of 300 mA to achieve current density of 8.6 kA/cm^2 (b) two section of length *2L* injection current 2I of 600mA to achieve current density of 8.6 kA/cm^2.

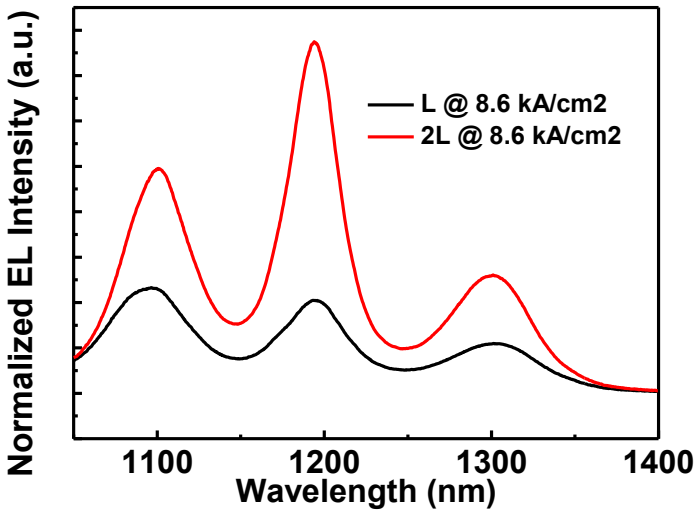

Figure 2.13: An example of measure spectra for length *L* and *2L*, at the same current density of 8.6 kA/cm^2. *2L* have higher intensity due to the amplification of light with increased cavity length.

Figure 2.13 shows an example of measured EL spectra at room temperature while pumping length *L* (e.g., 500 µm), then pumping length *2L* (e.g., 1000 µm), with the same current density. The net modal gain can then be calculated. The internal loss (α_i) can be deduced from the long-wavelength tail of the net modal gain spectra which is shown in Figure 2.14. Modal gain can then be converted from the net modal gain by the relation; modal gain = net

modal gain + α_i, where α_i is the internal loss. The modal gain span (gain bandwidth) is defined as the wavelength range above zero shown in figure 2.15.

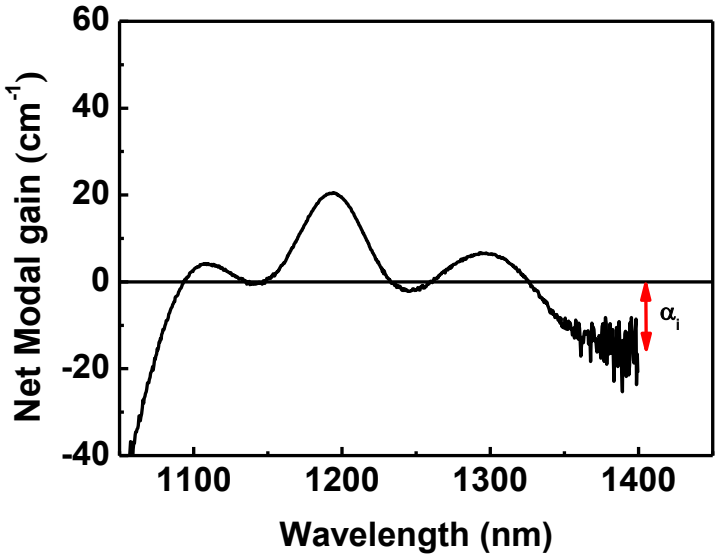

Figure 2.14: An example of net modal gain spectrum at current density of 8.6 kA/cm^2 . The internal loss α_i can be deducted at long wavelength.

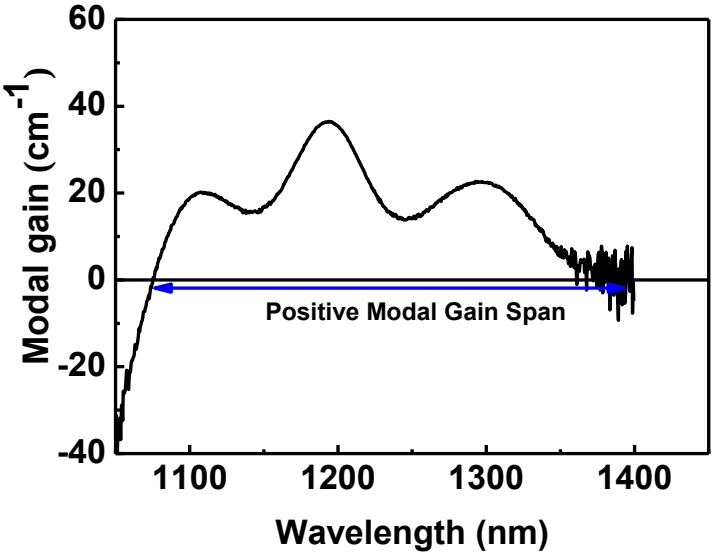

Figure 2.15: An example of modal gain (net modal gain + internal loss) spectrum.

2.5 Photonic Crystal Surface Emitting Lasers Designs

PCs are optical materials with a periodic refractive index pattern in which a photonic band structure is formed. The typical photonic band structure can be modelled in different ways such as the plane wave expansion (PWE) method [30], the finite difference time domain (FDTD) method [31] and couple wave theory (CWT) [32]. In a photonic band structure, a

band edge is a region where the gradient is zero. The photons in these states have zero group velocity which leads to the formation of standing waves within the crystal. By utilising the band edge as a resonator, the output power is coupled to the vertical direction by PC itself which gives rise to the surface-emitting function.

The PC layer is formed in the vicinity of the QD active layer. A typical unit cell, consisting of a square lattice of circular air holes is shown enlarged Figure 2.16, where *r* is the radius of the circular air hole and *a* is the lattice (unit cell) period. The lasing wavelength can be controlled by this lattice period. The period of a PC is λ/n (where *n* is the refractive index). The period is set to ~ 340 nm and ~ 370 nm to match the emission wavelength inside the device material and coincide with the gain peak of the ES and GS of the QD active layer. Coherent light emission from the optical gain media, designed around the edge of the photonic band structure, propagates with zero group velocity, and strongly couples with the 2D PC.

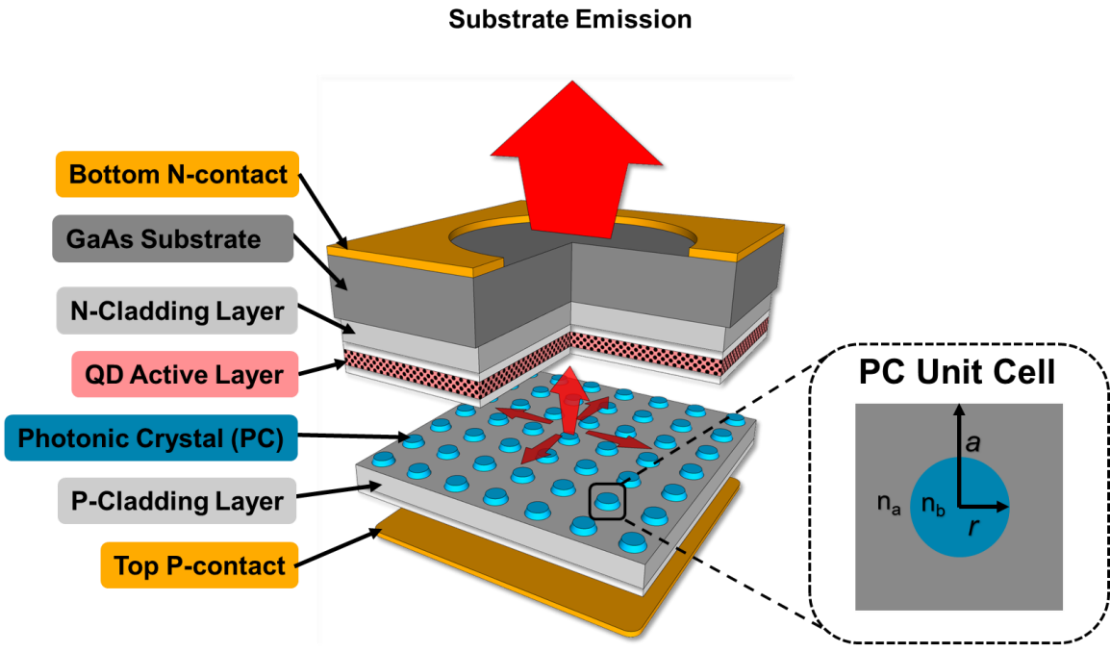

Figure 2.16: Schametic diagram of PCSEL.

There are many types of lattice structures in 2D PCs, but we can simplify by considering triangular and square lattices. Initial work on PCs used the triangular lattice structure; however, more recently PCs with a square lattice have been used in PCSELs due to their comparatively simple band structure [33]. The band structure of a 2D PC using a square lattice with circular atoms is shown schematically in Figure 2.17. At the X and M special points, only in-plane coupling (+ 90 and - 90 direction, as well as the -180 direction) can occur whereas out-of-plane coupling can occur at the Γ point [34]. The diffracted light waves propagate in four directions together to create 2D standing waves. Therefore, the Γ point

offers the most desirable characteristics as light is coupled out of plane at 90 degrees. An enlarged view of the band diagram at the Γ point is shown in Figure 2.18 (a). Four-band edges are formed at this point where usually one pair are degenerate (leaky), and the other pair are non-degenerate (non-leaky). The nature of the modes (leaky or non-leaky) is determined by the symmetry of the in-plane electric field [33], [35]. The corresponding in-plane electric field within the unit cell is shown in Figure 2.18 (b). Two modes (A and B) give asymmetric in-plane electric fields so light scattered in the vertical direction will be out of phase (destructive interference occurs) and so emit little light out-of-plane. These modes will be non-leaky. The other two modes (C and D) have symmetric in-plane electric fields, the light scattered in the vertical direction will be in phase (constructive interference occurs) and so emit light. This high out-of-plane loss results in difficulties in achieving lasing from these modes due to a high threshold current density and the small splitting of the modes as compared to the gain bandwidth. Therefore, most fabricated devices achieve lasing through modes A or B due to the low in-plane optical loss. However, the output slope efficiency is limited due to the symmetric shape of the circular atom.

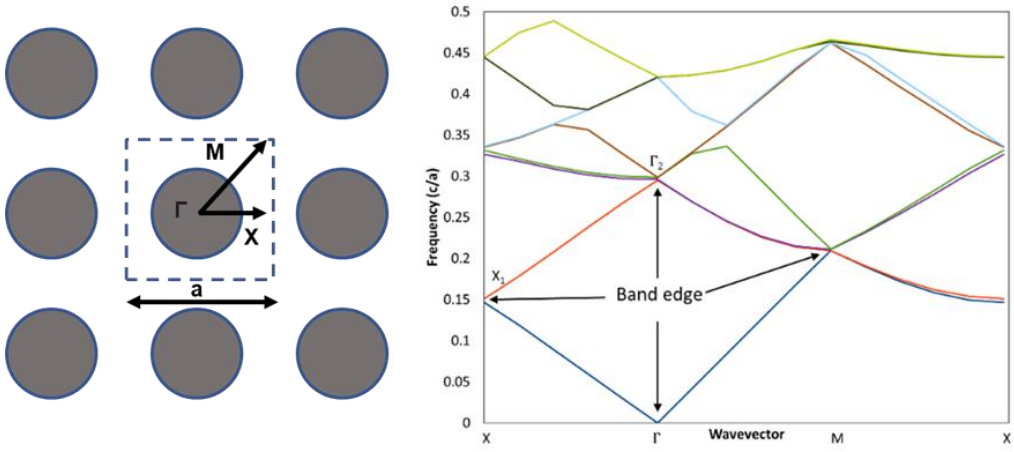

Figure 2.17 : Schematic of unit cell of a square lattice photonic crystal with circular atom at each lattice point and corresponding TE photonic band structure [42].

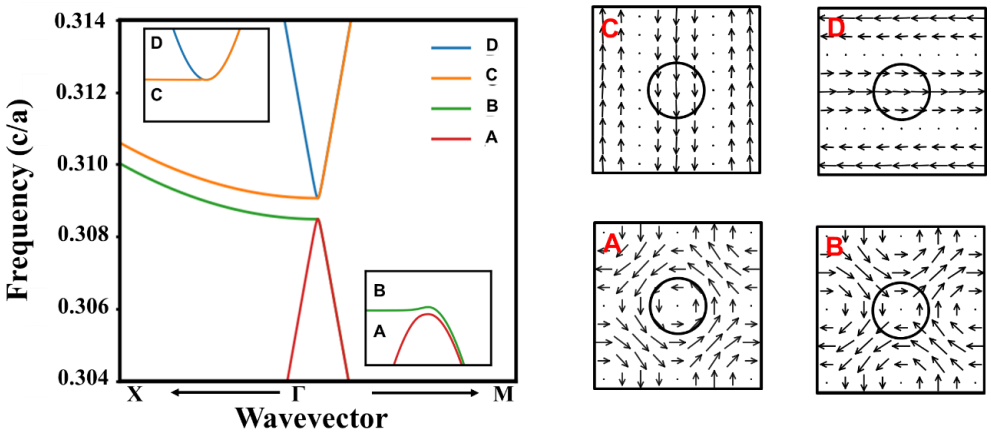

Figure 2.18 : Band structure of the PC. Black-arrows represent the direction of the electric field [43].

The engineering the geometry of the atom shape (air hole) or orientation of the atom shape of the unit cell can enhance the slope efficiency of the PCSELs devices. Breaking the 2D symmetry of the atom causes breaks in the symmetry of the in-plane fields and avoids destructive interference of the light output. The output efficiency was found to increase by changing the atom shape. Hirose *et al.* reported that the right-isosceles-triangle-shaped air hole has the watt-class output power compared to the circular atom due to the breaking in symmetry of the electric field [36]. Kurosaka *et al.* [37] further reduced the 2D symmetry by rotating the V-shaped air holes. Besides in-plane shape of the air hole, the vertical direction i.e., the etch depth of the atom shape is also an important parameter to improve the coupling coefficient and consequently the output efficiency can be increased. In PCSELs, the etch depth of the PC air hole is an important factor to consider when designing the PC as it determines the strength of surface emission [38]. For high output powers, PC voids need to be close to the active waveguide, and the height of the PC atom to be half the period. Taylor *et al.* simulated that the coupling coefficient increases with increasing the PC etch depth due to the mode overlap with the photonic crystal region [39]. The effect of etch depth of PC air pillar on threshold characteristics of PCSELs by optical pumping is carried out in GaSb and GaAs-based materials [40]-[42]. Lower threshold gain is achieved due to the enhanced coupling. Moreover, the etch depth increase results in a decrease in the effective mode index, and therefore a shift in wavelength can be obtained.

In addition to the atom shape in the in-plane and vertical direction, the feature size of the PC atom e.g., radius of a circular atom is also an important factor. Prior work involved simulation of a range of circular atom radii from 0 to 0.7 r/a (r/a is the ratio between the radius of the circular atom and the lattice period of the photonic crystals) and showed that the coupling strength is the strongest around 0.2 and 0.4 r/a [43]. Therefore, larger r/a should

have a higher output power due to the stronger coupling if the void of the PC is identical in size and shape.

2.6 Fabrication Methods of Photonic Crystal

Schematics of different methods to fabricate an electrically driven PCSEL are shown in Figure 2.19. Early PCSELs used wafer fusion to bond two wafers to embed the photonic crystal near an active layer [44]. The other method is where a PC is etched through the *p*-cladding layer covered with a transparent conductive layer such as ITO [45]. Another method is where a PC structure can be formed right above the active layers and is then encapsulated using the epitaxial regrowth technique [46]. The fabrication of PCSELs by epitaxial regrowth has emerged as a key technology due to the elimination of defects related to wafer bonding or reducing contact resistance of the device related to the transparent conductive layer fabrication approaches [47]. Moreover, the most prominent results have been obtained using the epitaxial regrowth process. With advancements in regrowth techniques, it is possible to fabricate both void/semiconductor contrast PCSELs [36] and all-semiconductor PCSELs [48]. The void/semiconductor PCSEL has demonstrated the best performance in terms of power and efficiency due to the presence of voids providing a high coupling coefficient) [47]. The void topology is modified by the regrowth method is extensively studied by McKenzie *et al* [49]. The deformed air-holes are like a "tear-drop" that clearly manifests either an increase or decrease of a particular degree of in-plane asymmetry by epitaxially regrowth processes.

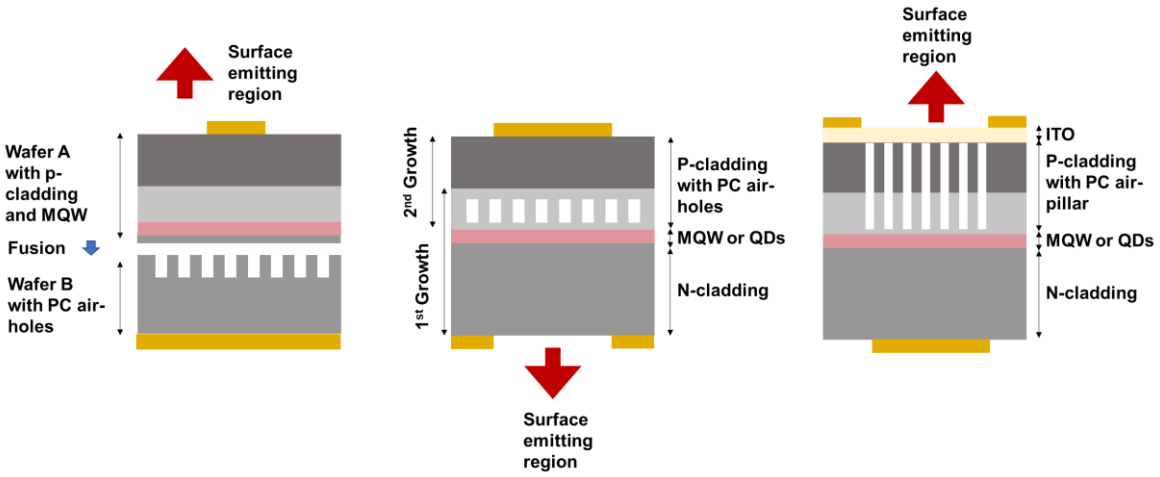

Figure 2.19: The schematic diagram of different fabrication methods (a) air-holes PCSEL by wafer fusion [44] (b) air-holes PCSEL by epitaxial regrowth [36] (c) air-pillar PCSEL by etching through *p*-cladding layer [45].

2.7 Fabrication of Photonic Crystal Surface Emitting Lasers

The fabrication process of PCSELs includes six lithography steps as shown below in the process flow diagram Figure 2.20. Before fabrication, the whole wafer was cleaved into quarter wafers using a diamond-tip scriber tool. Samples were then cleaned with acetone and IPA in an ultrasonic bath. After solvent-based cleaning, an O_2 plasma ash is followed to remove any photoresist stains from the semiconductor surface. The cleaning is important before each step of the fabrication process to remove all organic and inorganic contaminants. After cleaning the sample, the first lithography was performed to define the photonic crystals.

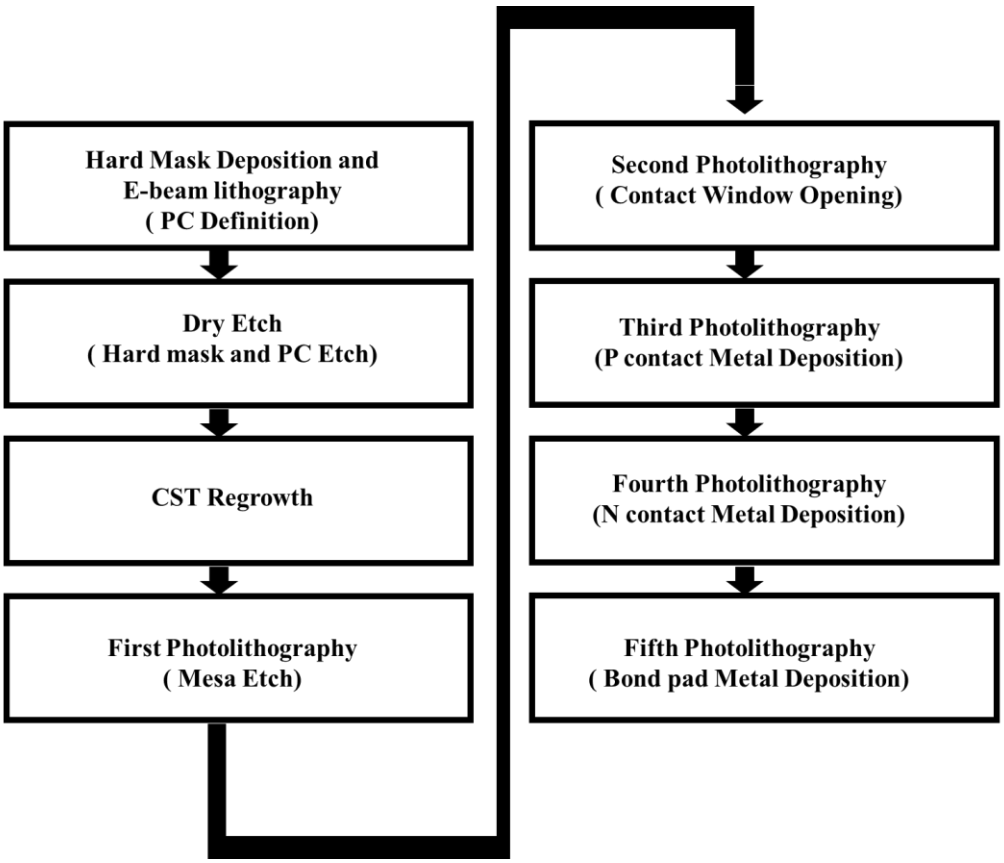

Figure 2.20: Fabrication of PCSEL flow diagram.

The three-dimensional view of the fabrication steps of the PC before regrowth is illustrated in Figure 2.21. The first lithography was EBL to define the PC and then the transferred patterns are etched into the top GaAs layer of the base wafer. The wafer is then regrowth to complete the p-i-n structure. Then standard laser fabrication processes are carried out. The second lithography was performed to define the electrical isolation between the devices, followed by the third and fourth lithography step to open window area for metal contact

deposition and *p*-contact deposition. Then, the fourth lithography step was carried out for *n*-contact deposition, followed by the lithography steps for bond pad deposition.

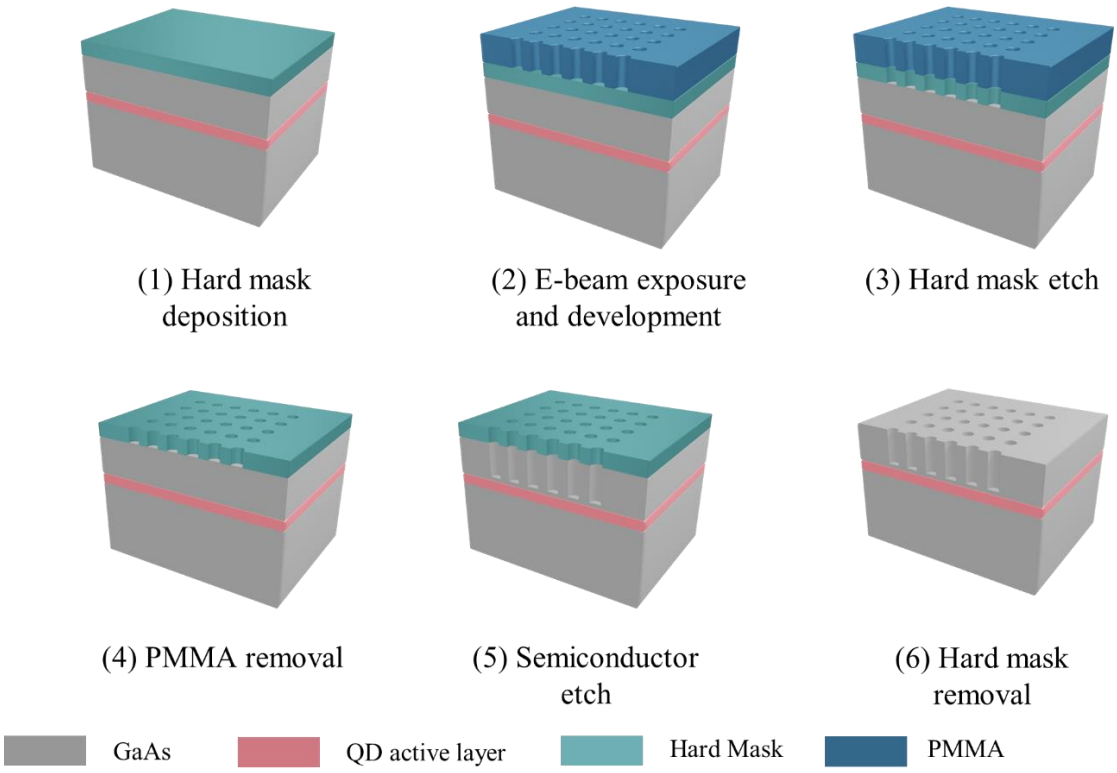

Figure 2.21: The schematic drawings for the process steps involved in the fabrication of photonic crystal before regrowth.

2.7.1 Lithography

Due to the small feature size (nm) of the photonic crystal, the high-resolution electron beam lithography was used for the definition of PC. The exposure dose is an important parameter that describes the required charge per unit area ($\mu C/cm^2$) to exposure the resist. To determine the optimum exposure dose, electron scattering in the material needs to be taken into consideration.

Table 2-6 : Parameters for lithography step.

Step	PMMA
Spin Resist	4000 rpm for 60 secs
Bake	150 C for 5 mins
Development	MIBK: IPA (1:3) for 90 secs

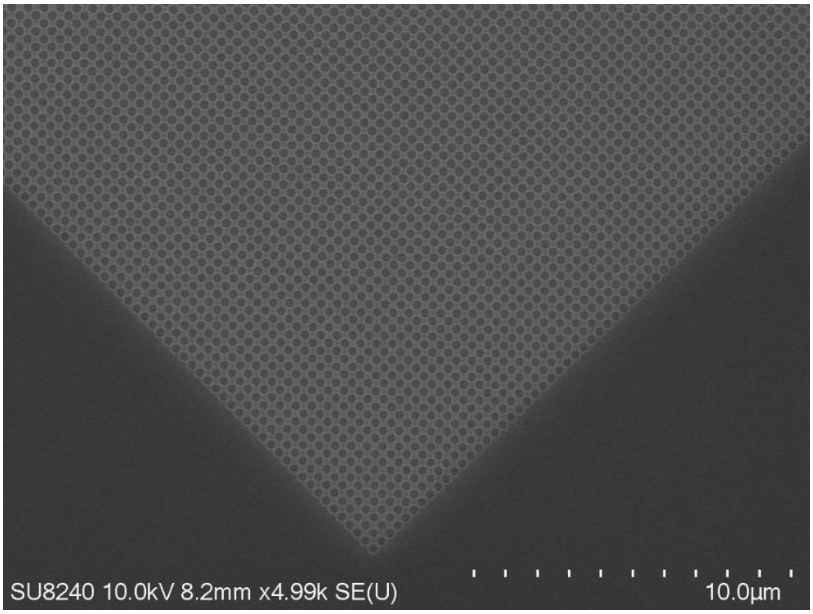

Figure 2.22: Plan View SEM image of dose test sample after development.

Moreover, the selection of the optimum beam spot size and beam step size are also critical steps for writing features where the resolution or pattern roughness are very critical. A modification of the exposure dose distribution on a sample is essential which is called proximity correction. The dose of the EBL needs to be chosen properly. Dose tests were firstly carried out to find the optimum dose before the real run of EBL for the sample. The positive resist PMMA was spun on the test sample. The recipe for EBL is shown in table 2.6. Figure 2.22shows SEM picture of the optimised dose test results of EBL for PMMA after development. As seen, the circular patterns (PC) are uniform from the edge to the centre and the patterns have well-defined shape.

2.7.2 Photonic Crystal Etch

For PCSELs, the plasma dry etch process is used to create the photonic crystal structure that provides the feedback mechanism for lasing. The optimization of this process is particularly important as it directly affects the performance of the laser. To create a well-defined photonic crystal structure, the etching process needs to be controlled to achieve high selectivity between the photonic crystal and the surrounding material. This can be achieved by adjusting the plasma chemistry and etching parameters to optimize the etching rate and selectivity.

The positive resists available for the EBL are very thin to resist dry etch process due to the thin nature of the resists. Alternative resist such as HSQ which is a negative e-beam resist can be used [50], however, the optimization of the EBL parameters is needed. Therefore, hard mask (SiO_2) is used in this work rather than soft mask alone despite the extra fabrication steps. To create the hard mask for pattern transference, the deposition of the 200 nm of SiO_2 by PECVD is firstly carried out after initial cleaning process, followed by the EBL and dry

etching of the SiO_2 by using the RIE 80+ tool. This acts as a hard mask for the etching of the underlying semiconductor. Through the hard mask, the *p*-GaAs layer is etched to desired depths by ICP etching with BCl_3/Cl_2 chemistry shown in table 2.3. SEM images of the PC (circular patterns) after ICP etching is shown in Figure 2.23. The hard mask is then removed, and epitaxial regrowth is undertaken.

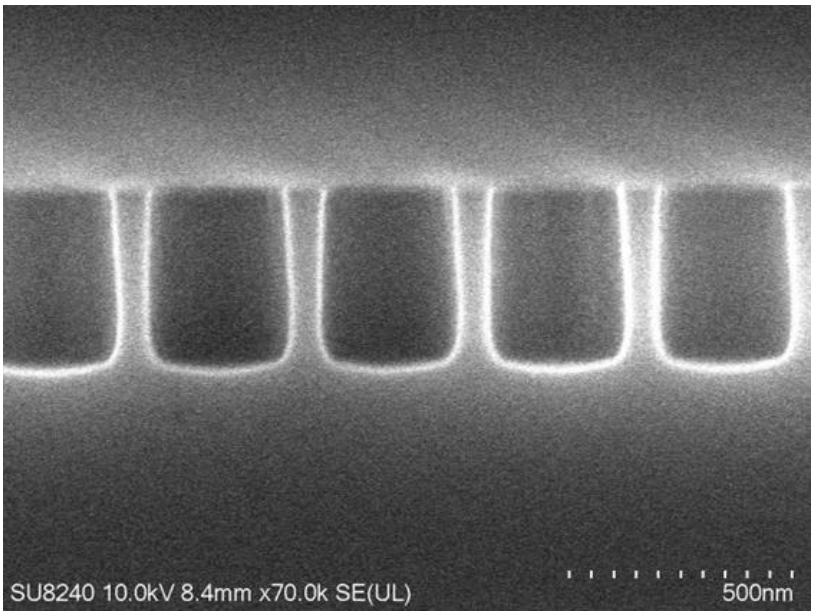

Figure 2.23: Cross-sectional SEM images of PC etch results after hard mask removal. The PC pattern shown in here is circular atom with r/a value of 0.4.

2.7.3 Epitaxial Regrowth

The wafers are cleaned in UV ozone to remove contaminants and etched in 10:1 buffered HF for one minute prior to regrowth. The regrowth was carried out by Dr. Neil Gerrard using a Thomas Swan Epilab close-coupled showerhead (CCS) metalorganic vapour-phase epitaxy (MOVPE) reactor in 1 × 3" configuration operating at a pressure of 100 mbar. Triethylaluminium (TMAI) and trimethylgallium (TMGa) were utilised as the group III-precursors with arsine (AsH_3) as the group-V source. The epitaxial structure of the regrowth consists of 400 nm of *p*-$Al_{0.35}GaAs$, the initial photonic crystal grating infill material. This was followed by 1500 nm of *p*-$Al_{0.37}GaAs$ cladding layer and 100 nm of *p*-GaAs doped capped layer. Figure 2.24 shows the cross-sectional SEM image of the void formation (411 nm in height) within the grating layer after regrowth.

Cross-sectional SEM images of the regrown PC structures are shown in Figure 2.24. The voids formed within the grating layer; they appear as a line of black features in the semiconductor matrix owing to the absence of material. The details of the regrowth process and formation of void can be found in this paper [51].

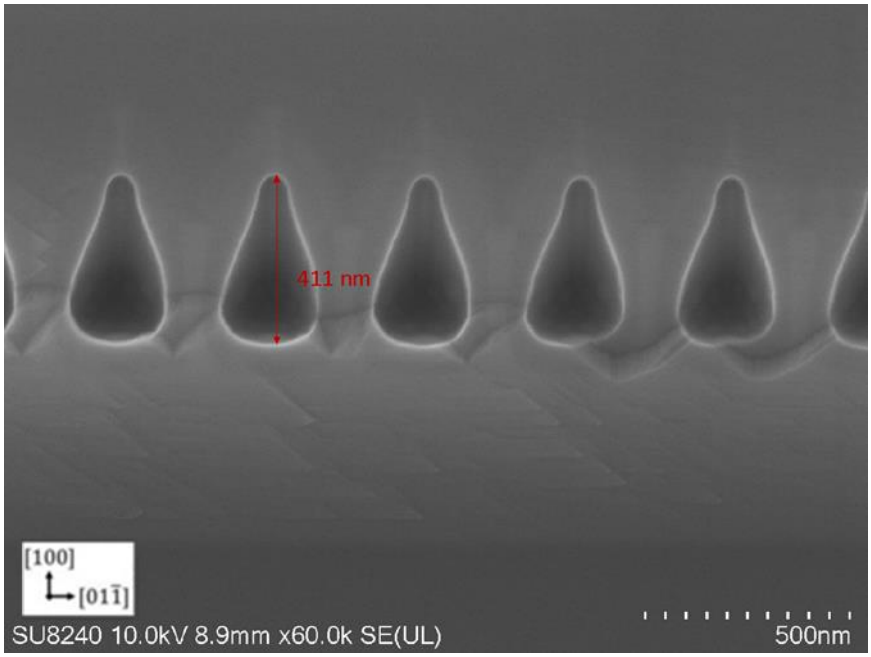

Figure 2.24: Cross-sectional SEM images of PC after regrowth.

2.7.4 Laser Diode Fabrication

After regrowth, ICP etching was preformed to form mesa areas to confine current injection and electrically isolate between devices. The current injection area is restricted by this isolation mesa. The size of the mesa ranges from 200 µm × 200 µm to 800 µm × 800 µm with a step of 200 µm with an approximate PC etch depth of 1000 nm. The square mesa is patterned with photolithography and ICP dry etch with the same chemistry descried in section 2.3. AZ photoresist was used as soft mask for the mesa etching. The resist was then exposed using photolithography since the patterns are > 1 µm. This was followed by deposition of an electrical insulation dielectric, window opening for metal deposition and deposition of a metal contact layer. The cross-sectional and three-dimensional view of the laser fabrication steps of the PCSEL after regrowth are illustrated in Figure 2.25. A dielectric layer (SiO_2) of 400 nm is deposited as an insulating film and the window opening for contact deposition (dielectric etching) is performed by using RIE etching as described in section 2.3.5. After the window opening, a square *p*-electrode was deposited on top of the device, followed by the *n*-electrode with a square window on the back-side of the device using photolithography and lift-off processes. The devices were then annealed at 400 ºC for 60 seconds. A thick layer of Au bond pad was finally deposited on the top of the device for direct probing and wire bonding during for electrical injection during device characterisation.

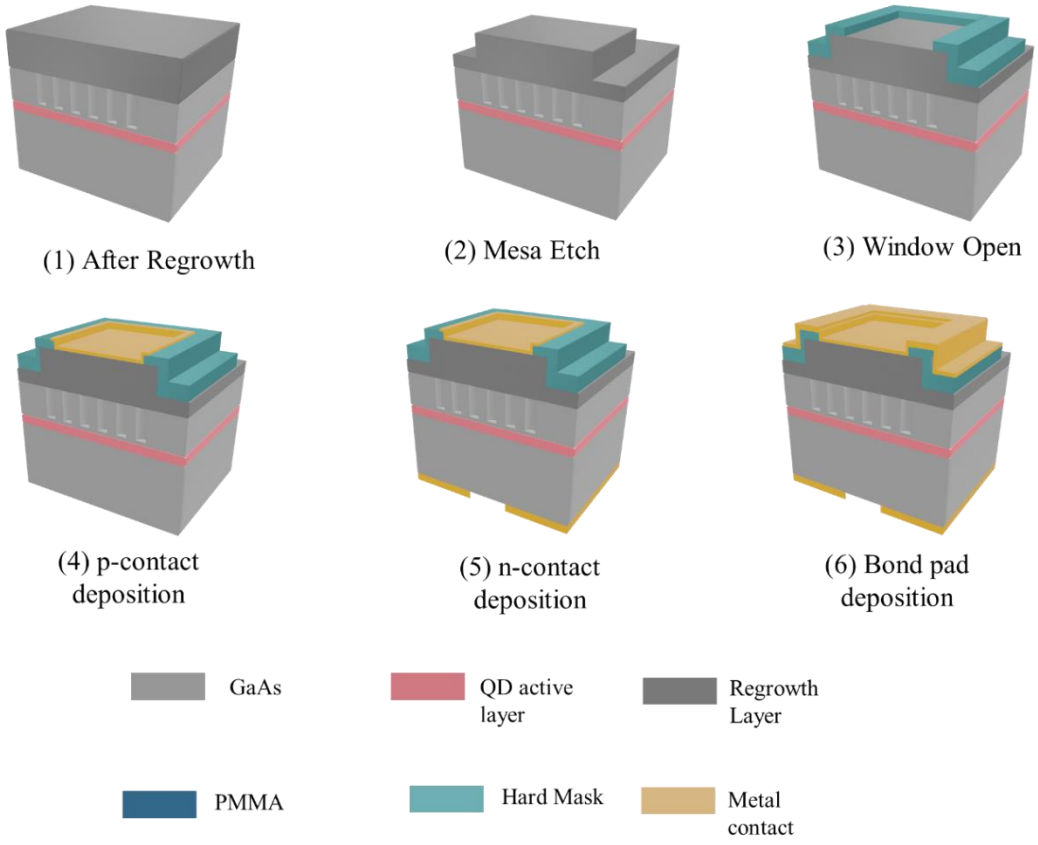

Figure 2.25: The schematic drawings for the process steps involved in the fabrication of photonic crystal after regrowth.

2.7.5 Electrical and Spectral Characterisation

The experimental setup used to characterise PCSELs is schematically shown in Figure 2.26. The devices are electrically driven by CW for electrical characterisation (IV) or quasi-CW condition (1% duty cycle, 10 μs pulse width) for LI and spectrum measurement. A LED and CCD camera were used to allow accurate probing of the *p*-electrode of the individual devices. The samples are measured at room temperature. The devices are tested on-wafer epi side-up placed on a copper block with a window for light emission from the window of the *n*-electrode. The power absorbed in the substrate can be calculated by equation . When the light beam travels through a material of length , *l*, with an absorption coefficient of α, the relation between injected power and the output power can be expressed as

$$P_{out} = P.\ e^{-\alpha l}$$

The doping concentration of the sample is $3\times10^{18}cm^{-3}$ and the 625 μm thick doped substrate. The absorption coefficient is ~ 18 cm^{-1} [52], [53]. Therefore, P_{out} is the 39% of P. The reflection of light at the interface between the substrate and the air can be determined by

$$R = \left(\frac{n2 - n1}{n2 + n1}\right)^2$$

The refractive index, *n*, of GaAs and air is 3.55 and 1 respectively. Therefore, 31% of power reflected by the substrate interface and only 69% light comes out of the devices. The total loss is 70% . P_{out} = $P_{measured}$/ (100-70) = 3.3* $P_{measured}$. The output power should be multiplied by a factor of ~ 3 of measured power. The power loss due to the substrate absorption and reflection at the substrate/air interface can be reduced by thinning the substrate and introducing anti-reflection coatings in future.

The light output from the device is collected by germanium photodiode based light meter. LabVIEW software is used to communicate between the instruments and record the results. Based on the LI curve, several important parameters can be extracted such as threshold current density when the dimension of the devices are known, slope efficiency which is the gradient of the LI curve. For spectral measurements, the optical spectra of the devices were recorded by coupling the output light into an OSA through a fibre. The OSA utilised in this experiment has a minimum resolution of 0.1 nm.

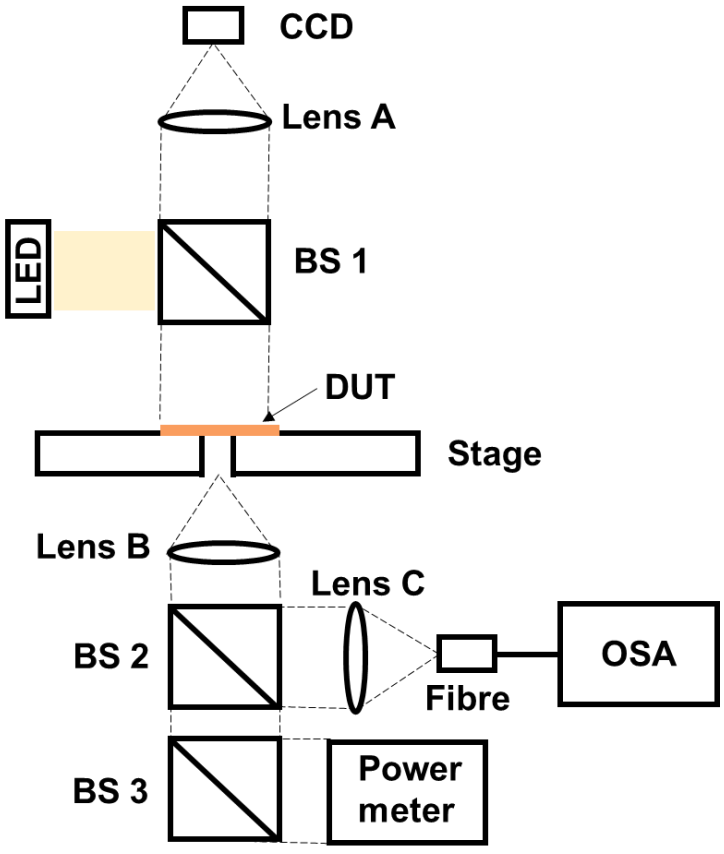

Figure 2.26: Schematic of experimental setup for light output and spectrum measurements of PCSEL.

Bibliography

[1] G. A. Alphonse, D. B. Gilbert, M. G. Harvey, and M. Ettenberg., "High-Power Superluminescent Diodes," *IEEE Journal of Quantum Electronics*, vol. 24, no. 12, p. 2454–2457, 1988.

[2] C. F. Lin and C. S. Juang, "Superluminescent Diodes with Bent Waveguide," *IEEE photonics technology letters*, vol. 8, no. 2, p. 206–208, 1996.

[3] A. Kafar, S. Stanczyk, G. Targowaki, T. Oto, I. Makarowa, P. Wisniewski, T. Suski and P. Perlin.,"High-optical-power InGaN superluminescent diodes with 'j-shape' waveguide," *Applied Physics Express*, vol. 6, no. 9, p. 092102, 2013.

[4] J. H. Liang, T. Maruyama, Y. Ogawa, S. Kobayashi, J. Sonoda, H. Urae, S. Tomita, Y. Tomioka and S. Kon., "High-power high-efficiency superluminescent diodes with J-shaped ridge waveguide structure," In *Conference Proceedings. 14th Indium Phosphide and Related Materials Conference*, p. 119–122, 2002.

[5] J. D. Thomson, H. D. Summers, P. J. Hulyer, P. M. Smowton, and P. Blood, "Determination of single-pass optical gain and internal loss using a multisection device," *Applied Physics Letters*, vol. 75, no. 17, p. 2527, 1999.

[6] N. Ozaki, D. T. D. Childs, J. Sarma, T. S. Roberts, T. Yasuda, H. Shibata, E. Watanabe, N. Ikeda, Y. Sugimoto, and R. A. Hogg., "Superluminescent diode with a broadband gain based on self-assembled InAs quantum dots and segmented contacts for an optical coherence tomography light source." *Journal of Applied Physics* 119, no. 8, p. 083107, 2016.

[7] P. D. L. Judson, K. M. Groom, D. T. D. Childs, M. Hopkinson, and R. A. Hogg, "Multi-section quantum dot superluminescent diodes for spectral shape engineering," *IET Optoelectronics*, vol. 3, no. 2, p. 100–104, 2009.

[8] G. R. Goldberg, A. Boldin, S. M. L. Andersson, P. Ivanov, N. Ozaki, R. J. E. Taylor, D. T. D. Childs, K. M. Groom, K. L. Kennedy, and R. A. Hoog., "Gallium Nitride Superluminescent Light Emitting Diodes for Optical Coherence Tomography Applications," *IEEE Journal of Selected Topics in Quantum Electronics*, vol. 23, no. 6, pp.1–11, 2017.

[9] G. R. Goldberg, D. H. Kim, R. J. E. Taylor, D. T. D. Childs, P. Ivanov, N. Ozaki, K. L. Kennedy, K. M. Groom, Y. Harada and R. A. Hoog., "Bandwidth enhancement in an InGaN/GaN three-section superluminescent diode for optical coherence tomography," *Applied Physics Letters*, vol. 117, no. 6, p. 061106, 2020.

[10] C. Shen, T. K. Ng, J. T. Leonard, A. Pourhashemi, S. Nakamura, S. P. Denbaars, J. S. Speck, A. Y. Alyamani, M. M. El-desouki, and B. S. Ooi., "High-brightness semipolar ($20\bar{2}1$) blue InGaN/GaN superluminescent diodes for droop-free solid-state lighting and visible-light communications," *Optics Letters*, vol. 41, no. 11, p. 2608, 2016.

[11] N. K. Dutta and P. P. Deimel, "Optical Properties of a GaAlAs Superluminescent Diode," *IEEE Journal of Quantum Electronics*, vol. 19, no. 4, p. 496–498, 1983.

[12] D. Li, C, Ma, J. Wang, F. Hu, Y. Hou, S. Wang, J. Hu, S. Yi, Y. Ma, J. Shi, J. Zhang, Z. Li, N. Chi, L. Xia and C. Shen., "High-Speed GaN-Based Superluminescent Diode for 4.57 Gbps Visible Light Communication," *Crystals*, vol. 12, no. 2, p. 191, 2022.

[13] Z. Y. Zhang, Z. G. Wang, B. Xu, P. Jin, Z. Z. Sun, and F. Q. Liu., "High-Performance Quantum-Dot Superluminescent Diodes," *EEE Photonics Technology Letters*, vol. 16, no. 1, p. 27–29, 2004.

[14] C. Jiang, H. Wang, H. Chen, H. Dai, Z. Zhang, X, Li, and Z. Yao., "Broadband Quantum Dot Superluminescent Diode with Simultaneous Three-State Emission," *Nanomaterials*, vol. 12, no. 9, p. 1431, 2022.

[15] S. K. Ray, K. M. Groom, M. D. Beattie, H. Y. Liu, M. Hopkinson, and R. A. Hogg., "Broad-Band Superluminescent Light-Emitting Diodes Incorporating Quantum Dots in Compositionally Modulated Quantum Wells," *IEEE photonics technology letters*, vol. 18, no. 1, p. 58-60, 2006.

[16] Z. Y. Zhang, I. J. Luxmoore, C. Y. Liu, Q. Jiang, K. M. Groom, D. T. D. Childs, M. Hopkinson, A. G. Cullis. And R. A. Hogg., "Effect of facet angle on effective facet reflectivity and operating characteristics of quantum dot edge emitting lasers and superluminescent light-emitting diodes," *Applied Physics Letters*, vol. 91, no. 8, p. 081112, 2007.

[17] Y. C. Xin, A. Martinez, T. Saiz, A. J. Moscho, Y. Li, T. A. Nilsen, A. L. Gray, and L. F. Lester., "1.3 μm Quantum Dot Multi-Section Super-Luminescent Diode with Extremely Broad Bandwidth," *IEEE Photonics Technology Letters*, vol. 19, no.9, p. 501-503, 2007.

[18] Y. C. Xin, Y. Li, A. Martinez, T. J. Rotter, H. Su, L. Zhang, A. L. Gray, S. Luong, K. Sun, Z. Zou, J. Zilko, P. M. Varangis, and L. F. Lester., "Optical gain and absorption of quantum dots measured using an alternative segmented contact method," *IEEE Journal of Quantum Electronics*, vol. 42, no. 7, p. 725–732, 2006.

[19] P. D. L. Judson, K. M. Groom, D. T. D. Childs, M. Hopkinson, N. Krstajic, and R. A. Hogg., "Maximising performance of optical coherence tomography systems using a multi-section chirped quantum dot superluminescent diode," *Microelectronics Journal*, vol. 40, no. 3, p. 588–591, 2009.

[20] C. Mack, "Introduction to Semiconductor Lithography," in *Fundamental Principles of Optical Lithography*, John Wiley & Sons, 2007.

[21] E. Zhirnov, S. Stepanov, W. N. Wang, Y. G. Shreter, D. v. Takhin, and N. I. Bochkareva, "Influence of cathode material and $SiCl_4$ gas on inductively coupled plasma etching of AlGaN layers with Cl_2/Ar plasma," *Journal of Vacuum Science & Technology A: Vacuum, Surfaces, and Films*, vol. 22, no. 6, p. 2336–2341, 2004.

[22] Y. Z. Juang, Y. K. Su, S. C. Shei, and B. C. Fang, "Comparing reactive ion etching of III–V compounds in Cl_2 /BCl_3 /Ar and CCl_2 F_2 /BCl_3 /Ar discharges," *Journal of Vacuum Science & Technology A: Vacuum, Surfaces, and Films*, vol. 12, no. 1, p. 75–82, Jan. 1994.

[23] M. M. Volatier, D. Duchesne, R. Morandotti, R. Arès, and V. Aimez, "Extremely high aspect ratio GaAs and GaAs/AlGaAs nanowaveguides fabricated using chlorine ICP etching with N 2-promoted passivation," *Nanotechnology*, vol. 21, no. 13, p. 134014, 2010.

[24] Z. Y. Zhang, Q. Jiang, M. Hopkinson, and R. A. Hogg., "Effects of intermixing on modulation p-doped quantum dot superluminescent light emitting diodes," *Optics express*, vol. 18, no. 7, p. 7055–7063, 2010.

[25] Z. Y. Zhang, Q. Jiang, I. J. Luxmoore, and R. A. Hogg, "A p-type-doped quantum dot superluminescent LED with broadband and flat-topped emission spectra obtained by post-growth intermixing under a GaAs proximity cap," *Nanotechnology*, vol. 20, no. 5, p. 055204, 2009.

[26] P. D. L. Greenwood, K. V. Patel, D. T. D. Childs, K. M. Groom, B. J. Stevens, M. Hopkinson, and R. A. Hogg., "Multi-contact quantum dot superluminescent diodes for optical coherence tomography," in *Novel In-Plane Semiconductor Lasers VIII SPIE*, vol. 7230, 2009.

[27] L. F. Lester, A. Stintz, H. Li, T. C. Newell, E. A. Pease, B. A. Fuchs, and K. J. Malloy., "Optical characteristics of 1.24-μm InAs quantum-dot laser diodes." *IEEE Photonics Technology Letters* 11, no. 8, p. 931-933, 1999.

[28] F. Tanoure, H. Sugawara, K. Akahane and N. Yamamoto., "Gain Measurement of Highly Stacked InGaAs Quantum Dot Laser with Hakki-Paoli Method", *Japanese Journal of Applied Physics*, vol. 52, no. 4S, p. 04CG13, 2013.

[29] P. Blood, G. M. Lewis, P. M. Smowton, H. Summers, J. Thomson, and J. Lutti., "Characterization of Semiconductor Laser Gain Media by the Segmented Contact Method," *IEEE Journal on Selected Topics in Quantum Electronics*, vol. 9, no. 5, p. 1275–1282, 2003, 2003.

[30] S. Shi, C. Chen, and D. W. Prather, "Plane-wave expansion method for calculating band structure of photonic crystal slabs with perfectly matched layers," *Journal of the Optical Society of America.* Vol. 21, no. 9 , p. 1769-1775, 2004.

[31] S, R. Dastjerdi, and M. Ghanaatshoar., "Finite difference time domain method for calculating the band structure of a 2D photonic crystal and simulating the lensing effect," In *Journal of Physics: Conference Series*, Vol. 454, No. 1, p. 012011, 2013.

[32] K. Sakai, J. Yeu, and S. Noda., " Coupled-wave model for triangular lattice photonic crystal with transverse electric polarisation," *Optics express*, vol. 16, no.9, p.60322, 2008.

[33] K. Sakai, E. Miyai, T. Sakaguchi, D. Ohnishi, T. Okano, and S. Noda, "Lasing Band-Edge Identification for a Surface-Emitting Photonic Crystal Laser," I*EEE Journal on Selected Areas in Communications*, vol. 23, no. 7, p. 1335–1340, 2005.

[34] K. Hirose, Y. Liang, Y. Kurosaka, A. Watanabe, T. Sugiyama, and S. Noda, "Watt-class high-power, high-beam-quality photonic-crystal lasers," *Nature photonics*, vol. 8, no. 5, Suppl, 2014.

[35] S. Fan and J. D. Joannopoulos., "Analysis of guided resonances in photonic crystal slabs." *Physical Review B* 65, no. 23, p. 235112, 2002.

[36] K. Hirose, Y. Liang, Y. Kurosaka, A. Watanabe, T. Sugiyama, and S. Noda, "Watt-class high-power, high-beam-quality photonic-crystal lasers," *Nature photonics*, vol. 8, no. 5, p. 406–411, 2014.

[37] Y. Kurosaka, S. Iwahashi, K. Sakai, E. Miyai, W. Kunishi, D. Ohnishi, and S. Noda., "Band structure observation of 2D photonic crystal with various V-shaped air-hole arrangements," *EICE Electronics express*, vol. 6, no. 13, p. 966–971, 2009.

[38] S. Iwahashi, K. Sakai, Y. Kurosaka, and S. Noda., "Air-hole design in a vertical direction for high-power two-dimensional photonic-crystal surface-emitting lasers," *Journal of the Optical Society of America B*, vol. 27, no. 6, p. 1204-1297, 2010.

[39] R. J. E. Taylor, P. Ivanov, G. Li, D. T. D. Childs, and R. A. Hogg, “Optimisation of photonic crystal coupling through waveguide design,” *Optical and Quantum Electronics*, vol. 49, no. 2, p. 1-26, 2017.

[40] K. B. Hong, L. R. Chen, H. T. Yen, W. C. Weng, B. H. Chuang, and T. C. Lu., “Impact of air-hole on the optical performances of epitaxially regrown p-side up photonic crystal surface-emitting lasers.” *IEEE Journal of Selected Topics in Quantum Electronics* 28, no. 1, p. 1-7, 2021.

[41] Z. L. Li, S. C. Lin, G. Lin, H. W. Cheng, K. W. Sun, and C. P. Lee, “Effect of etching depth on threshold characteristics of GaSb-based middle infrared photonic-crystal surface-emitting lasers,” *Micromachines (Basel)*, vol. 10, no. 3, 2019,

[42] Y. Kurosaka, K. Sakai, E. Miyai, S. Noda., “Controlling vertical optical confinement in two-dimensional surface-emitting photonic-crystal lasers by shape of air holes.” *Optics express* 16, no. 22, p. 18485-18494, 2008.

[43] B. C. King, “Gallium Arsenide Based Photonic Crystal Surface Emitting Lasers,” *PhD Thesis*, January, 2021.

[44] M. Imada, S. Noda, A. Chutinan, M. Murata, and G. Sasaki, “Semiconductor lasers with one- and two-dimensional air/semiconductor gratings embedded by wafer fusion technique,” *IEEE Journal on Selected Topics in Quantum Electronics*, vol. 5, no. 3, p. 658–663, May 1999,

[45] M. Y. Hsu, G. Lin, and C. H. Pan., “Electrically injected 1.3- μ m quantum-dot photonic-crystal surface-emitting lasers,” *Optics Express*, vol. 25, no. 26, p. 32697–32704, 2017.

[46] S. Noda, K. Kitamura, T. Okino, D. Yasuda, and Y. Tanaka, “Photonic-crystal surface-emitting lasers: Review and introduction of modulated-photonic crystals,” *IEEE Journal of Selected Topics in Quantum Electronics*, vol. 23, no. 6, Nov. 2017.

[47] K. Ishizaki, M. D. Zoysa, and S. Noda, “Progress in Photonic-Crystal Surface-Emitting Lasers † ,” *Photonics*, vol.6, no. 3, p. 96, 2019.

[48] D. M. Williams, K. M. Groom, B. J. Steven, D. T. D. Childs, R. J. E. Taylor, S. Khamas, R. A. Hogg, N. Ikeda, and Y Sugimoto., “Epitaxially regrown GaAs-based photonic crystal surface-emitting laser,” *IEEE Photonics Technology Letters*, vol. 24, no. 11, p. 966–968, 2012.

[49] A. F. McKenzie, B. C. King, K. J. Rae, S. Thoms, N. D. Gerrard, J. R. Orchard, K. Ns "Void engineering in epitaxially regrown GaAs-based photonic crystal surface emitting lasers by grating profile design." *Applied Physics Letters* 118, no. 2, p. 021109, 2021.

[50] J. Shen, F. Aydinoglu, M. Soltani, and B. Cui., "E-beam lithography using dry powder resist of hydrogen silsesquioxane having long shelf life," *Journal of Vacuum Science & Technology B*, vol. 37, no. 2, p. 021601, 2019.

[51] A. F. McKenzie, A. S. M. Kyaw, N. D. Gerrard, D. A. MacLaren, R. A. Hogg., "Kinetic influences on void formation in epitaxially regrown GaAs-Based PCSELs," *Journal of Crystal Growth*, vol. 602, 2023.

[52] W. G. Spitzer and J. M. Whelan, "Infrared absorption and electron effective mass in n-type gallium arsenide," Physics Review, vol. 114, no. 1, pp. 59–63, 1959.

[53] D. Lei "Trench Etched Polarisation Pinned Multimode Vertical Cavity Surface Emitting Lasers," *Ph.D. Thesis,* 2023.

Chapter 3: Effect of Ridge Waveguide Etch Depth on Quantum Dot Superluminescent Diodes

3.1 Introduction

This chapter discusses the effect of ridge waveguide etch depth on the characteristics of superluminescent diodes (SLDs) such as spectral bandwidth and output power, along with gain spectra measurements of the devices. This study presents characteristics of SLDs dependence on the etch depths for two extreme ridges etch depths: 470 nm (shallow-ridge waveguide that does not reach the optical mode) and 2100 nm (deep-ridge waveguide where the etch goes through the active element), shown in Figure 3.1.

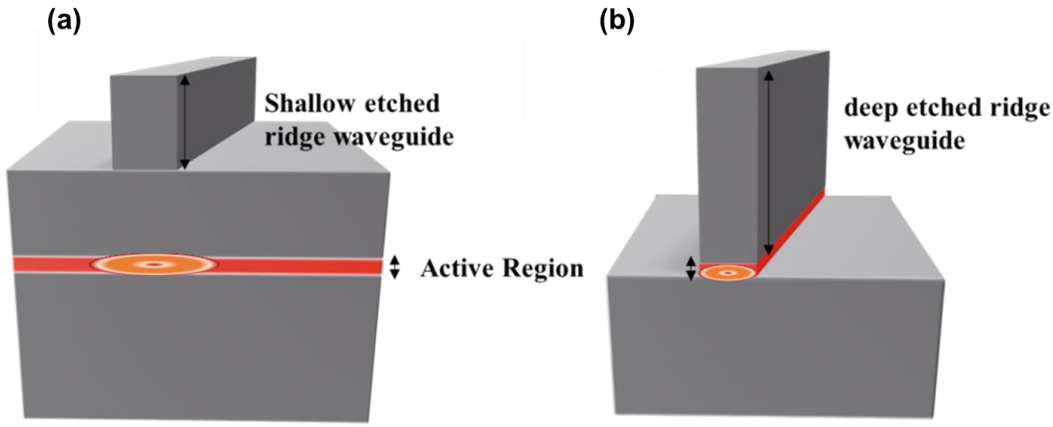

Figure 3.1: Schematic diagrams of (a) shallow-etched and (b) deep-etched ridge waveguide.

The electrical characteristics of both shallow and deeply etched ridge devices are firstly discussed to demonstrate electronic equivalence (and assumed opto-electronic equivalence) of the individual sections. The net modal gain spectra are reported, using the segmented contact gain measurement method [1]. For QD SLDs, emission power, device length and spectral shape and bandwidth are interlinked [2]. The length dependence of device power and spectral bandwidth of the SLDs are then discussed. It is observed that temperature changes can affect the bandwidth of the SLD due to carrier escape to higher states of the QD. This behaviour occurs in both shallow and deep ridge etch devices. A broadening in bandwidth is observed with increasing temperature. A discussion of temperature dependence

on QD SLDs is made by analysing the EL spectra. In terms of achieving moderate power and spectral bandwidth, the shallow-etched device delivers the best performance. Results suggest that if scattering losses can be reduced in the deeply etched structure, then this would provide better operating characteristics. One key novelty introduced is the use of very high temperatures to achieve broad spectral bandwidth operation. The poor thermal properties of the deeply etched QD SLD indicate that with Joule heating, the junction temperature raises by around 200-250 ºC, and this results in significant broadening of the emission (from 118 nm to 167 nm albeit with low power) due to de-population of low energy states and occupation of higher energy states. This effect is then harnessed in the shallow-etched SLD by raising the heat-sink temperature to 180 ºC to obtain 250 nm wide emission with an output power of 0.3 mW. It should be noted that this spectral bandwidth is achieved using standard QD laser epitaxial structures (i.e., no special layer structures [3]-[7] nor growth techniques [8]-[10]), just extreme operating temperatures.

3.2 Background

SLDs have attracted significant interest in developing broadband high-power light sources for biomedical imaging applications, such as optical coherence tomography (OCT) [11]-[13], which requires light sources that have moderate output power and a broad emission spectrum. Broad bandwidth light sources are essential to improve the axial resolution to distinguish finer features in specimens in OCT systems. Due to the strong multiple scattering nature of biological tissue [14], high-power and broad spectral bandwidth sources are required to enable greater penetration depth.

SLDs are broadband light emitters that combine the features of the high-power of laser diodes and the broad spectral bandwidth of light-emitting diodes. In SLDs, the spontaneous emission is optically amplified by stimulated emission in a gain medium [15]. A large spectral bandwidth due to this amplified spontaneous emission (ASE) is one of the most important features of the SLD as the resolution of the OCT system is governed by the coherence length of the optical source, which is inversely proportional to the bandwidth of the optical source. Several approaches have been employed to extend the bandwidth and power of the SLDs such as chirped QWs [16] QW intermixing [17], and multiple QWs (MQWs) [18] as the active medium. However, achieving a spectral bandwidth of greater than 100 nm is still a challenge. Recently, QD materials grown by the Straranski-Krastanow (S-K) growth method have been considered as an ideal light-emitting material to overcome the difficulty of obtaining a broad spectral bandwidth. Generally, a broad gain spectrum due to the inhomogeneous size distribution of QD in the active layer is a disadvantage for laser

devices. However, the wider spectral emission is beneficial for QD-SLDs. These active elements have a naturally inhomogeneous size distribution and demonstrate strong state-filling effects [19], [20]. Due to the delta-like DOS, and low number of states, the QD electronic states can be easily filled with the supplied carriers and the emission bandwidth should be extended in accordance with their discrete bandgap energies: ground state (GS), 1^{st} excited state (ES_1), 2^{nd} excited state (ES_2), and so on. However, these states have increasing degeneracy, so practically in QD SLDs, a spectral bandwidth is only achieved when the ASE from two states of the QD balance. This occurs at a particular current density range (and hence power) for a given QD SLD. Many techniques have been used to broaden the spectral width of QD SLDs such as multilayer stacks [21], post-growth annealing [22], and multiple dots-in-a-well for longer wavelengths [23] to improve the axial resolution of OCT systems. For QD SLDs, a spectral bandwidth beyond 160 nm has been achieved by simultaneous emission from the GS and ES of the QD [22], [24]. Most reports have focused on the investigation of active medium [23]-[27] or device structures [28]-[30] for improvements in bandwidth and power of the QD SLDs.

3.3 Gaps in Knowledge

There have been many studies on improving the spectral bandwidth of QD light sources [31]. However, the optimization of the SLDs through optimization of fabrication processes, such as etch depth is lacking, for example for shallow and deeply etched structures, see Figure 3.1. In laser applications, the importance of the etch depth is often discussed. In ridge waveguides, the lateral optical confinement is defined by the effective refractive index step that is formed between the etched and non-etched areas of the semiconductor material. Optical and current confinement can be improved by optimizing the etch depth and consequently the improvement in the performances of the laser devices such as slope efficiency [26] and threshold current can be achieved. In shallow etched laser devices, the optical confinement is relatively low since the waveguide is only etched through the contact layer and therefore there is a small refractive index step due to free carrier effects. The advantage of shallow ridge waveguides is that there are low scattering losses due to the reduced interaction between the optical mode a ridge sidewall. Deeply etched laser devices provide high current and optical confinement due to low lateral current leakage and high lateral refractive index step. Therefore, there is a low threshold current of the laser [32]-[35]. However, optical scattering loss associated with the etched ridge sidewall roughness can become a key limiting factor. This scattering loss is undesirable as it increases the threshold current and reduces the slope efficiency of the laser diode [36]. Also, if the etch goes deeper than the active element, oxidation may lead to a reduction in device lifetime. Therefore,

device performance such as temperature-dependent operation, efficiency, and threshold current can be improved in laser applications by optimising the etch depth [34].

Table 3-1: Comparison of key properties of shallow and deeply etched ridge.

	Shallow etched ridge waveguide	Deeply etched ridge waveguide
Heat extraction	**Very good**	**Very Poor**
Scattering Loss	**Low**	**High**
Capture of SE for amplification	**Low**	**High**
Sidewall current leakage	**Low**	**High**
Carrier diffusion	**High**	**Low**

Table 3-1 compares the shallow and deeply etched ridges with respect to various comparison factors and outlines the difference between the ridges. In shallow etched device, a small refractive index step leads to weak capture of SE for amplification since the waveguide is etched only through the contact layer. However, this is the main advantage since the sidewall current leakage is low due to the carrier interaction with the etched surface is negligible. A further benefit arises from form the reduced interaction between the optical mode and the ridge sidewall leading to lower scattering loss. Moreover, the heat extraction is very good since the carrier can flow freely in the active region. However, the weak current confinement can lead to large current spreading and influence on the current density. The spreading current is the current which do not originate from the recombination of electron-hole pairs in the regions below the contact stripe instead, it is caused by drift and diffusion of holes in the region beyond the contact. Shallow etched ridge waveguides are superior in terms of heat extraction, scattering loss and sidewall current leakage.

3.4 Methodology

The samples were grown on Si-doped (100) GaAs substrate in a molecular beam epitaxy (MBE) reactor by QD Laser Inc, Japan. The structures consist of a 300 nm *n*-type GaAs buffer layer followed by 20 nm *n*-type $Al_{0.2}Ga_{0.8}As$, 1440 nm $Al_{0.4}Ga_{0.8}As$, and 20 nm $Al_{0.2}Ga_{0.8}As$ which act as *n*-type cladding layers. The *p*-type cladding layers include 20 nm *p*-type $Al_{0.2}Ga_{0.8}As$, 1400 nm $Al_{0.4}Ga_{0.8}As$, and 20 nm $Al_{0.2}Ga_{0.8}As$. A 400 nm thick p^+ GaAs

layer was grown as a contact layer. The growth of the active region starts with 60 nm of undoped GaAs followed by 8 layers of InAs QD. Each layer has a 0.8 nm InGaAs layer strain reduced layer (SRL). An undoped GaAs barrier layer (35.5 nm) is inserted between the layers of QD to allow multi-layer stacks to be realised. Two different ridge etch depth devices were fabricated using standard techniques, which are described in section 2.3.2.3 Figure 3.3 shows the SEM images of the two samples with two ridge etch depths: (a) shallow ridge etch which is etched through only the highly *p*-doped layer (*p*-GaAs) (b) deep ridge which is etched completely through the active region (QD layer).

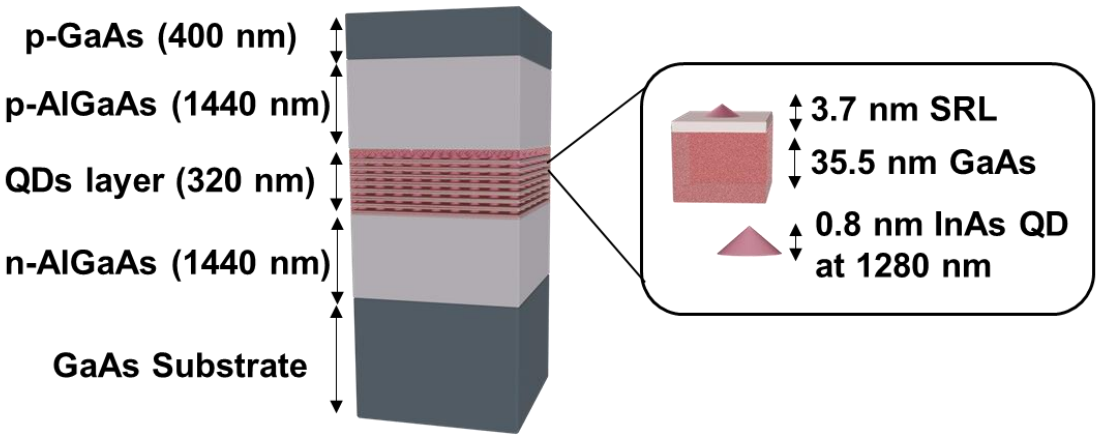

Figure 3.2: Schematic diagram of the QD layer structure.

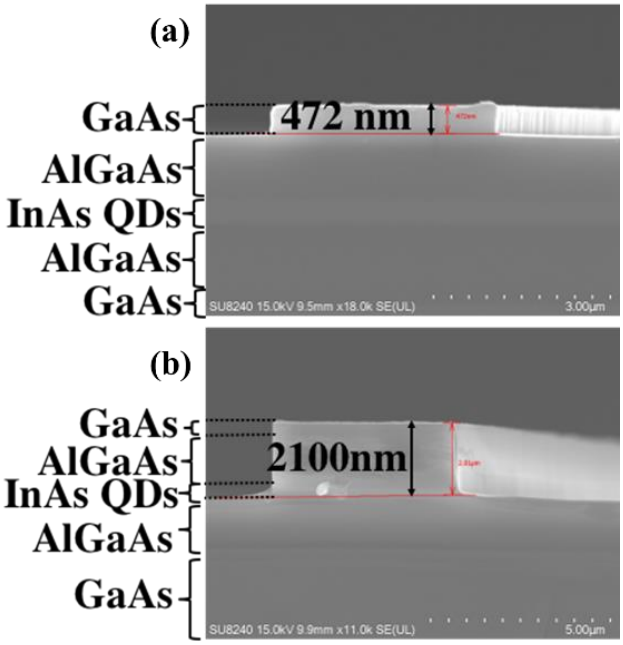

Figure 3.3: Cross-Sectional SEM images of ridge waveguide samples showing the etch depth (a) shallow-ridge (b) deep-ridge.

Figure 3.4 shows a schematic diagram and optical microscope image of the SLD. The waveguide structure of the SLD is a multi-section contacted waveguide where the optical feedback in the laser cavity is inhibited by tilting the waveguide. There are eight sections with an isolation gap between each section of 10 µm. Each section is 250 µm long and the ridge width is 5 µm. After fabrication, the devices were cleaved and mounted onto ceramic tiles using silver epoxy, and the devices were then wire bonded to enable testing. Measurements were performed under pulse (10 µs pulse width, 1% duty cycle) conditions to reduce self-heating effects. To minimize the effects of self-heating, a short pulse width with a low duty cycle is typically used. The shorter pulse width and lower duty cycle allow for more efficient heat dissipation between pulses, reducing the overall temperature rise of the device. For this work, 10 µs pulse with 1% duty cycle was chosen as it was the limit of the experimental setup. Measurements were at room temperature unless otherwise stated. Details of how the measurements are performed are discussed in section 2.4.

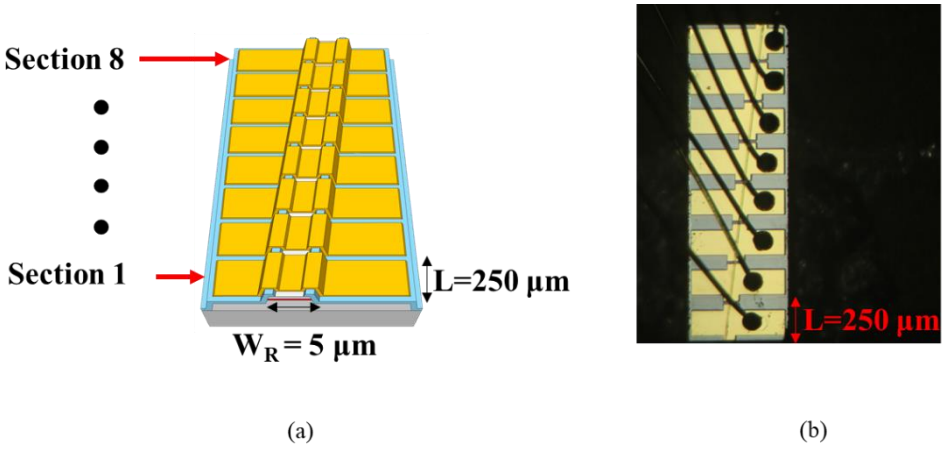

Figure 3.4: (a) Schematic and (b) microscopic images of the SLD.

3.5 Results and Analysis

3.5.1 Electrical Characteristics

For the segmented contact gain measurement [1], it is essential to have a device with identical sections electrically so that the opto-electronic properties of the sections can be assumed to be identical. As a result, gain and SE from each section is the same and net modal gain can be calculated. Figure 3.5 shows the current-voltage (I-V) measurements for each contact of the shallow-ridge and deep-ridge devices. For the shallow-ridge device, the differential resistance is ~10 Ω with an essentially identical turn-on voltage of 0.6 V which indicates that all the segments are electrically identical. For the deep-ridge device, the resistance is ~15 Ω which is higher than that of a shallow etch device, and the turn-on voltage is 0.9 V. The increase in the forward voltage of the deeply etched device may be caused by

the plasma damage in the active region during the dry etching process. The high resistance in deeply etch ridge device is due to the high carrier confinement.

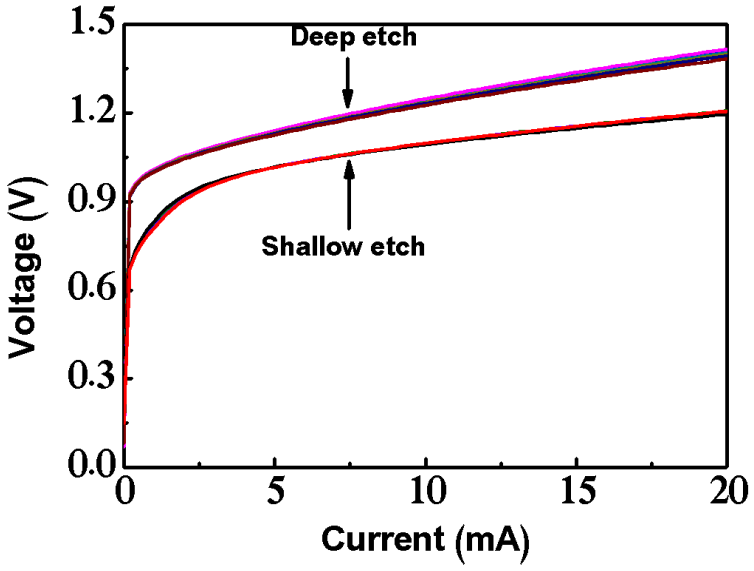

Figure 3.5: Current-voltage characteristics of eight sections of shallow and deeply etched devices.

Shallow etched ridge waveguides have a larger effective mode area and a lower optical confinement factor, which reduces the optical gain and increases the required threshold current for lasing. However, the wider ridge also reduces the resistance of the device, which decreases the turn-on voltage. On the other hand, deep etched ridge waveguides have high optical confinement factor. This reduces the threshold current required for lasing, but also increases the resistance of the device, resulting in a higher turn-on voltage. The self-heating effect can also contribute to the difference in turn-on voltage between shallow and deep etched ridges. In general, the self-heating effect is more pronounced in deep etched ridge waveguides due to their smaller cross-sectional area, which limits heat dissipation. The temperature increase can lead to a reduction in the carrier density and optical gain, and an increase in the resistance and threshold current. This results in a higher turn-on voltage for deep etched ridge waveguides compared to shallow etched ones. The sections were electrically isolated by etching of the highly *p*-doped GaAs contact layer and provided the isolation resistance of ~1 kΩ between adjacent contacts. The carrier densities are calculated using the isolating etch width of 5 μm. There may be overestimating of carrier density in the shallow etched structures since the current spreading is significant since the etch depth is just the highly doped GaAs contact layer.

3.5.2 Segmented Contact Gain

The gain spectra were obtained using the segmented contact gain measurement for both shallow and deep ridge devices. Figure 3.6 (a) presents the net modal gain spectra of the deep-ridge device over the current density range from 0.8 to 12 kA/cm^2 at room temperature.

The internal loss (α_i) can be deduced from the long-wavelength tail of the net modal gain spectra and amounts to 20 ± 5 cm^{-1}. This value is rather high, and this is attributed to imperfect device fabrication such as sidewall roughness of the waveguide which leads to higher scattering losses. A reduction in internal loss may be obtained by improving device fabrication. The gain spectrum is dominated by the GS emission at ~1297 nm as the carriers mainly fills the GS of the QD at low current density. A positive net modal gain of 6 cm^{-1} is achieved at 0.8 kA/cm^2. As the injection current increases, the GS of the QD tends to be fully filled due to the limited DOS with a saturated GS net modal gain of 15 cm^{-1} at 4 kA/cm^2. The reduction in GS gain at high current densities may be thermally generated and/or negative differential gain due to free-carrier effects [40]. The excess carriers gradually fill the higher energy levels and the emission from the ES_1 of the QD contributes to the gain spectra at ~1120 nm. The ES_1 net modal gain peak overtakes the GS at 4.2 kA/cm^2. The gain spectrum is shifted to a shorter wavelength (blue shift) which is attributed to state-filling effects at low current density. On further increasing the injection current, ES_1 becomes saturated, and a red shift of the gain spectrum is observed and is attributed to self-heating. The saturated peak net modal gain of ES_1 is 24 cm^{-1} at 8 kA/cm^2. The saturated modal gain of ES_1 should be two times larger than that of GS due to the two-fold degeneracy of the ES_1 compared to the GS [41]. Modal gains of the GS and ES_1 are measured to be 35 ± 5 cm^{-1} and 44 ± 5 cm^{-1}, respectively. The difference in the predicted and experimental value may be due to the self-heating effects at high current densities leading to the thermalization of carriers out of the dot and lost via non-radiative recombination or may be due to QD anisotropy [37]. At the highest current density, there is positive net-modal gain from the ES_2 of the QD emission at ~ 1140 nm.

Figure 3.6 (b) plots the net modal gain spectra of the shallow-ridge device over the current density range from 0.8 to 12 kA/cm^2 (note overestimation of J as discussed above) at room temperature. The internal loss at long wavelength is 10 ± 5 cm^{-1}, the increase in the loss with increasing current may be attributed to noise of amplified spontaneous emission or from optical spectrum analyzer. The optical spectrum analyzer can introduce additional noise into the system, particularly when measurements are taken at higher current levels. At low current density, the gain spectrum is mainly governed by the GS emission at ~ 1297 nm and no positive gain is achieved since it is still in the loss region.

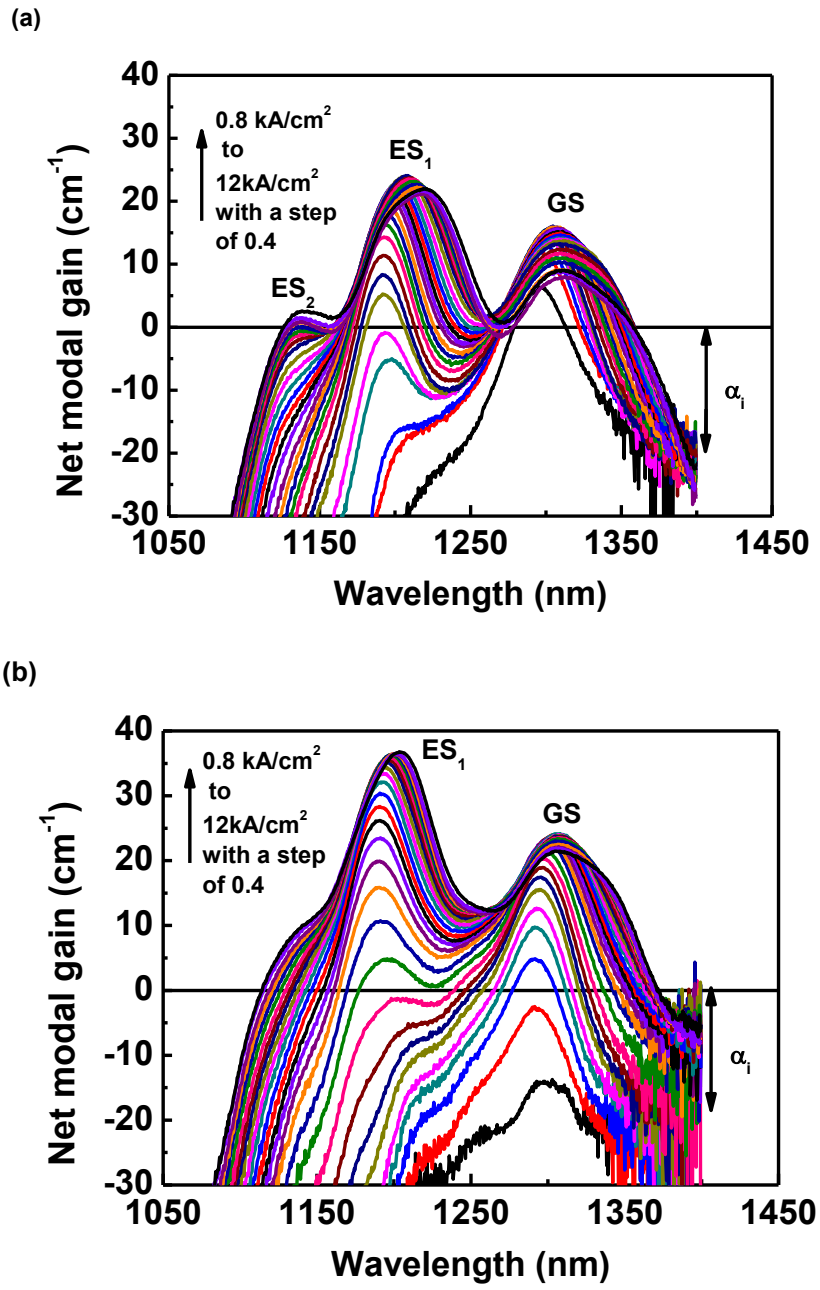

Figure 3.6: Net modal gain spectra of (a) deeply etched ridge (b) shallow etch ridge at different current density levels under the pulsed condition at room temperature.

Compared with the deep-ridge device, more carriers are needed to fill the dot states to achieve positive gain due to current spreading in the ridge because of the poor current confinement in the shallow-ridge device. In other words, there are more dots (and dot states) due to the effective width of the device being larger than the isolation contact. At 1.6 kA/cm^2, positive gain at the GS is observed, and the spectrum is shifted towards the shorter wavelength (blue shift) which is attributed to the state-filling effect, where carriers fill the discrete state of the QD. The GS peak experiences a blue shift until the current density of 2.8 kA/cm^2. From this current density, a redshift of the spectrum occurs. Further increase in the injection current leads to the GS gain saturation with a saturated net modal gain of 24

cm^{-1} is at 4.8 kA/cm^2. An asymmetric broadening and reduction in net modal gain are observed due to the self-heating/free carrier effects. The positive gain from ES_1 starts to emerge once saturation of the GS occurs and gradually increases with increased current density. Positive net modal gain from ES_1 is observed at ~ 1120 nm. The ES_1 net modal gain peak overtakes the GS at 6 kA/cm^2. Blue shifting appears up to 16 kA/cm^2 and then ES_1 gain saturates with a net modal gain of 35 cm^{-1} with further increasing current density. Again, a modal gain of the GS and ES_1 of 34 ± 5 cm^{-1}, and 45 ± 5 cm^{-1}, is achieved respectively. This is in broad agreement between the two sets of devices.

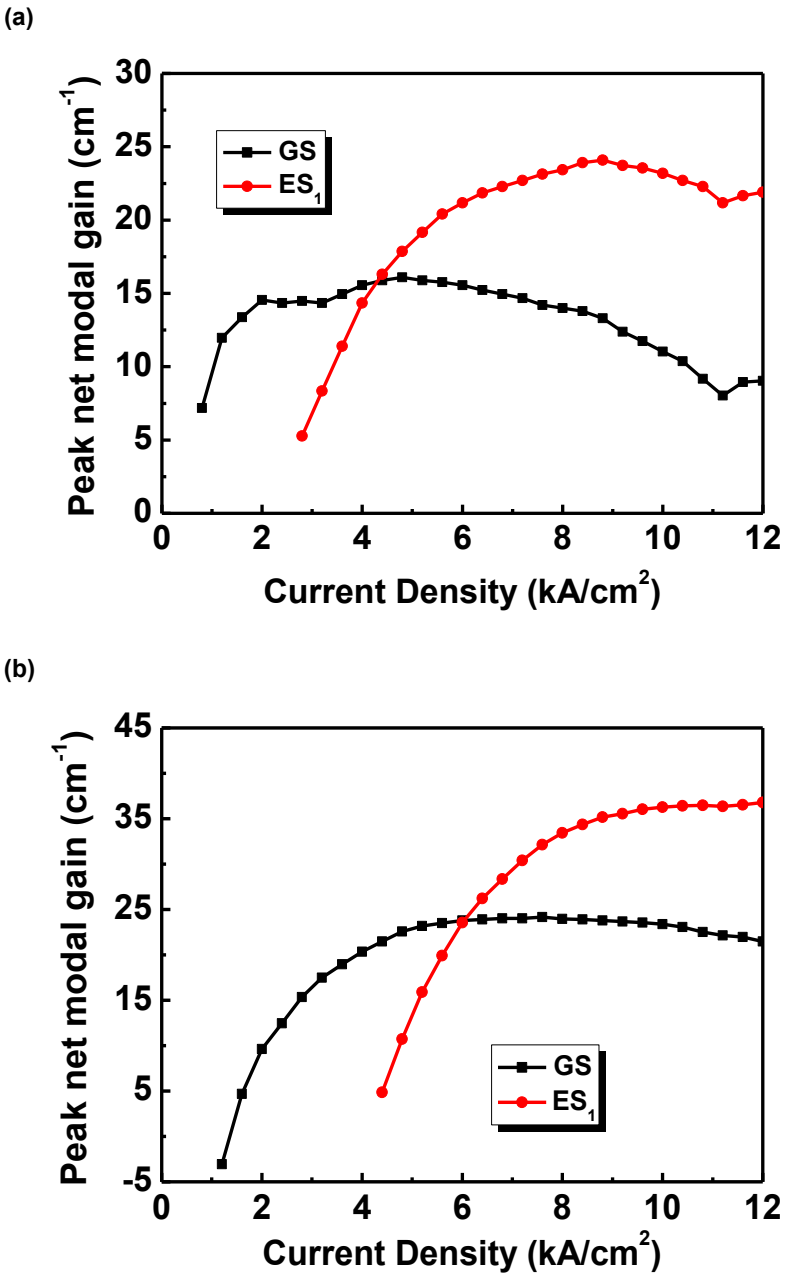

Figure 3.7: Peak net modal gain spectra of (a) deeply etched ridge (b) shallow etch ridge as a function of current density for the GS and ES_1.

The peak net modal gain for the QD states is plotted in Figure 3.7 for deep and shallow etched devices. The GS and ES states interception current density for deep and shallow etched devices are 4.2 and 6 kA/cm^2 respectively. The current density at which the ground state (GS) and excited state (ES) gain are equal should occur at the same current density in the two devices. However, assuming no current spreading effects (ridge width only of 5μm), values of 4.2 and 6 kA/cm^2 are obtained for the deep and shallow etched devices, respectively. Assuming that the value for the very deep etched ridge is correct, then the results indicate that there is an effective width of 7 μm for the shallow etched, 5 μm wide ridge.

3.5.3 Optical Characteristics

The cavity length is an important parameter as it effects on output power and spectral characteristics of SLDs [38]. The geometry of the current injection with an increasing length is shown in Figure 3.8. Each individual section is injected with the same current in order to maintain a uniform injected current density. Power-current density (P-J) is measured by increasing the cavity length of the segmented contact device SLDs to investigate the effect of length on output power, which is shown in Figure 3.8. The EL spectra of increasing cavity length are plotted in figure 3.11 to explore the effect of length on spectral coverage (defined in section 2.4.1).

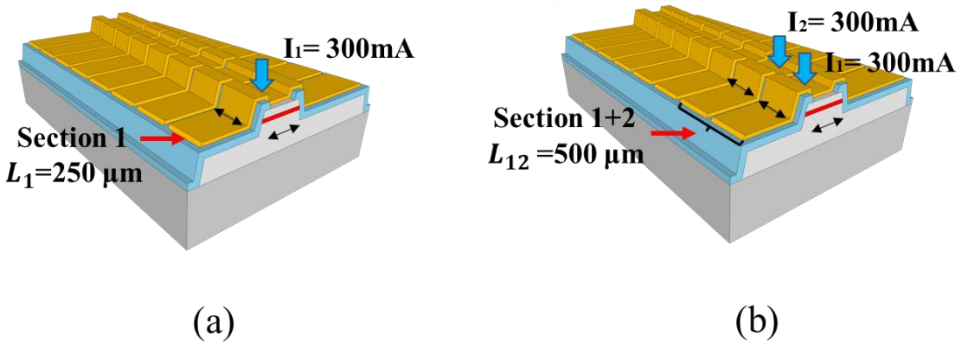

Figure 3.8: Schematic diagram of the device structure with (a) cavity length L_1 (b) increasing cavity length L_{12}.

Figure 3.9 plots the power as a function of current density for various length. Increasing in output power with length is observed for both deep and shallow ridge devices. Since ASE is proportional to e ^{gl}, an increase in power with increasing length is expected. The output power is increased with length since the photons generated inside the waveguide propagate along the length and generate further photons through stimulated emission. Due to the suppression of current spreading in deeply etched device, abrupt knee which indicates the lasing occurs for the longest contact length. However, the thermal effects in the deep etch

device is significant and therefore the optical output power is relatively low due to the thermal rollover. Higher output power is achieved in shallow etched device since the gain beats the thermal effects. The emission spectrum was investigated to ensure no parasitic lasing (Figure 3.10).

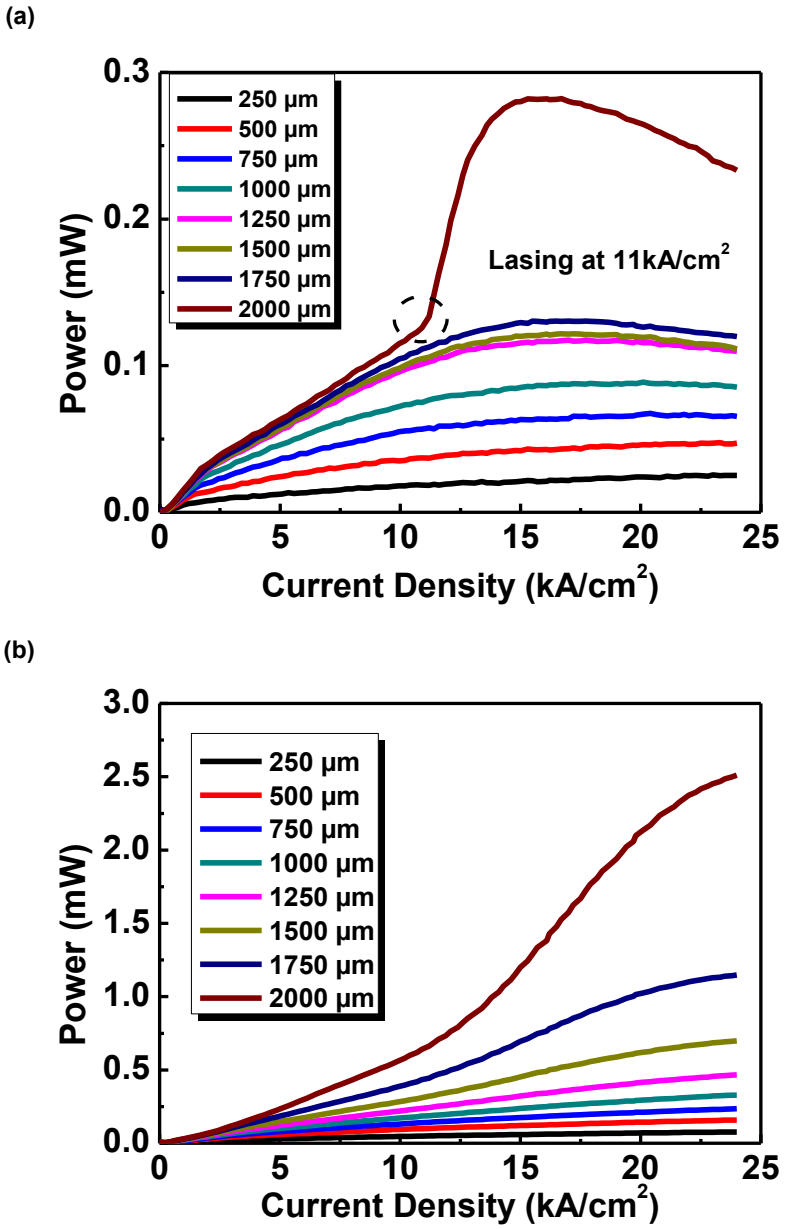

Figure 3.9: Output power as a function of current density for various lengths of (a) deeply etched ridge (b) shallow etch ridge.

For Figure 3.9 (a) (deeply etched ridge), the emitted power of the SLD is observed to increase with increasing cavity length. The P-J curves show that the output power rolls over at a comparatively low current density of 15 kA/cm^2. This is attributed to strong self-heating in the deep-ridge device due to poor heat extraction. The SLDs did not experience parasitic lasing except for a driven contact length of 2000 µm, which corresponds to the whole chip

length. For shorter driven contact lengths, the undriven absorber sections in addition to the tilted waveguide successfully inhibit lasing. However, for the longest cavity length, even though the tilted waveguide of the device is expected to suppress the cavity lasing, there was enough gain to overcome the total losses and lasing proceeds via ES_1 transition. Lasing was confirmed by the EL spectrum (Figure 3.10) collected from this device. Similar lasing behaviour from ES_1 occurs in these works [18]. The output power from deep-ridge SLD is low which is less than 0.15 mW before lasing occurs. Assuming a gain of $25cm^{-1}$ for ES_1 (Figure 3.6), the effective reflectivity of the as-cleaved tilted waveguide can be estimated to be 0.7%, in agreement with previous work [39]. AR coatings may further reduce this value, although the introduction of absorbing open-circuit sections seems a simple and low-cost method to inhibit parasitic lasing.

Figure 3.9 (b) shows the output power of the shallow etch device as a function of current density for various lengths. The increase in output power occurs with increasing cavity length. Output power of 2.5 mW is achieved for the longest contact length (2000 μm) and there is no significant knee suggesting lasing. The output power of the shallow etched device is 10 times higher than deeply etched device. Whilst shallow etched device is operating with even higher gain ($35cm^{-1}$ for ES_1), no lasing indicates that the effective reflectivity is lower by at least a factor of 10 (<0.07%). This can be expected due to the poor waveguiding of the shallow etched waveguide.

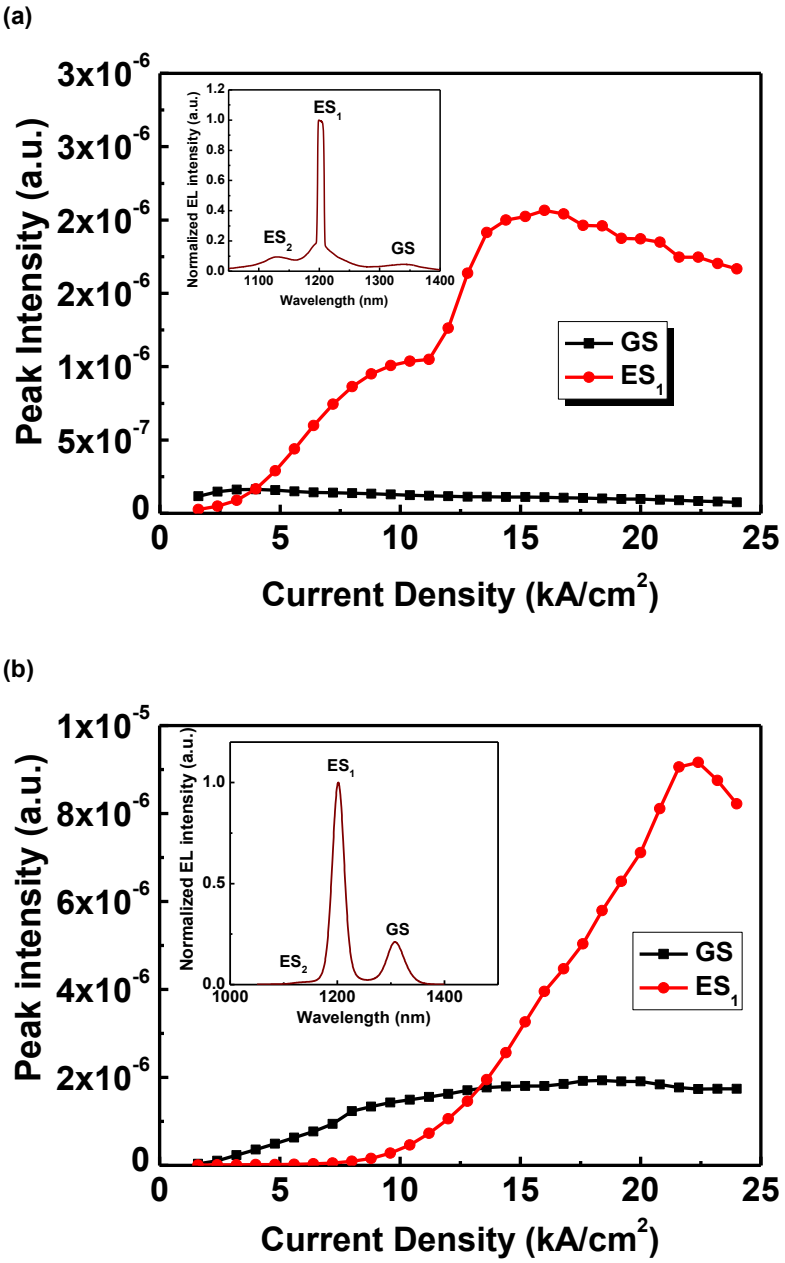

Figure 3.10: Peak EL intensity for GS and ES_1 versus current density of 2000 µm long (a) deeply etched ridge (b) shallow etched ridge device. The inset shows the spectrum at a current density of 24 kA/cm^2.

Figure 3.10 plots the peak value of the EL spectra as a function of current density for the longest length. From LI curve, two different behaviours are observed: parasitic lasing (for deeply etched device) and shallow no parasitic lasing (for shallow etched device). To confirm this lasing behaviour the peak value of EL intensity at various current density was carried out for the longest length. The insect shows the EL spectrum at highest injection current to further confirm the lasing. From Figure 3.10 (a), a sharp increase in the ES_1 peak intensity value indicates the point (11 kA/cm^2) where lasing occurs for the deeply etched devices. The inset figure further confirmed that the lasing is from ES_1 and the lasing line-

width is 11 nm. There is no sudden increase in EL peak value for shallow etched device which is shown in Figure 3.10 (b) and the inset figure shows broad EL emission spectrum. From this, we can confirm that the LI is purely due to the amplified spontaneous emission.

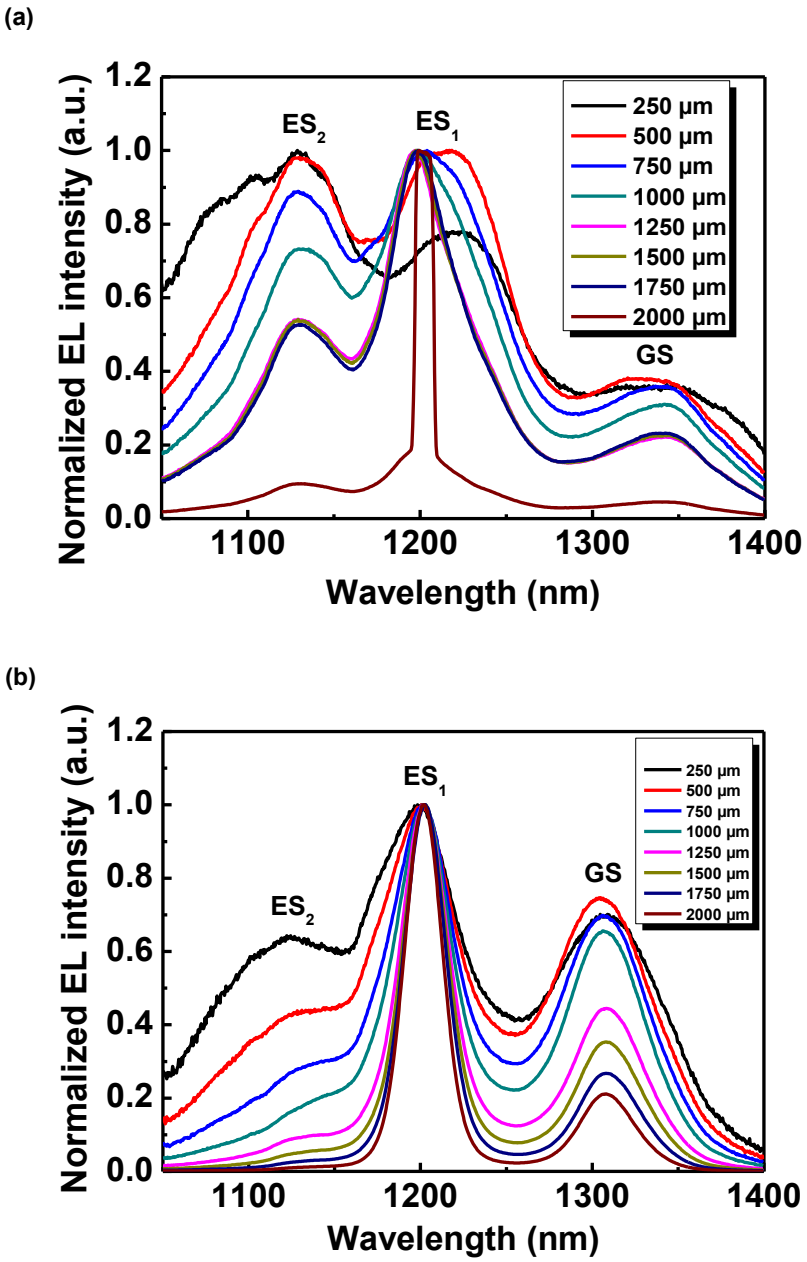

Figure 3.11: Normalized EL spectra at a current density of 24 kA/cm^2 for various lengths of (a) deeply etched ridge (b) shallow etch ridge device.

Figure 3.11 plots the EL spectra with increasing length at the current density of 24 kA/cm^2 to investigate the effect of length on the spectral coverage of SLD emission. From Figure 3.11 (a), the emission from GS is fully saturated and reduction in the intensity is occurred due to the thermal effect in deeply etched devices. Consequently, there is no contribution from GS of the QD to the spectral coverage for every chip length. Therefore, the spectral coverage is mainly dominated by the ES_1 and ES_2 of the QD. Combined contributions from

ES_1 and ES_2 emission at ~1200 nm and ~ 1120 nm respectively make the broadest spectral coverage. It is noted the spectral coverage becomes narrower by increasing the cavity length because of the ASE in the cavity. For the length above 1000 μm, the spectrum shape, as well as power, is almost identical until lasing occurs. For the shallow etched device, spectral coverage is the broadest for the shortest devices due to the combined contribution from GS, ES_1, and ES_2 at 1300 nm, 1200 nm, and 1120 nm respectively. The narrowing in spectral coverage is observed with length. Moreover, there is no contribution from ES_2 with increasing length makes the spectral coverage become narrower with length.

3.5.4 Trade-off between Power and Spectral Coverage with Chip Length

The broadest bandwidth in QD SLDs is achieved when the power from adjacent states is balanced for example where the power from GS and ES is balanced. For short device lengths a contribution from several higher energy states is observed, but the output power is low. For longer device lengths, power is increased (as power $\propto e^{gl}$) but there is a reduction in the number of states that contribute to the emission spectrum, and a narrowing of these individual transition line-width. In this section, the link between power and spectral coverage with length will be discussed experimentally.

Figure 3.12 plots the spectral coverage as a function of current density for various lengths of the deeply etched device. On inspection, the trace of all lengths is similar except for the shortest length. The figure is highlighted into five regions as follows: (I) grey region where the emission from GS is dominated, (II) green region where the GS and ES_1 emission is balanced, (III) blue region where the contribution from all the states (GS, ES_1 and ES_2) of the QD, (IV) red region where the reduction in GS occurs due to the thermal effect and only ES_1 emission contributes to the spectrum, (V) yellow region where the significant emission from ES_2 contribute to the spectrum and ES_1 and ES_2 dominates the spectral coverage. At the lowest current density, the GS mainly contributes to the spectrum and spectral coverage is around 50 nm for all the lengths except 250 μm (Region I). Increasing the current density introduces a contribution from ES_1 which results in broadening the spectral coverage due to the simultaneous contribution from the GS and ES_1 (Region II). The spectral coverage of around 150 ± 10 nm is achieved in that region given by the state separation plus the FWHM of the individual states (GS and ES) of the dot. A slight (10 nm) reduction in spectral coverage with length is due to the increasing role of amplification as mentioned above. Further increasing in current leads to a contribution from ES_2 for the shortest length (250 μm) and a spectral coverage of 225 nm is obtained (Region III). However, more carriers are needed to contribute from ES_2 for a length greater than 250 μm, and there is no emission from ES_2 in these current ranges. Moreover, the relative reduction in the intensity of GS

makes the spectral coverage reduce as only ES_2 contributed to the spectral coverage (Region IV). Carriers continue to fill ES_2 with a further increase in current. The spectral coverage is broadened again with the combined contribution of ES_1 and ES_2 in Region V. This behaviour for QD states has also been observed by other groups [40].

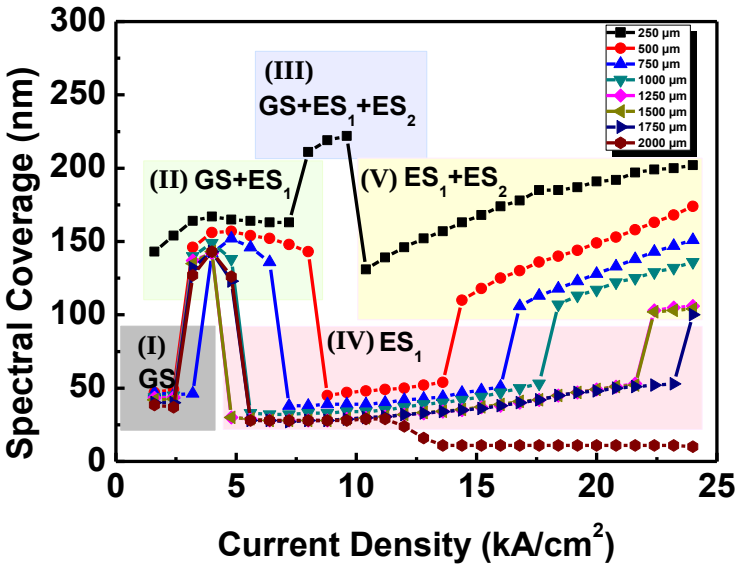

Figure 3.12: Spectral coverage as a function of current density for various lengths of the deeply etched device. The line is a guide to the eye only and is not fitted.

Figure 3.13 illustrates the evolution of the spectral coverage for shallow etched devices as a function of current density. There is systematic filling of the states with current density. Under low current density, the GS makes a significant contribution to the emission. Depending on the length/area of the device, the current density increases and emission from ES_1 is observed. Since more carriers are needed to fill the GS (due to carrier diffusion and underestimation of the device area) ES_1 appears at larger current densities. Increase in current density eventually contributes to ES_1 emission which results to broaden the spectral coverage due to the simultaneous contribution from the GS and ES_1, which is highlighted as green. As seen in that region, the spectral coverage decreases from 175 nm to 125 nm with an increase in length. This is because the line-width of the GS and ES_1 become narrower with length due to amplification inside the cavity. Further increasing current leads to contribution from ES_2 for the shortest chip length (250 µm) and spectral coverage of 250 nm is achieved. Except for the shortest chip length, there is no clear emission from ES_2. Further increasing current may lead to self-heating/free carrier effects reducing GS emission (Region IV) which is also observed in the deep-ridge device. At high current densities only ES_1 contributes, resulting in a spectral coverage of 50 nm. Due to the higher current spreading in shallow-ridge devices, there are insufficient carriers to generate sufficient ASE from ES_2

and therefore no emission from that state contributes to emission except for the 250 µm chip length.

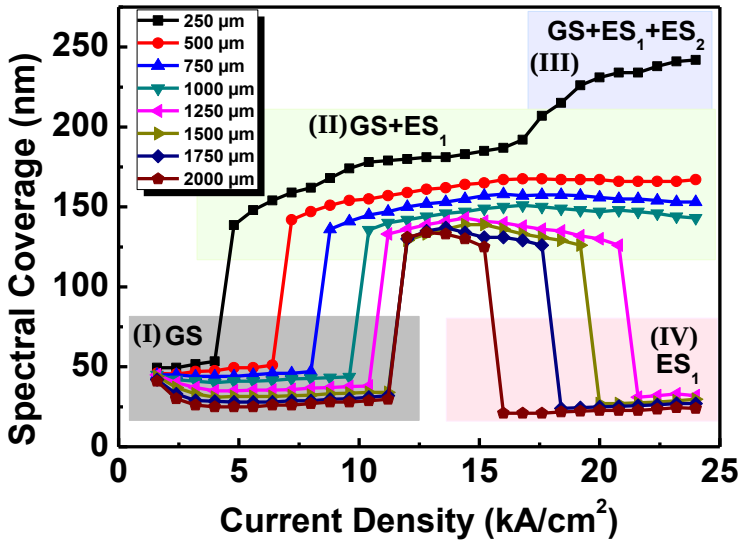

Figure 3.13: Spectral coverage as a function of current density for various lengths of the shallow etched device. The line is a guide to the eye only and is not fitted.

Figure 3.14 plot the spectral coverage as a function of power for the deeply etched device. The broadest spectral coverage is obtained from simultaneous emission from GS, ES_1, and ES_2 for the length of 250 µm. However, the output power is relatively small for this length. The power is increased by increasing chip length due to the ASE but is associated with a narrowing of the spectral width. With contributions from GS and ES_1 (Region II) or ES_1 and ES_2 (Region V), a spectral coverage of around 150 nm is achieved for a length greater than 250 µm. The results demonstrate a narrowing in spectral width with length due to amplification in the cavity, with only a few nm reductions in spectral bandwidth in that region. For example, in region II, the spectral coverage of 500 µm chip length is 155 nm and that of 2000 µm chip length is 145 nm which is 10 nm is a difference, but the power is increased two times from 0.025mW to 0.05mW highlighting the power and bandwidth trade-off.

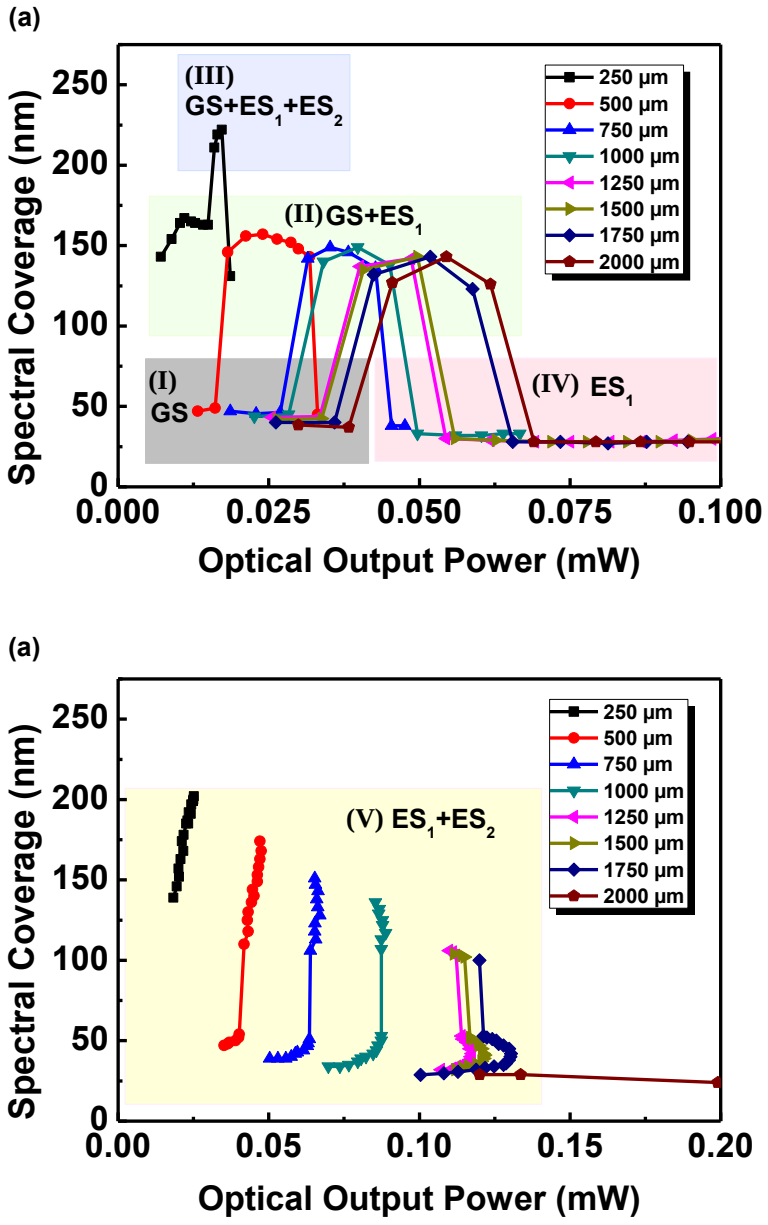

Figure 3.14: Spectral coverage as a function of power for various lengths of the deeply etched device. The line is a guide to the eye only and is not fitted.

Figure 3.15 plots the spectral coverage of the shallow etched device as a function of power. As shown in the figure, the shortest chip length (250 µm) has the broadest spectral coverage due to the combined contribution of emission from GS, ES_1, and ES_2, however, the output power is relatively small. The observation of ES_2 in the spectrum, yet absence of net-modal gain at this current density (Figure 3.6(b)) indicates the dominance of spontaneous emission rather than ASE for this length. A quick sanity check, considering e^{gl}, indicates only a 30% increase in intensity due to a gain of 10 cm^{-1} over a length of 0.025cm. Further increase in chip length results in an increase in output power and decrease in spectral bandwidth.

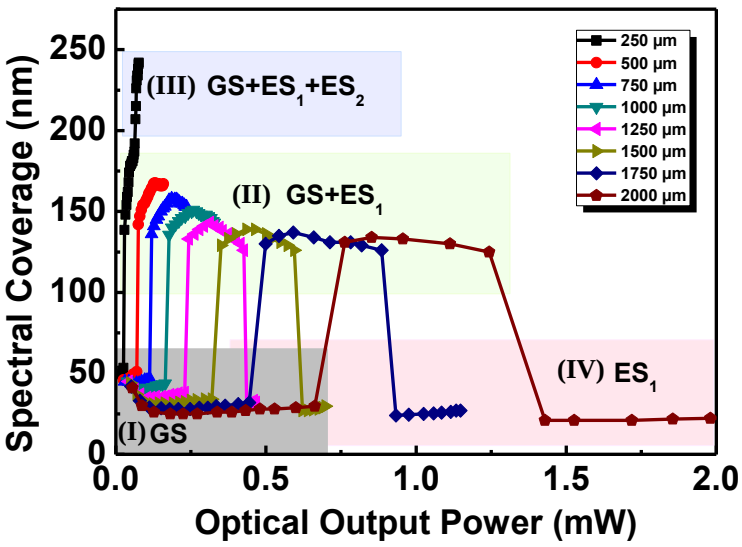

Figure 3.15: Spectral coverage as a function of power for various lengths of the shallow etched device. The line is a guide to the eye only and is not fitted.

Figure 3.16 replots the data from Figure 3.13 and Figure 3.14. For simplicity, the spectral coverage is chosen from region II (green) where the GS and ES_1 are balanced. Increasing the chip length implies an increase in output power and this is accompanied by a narrowing of the spectral coverage. This highlights that the choice of chip length is critical in the trade-off between output power and bandwidth, depending on the application requirements.

Figure 3.16 (b) shows the trade-off between power and spectral coverage of shallow etched device. Again, the spectral coverage is chosen from region II. Compared with the deep-ridge device which is shown in Figure 3.16 (b), there are only a few nm differences in spectral coverage, but the output power is much higher in the shallow-ridge device. In plotting the power and bandwidth as a function of length, current density (and any discrepancies in comparing these for the two etch depths) is removed from the discussion. The observed power difference is therefore attributed to the difference in internal loss in these two waveguide structures.

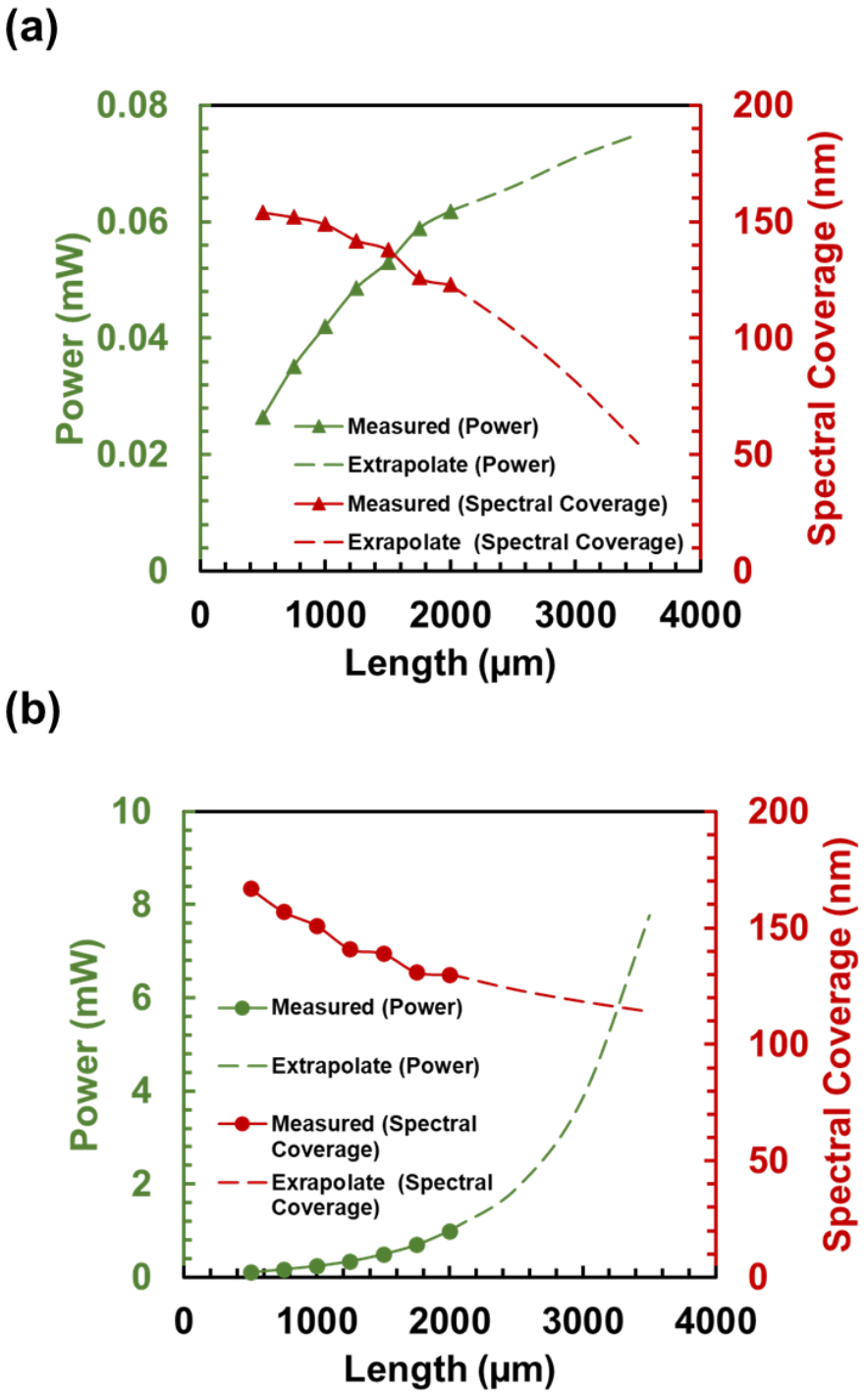

Figure 3.16: Power and spectral coverage as a function of the length of (a) deeply etched ridge (b) shallow etch ridge. The line is a guide to the eye only and is fitted.

The light sources for OCT applications require a broad bandwidth and moderate output power (mW level) to achieve high resolution and deep penetration depth, respectively. It can be concluded from Figure 3.16 that a maximum spectral coverage of ~150 nm is achieved for both shallow and deeply etched devices. The output power from the shallow ridge is higher than that of deep ridge and therefore, shallow etch QD SLD would be a better choice for OCT applications to achieve suitable penetration depth with adequate axial

resolutions. Optimizing the parameters for OCT applications involves balancing the trade-offs between spectral coverage, output power to achieve high axial resolution, and deep penetration depth. For example, in order to achieve high axial resolution, a broad bandwidth is required. The bandwidth can be increased by decreasing the coherence length or increasing the spectral width. However, this should be balanced with the need for deep penetration depth, which requires moderate output power. The choice of device structure and materials should be carefully considered to achieve the desired imaging results. It is worth noting that a more perfect deeply etched structure could potentially eliminate or reduce additional internal loss and may be a viable alternative for OCT applications if realized. Moreover, utilizing a thermo-electric cooler (TEC) to eliminate or reduce the self-heating effect can be a useful approach in optimizing the performance of a deep-etch ridge SLD light source for OCT applications. A TEC can provide active cooling to the device, thus reducing the temperature rise caused by self-heating.

To conclude, the carrier diffusion in the shallow etch devices is high and therefore the net modal gain saturation of the GS is at higher current density. However, the deeply etched devices have poor heat extraction and therefore there is significant roll over in output power with increasing current density. Moreover, internal loss value of the deeply etch devices is higher than shallow etched devices due to scattering losses at the etched sidewalls. As a result, the output power and gain of the shallow etched devices is higher than deeply etched ones.

3.5.5 Broad Temperature Range Characterisation

QD have several advantages over bulk and QW active region for SLDs. The 3D confinement of carriers in QD results in delta-like energy level in theory but in real QD broadening is expected from both inhomogeneous broadening due to a variation in the QD shape and size (inhomogeneous broadening) and homogeneous broadening due to carrier-carrier and carrier-phonon interactions [41], [42]. When the temperature increases, the homogeneous broadening is expected to increase due to increase phonon scattering and carrier escape. Consequently, increasing the homogeneous broadening increases the bandwidth [41] modestly. On the other hand, temperature increase causes carriers to thermalise to higher energy states [43] that can bring about greater changes in spectral bandwidth. For QD-based SLDs, spectral bandwidths beyond ~150 nm are still limited due to difficulties of carrier excitation to high energy states, such as ES_2 of the QD. Complicated epitaxial structures are needed for further broadening of the bandwidth. It has been observed that the increase in temperature can lead the carrier escape to the higher states of QD. The carrier filling to the higher state of the dots or homogeneous broadening can be an advantage for SLDs to achieve

ultra-broad bandwidth. In this section, the influence of the thermal effects on the spectral bandwidth and power of the QD SLDs is investigated. A study of the temperature dependence of spectral bandwidth may be made by analysing the EL spectra, and a broadening in line-width of EL spectra with increasing temperature has been observed The mechanisms that could account for this broadening are the effects of increased homogeneous broadening due to increased phonon scattering and thermal redistribution of the carriers into higher energy states.

For the EL spectra measurement of my devices, a chip length of 1750 μm was chosen to achieve the highest output power but to avoid parasitic lasing. The EL spectra at various current density at room temperature is firstly measured and plotted in Figure 3.17 and Figure 3.18 for deeply etched and shallow etched devices, respectively. The peak wavelength shifting with respect to current density for both geometries is plotted in Figure 3.19. This provides the wavelength shift with current. The junction temperature can be measured using the modal shift caused by cavity expansion and change in refractive index [44]. The EL spectra at various temperatures at constant current density is then measured and shown in Figure 3.20. The peak wavelength is tracked while increasing the temperature and is plotted in Figure 3.21. This provides the wavelength shift as a function of temperature. The wavelength is a common value between Figure 3.19 and Figure 3.21and hence can be substituted to provide the current induced change in junction temperature, ΔT_{jct}, as a function of current density.

Figure 3.17 shows the EL spectra of the deeply etched device as a function of current density at room temperature. Emission commences via the GS (~1300 nm) at low current density and upon increasing the injection current, saturation of the GS and appearance of ES_1 (~1200 nm) is observed. The ES_1 emission also becomes saturated while the ES_2 emission (~1100 nm) increases in intensity with further increasing current density. Due to the combined contribution of the ES_1 and ES_2, the spectral coverage of ~118 nm is achieved at 24 kA/cm^2.

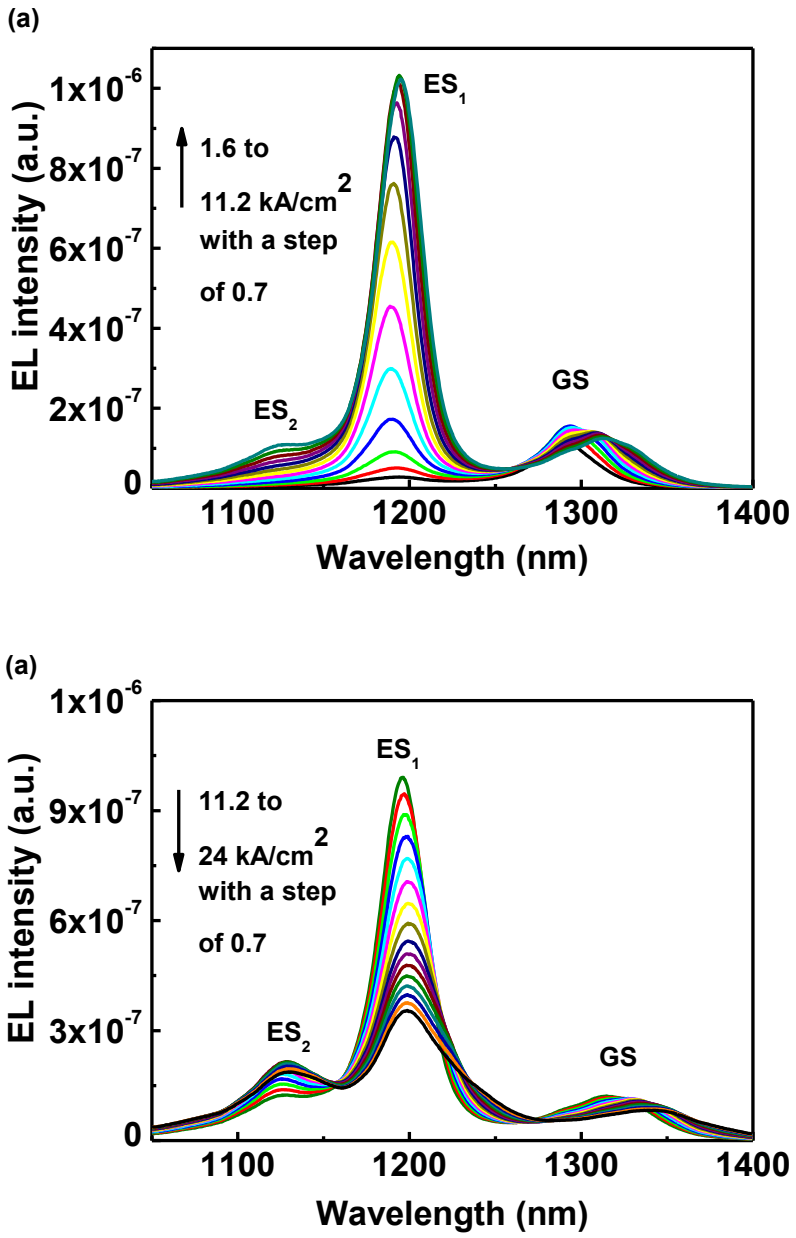

Figure 3.17: EL intensity at different current densities of the deeply etched device.

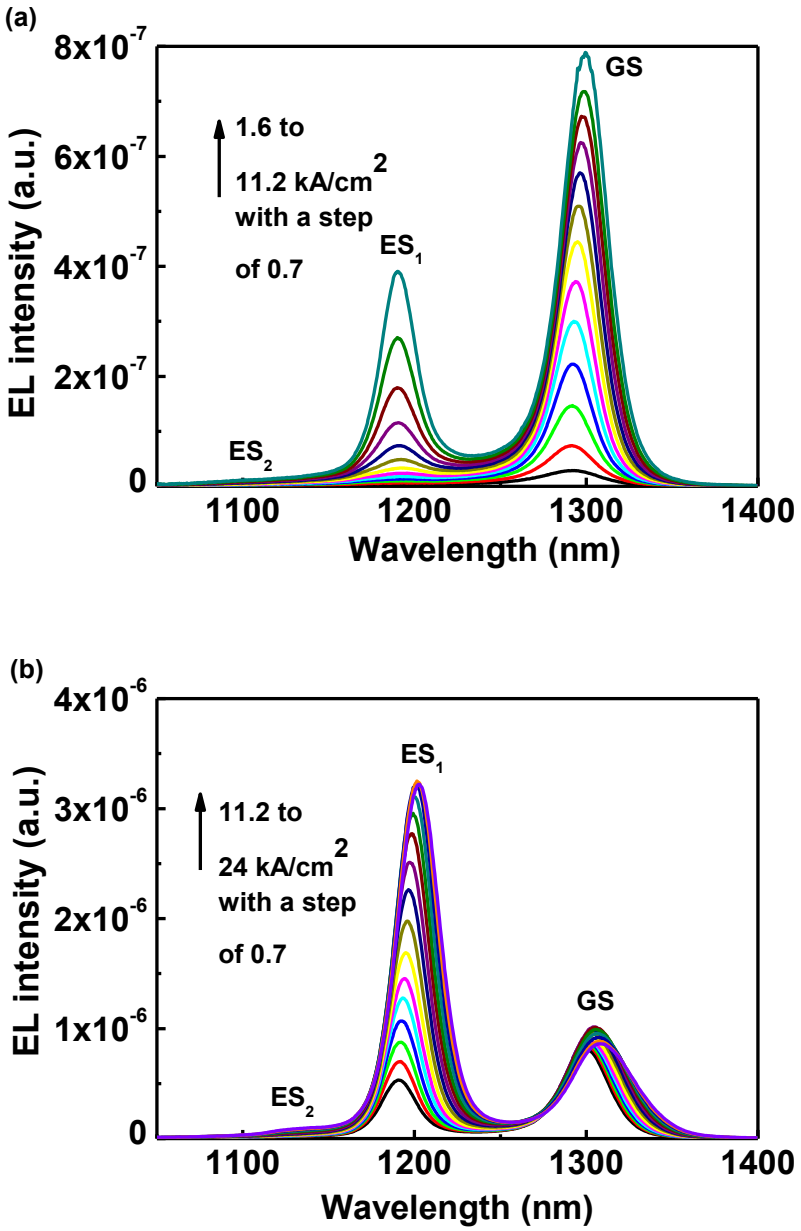

Figure 3.18: EL intensity at different current densities of the shallow etched device.

Figure 3.19 (a) shows the corresponding spectral peak position of deeply etched device as a function of current density. The peak wavelength is shifted to a longer wavelength (redshifted) with increasing current density attributed to thermal and free carrier effects. A redshift with increasing current density, $\Delta\lambda/\Delta J$, 2.3 nm per kA/cm^2 is observed for GS. The ES_1 peak wavelength is shifted to a shorter wavelength at the lowest current density. Further increasing in current density leads to the ES_1 saturation and then the wavelength shifts to the longer wavelength. A redshift of 0.6 nm per kA/cm^2 is observed for the ES_1 and ES_2. Figure 3.19 (b) plots the peak wavelength of the QD states of the shallow-ridge device as a function of current density. The shifting in wavelength with current density, $\Delta\lambda/\Delta J$, 0.8 nm per kA/cm^2 is observed for both GS and ES_1, which is 3 times lower than that observed in deeply

etched devices. This may be attributed to better heat extraction and reduced current densities.

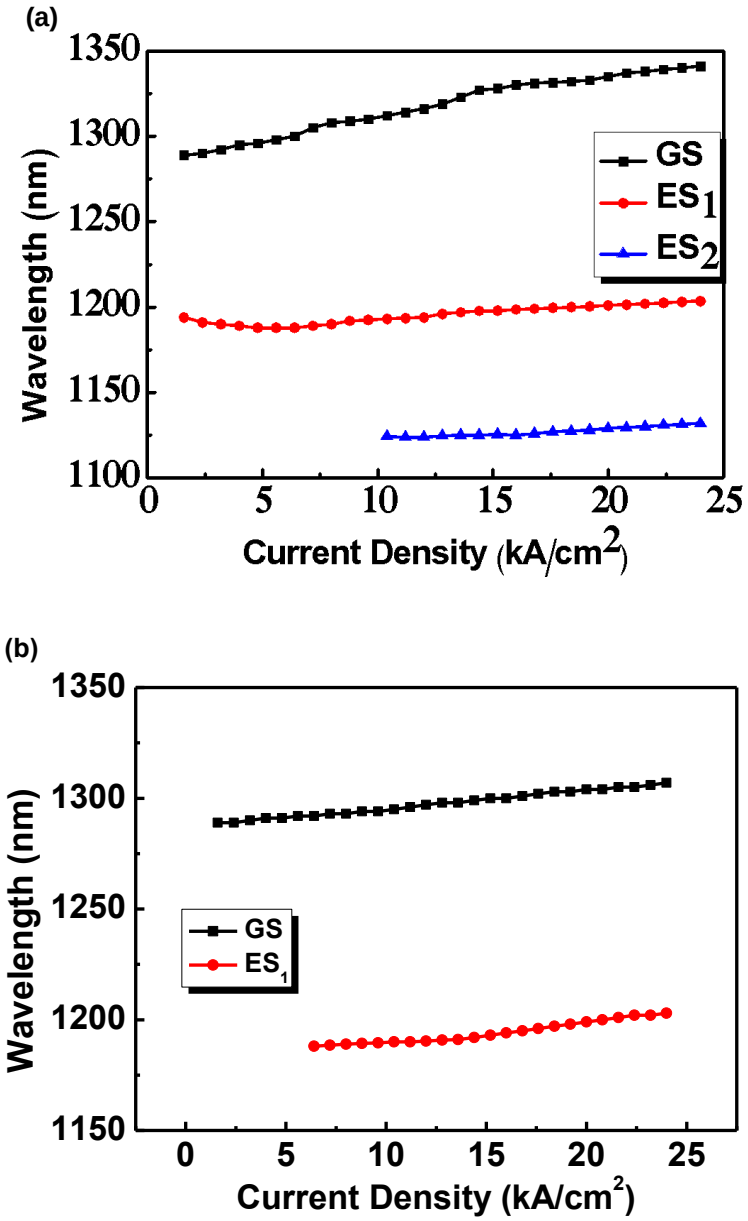

Figure 3.19: Peak wavelength as a function of current density (a) for the QD's GS, ES_1, and ES_2 of deeply etched ridge (b) for the QD's GS, ES_1 of shallow etch ridge. The line is a guide to the eye only and is not fitted.

Figure 3.20 (a) shows the normalized EL intensity of a deeply etched device over the temperature range from 20 to 65 ℃ at a constant current density of 24 kA/cm^2. Combined contribution from ES_1 and ES_2 emission result in a FWHM (defined in section in 2.4.2) of ~118 nm. By increasing the temperature, a broadening in the FWHM of ~167 nm is observed, attributed to the increase in homogeneous broadening of the QD with increase temperature [9].

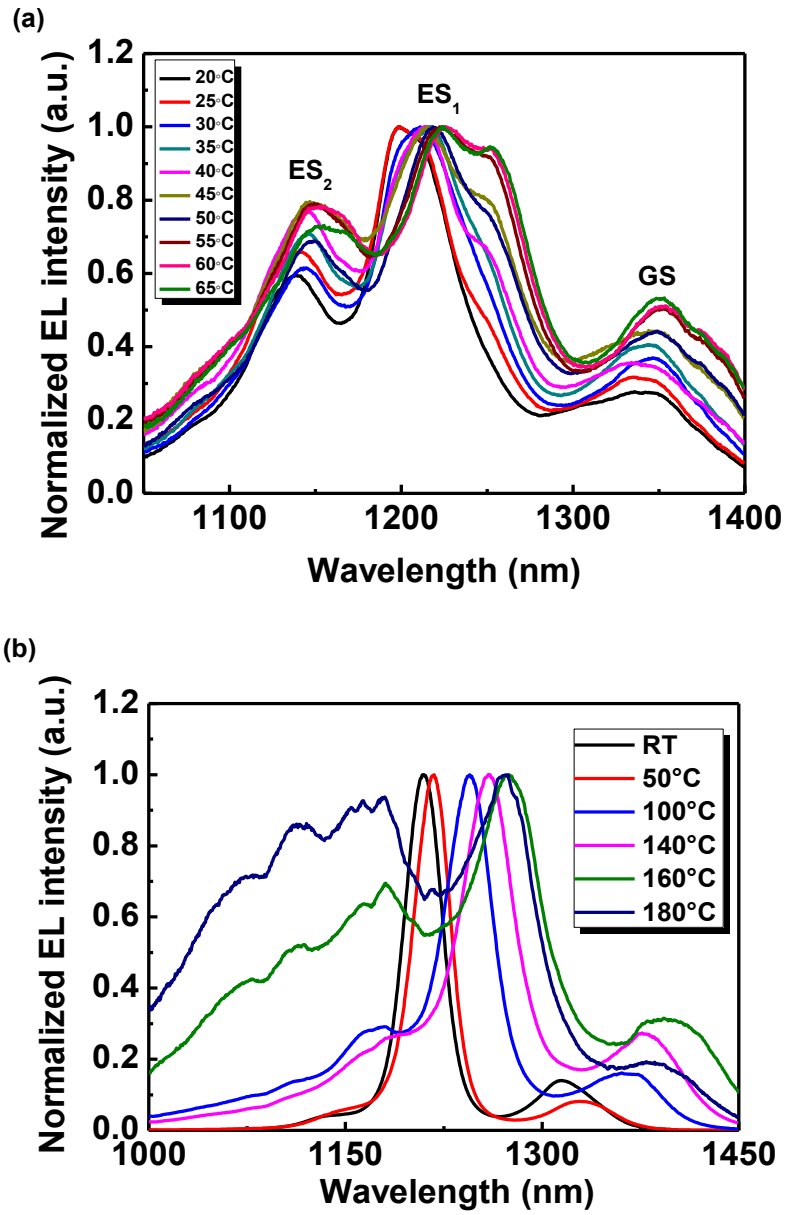

Figure 3.20: Normalized EL spectra of (a) deeply etched ridge (b) shallow etch ridge at a different temperature at a current density of 24 kA/cm^2.

Figure 3.20 (b) plots the normalized EL spectra at a current density of 24 kA/cm^2 over the temperature range of 50 to 180 ℃. Higher heatsink temperature operation is required in order to compared to deeply etched devices, and observe this homogeneous broadening of the QD. At room temperature, only two features are resolved corresponding to the GS and ES_1 of the QD. No significant emission from ES_2 is observed as this state is not occupied at this current density. As the temperature is increased, a small shoulder due to ES_2 of the QD appears at 100 ℃ as the carriers thermally redistribute into the higher states of the QD. Further increasing the temperature leads to a significant contribution from ES_2 and FWHM of ~ 250 nm is achieved with a combined contribution from both ES_1 and ES_2.

The shift in peak wavelength with current density can be caused by both thermal and free carrier effects. As the current density increases, the temperature of the device increases due to self-heating, which can cause a redshift in the peak wavelength. Additionally, as the carrier density increases, the refractive index of the device can also change, leading to a shift in the peak wavelength. In a shallow-ridge device, the ridge width and depth are typically smaller than in a deeply etched device, which can lead to better heat extraction and lower self-heating. This can result in a smaller shift in peak wavelength with current density. On the other hand, in a deeply etched device, the wider and deeper ridge can lead to higher current densities and stronger self-heating, resulting in a larger shift in peak wavelength with current density.

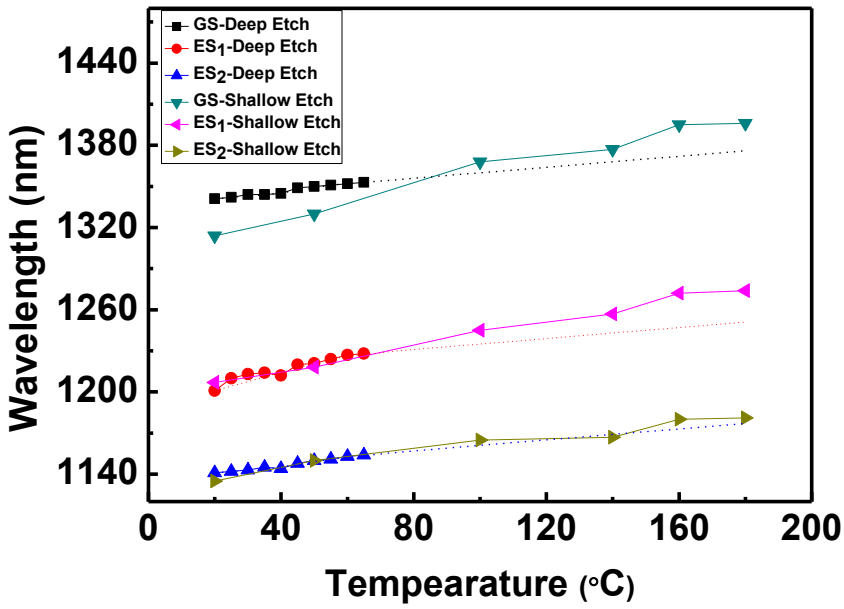

Figure 3.21: Peak wavelength as a function temperature for the QD's GS, ES_1, and ES_2 of deep and shallow etch devices.

The peak wavelength was traced with increasing temperature at constant current density. Figure 3.21 (a) shows a plot of spectral peak wavelength shift as a function of temperature for the deeply etched device. The wavelength shifts as a function of temperature, $\Delta\lambda/\Delta T$, is measured to be 0.2 nm/°C for GS, ES_1, and ES_2. The wavelength shifts as a function of current density, $\Delta\lambda/\Delta J$, are 2.3 and 0.6 nm/kAcm^{-2} for the GS and ES, respectively, which is shown in Figure 3.20. The difference in these values is attributed to the different effects of free-carriers on the band-gap renormalisation of the GS and ES of the QDs. Applying this data, the junction temperature as a function of current density, $\Delta T_{jct}/\Delta J$, are 3 and 11.5 °C/kAcm^{-2} is determined for the GS and ES respectively. Figure 3.21(b) shows a plot of

spectral peak shift as a function of temperature for the shallow etched device. The peak wavelength shift, $\Delta\lambda/\Delta T$, is measured to be 0.5 nm/°C. The wavelength shifts as a function of current density, $\Delta\lambda/\Delta J$, is 0.8 nm/kAcm^{-2}. The junction temperature, $\Delta T_{jct}/\Delta J$, for shallow-ridge device is 1.6 °C/kAcm^{-2}.

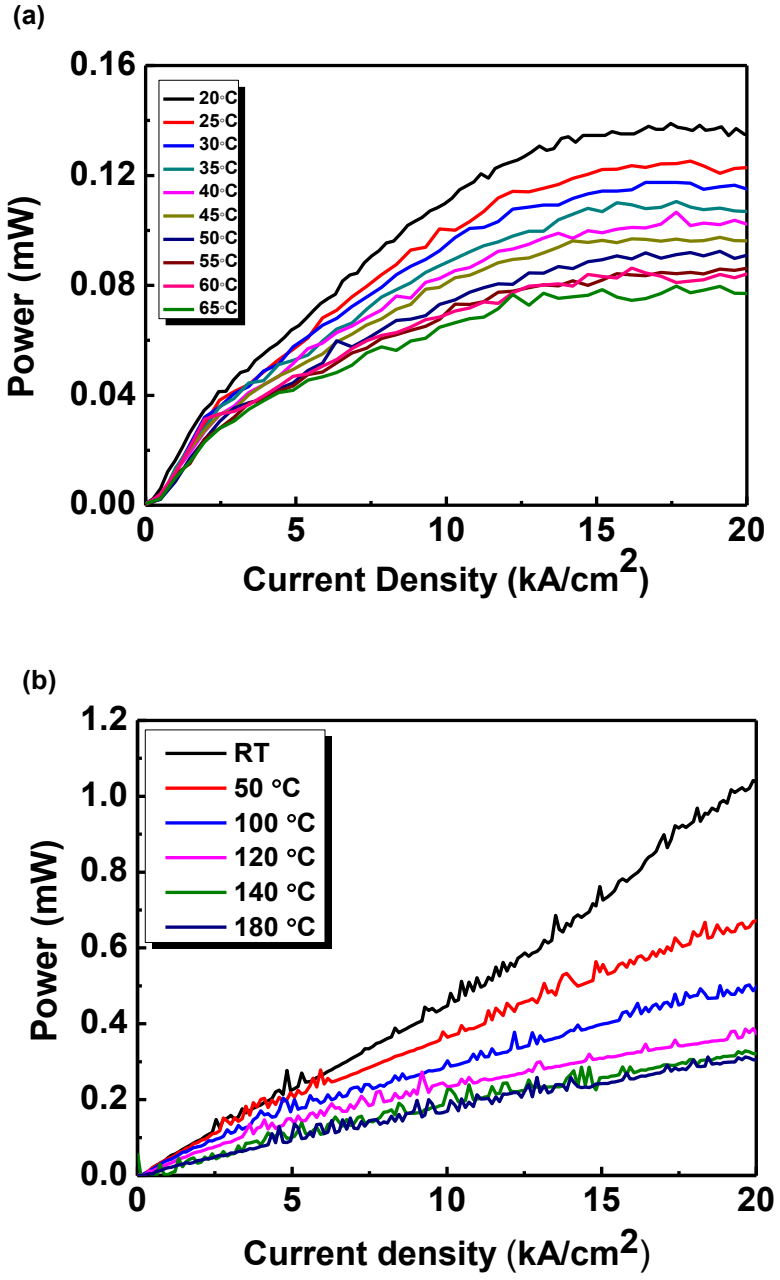

Figure 3.22: Output power as a function of current density at various temperatures of (a) deeply etched ridge (b) shallow etch ridge.

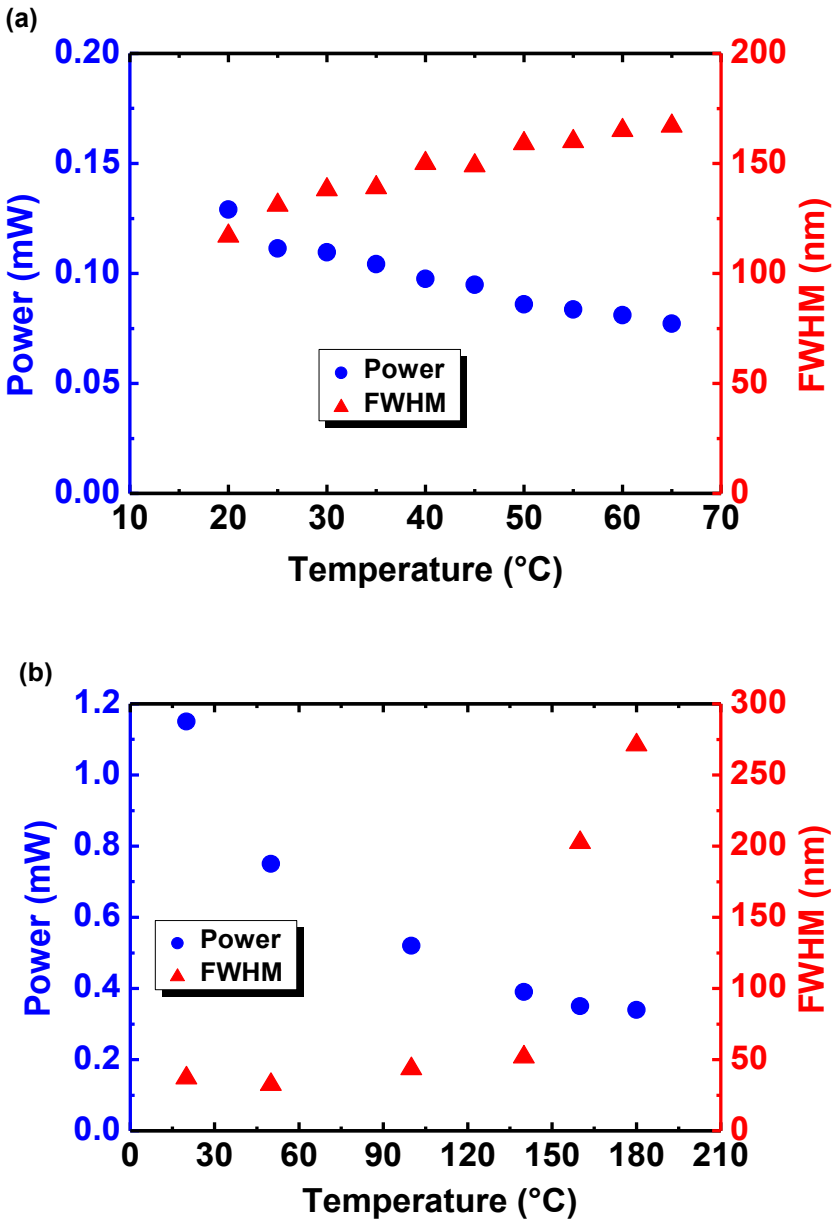

Figure 3.23: Output power and spectral coverage as a function of temperature of (a) deeply etched ridge (b) shallow etch ridge.

The LI characteristics and the temperature dependence of deeply etched devices were shown in Figure 3.22(a). The data shows several noise spikes that can be disregarded as measurement noise on visual inspection. The output power at 20 ℃ is 0.12 mW at 10 kA/cm^2 and rolled over and reduced in power by increasing current density due to self-heating.

The temperature dependence of the optical output power as a function of current density for the shallow etched device is shown in Figure 3.22 (b). The measured power from the device is 1.2 mW at 20 ℃. The output power falls with increasing temperature and a power of 0.3 mW is achieved at highest operation temperature, 180 ℃. Thermal rollover in the shallow-

ridge device is not as obvious as the deep-ridge device, attributed to the better heat extraction in the shallow ridge.

The light output power and FWHM relation as a function of temperature for the deeply etched ridge device is plotted in Figure 3.23 (a). A significant increase in FWHM is observed with increasing temperature in the deeply etched device. However, the output power is relatively low. Figure 3.23 (b) plots the FWHM and power as a function of temperature for shallow etched device. The FWHM is ~ 50 nm with the main contribution of the ES_1 of the QD at the operation temperature of up to 150 °C. Further increase in temperature results insignificant emission from the ES_2 and the FWHM of ~ 250 nm is achieved due to the combined contribution from both ES_1 and ES_2 of the QD. The power is decreased from 2.5 mW to 0.3 mW with increasing temperature.

3.5.6 High Temperature Gain Analysis

The segmented gain is given by the ratio of *2L* and *L* and therefore this technique may not be suitable for high temperature measurement due to the red shift of the spectrum with local heat. In addition to the reasonably high power for such a short device, further evidence for the device operating with gain (i.e., as an SLD) was required.

Therefore, the Hakki Paoli gain measurement technique was used to determine the gain properties of the QD heterostructure at high temperature. It can be seen from Figure 3.22 that the output power from the deeply etched ridge is relatively small, therefore the shallow ridge device is used to measure the gain. Here, a 375-μm-length (*L*) Fabry-Perot (FP) cavity was used to measure the net modal gain of the sample (Courtesy Dr. Iain Butler).

Figure 3.24 plots the net modal gain spectra of QD GS energy level as a function of operating temperature. At 27 ºC, the gain spectrum is dominated by the GS states at ~1298 nm. The GS gain spectrum shifts to the longer wavelength (red shifts) with increasing temperature. A positive gain from the GS at ~1361 nm is achieved even under 147 °C operation. Additionally, a temperature-dependent broadening in the GS gain spectra is observed. There is no positive gain from ES_1 observed, due to the low current density of these laser diodes engineered for GS emission. The broadening of modal gain can be attributed to the homogeneous broadening of dots due to increasing temperature or increasing current density.

Figure 3.25 shows the dependence of the peak net modal gain for different temperature operation. At the lowest operating temperature (27 ºC), the peak modal is observed at low current density, followed by a dramatic increase with increasing current density. It is noted

that there is an increase in current density to achieve the positive gain with further increase in temperature. This may be due to the carrier thermalization and escape to carrier to higher states, therefore, more carriers are needed to achieve positive gain. However, it is worth noting that moderately high peak modal gain of 5cm^{-1} persists at 177 ºC temperature operation. This implies that the GS energy level carrier transition overcome the loss despite the thermalization of carriers to higher energy level.

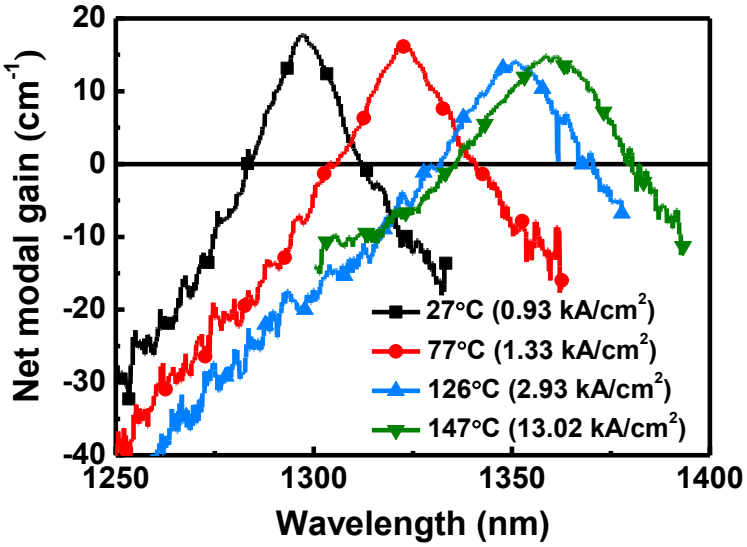

Figure 3.24: Net modal gain spectra under various operating temperature.

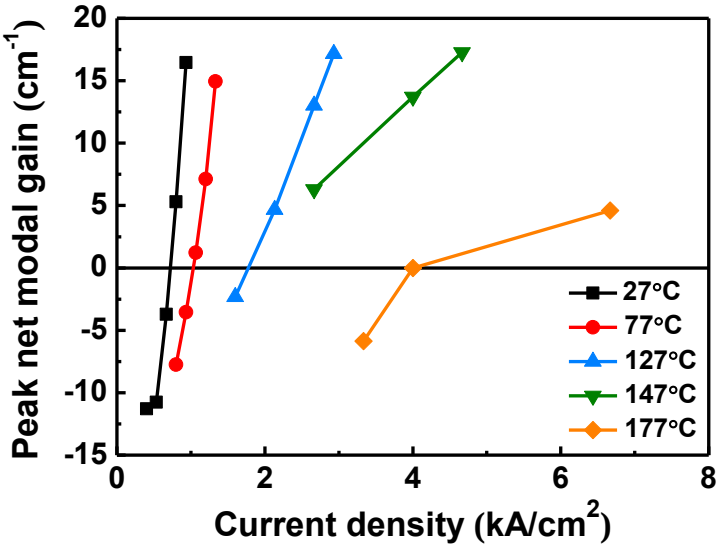

Figure 3.25: Peak net modal gain against current density as a function of operating temperature.

3.6 Conclusions

This chapter performed an analysis on the effect of ridge etch depth on QD SLD performance. The main application area for the SLD is OCT where the bandwidth and output powers are critical to achieve high axial resolution and deep penetration depth. A literature review of QD SLDs was discussed, and it was noted that studies concentrated on materials and device structure of the SLD to achieve broad bandwidth and high output power. It was clear that a study of fabrication parameters such as etch depth was required. A study to verify the losses, modal gain, output power, spectral bandwidth, and current confinement in the ridge with extreme cases of etch depth was carried out. It was found that the output power from shallow etched devices is higher than that of deeply etched devices mainly due to the high optical losses in deep-ridge devices. The internal loss of the deep-ridge device (10 cm^{-1}) is two times higher than that of the shallow etch (5 cm^{-1}). The saturated net modal gain of GS and ES in the shallow-ridge device is therefore 5 cm^{-1} higher than that of the deep-ridge device due to low scattering loss. The current density for GS saturation is two times higher in the shallow-ridge device due to poor current confinement. Good current confinement (uniform across the ridge, and no leakage) is desirable in SLD applications, however, etching through the intrinsic region to achieve this results in high loss and significant self-heating effects in the ridge. Therefore, shallow-ridge devices are more desirable in SLD applications.

The emission power and bandwidth are interlinked with respect to length. The lowest state of the dots is firstly filled by the carriers and then higher states are filled. Usually, the broadest bandwidth is achieved when two states of the QD are balanced (GS and ES_1, or ES_1 and ES_2). However, self-heating effects result in a decrease in occupation of the states at high current density. The shortest devices achieve the broadest bandwidth due to the combined contribution from all three states of the dots (GS+ES_1+ES_2), however, the output power is low since there is no significant amplification for this length. Similar behaviours occur in both deep and shallow etch devices. The shallow-ridge SLD exhibiting output power of ~1 mW and spectral coverage of ~150 nm is achieved for the length of 1750 µm.

The influence of thermal effects on SLDs was also studied for both etch depths. When the temperature increases, the homogeneous broadening of the QD also increases due to the increased phonon scattering and thermalization of carriers into higher states of the QD. In a deep-ridge device, an increase in FWHM of SLD emission from 118 nm to 167 nm occurs due to the homogenous broadening of the dots. However, the output power is low in these deep-ridge devices because of the large scattering loss and self-heating effects in the ridge.

In shallow etched device, moderate output power (~ 0.35 mW) is achieved even at high operating temperatures. The benefit of the carrier thermalization into the higher states of the dots (ES_2) make the bandwidth increases from 50 nm to 250 nm because of the combined contribution of ES_1 and ES_2 with increasing temperature. A peak net modal gain of $5cm^{-1}$ is achieved at 177 ºC temperature operation.

The shallow etched devices provide the best performance in terms of achieving moderate power levels and broad bandwidth. Results suggest that if scattering losses can be reduced in the deeply etched structure, then this would provide the best operating characteristics. However, the use of high junction temperatures in the shallow etched devices was shown to provide very broad spectral bandwidths using standard QD laser epitaxial structures.

3.7 Future Work

The scattering losses in the ridge waveguide may be reduced by optimizing the sidewall roughness in the deeply etched structure, this would provide better operating characteristics, and may allow the power gap between the shallow and deep etched devices to be bridged. Moreover, the bandwidth may further be improved by short circuiting the absorber section. To improve the output power, the longer chip design with multi-sections can be developed since the output power is related to length and longer chip should give rise in output power, and non-uniform current densities may be introduced. A longer-term study that is required is the long-term reliability of devices operated under extreme heat to obtain high spectral bandwidth.

Bibliography

[1] P. Blood, G. M. Lewis, P. M. Smowton, H. Summers, J. Thomson, and J. Lutti., “Characterization of Semiconductor Laser Gain Media by the Segmented Contact Method,” IEEE Journal on Selected Topics in Quantum Electronics, vol. 9, no. 5, p. 1275–1282, 2003, 2003.

[2] M. Rossetti, J. Napierala, N. Matusuchek, U. Achatz, M. Duelk, C. Velez, A. Castiglia, N. Grandjean, J. Dorsaz, and E. Feltin., "Superluminescent light emitting diodes: the best out of two worlds." In Moems and Miniaturized Systems Xi SPIE, vol. 8252, p. 54-66. 2012.

[3] I. K. Han, H. C. Bae, W. J. Cho, J. I. Lee, H. L. Park, T. G. Kim, J. I. Lee., “Study of chirped quantum dot superluminescent diodes,” Japanese journal of applied physics, vol. 44, no. 7 S, p. 5692-5695, 2005.

[4] Y. C. Yoo, L. K. Han, and J. L. Lee, “High power broadband superluminescent diodes with chirped multiple quantum dots,” Electron Letter, vol. 43, no. 19, p. 1, 2007.

[5] P. Bardella, M. Rossetti, and I. Montrosset, “Modeling of broadband chirped quantum-dot super-luminescent diodes,” IEEE Journal on Selected Topics in Quantum Electronics, vol. 15, no. 3, p. 785–791, 2009.

[6] L. H. Li, M. Rossetti, and A. Fiore., “Chirped multiple InAs quantum dot structure for wide spectrum device applications,” Journal of crystal growth, vol. 278, no. 1-4, p. 680-684, 2005.

[7] Z. Y. Zhang, Q. Jiang, M. Hopkinson, and R. A. Hogg., “Effects of intermixing on modulation p-doped quantum dot superluminescent light emitting diodes,” Optics express, vol. 18, no. 7, p. 7055–7063, 2010.

[8] S. K. Ray, K. M. Groom, M. D. Beattie, H. Y. Liu, M. Hopkinson, and R. A. Hogg., “Broad-Band Superluminescent Light-Emitting Diodes Incorporating Quantum Dots in Compositionally Modulated Quantum Wells,” IEEE photonics technology letters, vol. 18, no. 1, p. 58-60, 2006.

[9] C. K. Chia, S. J. Chua, J. R. Dong, and S. L. Teo., “Ultrawide band quantum dot light emitting device by postfabrication laser annealing,” Applied Physics Letters, vol. 90, no. 6, p. 061101, 2007.

[10] S. Haffouz, P. J. Barrios, R. Normandin, D. Poitras, and Z. Lu., "Ultrawide-bandwidth, superluminescent light-emitting diodes using InAs quantum dots of tuned height," Optics letters, vol. 37, no. 6, p. 1103-1105, 2012.

[11] A. F. Fercher, W. Drexler, C. K. Hitzenberger, and T. Lasser., "Optical coherence tomography - principles and applications," Reports on Progress in Physics, vol. 66, no. 2, p. 239–303, 2003.

[12] V. R. Shidlovski and J. Wei., "Superluminescent diodes for optical coherence tomography," In Test and Measurement Applications of Optoelectronic Devices SPIE, vol. 4648, p. 139–147, 2002.

[13] D. Huang, E. A. Swanson, C. P. Lin, J. S. Schuman, W. G. Stinson, W. Chang, M. R. Hee, T. Flotte, K. Gregory, C. A. Puliafito, and J. G. Fujimoto., "Optical coherence tomography.," Science, vol. 254, no. 5035, p. 1178–81, 1991.

[14] D. Childs, S. Matcher, and R. Hogg, "Lasers and SLEDs for optical coherence tomography," In International Conference on Transparent Optical Networks IEEE, p. 1-4, 2015.

[15] G. A. Alphonse, D. B. Gilbert, M. G. Harvey, and M. Ettenberg., "High-Power Superluminescent Diodes," IEEE Journal of Quantum Electronics, vol. 24, no. 12, p. 2454-2457, 1988.

[16] C. F. Lin and B. L. Lee., "Extremely Broadband AlGaAs/GaAs Superluminescent diodes," Applied Physics Letters, vol. 71, p. 1598-1600, 1997.

[17] T. K. Ong, M. Yin, Z. Yu, Y. C. Chan and Y. L. Lam., "High-performance quantum well intermixed superluminescent diodes," Measurement Science and Technology, vol. 15, no. 8, p. 1591, 2004.

[18] J. D. Thomson, H. D. Summers, P. J. Hulyer, P. M. Smowton, and P. Blood, "Determination of single-pass optical gain and internal loss using a multisection device," Applied Physics Letters, vol. 75, no. 17, p. 2527, 1999.

[19] Z. Sun, D. Ding, Q. Gong, W. Zhou, B. Xu, and Z. G. Wang., "Quantum-dot superluminescent diode: A proposal for an ultra-wide output spectrum," Optical and quantum Electronics, vol. 31, no. 12, p. 1235-1246, 1999.

[20] Z. Y. Zhang, R. A. Hogg, X. Q. Lv, and Z. G. Wang., "Self-assembled quantum-dot superluminescent light-emitting diodes," Advances in Optics and Photonics, vol. 2, no. 2, p. 201-228, 2010.

[21] L. H. Li, M. Rossetti, A. Fiore, L. Occhi, and C. Velez., “Wide emission spectrum from superluminescent diodes with chirped quantum dot multilayers,” Electron Letter, vol. 41, no. 1, p. 41-43, 2005.

[22] Z. Y. Zhang, R. A. Hogg, B. Xu, P. Jin, and Z. G. Wang., “Realization of extremely broadband quantum-dot superluminescent light-emitting diodes by rapid thermal-annealing process,” Optics letters, vol. 33, no. 11, p. 1210-1212, 2008.

[23] S. K. Ray, K. M. Groom, R. Alexander, K. Kennedy, H. Y. Liu, M. Hopkinson, and R. A. Hogg., “Design, growth, fabrication, and characterization of quantum dot broadband superluminescent light emitting diode,” Journal of Applied Physics, vol. 100, no.10, p. 103105, 2006.

[24] Y.-C. Xin, A. Martinez, T. Saiz, A. J. Moscho, Y. Li, T. A. Nilsen, A. L. Gray, and L. F. Lester., “1.3 μm Quantum Dot Multisection Superluminescent Diode with Extremely Broad Bandwidth,” IEEE Photonics Technology Letters, vol. 19, no. 7, p. 501-503, 2007.

[25] Z. Y. Zhang, R. A. Hogg, P. Jin, T. L. Choi, B. Xu, and Z. G. Wang, “High-Power quantum-dot superluminescent LED with broadband drive current insensitive emission spectra using a tapered active region,” IEEE Photonics Technology Letters, vol. 20, no. 10, p. 782–784, 2008.

[26] Z. Y. Zhang, Q. Jiang, I. J. Luxmoore, and R. A. Hogg, “A p-type-doped quantum dot superluminescent LED with broadband and flat-topped emission spectra obtained by post-growth intermixing under a GaAs proximity cap,” Nanotechnology, vol. 20, no. 5, p. 055204, 2009.

[27] S. Haffouz, P. J. Barrios, R. Normandin, D. Poitras, and Z. Lu., “Ultrawide-bandwidth, superluminescent light-emitting diodes using InAs quantum dots of tuned height,” Optics letters, vol. 37, no. 6, p. 1103-1105, 2012.

[28] A. Kafar, S. Stanczyk, G. Targowski, T. Oto, I. Makarowa, P. Wisniewski, T. Suski and P. Perlin., “High-optical-power InGaN superluminescent diodes with ‘j-shape’ waveguide,” Applied Physics Express, vol. 6, no. 9, p. 092102, 2013.

[29] G. A. Alphonse, “Angled Stripe Superluminescent Diodes”, In Conference Proceedings IEEE Lasers and Electro-Optics Society, 1990

[30] P. D. L. Judson, K. M. Groom, D. T. D. Childs, M. Hopkinson, and R. A. Hogg, “Multi-section quantum dot superluminescent diodes for spectral shape engineering,” IET Optoelectronics, vol. 3, no. 2, p. 100–104, 2009.

[31] A. Kafar, S. Stanczyk, D Schiavon, T. Suski, and P. Perlin., "Review on optimization and current status of (Al, In) GaN superluminescent diodes." ECS Journal of Solid State Science and Technology 9, no. 1, p. 015010, 2019.

[32] F. Toor, D. L. Sivco, H. E. Liu, and C. F. Gmachl, "Effect of waveguide sidewall roughness on the threshold current density and slope efficiency of quantum cascade lasers," Applied Physics Letters, vol. 93, no. 3, p. 031104, 2008.

[33] L. Redaelli, M. Martens, J. Piprek, H. Wenzel, C. Netzel, A. Linke, Yu. V. Flores, S. Einfeldt, M. Kneissl, and G. Tränkle., "Effect of ridge waveguide etch depth on laser threshold of InGaN MQW laser diodes," In Gallium Nitride Materials and Devices VII SPIE, vol. 8262, p. 186-193, 2012.

[34] S. K. Ray, K. M. Groom, R. A. Hogg, H. Y. Liu, M. Hopkinson, T. Badcock, D. J. Mowbray, and M. S. Skolnick., "Improved temperature performance of 1.31-μm quantum dot lasers by optimized ridge waveguide design," IEEE Photonics Technology Letters, vol. 17, no. 9, p. 1785–1787, 2005.

[35] F. Toor, D. L. Sivco, and C. F. Gmachl, "Effect of waveguide side-wall roughness on the performance of quantum cascade lasers," in Novel In-Plane Semiconductor Lasers VIII SPIE, vol. 7230, p. 363-373, 2009.

[36] T. Feng, T. Hosoda, L. Shterengas, A. Stein, G. Kipshidze, and G. Belenky, "Two-Step Narrow Ridge Cascade Diode Lasers Emitting Near 2 μm," IEEE Photonics Technology Letters, vol. 29, no. 6, p. 485–488, 2017.

[37] I. M. E. Butler, W. Li, S. A. Sobhani, N. Babazadeh, I. M. Ross, K. Nishi, K. Takemasa, M. Sugawara, D. T. D. Childs, and R. A. Hogg., "Size anisotropy inhomogeneity effects in state-of-the-art quantum dot lasers," Applied Physics Letters, vol. 113, no. 1, p. 012105, 2018.

[38] K. Imanaka, "Cavity Length Dependence of Optical Characteristics in High Power Narrow Stripe GaAs Superluminescent diodes," IEEE Photonics Technology Letters, vol. 2, no. 10, p. 705–707, 1990.

[39] Z. Y. Zhang, I. J. Luxmoore, C. Y. Liu, Q. Jiang, K. M. Groom, D. T. D. Childs, M. Hopkinson, A. G. Cullis. And R. A. Hogg., "Effect of facet angle on effective facet reflectivity and operating characteristics of quantum dot edge emitting lasers and superluminescent light-emitting diodes," Applied Physics Letters, vol. 91, no. 8, p. 081112, 2007.

[40] M. Rossetti, A. Markus, A. Fiore, L. Occhi, and C. Velez., “Quantum dot superluminescent diodes emitting at 1.3 μm,” IEEE Photonics Technology Letters, vol. 17, no. 3, p. 540–542, 2005.

[41] M. Sugawara, K. Mukai, Y. Nakata, H. Ishikawa, and A. Sakamoto, “Effect of homogeneous broadening of optical gain on lasing spectra in self-assembled InxGa1-xAs/GaAs quantum dot lasers,” Physical Review B, vol. 61, no. 11, p. 7595–7603, 2000.

[42] A. v. Uskov, I. Magnusdottir, B. Tromborg, J. Mørk, and R. Lang., “Line broadening caused by Coulomb carrier-carrier correlations and dynamics of carrier capture and emission in quantum dots,” Applied Physics Letters, vol. 79, no. 11, p. 1679–1681, 2001.

[43] K. Nishi, T. Kageyama, M. Yamaguchi, Y. Maeda, K. Takemasa, T. Yamamoto, M. Sugawara, and Y. Arakawa., “Molecular beam epitaxial growths of high-optical-gain InAs quantum dots on GaAs for long-wavelength emission,” Journal of Crystal Growth, vol. 378, p. 459–462, 2013.

[44] I. M. E. Butler, “Structural and Opto-Electronic Properties of GaAs and InP Based Quantum Dot Lasers,” *PhD Thesis*, Queen's University Belfast, 2020.

Chapter 4: Hybrid Quantum Well /Quantum Dot Superluminescent Diodes

4.1 Introduction

In this chapter, new designs of hybrid quantum well/ quantum dot (QW/QD) structures utilising an increased number of layers of QD with high dot density are reported in order to enhance the modal gain while maintaining the broad gain spectrum, with a view to future engineering to realise a broad spectral bandwidth. The designs of hybrid QW/QD active regions are shown in table 4-1. The structures are grown by collaborators QD lasers Inc., (Japan). The state separation of these structures is larger than in previously reported in the literature [1] and the QW emission wavelength has been shifted from 1130 nm to 1080 nm to align with ES_2 transition. Furthermore, these structures exhibit a high dot density of ~ $6x10^{10}$ cm^{-1} which is a two-fold increase in dot density as compared to previous studies [2]. As a result of these advancements, it is expected that these structures will exhibit an increase in saturated gain with broad gain spectrum. Specifically, the "chirped" structure (AJ) aims to achieve a broad bandwidth of SLD emission by introducing "chirped" QD layers, and a digital alloy, triangular QW.

Table 4-1: Active regions of the three different SLD devices.

	Active Regions
Device AG	5 layers of QDs with emission wavelength at 1280 nm and a single QW at 1080 nm
Device AE	9 layers of QDs with emission wavelength at 1280 nm and a single QW at 1080 nm
Device AJ	9 layers of chirped QDs with emission wavelength at 1280 nm and 1230 nm alternatively and a digital alloy QW at 1080 nm

In order to access the gain characteristics of the QW/QD active element, multi-section device is utilised [3]. The electrical characteristics are initially characterised in order to establish

electronic equivalence (and assumed opto-electronic equivalence) of the individual device sections. The electronic structure of the active element is then investigated through the use photocurrent spectroscopy (performed at zero bias), and an analysis of the current density dependence of the electroluminescence and gain spectrum. A noteworthy contribution of this work is the utilisation of high dot density to achieve high modal gain of SLDs with broader gain spectrum. Due to the high-density QD, the use of lower number of dot layer (QW/5 layers of QDs) results in higher modal gain value of 25 cm^{-1} modal gain value and a broader gain spectrum spanning ~350 nm compared to previous studies where a higher number of dot layer (QW/6 layers of QDs) resulted in lower modal gain value of 12 cm^{-1} with modal gain spanning of 300 nm) [1]. The comparison of the number of dot layers (5 and 9 layers of QDs) of hybrid QW/QD is then conducted to evaluate their effect on the modal gain value. An increase in modal gain value is observed with increased number of dot layer. However, a corresponding increase in the number of carriers is necessary to saturate the states of the dots to get emission from QW. At last, the comparison of "unchirped" (AE) and "chirped" (AJ) in terms of modal gain and spectral bandwidth is presented. The "chirped" of the QD in AJ leads to improved gain "flatness" and enhancement of full-width half maximum (FWHM) of SLD emission. Based on these findings, a new design for broad FWHM QW/QD active elements is presented.

4.2 Background

QD heterostructures are a promising option in order to improve the performance of optical devices due to their reduced DOS. Optical devices that utilise QD structures have displayed high thermal stability [4], low threshold [5], wide spectral bandwidths [6],[7]. However, the reduced DOS of QD that facilitate a low transparency current is accompanied by a much smaller modal gain than QW devices. Furthermore, due to the low dot density, and the need for comparatively large barrier widths (due to strain coupling between layers), there is also a small overlap of QD layers with the optical field, further reducing modal gain. For laser diodes, this readily saturable modal gain is an issue as gain is needed to overcome the total losses and produce lasing. In general, the modal gain obtained from a single layer of dots is insufficient to overcome the total losses. To enhance the modal gain of the laser devices, different approaches can be applied such as increasing the number of QD layers [8]-[10], increasing dot density [11], increasing optical confinement [12] or improving the material gain via epitaxy [13]. The studies have reported the influence of highly stacked QD layers and/or high-density QD layers on the laser characteristics through experiments and numerical calculations. The improvement in characteristic temperature (T_0) and modulation speed is observed by increasing the saturated gain for high-speed QD lasers [11],[14].

The QD SLDs have also attracted significant attention [15]-[17] as they can provide naturally broad bandwidth due to the large inhomogeneity of QD. Although their broad bandwidth is disadvantageous for laser diodes, they meet the needs of many applications requiring bright sources with broadband emission and high beam directionality. Broad bandwidth SLDs have been widely used in a range of applications such as optical gyro sensors [18], wavelength division multiplexing [19], and biomedical imaging [20]. Recent interest has focused on applications in OCT where cheap, compact, high-power broadband light sources are required to realise low-cost point-of-care screening and diagnosis [21], [22].

SLDs based on InAs QD active regions were first proposed by Wang *et al.* [23] and has been intensively studied to improve the spectral bandwidth [24]-[28] and the output power [29]-[32] in order to improve the resolution and penetration depth of OCT systems. The continuous advancement in broadening the spectral bandwidth of QD-based SLDs has been made by modifying the active region structures in different ways such as using multiple-layer stacked structures [33], chirping the QD layers [34]-[36], post-growth annealing [27], and dot-in-well (DWELL) structures [37].

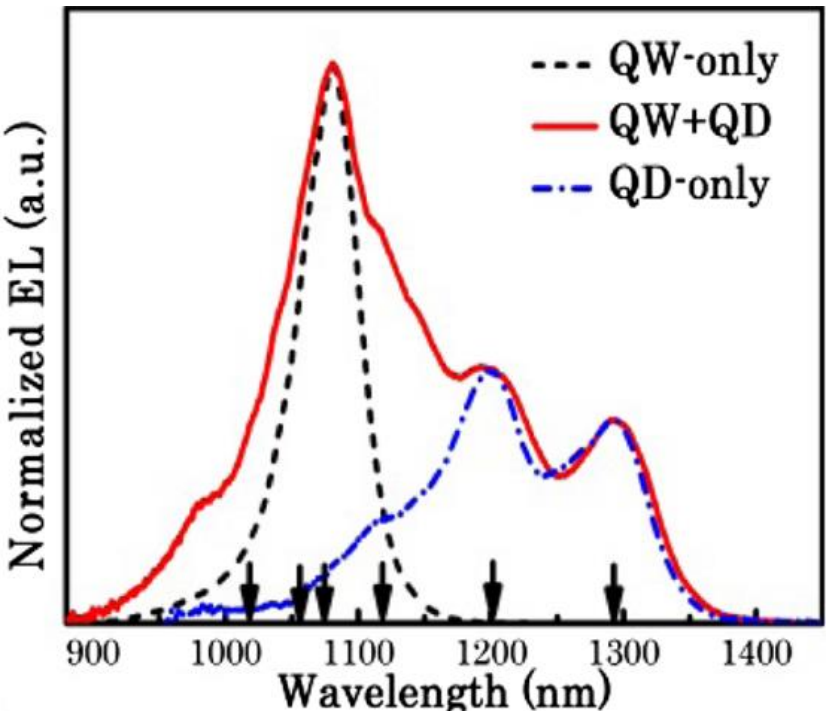

Figure 4.1: Normalized EL spectra showing for QW only,QD only and hybrid QW/QD [1].

The maximum spectral bandwidth is achieved when the gain due to the first excited states (ES) and the ground states (GS) are balanced and there is usually spectral modulation due to the state separation and ensemble line-width of the dots. The spectral modulation in QD structures is usually large unless there is a special modification in the growth parameters.

The spectral dip due to the state separation of the dots is undesirable for OCT due to the possibility of a reduction in resolution (ghost images). This modulation can be reduced by introducing chirped QD layers i.e., varying the emission wavelength of individual QD layers in a multilayer stack [38]. Early publications on QD-based SLDs show a spectral bandwidth of not more than ~150 nm [39]-[41] due to the increasing degeneracy of the QD transitions with increasing energy. By introducing a single quantum well to emit at a wavelength coincident with the second excited state of the QD (schematically shown in Figure 4.1), the spectral bandwidth is further broadened to greater than 200 nm since the QW offsets losses associated with the second excited state [42],[43].

In addition to the spectral bandwidth, the output power is also an important parameter for OCT systems in order to obtain deep penetration in skin tissue. The primary factors for obtaining high output power from QD SLDs is to increase the modal gain and chip length while ensuring that lasing is prevented. The exponential increase in output power is expected when increasing the gain and/or length. The effect of chip length on the output power is widely discussed in chapter 3. Improvements in the output power is studied by other groups by modifying the device structure such as adding the amplifier sections [44], tapered pumped area [45], very wide ridge width, J-shaped waveguide [46], by using active multimode interferometer [47] and etched V grooves [48]. However, modifying the device structure comes with complications in fabrication, and impractical beam-shape due to a large ridge width. Therefore, increasing the modal gain to improve the output power has become an important factor. It has been demonstrated that the enhancement of the QD gain can be achieved by increasing the number of stacked QD layers or higher dot density in QD lasers. However, further studies of the gain characteristics of SLDs while maintaining the broad spectral bandwidth and broad gain spectrum span is required.

4.3 Gaps in Knowledge

SLDs utilising a hybrid QW/QD structure is able to achieve the broadest emission bandwidth so far, as compared to QD-only or QW-only structures [49],[50]. Chen *et al.* show an enhanced spectral coverage by using hybrid QW/QD structures and an OCT resolution of ~ 2.9 μm was predicted [43]. An emission spectral bandwidth of 213 nm with modal gain spanning of 300 nm was achieved by using hybrid QW/QD structures [1], [42]. That hybrid QW/QD structure contained six layers of QD with the dot density of ~ $3x10^{10}$ cm^{-2} resulting in a low saturated gain of 12 cm^{-1} for the GS. For many OCT applications, high power is required for deep penetration depth, requiring QD actives with higher saturated gain. A study

of the gain properties of commercial, high-quality QD gain materials, with a view to application in broadband SLDs is required.

4.4 Methodology

The hybrid QW/QD structures were grown by an MBE system on a (100) Si-doped GaAs substrate by QD laser Inc, Japan. The epitaxy structures are essentially identical to the previous structure which is described in section 3.4 except for the active region design. The schematic of the active region of three hybrid QW/QD structures is shown in Figure 4.4. The thickness of the active layer is adjusted to maintain a constant average confinement factor per layer.

As shown in Figure 4.2 (a), the growth of the active region for device A starts with 79.5 nm of undoped GaAs and 7 nm of $In_{0.29}Ga_{0.71}As$ single QW, followed by 59.5 nm of undoped GaAs barrier. Above this, there were five layers of InAs QD layers. Each QD layer contains 0.8 nm of InAs, capped with a 3.7 nm InGaAs strain reducing layer (SRL) to relax the strain of the InAs QD due to the lattice mismatch between InAs and GaAs, allowing long wavelength emission [51]. The five layers of InAs QD were separated by a 58.5 nm of undoped GaAs barrier.

As seen in Figure 4.2 (b), the growth for structure AE begins with 56.5 nm of undoped GaAs followed by 7 nm of $In_{0.29}Ga_{0.71}As$ single QW and 36.5 nm of GaAs barrier layer. This was followed by the nine layers of InAs QD with emission wavelengths at 1280 nm. Each QD layer consists of 0.8 nm of InAs and is capped with a 3.7 nm InGaAs SRL. The undoped GaAs barrier layer with a thickness of 58.5 nm is inserted between the nine layers of InAs QD.

As illustrated in Figure 4.2 (c), the growth of the active region for AJ consists of 56.5 nm of undoped GaAs, 7 nm of $In_{0.29}Ga_{0.71}As$ asymmetric triangle digital alloy QW, and 36.5 nm of undoped GaAs layer. This asymmetric triangular QW was grown to achieve further broadening in the emission of the QW by providing higher-order QW transition [54]. Five layers of InAs QD with emission wavelengths at 1280 nm (Type A QD) and four layers of InAs QD with emission wavelength at 1230 nm (Type B QD) in the sequence of A/B/A/B/A/B/A were grown above the QW layer. Type A QD were grown by 0.8 nm of InAs and capped with a 3.7 nm InGaAs SRL whereas Type B QD were directly covered by GaAs capped layer. The chirped QD are designed to spectrally overlap the dots, providing smaller spectral modulation to the emission profile [13].

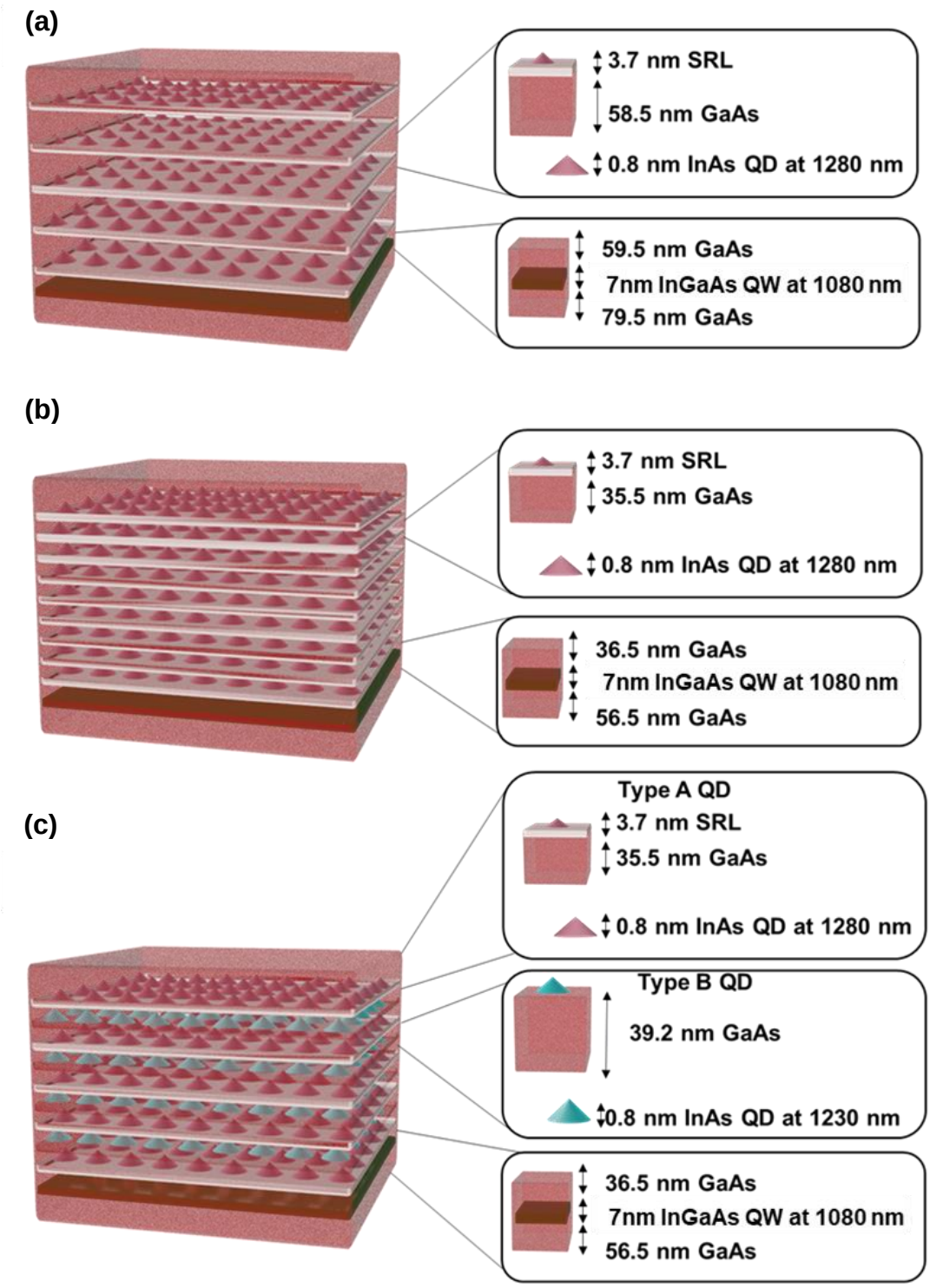

Figure 4.2: Schematic of active region for (a) AG, (b) AE, and (c) AJ.

To access the electronic properties of the active element, PC was obtained from optical access pin mesa diodes. The PC spectra are taken using spectrally filtered white light incident on the surface of the sample. An optical chopper is applied to modulate the incident light. The PC signal is obtained by using standard lock-in amplifier techniques. A source-measurement unit (SMU) is used to apply 0V DC bias to the sample in the growth direction. To characterise the gain, absorption, and spontaneous emission spectra to be measured, the

wafers were processed into a segmented contact SLD device. As discussed in detail in chapter 3, the etch depth of the ridge waveguide geometry plays an important role in optical and current confinement. The shallow etch is a better choice for the fabrication of an SLD since it provides minimal scattering loss, however, there is weak optical and current confinement. Therefore, the SLD ridge waveguide in this chapter is designed to etch through *p*-cladding layer, but not penetrate through the active core layer, termed as "mid-etch" ridge waveguide. The cross-sectional SEM image of the etch test structure is shown in Figure 4.3.

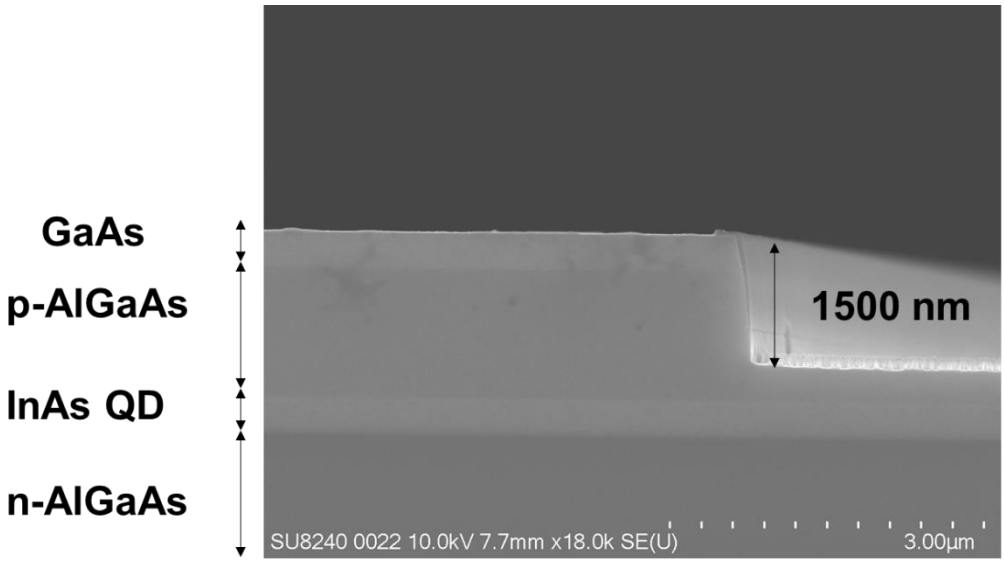

Figure 4.3: Cross-sectional SEM image of mid-etch ridge waveguide.

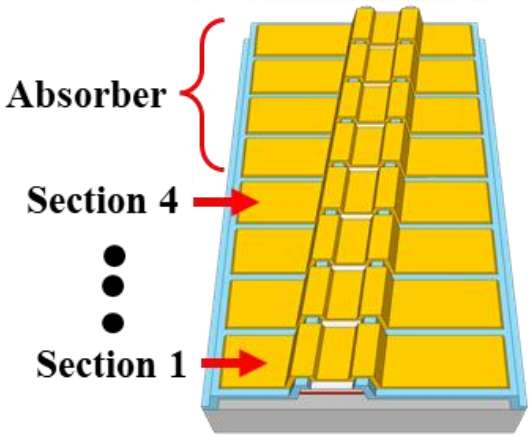

Figure 4.4: Schematic image of segmented contact SLD.

There are eight sections with an isolation gap between each section of 10 µm. Each section is 250 µm long and the ridge width is 7 µm. The waveguide is 7º tilted to inhibit optical feedback in the laser cavity. To further suppress lasing, the last four sections are used as (open-circuit) absorbers while obtaining the EL spectra [52]. The schematic image of the SLD is shown in Figure 4.4. Measurements were performed at room temperature under

quasi-CW (10 µs pulse width, 1% duty cycle) condition to reduce thermal effects. The devices are not wire bonded and probed directly during the characterization.

4.5 Results and Analysis

4.5.1 Photocurrent Spectra

In order to study the effect of the QW in the hybrid QW/QD structures, PC spectra from mesa diodes of QD only and hybrid QW/QD structures were measured (courtesy Dr. Soroush A. Sobhani).

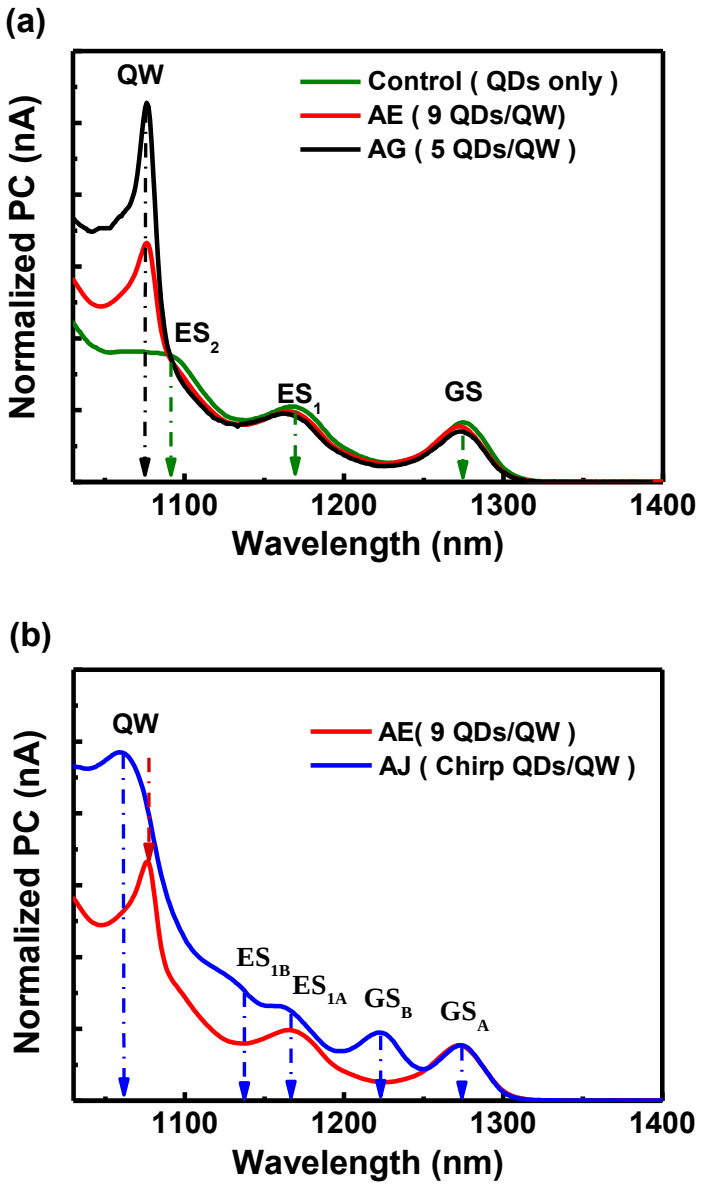

Figure 4.5: PC spectra at 0 V (short-circuit) for (a) AG, AE and control sample (b) AE and AJ – Courtesy of Dr. Soroush A. Sobhani.

Figure 4.5 compares photocurrent (PC) spectra for the control sample (QD only) and hybrid QW/QD samples (AG, AE and AJ) as a function of wavelength. The control (QD only)

sample is used only to verify the effect of single QW in hybrid QW/QD structures in the PC spectrum. In Figure 4.5 (a), a series of well-resolved features arising from the InAs QD interband transitions (GS, ES_1, ES_2, etc) are observed at ~1275 nm, ~1170 nm, and ~1095 nm respectively for the control (QD only) sample. A similar spectrum is observed for the hybrid QW/QD (AE and AG) sample and a very good agreement between the GS and ES_1 between control (QD only) and hybrid QW/QD sample. A small shoulder related to the ES_2 is partially resolved at ~1195 nm. However, a strong PC signal peak is observed at ~1080 nm which is attributed to the QW for hybrid QW/QD sample.

Figure 4.5 (b) shows the normalized short-circuit PC spectra for AE and AJ to study the effect of chirped QD on the electronic structure (and hence emission spectrum). The state separation between is GS and ES of the unchirped QD is large (~75 nm), and therefore the emission spectrum has a large spectral modulation. This is a drawback for the OCT system as it impacts the dynamic range of an OCT imaging system due to the presence of sidelobes in the interferogram. The effect of chirped QD is to reduce the spectral modulation by spectrally overlapping the QD. In PC spectra, in addition to peaks at ~1275 nm and ~1170 nm which are related to type A QD, two more features at ~1220 nm and ~1130 nm are also clearly observed which is attributed to Type B QD. The PC peak at 1050 nm is attributed to QW. Compared to AE, the QW peak for sample AJ is much broader, and is attributed to the asymmetric triangular profile.

4.5.2 Electrical Characteristics

For segmented contact gain measurement, it is essential to have a device with identical sections for the same turn-on voltage and differential resistance so that the ASE from each section may be assumed to be identical and net modal gain can then be reliably calculated. Figure 4.6 shows the current-voltage (I-V) measurements of the three hybrid QW/QD sample. For the AG device, the differential resistance is ~ 15 Ω with an essentially identical turn-on voltage of ~ 0.9V which indicates that all the segments are electrically identical. For the AE device, the resistance is ~ 13 Ω and the turn-on voltage is 0.9 V. For the AJ device, the resistance is ~ 12 Ω and the turn-on voltage is 0.9 V. The electrical characteristics of SLDs from three hybrid QW/QD structures are almost identical with only a few ohms differences in resistance value from device-to-device variation due to separate fabrication processes. This level of identicality for the I-V characteristics of the sections has been found to be sufficient to allow reliable gain measurements [35], [53].

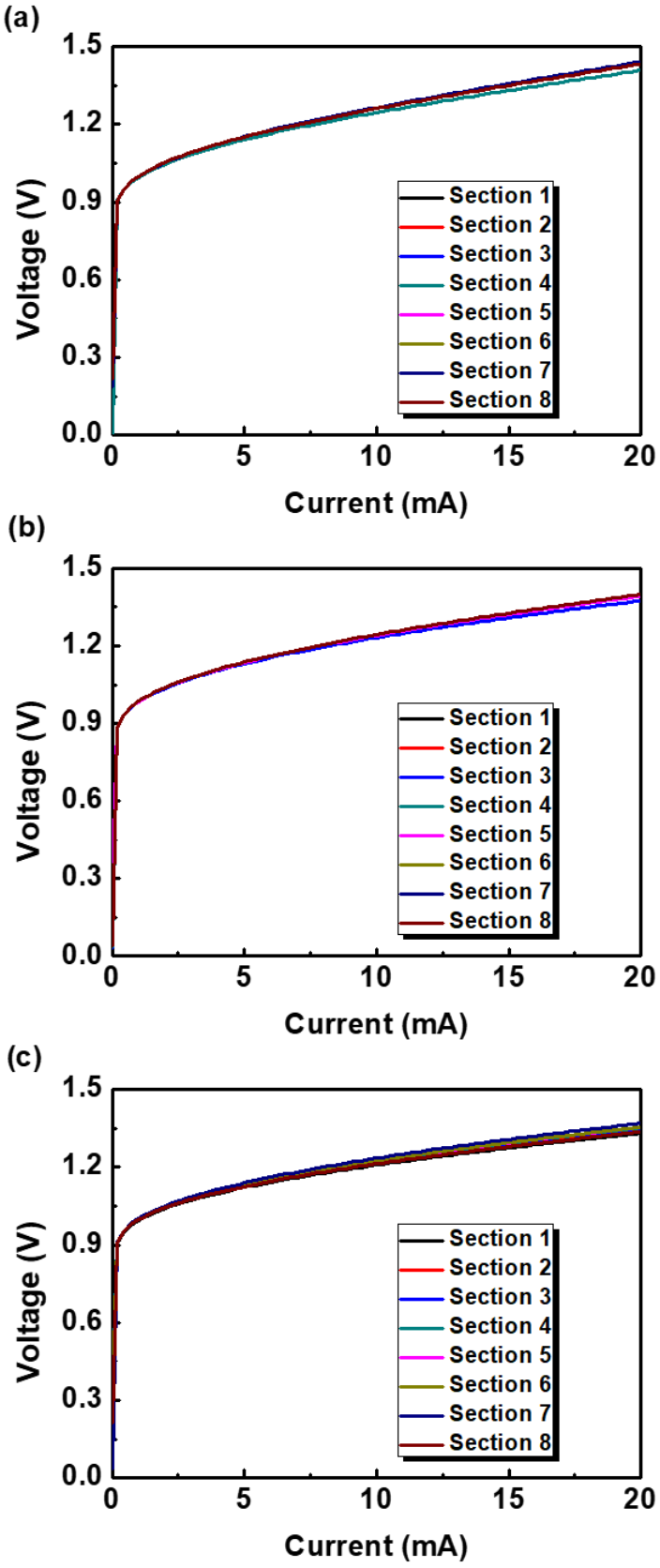

Figure 4.6: Current-voltage characteristics of eight sections of (a) AG (b) AE and (c) AJ.

4.5.3 Broadband Emissions

To observe the spectral emission bandwidth from these hybrid QW/QD devices, the electroluminescence (EL) emission spectra were measured. Figure 4.7 plots EL spectra of 5

layers of QDs and a single QW (AG) sample at different injection current. The GS and ES_1 of the QD saturation occur at lower current density due to the reduced number of dot layer and consequently the emission from the QW occurs. At low injection current density, the emission spectrum shows two features at ~1285 nm, ~1195 nm corresponding to the GS, and ES_1 of the QD. Around 10 nm red-shift in the EL spectrum is observed as compared to the PC and is attributed to the different bias conditions producing a stark-shift of the QD emission. With increasing current density, the GS of the QD becomes saturated and the ES_1 strongly dominates the emission spectrum. Due to the higher degree of degeneracy of ES_1, it is expected that ES_1 starts to saturate at higher current densities. Once the ES_1 emission starts to saturate, a third emission peak starts to appear at the emission wavelength of ~1100 nm. The EL intensity of the third peak is attributed to emission from QW, and it continues to increase in intensity whilst the other two peaks related to QD become saturated and drop in intensity with increasing current density. The intensity of the third emission peak becomes considerably stronger than the QD-related emission. The device is operated under quasi-CW conditions, and thermal issues cannot be completely ignored because of the high injection current density of 17 kA/cm^2 in the narrow ridge devices. A ~35 nm red shifting occurs in the GS with a reduction in the peak intensity with increasing current density and therefore it can be concluded that thermal effects (Joule heating of the junction) in these structures is strong. These thermal effects may be removed in future by mounting *p*-side down on a tile and using a thermoelectric cooler (TEC) for active cooling. In SLDs, the broadest bandwidth is achieved when the power from adjacent states is balanced, for example where the power from GS and ES_1 is balanced. The expected spectral coverage from this structure is therefore ~240 nm with simultaneous emission from GS, ES_1 from QD, and QW at half maximum. However, the reduction of GS emission intensity due to thermal effects results in a reduced spectral coverage of ~ 140 nm. This is due to the combination of emission from ES_1 of the QD and the QW.

Figure 4.8 shows the spectral coverage of SLD emission and FWHM of the individual states as a function of current density for device AG. The spectral coverage is ~140 nm at 3 kA/cm^2 with the combined contribution of GS and ES_1. Increasing current density led to a reduction in spectral coverage, however, the emission from QW compensates for the reduction of FWHM of the lowest state of QD (GS) and maintains the spectral coverage to its maximum (~140 nm). Further increasing the current density led to reduction in intensity of both GS and ES_1 and therefore the spectral coverage is only contribution from the QW.

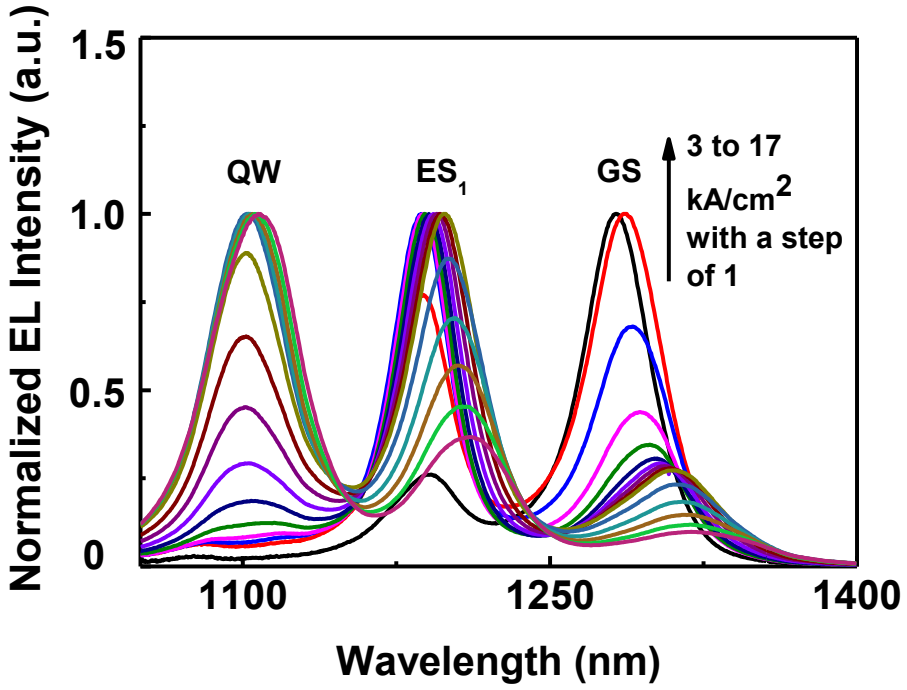

Figure 4.7: Normalized EL spectra for AG at various current density.

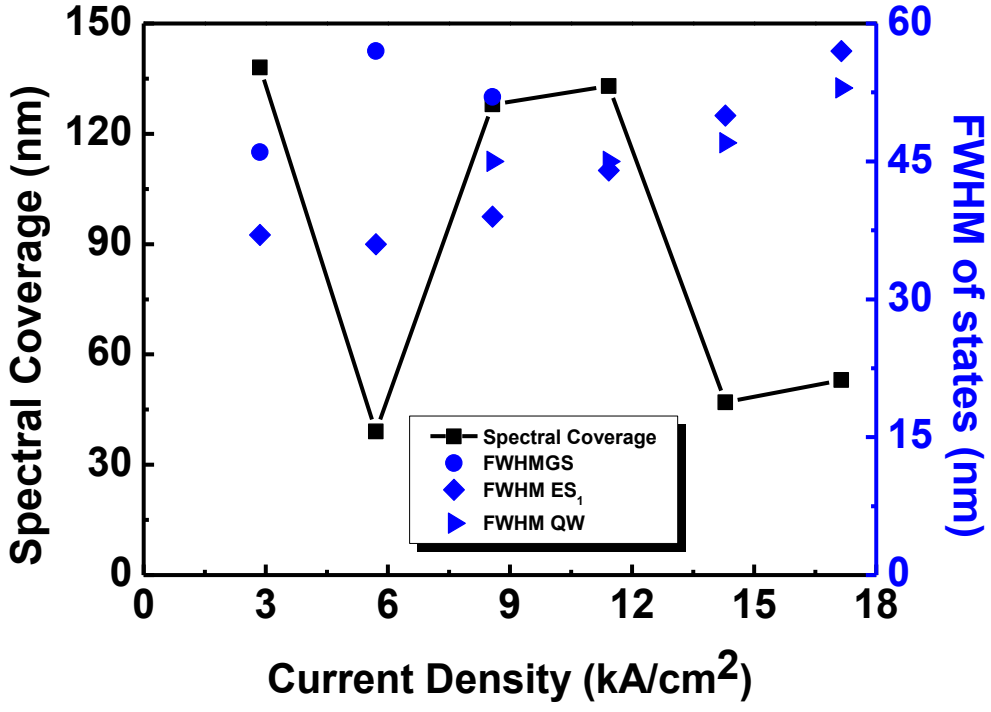

Figure 4.8: Spectral Coverage of SLD emission and FWHM of individual states of QD as a function of current density for AG.

The EL spectrum at various current densities for 9 layers of QDs and a single QW (AE) sample is presented in Figure 4.9. Initially, GS peak is observed at ~1285 nm and increases in intensity with increasing current density until it saturates. A ~20 nm red shifting occurs

in the GS once it is saturated along with a reduction in intensity by further increasing current density. With further increasing current density, ES_1 peak is occurred at ~1195 nm. Due to the increased number of dot layers, the saturation of the ES_1 is expected to occur at a very high current density. The saturation of the ES_1 does not occur at the highest current density. Therefore, there is no significant emission from QW since QD of ES_1 are still filling with the carrier. Due to the lack of emission from the QW at a shorter wavelength, the spectral coverage of ~ 135 nm is achieved from the contribution from the QD GS and ES_1 emission.

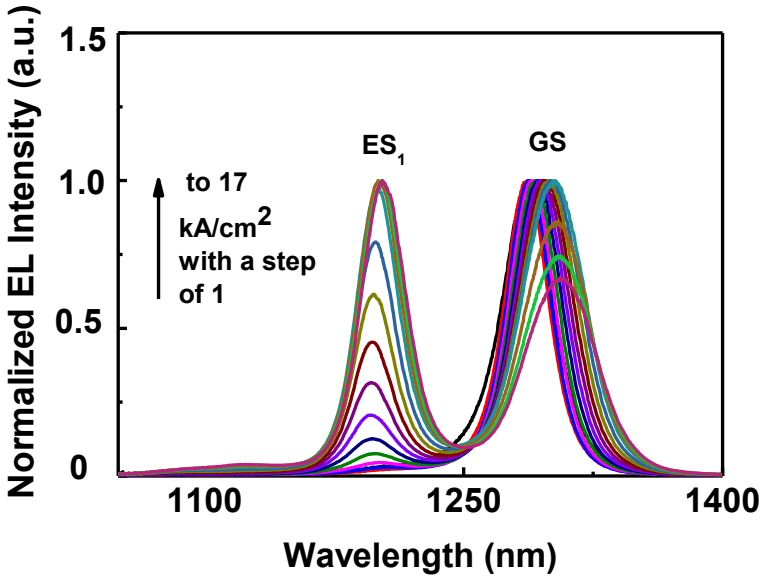

Figure 4.9: Normalized EL spectra for AE at various current density.

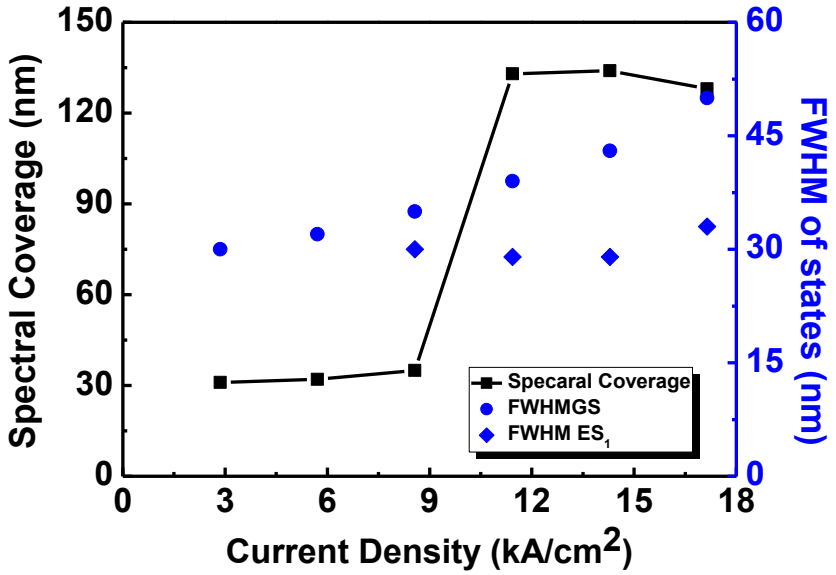

Figure 4.10: Spectral Coverage of SLD emission and FWHM of individual states of QD as a function of current density for AE.

Figure 4.10 shows the spectral coverage of SLD emission and FWHM of the individual states as a function of current density for device AE. The spectral coverage is only ~ 30 nm at current density of up to 9 kA/cm^2. The emission from ES_1 contributes to the spectral coverage of SLD emission and ~135 nm is obtained at 11 kA/cm^2, which is about four times higher in current density compared to AG (QW/5QDs). Since there are more layers of the dots, the ES_1 is still not fully saturated at the highest injection current density of 17 kA/cm^2 and therefore the overall spectral coverage of SLD emission is ~ 135 nm. The QD region of the devices discussed so far are the "unchirped" and therefore the spectral dip is large which is undesirable for OCT systems. Introduction of chirp QD layers which vary the emission wavelength of individual QD layers in multilayer stacks can reduce the spectral dip.

Figure 4.11 shows EL emission spectra at various injection current for 9 layers of chirp QD and a single asymmetric triangular QW (AJ) sample. The effect of "chirped" QD on the emission spectra is the reduction in the modulation of the spontaneous emission. There are two peaks centred at ~1285 nm and ~ 1235 nm which is attributed to GS emission of QD from type A (GS_A) and type B (GS_B) at low injection current. Increasing the current density led to the emission of another peak at ~1190 nm, related to the ES_1 of type A QD. Further increasing the current density leads to the dipless spectral modulation in the GS of the QD, followed by the emission of ES_2 of type B QD. A small shoulder can be seen at ~1120 nm which may be due to the contribution from QW. However, there is not enough carrier to fill to that state as the higher order of the QD not saturated at this current density due to the large number of QD layer. The FWHM of SLD emission (defined in section 2.4.1) of ~ 160 nm is achieved from the contribution of type A and B QD emission. This FWHM is ~20 nm broader compared to both AG (QW/5QDs) where the spectral coverage is contribution from ES_1 and QW and AE (QW/9QDs) where the spectral coverage is contribution form GS and ES_1.

Figure 4.12 plots the FWHM of SLD emission and FWMH of individual states of QD as a function of current for device AJ. At low current density, the FWHM of SLD emission of ~90 nm is obtained from the contribution from Type A and Type B GS of QD. The alternative wavelength position of the ES_1 benefit the sightly broader in the overall FWHM which is about 160 nm at 9 kA/cm^2. Increasing the current density led to the reduction in the GS of the dots. If there is QW emission from this structure and better heat extraction to minimise the reduction in GS intensity, the smooth FWHM of SLD emission of ~ 240 nm can be achieved. Regarding the "strong" and "weak" definitions used earlier, "strong dip" in their EL spectra, may not be optimal for OCT imaging due to the possibility of ghost imaging resulting from insufficient coherence length or spectral bandwidth of the light source. In

contrast, in Figure 4.11, with its smoother spectrum and weaker dip, this may be more suitable for OCT applications.

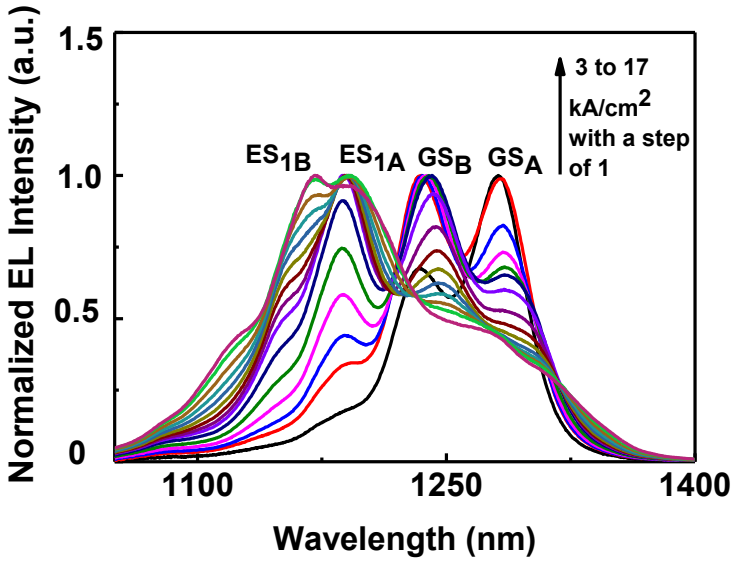

Figure 4.11: Normalized EL spectra for AJ at various current density.

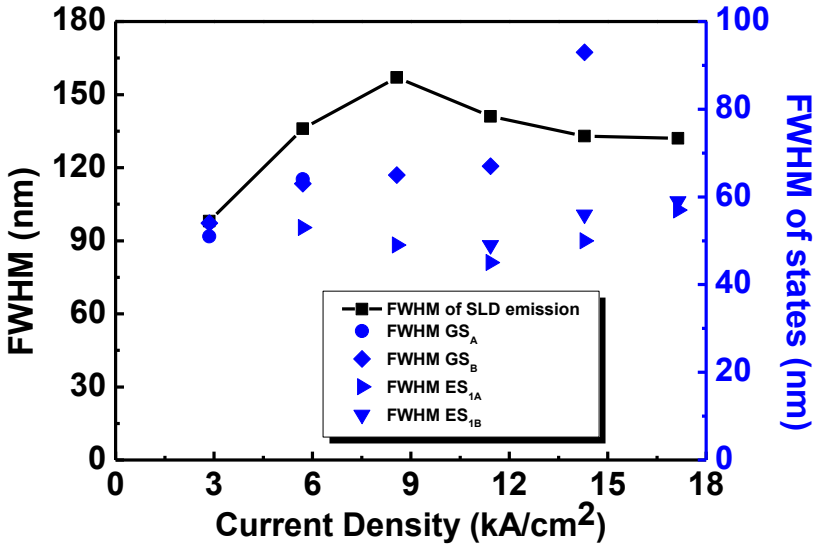

Figure 4.12: FWHM of SLD emission and FWHM of individual states of QD as a function of current density for AJ.

4.5.4 Segmented Contact Gain

Increasing the number of dot layers and dot density of the QD is expected to enhance the saturated modal gain [58], [59]. To study the effect of hybrid QW/QD active design on modal gain, it is measured by using the segmented contact gain method. The modal gain can be converted from the net modal gain by the relation; modal gain = net modal gain+ α_i, where α_i is the internal loss.

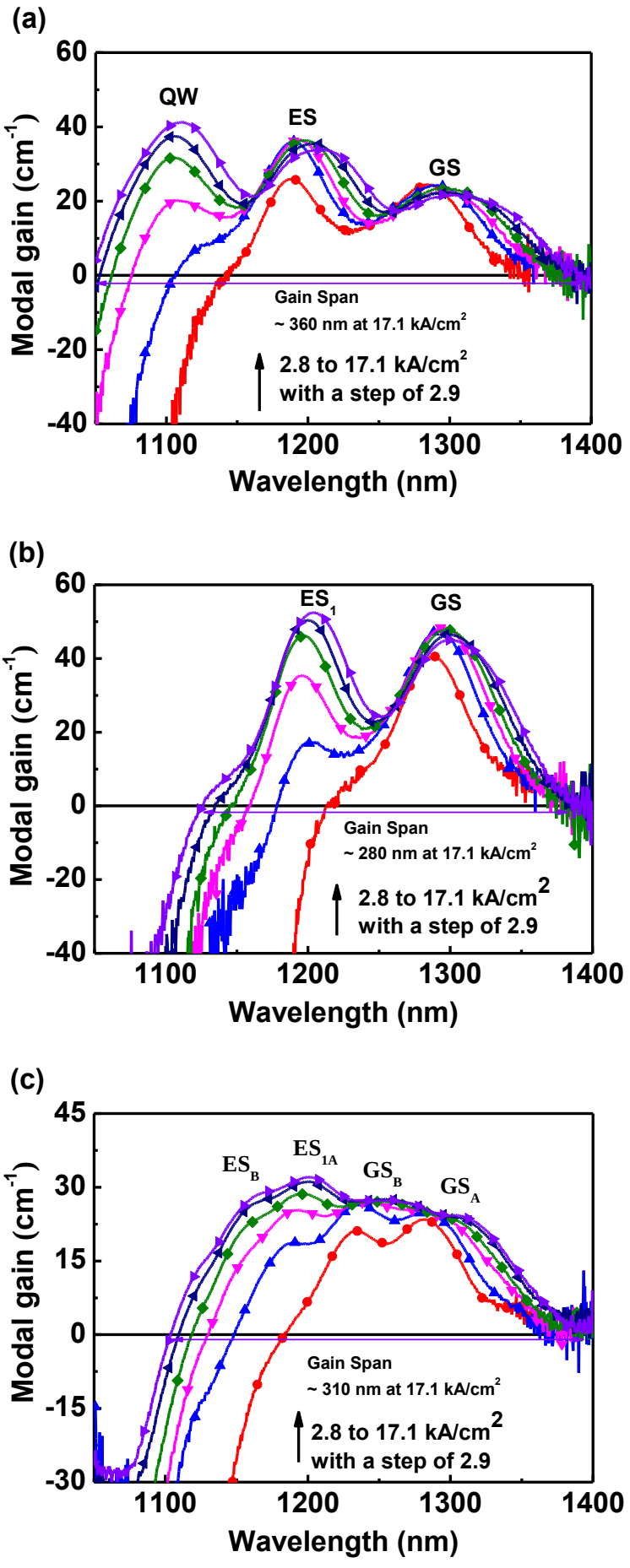

Figure 4.13: Modal gain spectra for (a) AG (b)AE (c) AJ at a function of current density.

Figure 4.13 (a) plots the modal gain spectrum of 5 layers of QD and a single QW (sample AG) at a range of current densities. At 2.8 kA/cm^2, gain peaks are observed at wavelengths of ~1285 nm and ~1195 nm, attributed to GS and ES_1 emission of the QD, respectively. With increasing current density, the modal gain of the GS remains static at 24 ± 1 cm^{-1} which is attributed to the saturation of the gain and the modal gain peak broadens with increasing injection current due to free carrier effects [54]. Despite the fewer number of dot layers, this GS saturated modal gain value is higher than reported in previous work which has 6 layers of QD and a single QW with the saturated GS gain value of 12 ± 1 cm^{-1} [43]. This enhanced QD modal gain is attributed to the increased QD dot density in the present samples. Further increasing the current density leads to a slight reduction in the GS peak values and a wavelength shift to longer wavelength which is related to free carrier and thermal effects.

However, the gain from ES_1 continues to increase with increasing current density and appears to saturate at 8.6 kA/cm^2 with a saturated modal gain of 36 ± 1 cm^{-1}. At higher current density, a significant gain peak at ~1100 nm appears which is attributed to the emission from the QW and rapidly grows to dominate the gain spectrum at the highest current density. With the contribution from the QW, the modal gain spans ~360 nm which is from 1040 to 1400 nm at this current density. There is a significant improvement in the modal gain value as well as the modal gain span as compared to previous work in [42].

Figure 4.13 (b) shows the modal gain spectra obtained from 9 layers of QD and a single QW sample (AE) at various current densities. The gain peaks are observed at ~1285 nm and ~1195 nm for GS and ES, respectively. A saturated modal gain value of 48 ± 1 cm^{-1} is observed for the GS which is around two times higher than that of the QW/5 QD sample (AG) because due to the higher number of dot layers. Further increasing the current density leads to an increase in gain for ES_1. At highest current density, an ES_1 gain of 52 ± 1 cm^{-1} is achieved. However, the gain is not fully saturated at this current density due to the limitation of the current source, as this current density is the highest that can be achieved. Due to the increased number of layers of dots, more carriers are needed to fill ES_1 to fully saturate the dots, before filling the QW. Therefore, there is no significant positive gain value from the QW since it is still at alow carrier density. The modal gain spans ~ 280 nm, from ~1120 to ~1400 nm for this device. The gain span is smaller than that of AG since there is no emission related to the QW. However, this device (AE) achieves two times higher in modal gain values compared to AG due to the increased number of dot layers.

Figure 4.13 (c) shows the modal gain spectra obtained from a sample (AJ) with 9 layers of chirped QD with emission wavelength at ~1280 nm and ~1230 nm (alternating in the QD

stack) and a digital alloy QW at 1080 nm at various currents density. The positive modal gain from the GS of type A and B QD appears at wavelengths of ~1285 nm and ~1235 nm with the gain value of 23 ± 1 cm^{-1} and 21 ± 1 cm^{-1} respectively. Further increasing current density leads to the saturation of type A GS with the saturated gain value of 25 ± 1 cm^{-1} at 8.6 kA/cm^2. This is followed by the GS saturation of type B QD with a value of 27 ± 1 cm^{-1} and contribution from the ES_1 of type A QD to the gain spectrum at a wavelength of ~1180 nm. Type A QD contribute ES_1 gain to the gain spectrum at ~1185 nm with the value of 19 ± 1 cm^{-1} at a current density of 8.6 kA/cm^2, at which the saturation of the type A and B of GS occurs. Further increasing current density makes the contribution from type B ES_1 of the QD at ~ 1160 nm. The gain value of the ES_1 still increases with increasing current density. There is no significant contribution to the gain spectrum from the QW/QD. The modal gain spans ~310 nm, from ~1090 to ~1400 nm at the highest current density.

The saturated GS gain value for these 9 layers of alternative QD with "chirped" layers/QW sample (AJ) has a smaller gain compared to the gain value of 9 layers of unchirped QD/QW sample (AE). This is due to the spectral overlapping of the dot layers results in a reduction in gain value. However, this value is still two times higher compared to the previous work due to the high dot density [42]. Moreover, the alternative of type A and type B chirped QD sample yields an almost flat-topped, broad gain spectrum. Results suggests that if gain from the QW by further increasing current density is achieved, this would provide a flat-topped ultrabroad gain spectrum.

Figure 4.14 (a) shows the peak modal gain as a function of current density from 5 layers of QD and a single QW sample (AG). Due to the lower number of dot layers, the evolution of GS and ES_1 state occupancies are observed at low injection current. The GS and ES_1 states intercept at a current density of around 3 kA/cm^2. Increasing current density results in the saturation of the GS gain (24 ± 1 cm^{-1}) followed by the rapid increase in ES_1 peak gain. Due to the two-fold degeneracy of the ES compared to the GS, the saturated gain of ES_1 should be two times larger than that of GS. The expected ES_1 saturation modal gain is ~ 50 cm^{-1}. However, the peak saturated modal gain from ES_1 is 36 ± 1 cm^{-1}. As discussed in the previous chapter, the difference in experimental value and the expected value may be due to self-heating effects at high current density that makes the thermalization of carriers out of the dots and their loss via non-radiative recombination. QD asymmetry may also be a factor in the lower ES gain [55]. The saturation in the modal gain of ES_1 is observed and the gain of QW increases with increasing current density. The positive gain from the QW appears at a current density of 6 kA/cm^2 and eventually dominates at high injection current density.

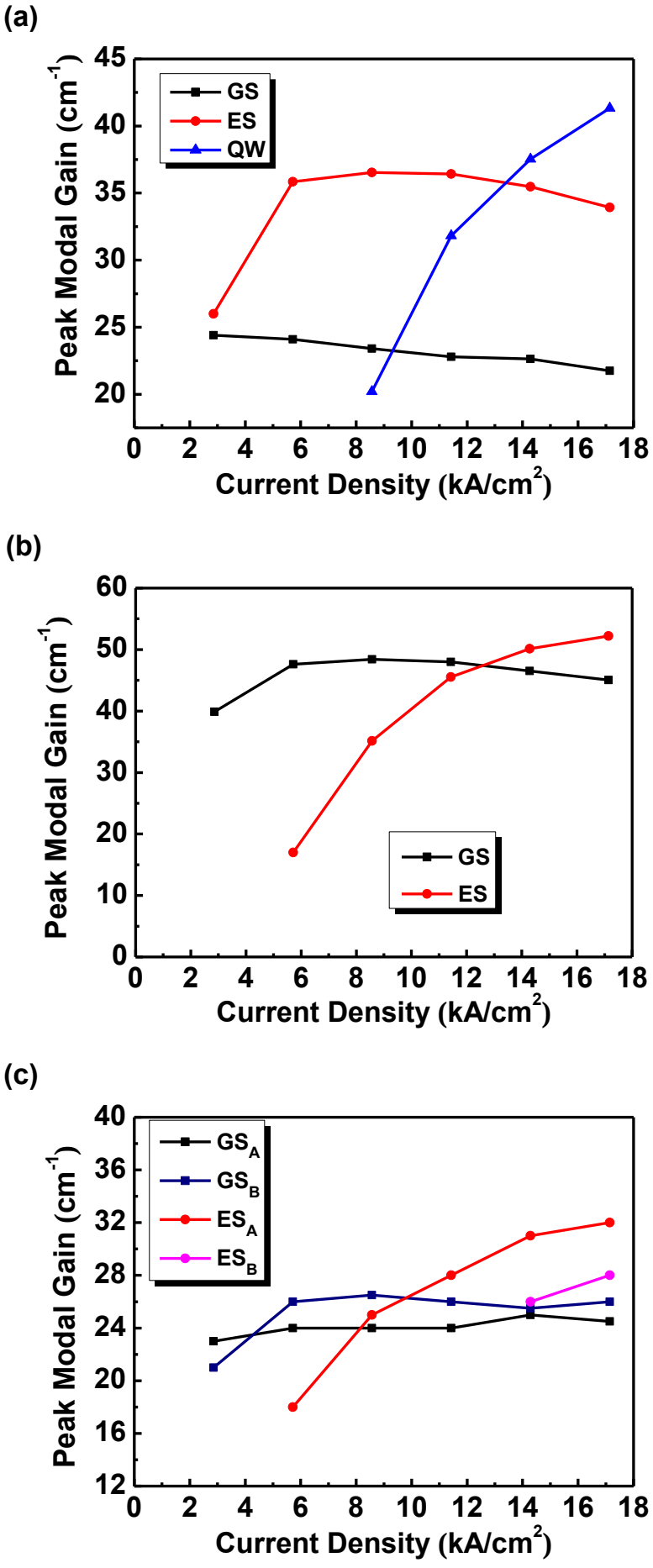

Figure 4.14: Peak modal gain for (a) AG (b) AE and (c) AJ as a function of current density.

Figure 4.14 (b) plots the peak modal gain as a function of the current density from 9 layers of QD and a single QW sample (AE). The peak modal gain of ES_1 appears with increasing current density and overtakes the GS at ~ 12kA/cm^2. At the highest current density, the peak modal gain of 52 ± 1 cm^{-1} from the ES_1 of the QD is achieved and there is no gain from the QW.

Figure 4.14 (c) shows the peak modal gain as a function of the current density from 9 layers of chirped QD and QW sample (AJ). The peak modal gain with the value of 23 ± 1 cm^{-1} and 21 ± 1 cm^{-1} from the GS of type A and B QD appears at low current density. Increasing current density, positive modal gain of the GS of type A and B QD are almost identical. Further increasing the current density, positive gain from ES_1 of the Type A QD begins at a current density of 6 kA/cm^2. The monotonous increase in the peak gain of ES_1 can be observed indicating that ES_1 is not yet saturated.

The purpose of high dot density hybrid QW/QD is to achieve high modal gain while maintaining a broad spectral bandwidth. From the modal gain spectra, it has been proved that a sample with a low number of QD layers (AG) can provide a high gain value. The QW/ "chirped" QD can also provide a broad, flat-top gain span with relatively high modal gain value.

4.6 Conclusions

This chapter performed an analysis on hybrid QW/QD SLDs with high-density of QD layers to achieve high modal gain. A single QW introduced into a multilayer QD structure can results in an ultrabroad spectral bandwidth. Three hybrid QW/QD SLD devices are compared. All these structures have higher modal gain compared to previous hybrid QW/QD structures due to the high dot density and the gain spectrum is wider due to the spectral positioning of the QW to shorter wavelength.

Firstly, the 5 layers of QDs and QW (AG) sample gave the high modal gain value of 25 cm^{-1} and the positive modal gain spanning of ~ 350 nm. However due to the large self-heating effects on these devices, a spectral coverage of ~140 nm was achieved. By eliminating this heating effect, a spectral coverage of ~260 nm may be achieved. The effect of the number of QD stacked layers on the modal gain is also discussed. Compared with 5 layers of QDs and QW (AG) device, 9 layers of QDs and QW (AE) device gave two times higher saturated modal gain values. However, due to the absence of emission from the QW structure the positive modal gain spanning ~280 nm is achieved with the spectral coverage of ~135 nm. Finally, the hybrid QW/QD structure with "chirped" QD was studied. 9 layers of stacked QD layer is used to achieve high modal gain. The benefit of this device is that the

broad flat-top gain span of ~310 nm with smooth spectral bandwidth of ~160 nm was achieved.

4.7 Future Work

The “chirped” QD layers (AJ) can have the advantage of flatter gain spectra which is desirable for OCT systems. Due to the large number of QD layers in the chirped structure studied, there is lack of emission from the QW. The fewer number of QD layers with high dot density (AG) can give the benefit of broader spectral coverage due to the emission from the QW with relatively high saturated modal gain values from the QD ES and GS. Therefore, by taking the benefits from these two structures, a structure with 5 layers of “chirped” QD / QW should provide emission from the QW and consequently have a broad FWHM of SLD emission. The next step would be to fabricate these SLDs and by mounting *p*-side down on a tile and using a TEC for active cooling, ameliorate thermal effects to minimise the reduction in intensity with increasing current density. Subsequently, it would be good to utilise these SLDs as the light sources in an OCT system.

Bibliography

[1] S. M. Chen, K. J. Zhou, Z. Y. Yang, D. T. D. Childs, M. Hugues, A. J. Ramsay, and R. A. Hogg., "Ultra-broad spontaneous emission and modal gain spectrum from a hybrid quantum well/quantum dot laser structure," *Applied Physics Letters*, vol. 100, no.4, p. 41118, 2012.

[2] S. M. Chen, K. J. Zhou, Z. Y. Yang, D. T. D. Childs, J. R. Orchard, R. A. Hogg, K. Kennedy, and M. Hughes., "Hybrid quantum well/quantum dot structures for broad spectral bandwidth devices," In *Physics and Simulation of Optoelectronic Devices XX SPIE*, vol. 8255, p. 92-98, 2012.

[3] J. D. Thomson, H. D. Summers, P. J. Hulyer, P. M. Smowton, and P. Blood, "Determination of single-pass optical gain and internal loss using a multisection device," *Applied Physics Letters*, vol. 75, no. 17, p. 2527, 1999.

[4] K. Mukai, Y. Nakata, K. Otsubo, M. Sugawara, N. Yokoyama, and H. Ishikawa, "High characteristic temperature of near-1.3- μm InGaAs/GaAs quantum-dot lasers at room temperature," *Applied Physics Letters,* vol. 76, no. 23, p. 3349-3351, 2000.

[5] D. G. Deppe, K. Shavritranuruk, G. Ozgur, H. Chen, and S. Freisem., "Quantum dot laser diode with low threshold and low internal loss," *Electronics Letters*, vol. 45, no. 1, p. 54-56, 2009.

[6] C. F. Lin and B. L. Lee., "Extremely Broadband AlGaAs/GaAs Superluminescent diodes," *Applied Physics Letters*, vol. 71, p. 1598-1600, 1997.

[7] Z. Y. Zhang, Z. G. Wang, B. Xu, P. Jin, Z. Z. Sun, and F. Q. Liu., "High-Performance Quantum-Dot Superluminescent Diodes," *IEEE Photonics Technology Letters*, vol. 16, no. 1, p. 27-29, 2004.

[8] A. Salhi, G. Raino, L. Fortunatio, V. Tasco, L. Martiradonna, M. T. Todaro, M. D. Giorgi, R. Cingolani, A. Passaseo, E. Luna, A. Trampert, and M. D. Vittorio., "Linear increase of the modal gain in 1.3 μm InAs/GaAs quantum dot lasers containing up to seven-stacked QD layers." *Nanotechnology* 19, no. 27, p. 275401, 2008.

[9] A. Matsumoto, K. Akahane, T. Umezawa, S. Nakaijima, and N. Yamamoto., "Influence and its Optimal Design of Number of Stacked Layer in Quantum-Dot Lasers." *physica status solidi (a)* 216, no. 1, p. 1800502, 2019.

[10] Y. Tanaka, M. Ishida, K. Takada, T. Yamamoto, H. -Z. Song, Y. Nakata, M. Yamaguchi, K. Nishi, M. Sugawara, and Y. Arakawa., "25 Gbps direct modulation in 1.3μm

InAs/GaAs high-density quantum dot lasers," *CLEO/QELS: 2010 Laser Science to Photonic Applications*, p. 1–2, 2010.

[11] Y. Tanaka, M. Ishida, K. Takada, Y. Maeda, T. Akiyama, T. Yamamoto, H. Z. Song, M. Yamaguchi, Y. Nakata, K. Nishi, M. Sugawara and Y. Arakawa., "1.3 μm InAs/GaAs High-Density Quantum Dot Lasers," In *IEEE LEOS Annual Meeting Conference Proceedings*, p. 668-669, 2009.

[12] N. Kirstaedter, O. G. Schmidt, N. N. Ledentsov, D. Bimberg , V. M. Ustinov, A. Yu. Egorov, A. E. Zhukov, M. V. Maximov, P. S. Kop'ev, *A. F. Loffe, and* Zh. I. Alferov "Gain and differential gain of single layer InAs/GaAs quantum dot injection lasers." *Applied physics letters* 69, no. 9, p. 1226-1228, 1996.

[13] D. G. Deppe, K. Shavritranuruk, G. Ozgur, H. Chen, and S. Freisem., "Quantum dot laser diode with low threshold and low internal loss," *Electronics Letters*, vol. 45, no. 1, p. 54-56, 2009.

[14] Z. Yao, C. Jiang, X. Wang, H. Chen, H. Wang, L. Qin, and Z. Zhang., "Recent Developments of Quantum Dot Materials for High Speed and Ultrafast Lasers," *Nanomaterials*, vol. 12, no. 7, p. 1058, 2002.

[15] S. K. Ray, K. M. Groom, R. Alexander, K. Kennedy, H. Y. Liu, M. Hopkinson, and R. A. Hogg., "Design, growth, fabrication, and characterization of quantum dot broadband superluminescent light emitting diode," *Journal of Applied Physics*, vol. 100, no.10, p. 103105, 2006.

[16] Y. O. Kostin and S. D. Yakubovich., "Two-section broadband superluminescent diodes Related content," *Quantum Electronics*, vol. 39, no.5, p. 421-424, 2009.

[17] M. Rossetti, A. Markus, A. Fiore, L. Occhi, and C. Velez., "Quantum dot superluminescent diodes emitting at 1.3 μm," *IEEE Photonics Technology Letters*, vol. 17, no. 3, p. 540–542, 2005.

[18] P. Marten, K. Petermann, E. Weidel, and R. Ulrich., "Low-drift fibre gyro using a superluminescent diode." *Electronics Letters* 10, no. 17, p. 352-353, 1981.

[19] S. J. Park, C. H. Lee, K. T. Jeong, H. J. Park, J. G. Ahn, and K. H. Song.,"Fiber-to-the-home services based on wavelength-division-multiplexing passive optical network." *Journal of lightwave technology* 22, no. 11, 2582, 2004.

[20] V. R. Shidlovski, and J. Wei., “Superluminescent diodes for optical coherence tomography.” In *Test and Measurement Applications of Optoelectronic Devices SPIE*, vol. 4648, pp. 139-147. 2002.

[21] M. Rossetti, L. H. Li, A. Fiore, L. Occhi, and C. Velez., “Quantum dot superluminescent diodes,” In *Handbook of Self Assembled Semiconductor Nanostructures for Novel Devices in Photonics and Electronics*, p. 565-567, 2008

[22] M. Duelk, and K. Hsu., “SLEDs and swept source laser technology for OCT.” *Optical Coherence Tomography*, p.257, 2015.

[23] Z. Sun, D. Ding, Q. Gong, W. Zhou, B. Xu, and Z. G. Wang., “Quantum-dot superluminescent diode: A proposal for an ultra-wide output spectrum,” *Optical and quantum Electronics*, vol. 31, no. 12, p. 1235-1246, 1999.

[24] Z. Y. Zhang, Z. G. Wang, B. Xu, P. Jin, Z. Z. Sun, and F. Q. Liu., “High-Performance Quantum-Dot Superluminescent Diodes,” *IEEE Photonics Technology Letters*, vol. 16, no. 1, p. 27-29, 2004.

[25] S. Haffouz, P. J. Barrios, R. Normandin, D. Poitras, and Z. Lu., “Ultrawide-bandwidth, superluminescent light-emitting diodes using InAs quantum dots of tuned height,” *Optics letters*, vol. 37, no. 6, p. 1103-1105, 2012.

[26] L. H. Li, M. Rossetti, A. Fiore, L. Occhi, and C. Velez., “Wide emission spectrum from superluminescent diodes with chirped quantum dot multilayers,” *Electron Letter*, vol. 41, no. 1, p. 41-43, 2005.

[27] Z. Y. Zhang, R. A. Hogg, B. Xu, P. Jin, and Z. G. Wang., “Realization of extremely broadband quantum-dot superluminescent light-emitting diodes by com thermal-annealing process,” *Optics letters*, vol. 33, no. 11, p. 1210-1212, 2008.

[28] Q. L. Liu, C. C. Hou, H. M. Chen, J. Q. Ning, Q. Z. Li, Y. Q. Huang, Z. Y. Zhao, Z. G. Wang, P. Jin, Z. Y. Zhang., “Effects of Modulation P-Doping on Thermal Stability of InAs/GaAs Quantum Dot Superluminescent Diodes,” *Journal of Nanoscience and Nanotechnology*, vol. 18, no. 11, p. 7536-7541, 2018.

[29] F. Koyama., “High power superluminescent diodes for multi-wavelength light sources,” In *Conference Proceedings. LEOS'97. 10th Annual Meeting IEEE Lasers and Electro-Optics Society*, vol. 1, p. 333–334, 1997

[30] D. C. Heo, J. D. Song, W. J. Choi, J. il Lee, J. C. Jung, and I. K. Han., "High power broadband InGaAs/GaAs quantum dot superluminescent diodes," Electronic Letter, vol. 39, no. 11, p. 862-863, 2003.

[31] R. Cahill, P. P. Maaskant, M. Akhter, and B. Corbett., "High power surface emitting InGaN superluminescent light-emitting diodes," *Applied Physics Letters*, vol. 115, no. 17, p. 171102, 2019.

[32] T. K. Ong, M. Yin, Z. Yu, Y. C. Chan and Y. L. Lam., "High-performance quantum well intermixed superluminescent diodes," *Measurement Science and Technology*, vol. 15, no. 8, p. 1591, 2004.

[33] X. Q. Lv, N. Liu, P. Jin, and Z. G. Wang., "Broadband emitting superluminescent diodes with InAs quantum dots in AlGaAs matrix," *IEEE Photonics Technology Letters*, vol. 20, no. 20, p. 1742-1744, 2008.

[34] P. Resneau, A. Enard, Y. Robert, M. Calligaro, M. Krakowski, M. Hopkinson, P. Bardella, M. Gioannini, M. Rossetti, I. Montrosset, M. Blazek, W. Elsaesser, J. Lynn, and S. Duffy, "High power performances of broad bandwidths superluminescent diodes (SLDs) based on chirped-quantum-dot structures operating at 1100 and 1200 nm for optical coherence tomography (OCT) applications." in *CLEO/Europe and EQEC 2009 Conference Digest*, p. CB3_5, 2009.

[35] P. D. L. Judson, K. M. Groom, D. T. D. Childs, M. Hopkinson, N. Krstajic, and R. A. Hogg., "Maximising performance of optical coherence tomography systems using a multi-section chirped quantum dot superluminescent diode," *Microelectronics Journal*, vol. 40, no. 3, p. 588–591, 2009.

[36] L. H. Li, M. Rossetti, A. Fiore, L. Occhi, and C. Velez., "Wide emission spectrum from superluminescent diodes with chirped quantum dot multilayers," *Electron Letter*, vol. 41, no. 1, p. 41-43, 2005.

[37] S. K. Ray, K. M. Groom, M. D. Beattie, H. Y. Liu, M. Hopkinson, and R. A. Hogg., "Broad-Band Superluminescent Light-Emitting Diodes Incorporating Quantum Dots in Compositionally Modulated Quantum Wells," IEEE photonics technology letters, vol. 18, no. 1, p. 58-60, 2006.

[38] I. K. Han, H. C. Bae, W. J. Cho, J. I. Lee, H. L. Park, T. G. Kim, J. I. Lee., "Study of chirped quantum dot superluminescent diodes," *Japanese journal of applied physics*, vol. 44, no. 7 S, p. 5692-5695, 2005.

[39] N. Liu, P. Jin, and Z. G. Wang., "InAs/GaAs quantum-dot superluminescent diodes with 110 nm bandwidth," *Electronics Letters*, vol. 41, no. 25, p. 55-56, 2005.

[40] H. S. Dijie, C. E. Dimas, D. N. Wang, B. S. Ooi, J. C. M. Hwang, G. T. Dang, and W. H. Chang., "InGaAs/GaAs Quantum-Dot Superluminescent Diode for Optical Sensor and Imaging," *IEEE Sensors Journal*, vol. 7, no. 2, pp. 251–257, 2007.

[41] Z. Y. Zhang, R. A. Hogg, X. Q. Lv, and Z. G. Wang., "Self-assembled quantum-dot superluminescent light-emitting diodes," *Advances in Optics and Photonics*, vol. 2, no. 2, p. 201-228, 2010.

[42] S. Chen, K. Zhou, Z. Zhang, J. R. Orchard, D. T. D. Childs, M. Hugues, O. Wada and |R. A. Hoggs., "Hybrid quantum well/quantum dot structure for broad spectral bandwidth emitters," *IEEE Journal of Selected Topics in Quantum Electronics*, vol. 19, no. 4, p. 1900209-1900209, 2013.

[43] S. Chen, W. Li, Z. Y. Zhang, D. T. D. Childs, K. Zhou, J. Orchard, K. Kennedy, M. Hugues, E. Clarke, I. Ross, O. Wada and R. A. Hogg., "GaAs-Based Superluminescent Light-Emitting Diodes with 290-nm Emission Bandwidth by Using Hybrid Quantum Well/Quantum Dot Structures," *Nanoscale Research Letters* 1, vol. 10, no. 1, p. 1-8, 2015.

[44] Z. C. Wang, P. Jin, X.Q. Lv, X.K. Li and Z.G. Wang., "High-power quantum dot superluminescent diode with integrated optical amplifier section." *Electronics letters* 47, no. 21, p. 1, 2011.

[45] A. F. Forest, M. Krakowski, P. Bardella, and M. A. Cataluna., "High-power quantum-dot superluminescent tapered diode under CW operation." *Optics Express* 27, no. 8, p. 10981-10990, 2019.

[46] A. Kafar, S. Stanczyk, G. Targowski, T. Oto, I. Makarowa, P. Wisniewski, T. Suski and P. Perlin., "High-optical-power InGaN superluminescent diodes with 'j-shape' waveguide," Applied Physics Express, vol. 6, no. 9, p. 092102, 2013.

[47] Z. Zhang, T. Minato, P. Navaretti, Y. Hinokuma, M. Duelk, C. Velez, and K. Hamamoto., "High-Power (> 110 mW) Superluminescent Diodes by Using Active Multimode Interferometer." *IEEE Photonics Technology Letters* 22, no. 10, p. 721-723, 2010.

[48] Y.C. Yoo, I.K. Han and J.I. Lee., "High power broadband superluminescent diodes with chirped multiple quantum dots." *Electronics Letters* 43, no. 19, p. 1, 2007.

[49] T. K. Ong, M. Yin, Z. Yu, Y. C. Chan and Y. L. Lam., “High-performance quantum well intermixed superluminescent diodes,” *Measurement Science and Technology*, vol. 15, no. 8, p. 1591, 2004.

[50] T. H. Ko, Desmond C. Adler, J. G. Fujimoto, D. Mamedov, V. Prokhorov, V.Shidlovski, and S. Yakubovich., “Ultrahigh resolution optical coherence tomography imaging with a broadband superluminescent diode light source,” *Optics Express* 12, no. 10, p. 2112-2119, 2004.

[51] R. Murray, D. Childs, S. Malik, P. Siverns, C. Roberts, J. H. Hartmann, and P. Stavrinou., "1.3 μm room temperature emission from InAs/GaAs self-assembled quantum dots." *Japanese Journal of Applied Physics* vol. 38, no. 1S, p. 528, 1999.

[52] G. R. Goldberg, D. H. Kim, R. J. E. Taylor, D. T. D. Childs, P. Ivanov, N. Ozaki, K. L. Kennedy, K. M. Groom, Y. Harada and R. A. Hoog., “Bandwidth enhancement in an InGaN/GaN three-section superluminescent diode for optical coherence tomography,” *Applied Physics Letters*, vol. 117, no. 6, p. 061106, 2020.

[53] P. D. L. Judson, K. M. Groom, D. T. D. Childs, M. Hopkinson, and R. A. Hogg, “Multi-section quantum dot superluminescent diodes for spectral shape engineering,” *IET Optoelectronics*, vol. 3, no. 2, p. 100–104, 2009.

[54] H. Shahid, D. T. D. Childs, B. J. Stevens, and R. A. Hogg, “Negative differential gain due to many body effects in self-assembled quantum dot lasers,” *Applied Physics Letter*, vol. 99, no. 6, p. 61104, 2011.

[55] I. M. E. Butler, W. Li, S. A. Sobhani, N. Babazadeh, I. M. Ross, K. Nishii, K. Takemasa, M. Sugawara, D. T. D. Childs, and R. A. Hogg., “Size anisotropy inhomogeneity effects in state-of-the-art quantum dot lasers." *Applied Physics Letters* 113, no. 1, p. 012105, 2018.

Chapter 5: Quantum Dot based Photonic Crystal Surface-Emitting Lasers

5.1 Introduction

Photonic crystal surface-emitting lasers (PCSELs) are a relatively recent development in the field of semiconductor lasers, which incorporates a two-dimensional (2D) photonic crystal (PC) into a semiconductor laser structure. They draw significant attention due to their high-power single-mode vertical emission with narrow divergence [1], beam steering [2], control of the wavelength, and polarisation [3]. In this chapter, epitaxially regrown GaAs-based PCSELs utilising self-assembled InAs QD, exhibiting lasing at room temperature will be discussed. The ability to utilise both the ground-state (GS) and excited-state (ES) of the QD allows multiple emission wavelengths from one heterostructure. The choice of the grating periods allows lasing at the GS or ES of the QD, 90 nm apart in wavelength. The effect of the device area, PC structure (square, circle, height) and crystallographic orientation of the PC on device performance will be discussed.

5.2 Background

Semiconductor lasers emitting a wavelength within the O-band (1260-1360 nm) and C-band (1530-1565 nm) have attracted significant attention in optical communication due to the minimum dispersion and attenuation for standard single-mode fibre [4]. Traditionally, GaAs-based lasers cover the wavelength range of ~ 0.7 μm to ~ 0.9 μm, GaN-based lasers cover the shorter wavelengths and InP-based lasers cover the longer wavelengths ~ 1.2 μm to 1.7 μm. Strained GaAs quantum well (QW) lasers (utilising InGaAs) increase the lasing wavelength of GaAs-based structures to ~ 1.1 μm. However, it has so far been impossible to reach the telecoms wavelengths of ~ 1.3 μm using InGaAs QWs before defects became too extensive resulting in a failure to lase [5]. Therefore, the commercial market in the fibre-optical communication wavelength ranges (1.2-1.7μm) is dominated by InP-based QW lasers. However, InP/InGaAsP/AlInGaAs has a small conduction band offset compared to InGaAs/GaAs resulting in a lower characteristic temperature, T_0. Due to the poor temperature stability, InP-based lasers usually require an active cooling system to maintain a suitable operating temperature and hence increase the cost and power consumption using this type of laser. Moreover, InP materials are also quite fragile and comparatively difficult material to work with, have higher substrate costs, and are only able to be grown on smaller wafer sizes (4"). On the other hand, GaAs can be grown on larger wafer size (6") and

therefore the manufacturing cost is much lower (similar fabrication costs for more chips per wafer). More importantly, GaAs-based lasers offer high-temperature, high-power operation due to their larger band offsets.

The development of epitaxial process has allowed GaAs-based QD to cover 1.2 to 1.55 μm range which is not easily accessible by typical QW structures. Compared with GaAs-based QWs, InGaAs/GaAs QD are more promising because of the 3D carrier confinement, low threshold current densities, and temperature insensitivity [6]–[9]. Hence, 1.3 μm QD-based devices are ideal candidates for optical communications. In order to extend the emission wavelength of GaAs-based materials, there has been a large research effort to investigate GaAs-based QD materials. In 1998, a new GaAs-based approach to 1.3 μm edge-emitting lasers was demonstrated using InGaAs QD and have since been studied extensively.

Most GaAs-based QD lasers demonstrated in 1.3 μm wavelength range so far are edge-emitting lasers (EELs) such as Fabry-Perot (FP) [10]–[14] or Distributed feedback (DFB) lasers [15]. EELs have the light emission parallel to the wafer's surface, but they have asymmetric beam-divergence and multimode oscillation if the emission area is widened to enhance output power. Therefore, are not able to operate with high-power single-mode operation. Moreover, the packaging cost for this type of lasers are usually high due to the requirement of facet cleaving to create mirrors, optical coating of the facet, and die-bonding to a heatsink before parametric testing can be performed. On the other hand, vertical cavity surface emitting laser (VCSEL) is an attractive alternative for GaAs-based QD laser, which are widely used in optical communication[16]–[18].Even though the VCSEL can provide a symmetric low divergence circular beam, for high output power a larger area is required, and this leads to multimode operation. Moreover, the operating wavelength range for VCSELs is limited. Therefore, both EELs and VCSELs present challenges for the simultaneous achievement of high-power and high-quality beams due to the large emission area. Therefore, a laser diode class that can provide high-power coherent lasing over a large emission area is highly attractive for various applications. PCSELs are one such laser diode class that has potential to meet this requirement. The PCSELs use a PC structure to control the emission properties of laser, which allows for high-power coherent lasing over a large emission area. PC is based on the periodic variation of the refractive index to control the propagation of light. This variation of refractive index can be done by having alternative lower or higher dielectric constant materials in one or two or three dimensions [19]. The simple PC structure is constructed by two periodically stacked dielectrics which are denoted as a one-dimensional (1D) PC structure. An ideal 2D PC structure, which is attracting particular attention in recent years, is periodic in two directions and homogeneous in the

third direction. A three-dimensional (3D) PC is challenging in terms of ease and reliability of fabrication. In this thesis, a 2D PC is adopted as it can be practically constructed and has the ability to manipulate light in a planer direction and vertical emission due to second-order grating [20]. The designs of a 2D PC are key in determining how light propagates through a structure. Important factors to consider in PC design include lattice structure, PC atom shape (etch depth, feature size), and the crystallographic orientation of the PC.

5.2.1 Progress of Photonic Crystal Surface Emitting Lasers

Figure 5.1 schematically summarises the progress of PCSEL technologies. The first PCSEL was demonstrated in 1999 using an organic gain medium [21] and also in InP by wafer fusion [22]. By utilising the band edge mode at the Γ point of a triangular lattice point of PC, the output beam was coupled out in the surface normal direction enabling single-mode oscillation over a large area.

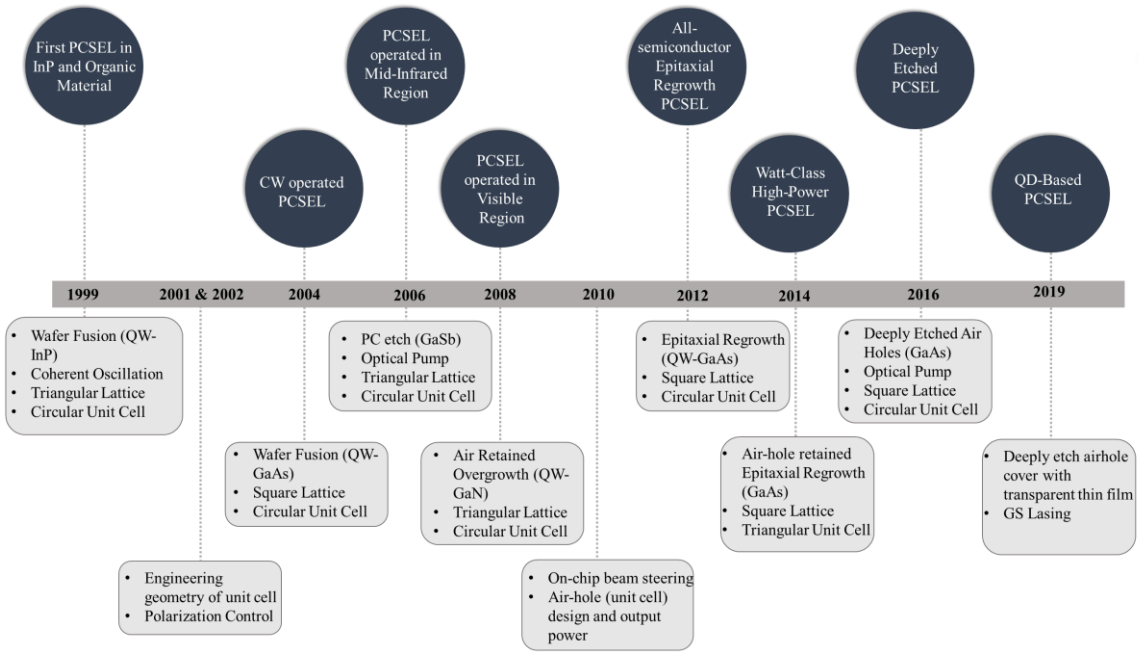

Figure 5.1: Progress of PCSEL Technology.

Following the initial demonstration of the PCSEL, a variety of functionalities and concepts have been demonstrated including the control of the wavelength, polarisation, and beam shape by manipulating the electromagnetic field distribution in the lasing plane. The first demonstration and early research on PCSELs were performed by using a triangular lattice PC atom shape [22], [23]. Towards a high-power single-mode operation with controllability, relevant research of PCSELs was thereafter shifted to photonic crystals with a square lattice structure [24], [25]. The first continuous-wave operated PCSEL was reported in 2004 [26]. To achieve stable 2D coherent oscillation of PCSELs with square lattice PC structure, it is especially important to form a PC with a larger refractive index contrast. In 2010, Iwahashi

et al. studied the air-hole shape of photonic-crystal lasers in the vertical direction to increase the radiation constant for surface emission to achieve high-power [27]. In the same year, new functionality of the PCSEL was introduced by Y. Kurosaka *et al*. to obtain on-chip controllability of the beam direction which opens possible applications in autonomous vehicles [2]. In 2016, the first optically pumped QD-based PCSEL was discovered by deeply etching PC air holes [28]. By depositing conductive layer such as ITO allows the electrical injection of QD-PCSELs [31], [30]. Research into PCSELs has been carried out on the different material systems such as GaN [31]-[34], GaAs [35], [36], InP [37], and GaSb [38]-[40] where the wavelength spans the visible to THz region which is shown in Figure 5.2.

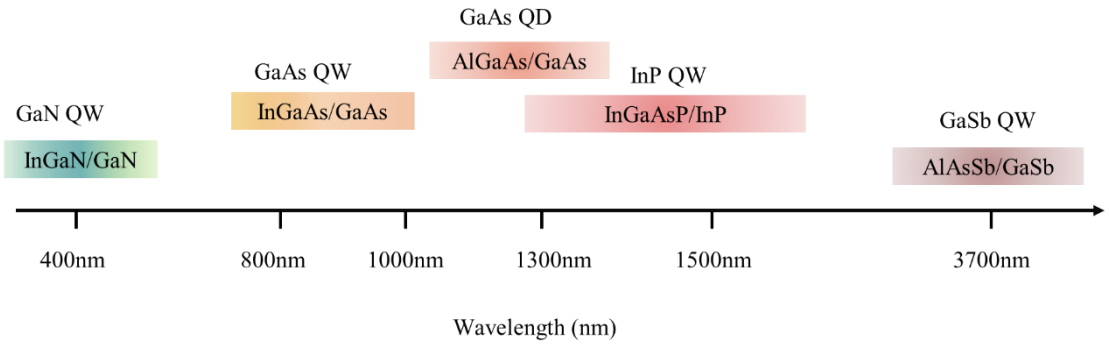

Figure 5.2: Schematic of spectral coverages of different materials for PCSEL.

5.2.2 Photonic Crystal Surface Lasers Operating Conditions

PCSELs are a type of laser that utilises the band-edge effects of 2D PC. At the band edge, the group velocity becomes zero and therefore the light waves propagating in various 2D directions are coupled with one another and 2D stand wave is constructed over a broad area. For the PCSEL to begin lasing, the threshold gain must be greater than the combined effect of internal losses, in-plane and out-of-plane coefficients. This can be defined as

$$g_{th} = \alpha_i + \alpha_{\perp} + \alpha_{//} \tag{5.1}$$

α_i is the internal loss due to the absorption, defects in the materials, or other mechanisms. $\alpha_{//}$ is the in-plane cavity loss, also known as in-plane coupling coefficient. For FP laser the light propagates in the plane of the epitaxial layers and is reflected by parallel-cleaved facets. Therefore, this in-plane coupling is desirable as it allows the efficient transfer of light between the different optical modes within the laser cavity. However, for the PCSEL, the confinement of light in the vertical direction is critical for high-performance laser operation. Therefore, $\alpha_{//}$ can lead to loss of optical power as it allows light to escape the cavity in the direction parallel to the surface and therefore low values of $\alpha_{//}$ are desirable. $\alpha_{\perp}$ is defined as the coupling coefficient between the guided resonance mode (in-plane light) and out-of-plane radiation. The guided mode is the mode that is confined within the photonic crystal

structure, and it is responsible for lasing acting in the PCSEL. The out-of-plane radiation mode is the mode that leaks out of the structure in the vertical direction. A high $\alpha_{\perp}$ value implies a low coupling strength between the guided mode and out-of-plane strength (i.e., low confinement of light in the vertical direction) and thus high loss whereas a low $\alpha_{\perp}$ implies low loss and high confinement of light in the vertical direction. The efficiency of PCSEL is defined by

$$\frac{dP}{dI} = \frac{h\upsilon}{e}\eta_i \frac{\alpha_{\perp}}{\alpha_{\perp} + \alpha_{//} + \alpha_i}\eta_{up} \tag{5.2}$$

where ηi is the internal quantum efficiency η_{up} is the efficiency of useful surface emitting power from device, P is the output power, I is the current. The optimising of α_i , $\alpha_{//}$ and $\alpha_{\perp}$ through the PC region in PCSEL is an active area of research as it holds potential for achieving high-efficiency and high-power surface-emitting lasers for various applications.

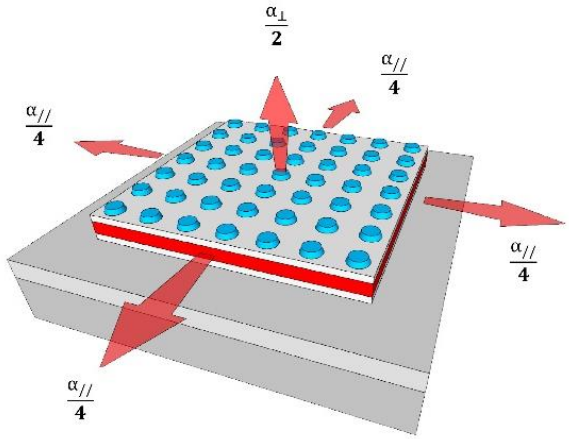

Figure 5.3: Schematic of loss mechanism in PESEL.

5.3 Gaps in Knowledge

Research in the field of PCSELs has been growing rapidly and there has been significant progress made in a variety of material systems with wavelengths ranging from visible to THz by utilising different fabrication methods such as wafer fusion [41], deposition of conducting layer over "PC-slab-on substrate" [42] and epitaxial regrowth [43]. The fabrication of PCSELs using epitaxial regrowth has emerged as a promising method due to the elimination of defects associated with wafer bonding. With the advancements in regrowth techniques, it is now possible to fabricate both void/semiconductor contrast PCSEL [44] and all-semiconductor PCSELs [35] and therefore the use of epitaxial regrowth has become a promising approach. The void/semiconductor PCSEL has been demonstrated the best performance in terms of power and efficiencies [45] due to the presence of voids

providing a high coupling coefficient because of the high refractive index difference between void (n~1) and semiconductor (n~3).

As the gain medium in epitaxially regrown PCSELs, QWs have so far been used universally. QD active media offer a number of advantages. QDs offer extended wavelength of operation as compared to QWs (e.g., 1.3 μm lasers on GaAs substrates), temperature-insensitive operation [6], low threshold current density [46], [47], and feedback insensitivity [48], especially interesting for silicon photonics [49]. Additionally, the ability to utilise both the GS and ES of the QD allows multiple emission wavelengths from one heterostructure [50], with the ES offering both higher saturated gain and direct modulation rates [51]. It has been demonstrated that QD PCSEL can be fabricated utilising deep etching techniques through *p*-cladding [28], in conjunction with the incorporation of transparent contact layer [30]. However, to date, QD PCSEL through epitaxial regrowth method have not been reported in the literature.

In this chapter, epitaxially regrown QD-based PCSELs will be discussed. The choice of the grating period of different devices on the same wafer allows emission at the GS and ES of the QD, 90nm apart in wavelength. The epitaxial re-growth processes are described, and the effect of PCSEL device area, PC atom shape (etch depth, feature size, and corresponding re-grown feature), and crystallographic orientation of the PC on device performance are explored.

5.4 Base Wafer and Regrowth Structure

The base epitaxy structure was grown on GaAs substrate in a molecular beam epitaxy (MBE) reactor by QD Laser Inc, Japan. The schematic and TEM pictures of the QD active region is shown in Figure 5.4. The structure consists of a 300 nm *n*-type GaAs buffer layer followed by 20 nm *n*-type $Al_{0.2}Ga_{0.8}As$, 1440 nm $Al_{0.4}Ga_{0.8}As$, and 20 nm $Al_{0.2}Ga_{0.8}As$ which act as *n*-type cladding layers. This is followed by 8 layers of QD layer and 388 nm of *p*-GaAs. The growth of the active region starts with 60 nm of undoped GaAs followed by 8 layers of InAs QD. The thickness of the InAs layer is 0.8 nm and an undoped GaAs barrier layer (39.2 nm) is inserted between the layers of QD to allow the multiple layers stacks. The emission of the GS and ES of the QD is centred at ~1230 nm and ~1140 nm. The schematic of the base epitaxy structure is shown in Figure 5.5 (a). The PC patterns consisting of periodic air holes were patterned by using EBL and ICP dry etching on the top GaAs layer which is shown in figure b. The details of the fabrication steps are explained in section 2.7. Finally, *p*- AlGaAs cladding layer and a *p*-GaAs highly doped layers were grown by metalorganic vapour phase epitaxy (MOVPE) in collaboration with III-V Epi Ltd. The schematic of the PCSEL after

regrowth is shown in Figure 5.5 (c). Following regrowth, a mesa is etched to a depth of 1000 nm using a combination of photolithography and dry etch process to electrically isolate the devices. This depth was chosen to maximise electrical isolation, but not provide a facet to the in-plane optical mode. The mesa size ranges from 200 μm^2 to 800 μm^2 with a step of 200 µm. A SiO_2 passivation layer was then deposited across the wafer with a contact window etched. This was followed by metal deposition of *p*-type and *n*-type contact with an emission aperture defined at the bottom *n*-contact. Fabrication was then completed by the deposition of a thick bond pad on the top surface. Figure 5.6 shows the schematic of PCSEL device.

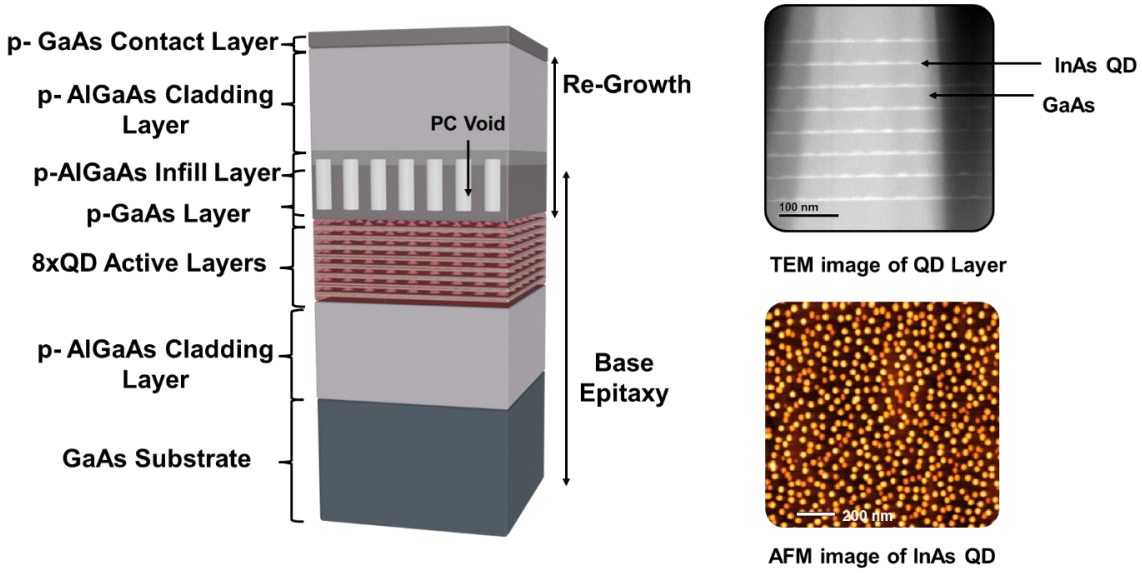

Figure 5.4 : Schematic of the 8 layers of QDs active region. TEM image showing the QD layers and AFM image showing the high-density QD.

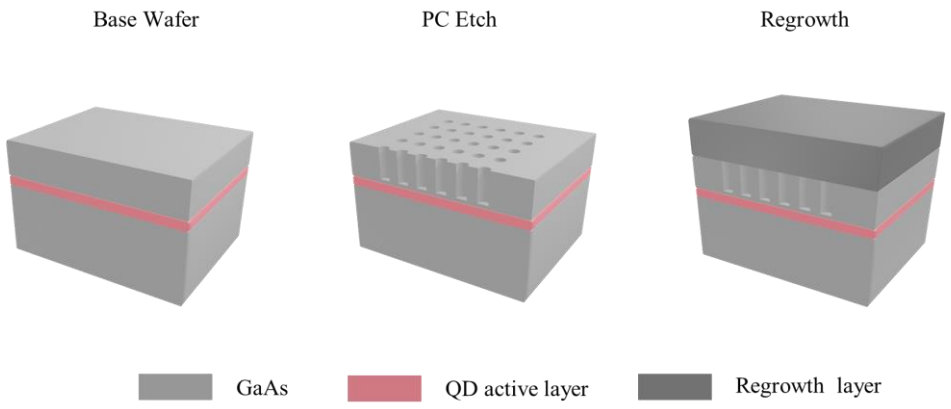

Figure 5.5: Schematic of the (a) base wafer (b) base wafer after PC etched (b) regrown PCSEL structure.

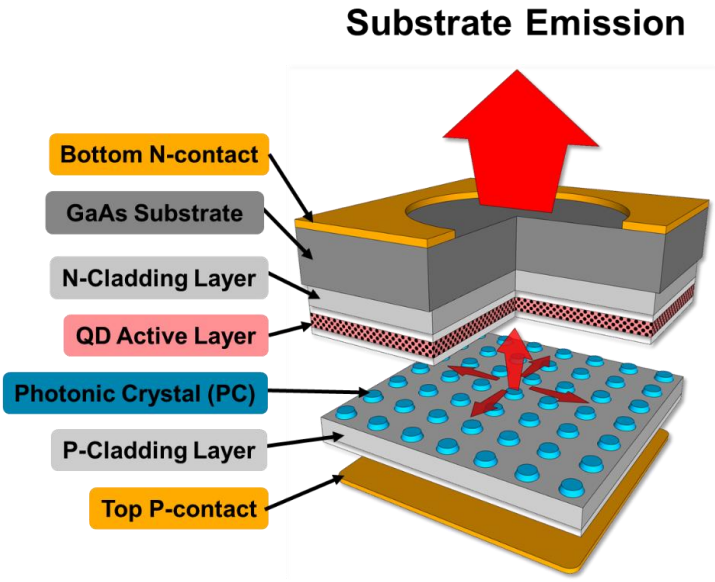

Figure 5.6: Schematic diagram of PCSEL.

5.5 Measurement and Analysis

This chapter focuses on the effect of PCSEL design parameters on the electrical and optical performance of the devices. In each section one design feature is changed. The design features include as follows.

- Changing the grating period to allow the GS and ES emission of monolithically integrated QD PCSELs
- Changing the circular atom radius of the PC (0.2 and 0.4 r/a)
- Changing the PC etch depth (300 nm and 400 nm)
- Changing the atom shape of the PC (Circle and Triangle)
- Changing the PC orientation (90-degree and 45-degree)
- Varying the device mesa size for power scaling

In the evaluation and comparison of different devices, it is important to consider the fabrication process and the number of good devices obtained across the wafer. For instance, the selection of specific devices for comparison may depend on the quality of the fabricated devices. This can involve choosing devices of a particular size and grading period, or with specific etch depths, based on the yield of good devices obtained during fabrication. As such, the selection of particular devices for comparison may not always be based on a uniform set of parameters, but rather on the availability of good quality devices from the fabrication process. For example, in the comparison of different devices, a device size of 200 μm and a PC etch depth of 600 μm may be chosen, based on the quality of the devices obtained during fabrication. This underscores the importance of yield optimization during the fabrication

process and highlights the need to carefully consider the quality of the devices when making comparisons between different devices.

5.5.1 Two States Lasing

In this section, novel epitaxially regrown QD-based PCSEL devices with both GS and ES lasers monolithically integrated on one wafer will be discussed. Since the lasing wavelength of the PCSEL is related to the period of the PC as the period of PC is ~λ/n where n is the refractive index, designing the lattice period of PC to match with GS and ES wavelength of the QD will be able to achieve the two states lasing using just one epitaxial structure. The designed lattice period for ES lasing is 338 nm with a target lasing wavelength of ~ 1150 nm. However, the patterning of the EBL from wafer to wafer makes a slight difference in the lattice period and has a variation of ± 5 nm. The targeted GS lasing wavelength is 1230 nm with a lattice period of 372 nm. The PC patterns are circular air holes on square lattices and the PC etch depth 400 nm. Square lattice periods of 372 nm and 338 nm with circular atom shapes are patterned to emit the lasing wavelength around the gain peak of the GS and ES of QD. The r/a is ~ 0.2 r/a. After the regrowth, a mesa size of 400 µm x 400 µm is etched to an etch depth of 1000 nm. The details of the fabricated device parameters is shown in Table 5-1. Figure 5.7 shows SEM pictures of the PC regions with two different grating periods before the regrowth.

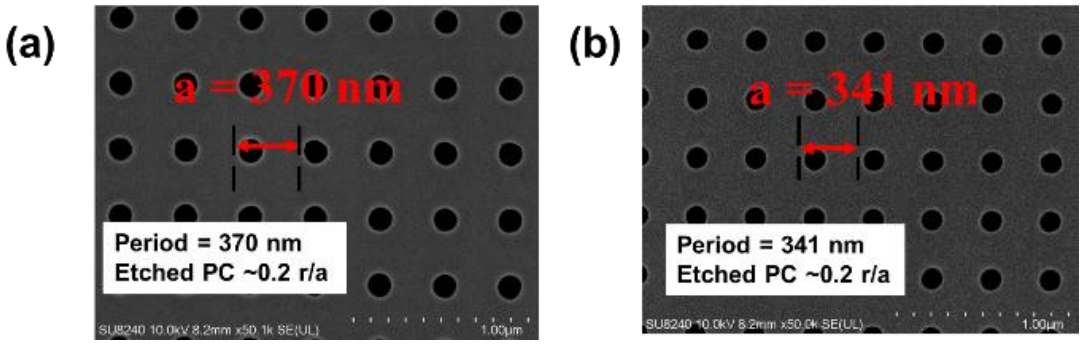

Figure 5.7: Plan view SEM images of a photonic crystal with circular air holes with (a) a period of 370 nm aiming GS lasing (b) period of 341 nm aiming ES lasing.

Table 5-1: PC design parameters of fabricated devices.

Device No.	r/a	Lasing Wavelength	Lattice Period	PC Etch Depth	Mesa Area
Device A	~ 0.2 r/a	ES	341 nm	~ 400nm	400 µm x 400 µm
Device B	~ 0.2 r/a	GS	370 nm		

The current-voltage (IV) relationship of the two devices from the same wafer is plotted in Figure 5.8. Both devices have the same turn-on voltage of 1.05 V with a series resistance of 1.2 ± 1 Ω. Figure 5.9 shows the LI characteristics of PCSEL with periods of 370 nm (GS lasing) and 341 nm (ES lasing). The threshold currents are 1.1 A and 1.6 A with a slope efficiency of 13.4 mW/A and 9.5 mW/A for GS and ES, respectively. The threshold current of ES is higher than that of the GS because of the higher degeneracy of the ES and the need to saturate the GS gain to achieve ES lasing. The maximum output power for GS is 12 mW at 1.8 A and for ES is 15 mW at 3 A, where the output power is limited by the drive current and is underestimated by a factor of around 3 because of the substrate absorption and reflection at the substrate/air interface. Figure 5.10 shows the sub-threshold electroluminescent spectrum showing the GS and ES emission and lasing spectra of GS and ES. The blue line indicates the GS leasing with a peak wavelength at ~1230 nm and the red line indicated the ES lasing with the peak wavelength of ~1141 nm at 2A.

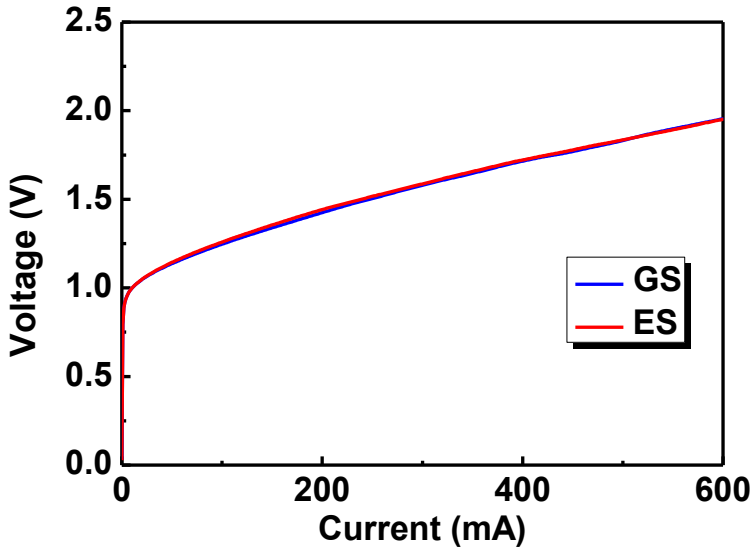

Figure 5.8: Current-voltage relationship of ground state and excited state devices.

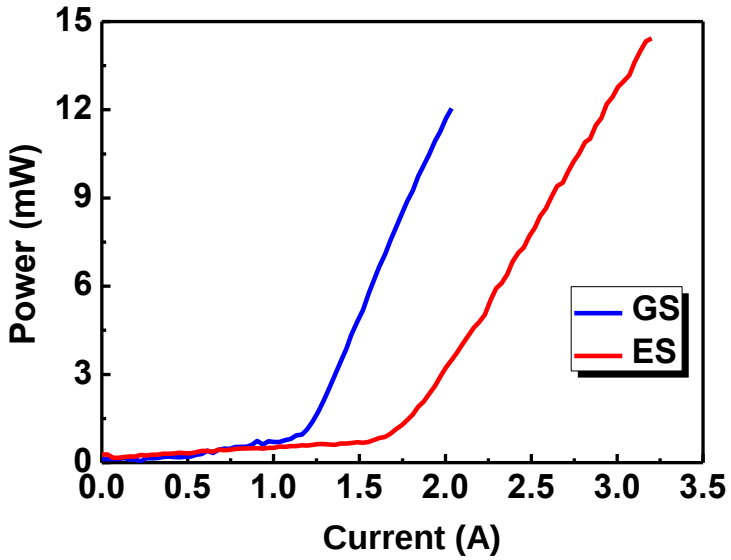

Figure 5.9: Current-light output power relationship of ground state (blue) and excited state (red) emission devices.

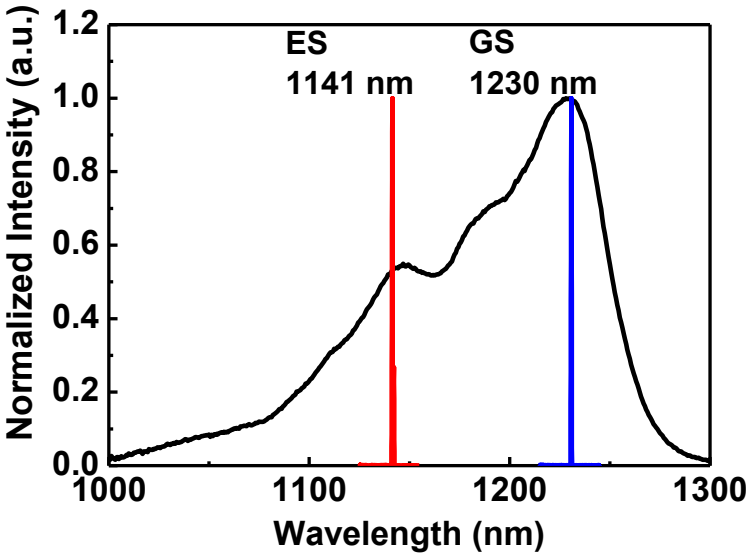

Figure 5.10: Lasing spectra at 2A, superimposed on the spontaneous emission spectra at 0.5A. Both are obtained under quasi-CW conditions at room temperature.

5.5.2 Effect of Circular Atom Radius

The circular atom unit cell of the PCSEL is schematically shown in Figure 5.11 where the etched region effective refractive index (n_b) embedded at each lattice point in an un-etched region of effective index (n_a). Previous simulation work [53] has shown an increase in coupling coefficient with increasing circular atom radius. In this section, the experimental

results of effect of circular atom radius on the lasing performances of the epitaxially regrown QD-based PCSEL will be discussed.

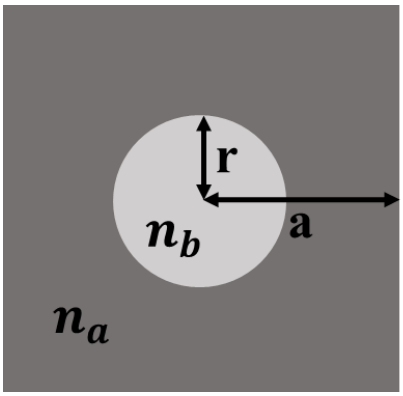

Figure 5.11 The photonic crystal unit cell that is to be considered in this chapter. r is the radius of the circular atom, a is the lattice period, n_a is the effective mode index of the slab, and n_b is the effective mode index of the atom.

The PC patterns are circular air holes with square lattices and the PC etch depth is 400 nm. The r/a of 0.2 and 0.4 are chosen by changing the diameter of the circle while keeping the same lattice period because these r/a have the highest coupling strength [52]. The targeted r/a is 0.2 and 0.4 r/a, there is a slight difference between the designed and actual fabricated values due to the fabrication process such as e-beam lithography and etch profiles of the circular air holes. Square lattice periods of ~ 344 ± 4 nm with circular atom shapes are patterned to emit the lasing wavelength around the gain peak ES (~1150 nm) of the QD. After regrowth, a mesa size of is 600 μm x 600 μm is etched to an etch depth of 1000 nm. The details of the fabricated device parameters are shown in Table 5-2.

Table 5-2: PC design parameters of fabricated device.

Device No.	Fabricated r/a	Fabricated Diameter	Fabricated Lattice Period	Etch Depth	Mesa Size
Device C	~ 0.19 r/a	130 nm	340 nm	~ 424nm	600 μm x 600 μm
Device D	~ 0.35 r/a	244 nm	348 nm	~ 420 nm	

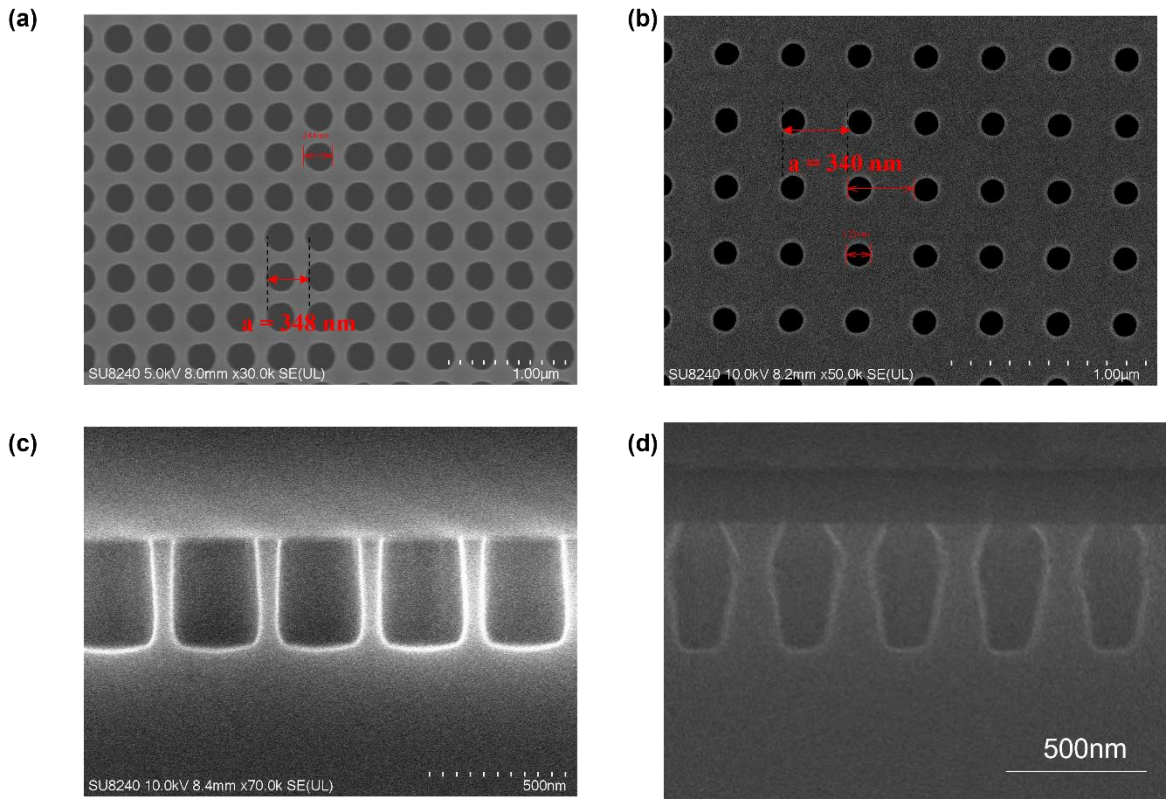

Figure 5.12: Plan view SEM images of circular atom with square lattice (a) large r/a (b) small r/a before regrowth. Side view SEM images of (c) large r/a (d) small r/a before regrowth.

Figure 5.12 shows SEM pictures of the plan and side view of the PC regions before regrowth. The difference in etch profiles between two devices is attributed to the dry etch processes such as chamber temperature or the small diameter of the circular air hole. This causes a significant difference in void shapes between the two devices after the regrowth process. The SEM images of the PC regions after the regrowth process are shown in Figure 5.13.

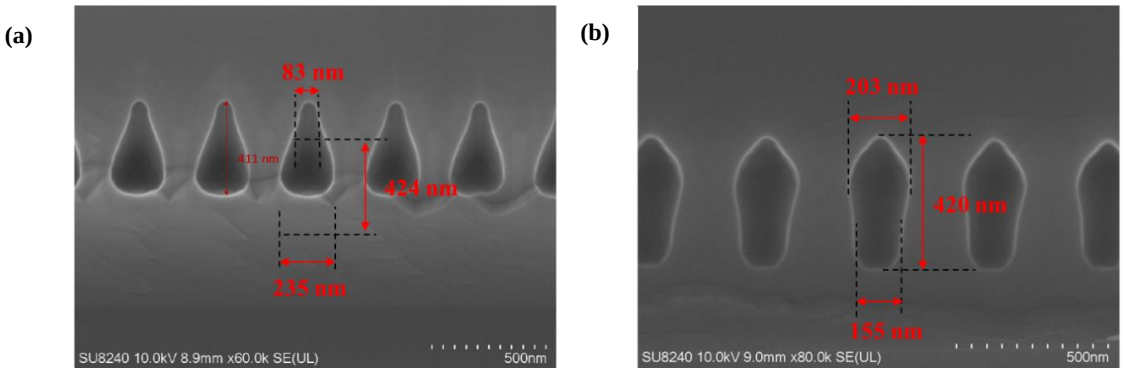

Figure 5.13: Side view SEM images of (a) large r/a (b) small r/a after regrowth.

The current-voltage (IV) relationship of the two devices is plotted in Figure 5.14. Both devices have the same turn-on voltage of 0.9 V with a series resistance of 1.4 ± 1 Ω. A slight

difference in series resistance may be related to a device-to-device variation such as cleaning steps during the fabrication process or may be the area of the current flow from anode to cathode (i.e., current can only flow through semiconductor area avoiding the void area and so the larger void, the smaller current can flow and hence high resistance). In the presence of voids, the area of the current flow is restricted, and this can lead to an increase in the series resistance of the device. In other words, the larger the void, the smaller the current flow, resulting in higher resistance.

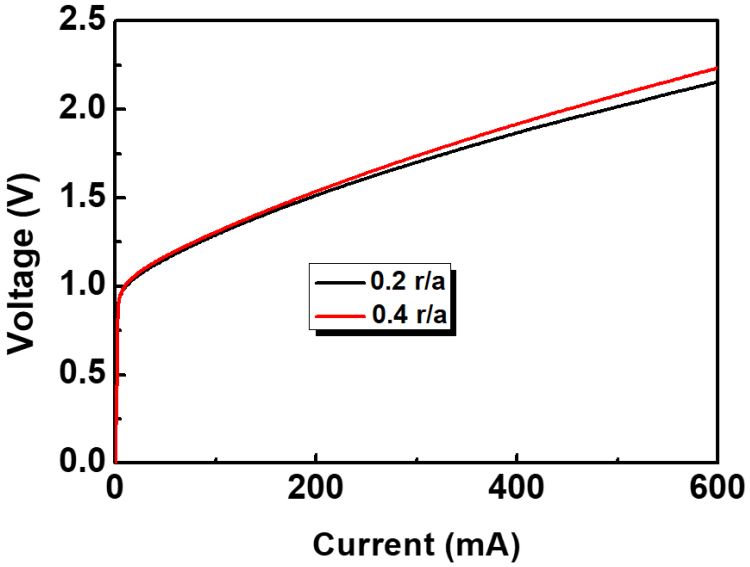

Figure 5.14: Current-voltage relationship of two r/a devices with different void geometries.

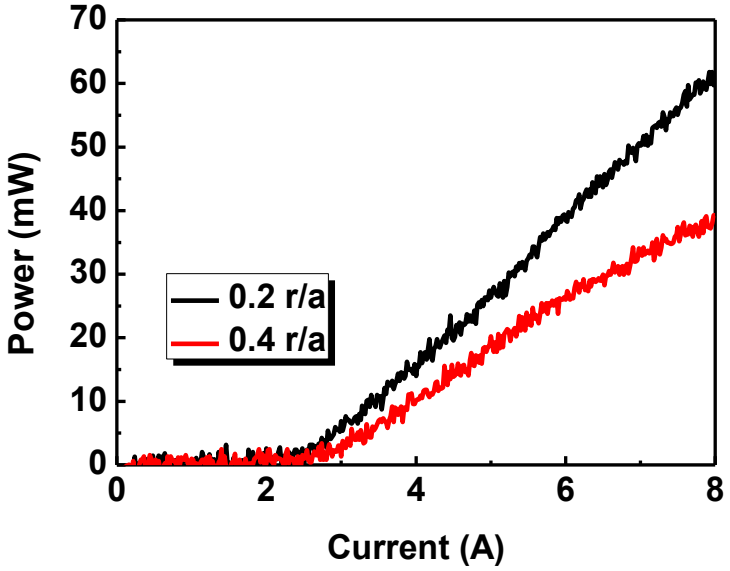

Figure 5.15: Current-light output power relationship of two r/a devices with different void geometries.

The current-power (LI) measurement is shown in Figure 5.15. The threshold currents for devices C and D are 2.6 A and 2.9 A with slope efficiencies of 11.35 mW/A and 7mW/A, respectively. The small r/a (device A) has a slightly lower threshold current. The maximum output power at 8A (current limit) is 40 mW and 60 mW for devices C and D, respectively. The previous simulation work showed that the larger r/a should give a higher output power due to the higher coupling coefficient [53]. However, the experimental results from two r/a devices showed that the smaller r/a has a higher output power than the larger r/a. One thing to note here is that the void shapes (sizes) of the two devices are totally different shapes and therefore the effective refractive indexes from these two will be different.

The lasing spectra for both devices are shown in Figure 5.30. Device C and D have peak lasing wavelength of 1147 nm and 1151 nm, respectively. This ~ 4 nm difference in peak lasing wavelength is attributed to the difference in void shape (and therefore difference in effective refractive index) or a slight difference in the period of the lattice due to device-to-device variation. It has shown that the change in the void shape can also affect the lasing wavelength as well as the resistance of the devices [33].The lasing spectra is measured at 2A. In order to fully analyse this data, band-structure measurements are required to determine the zone centre frequencies in order to determine the PC coupling coefficients [54]. This is due to the very different PC atom shapes. Then, the in-plane loss may be determined through coupled-mode theory [55] or Monte-Carlo simulation [56]. This would then allow the comparison of the two threshold currents and slope efficiencies.

5.5.3 Effect of Atom Shape

The engineering the atom shape provides not only the corresponding light emitting controllability [55] but also high-power operation [26] . In this section, the effect of circular and triangular air holes on the optical characteristics of the QD-PCSEL devices will be discussed. The circle and triangle air holes with square lattice are selected for comparison due to the simplicity of the designs, fabrication, and regrowth.

Plan view and side view SEM images of the PC before regrowth are shown in Figure 5.16. A cross-section of the triangular atom shape after the regrowth is not carried out and therefore the exact shape, width and depth are unknown. Therefore, the void shape is ignored when comparing of the optical performance of two devices. McKenzie et al. conducted a study on void engineering in epitaxially regrown GaAs QW-based photonic crystal surface-emitting lasers (PCSELs) using metalorganic vaporphase epitaxy regrowth [56]. The study focused on two different void geometries, cylindrical pill-like shape and ellipsoidal in shape, with varying sizes and heights due to the different in etch profiles before regrowth. The

cylindrical voids were found to be bound by near-vertical sidewalls and had a diameter and height of 50 nm and 120 nm, respectively, while the ellipsoidal voids had a diameter of 110 nm and a height of approximately 155 nm. The results showed that the cylindrical voids were situated above each grating feature and played a significant role in the coupling coefficient for the laser. In contrast, the ellipsoidal voids were deeper and closer to the active region, resulting in a better performance for the laser. From this, we can see that the difference in void shape have impact on device performance. In this work, the void shape are “raindrop shape” and “ waisted ellipsoid shape” due to the etch profile . It is challenging to directly compare the devices in this work with those reported in the McKenzie paper due to the difference in the active region material as well as void shape.

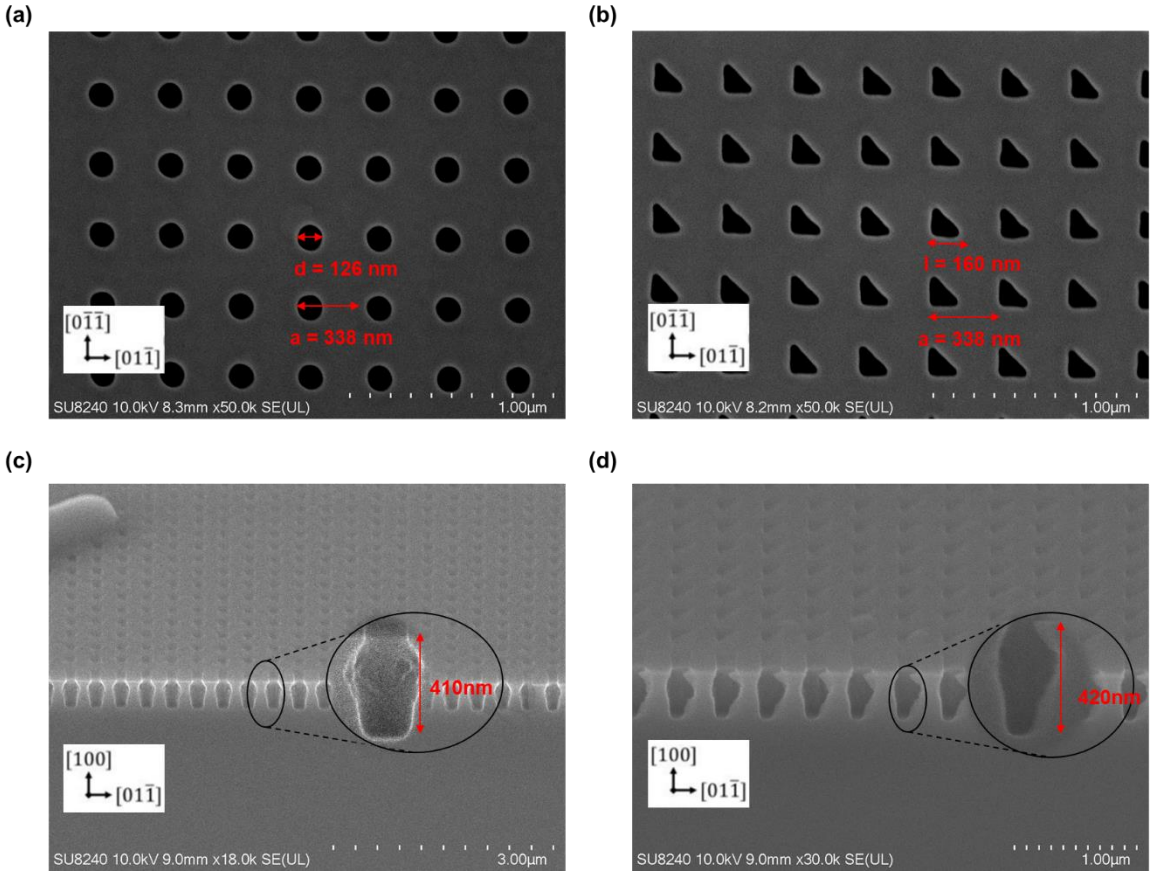

Figure 5.16: Plan view SEM images of (a) circular atom shape (b) triangular atom shape before regrowth. Side view SEM images of (c) circular atom shape (d) triangular atom shape before regrowth.

Table 5-3: PC design parameters of fabricated devices.

Device No.	Atom shape	Etch depth	Fabricated r/a or l/a	Fabricated Diameter or length	Fabricated Lattice period
Device G	Circle	~ 400 nm	~ 0.2 r/a	~ 124 nm	~ 338 nm
Device H	Triangle	~ 400 nm	~ 0.5 l/a	~ 140 nm	~ 338 nm

The IV characteristics of devices G and H are shown in Figure 5.17. The identical turn-on voltage of 1V for both devices and the series resistances are 1.5 Ω and 1.6 Ω for devices G and H, respectively.

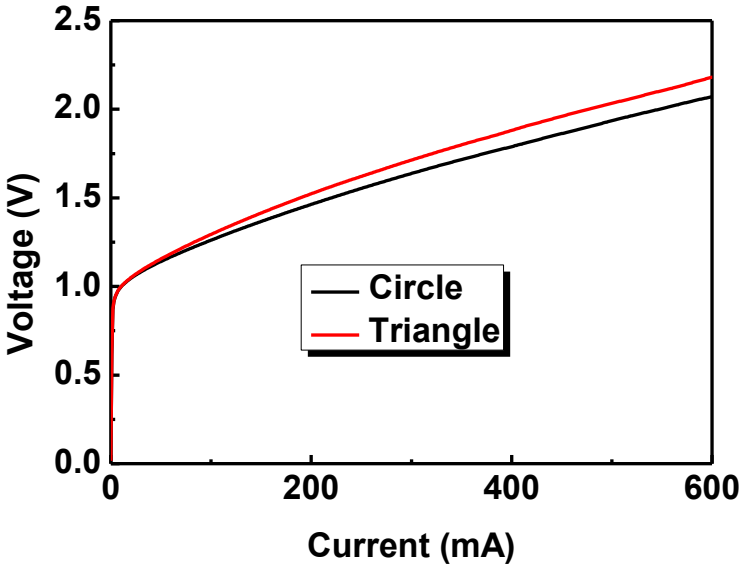

Figure 5.17: Current-voltage relationship of two atom shape devices.

Figure 5.18 shows the LI characteristics. The threshold currents are 0.6 A and 1.8 A with a slope efficiency of 4.2 mW/A and 4.4 mW/A for devices G and H, respectively. The triangular atom shape PCSEL (device H) has higher threshold current as expected due to the asymmetry shape lead to the higher out-of-plane loss. A very high current cannot be injected because of the smaller mesa area of the device. The severe over current can lead to localized heating and can cause contact damage or the laser diode no longer functions properly. Therefore, maximum power at the maximum current injection of 2.5 A is 3 mW and 6 mW for triangular and circular atom shapes. The triangular atom shape has lower output power due to the limitation of current but a slightly higher slope efficiency. The increase in the current injection area and high current may give higher output power compared to a circular

atom. A full analysis of the operating characteristics again requires significant further work in terms of determining microscopic in-plane scattering coefficients and associated macroscopic device loss parameters. The lasing spectrum of both devices is shown in Figure 5.19. The peak wavelength of the spectrum is 1151 nm and 1152 nm for device G and H, respectively. The lasing spectra is measured at 2A. There is a ~ 2 nm difference in lasing wavelength which may be attributed to the different effective refractive index of the devices.

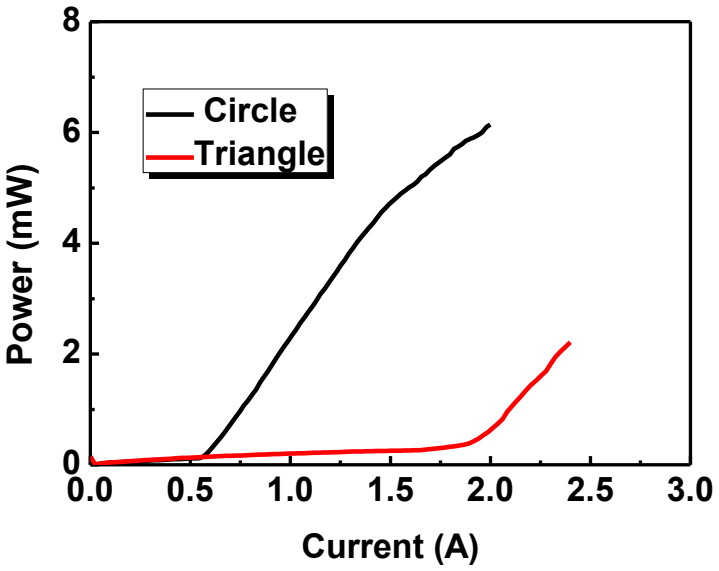

Figure 5.18: Current-light output power relationship of two atom shape devices.

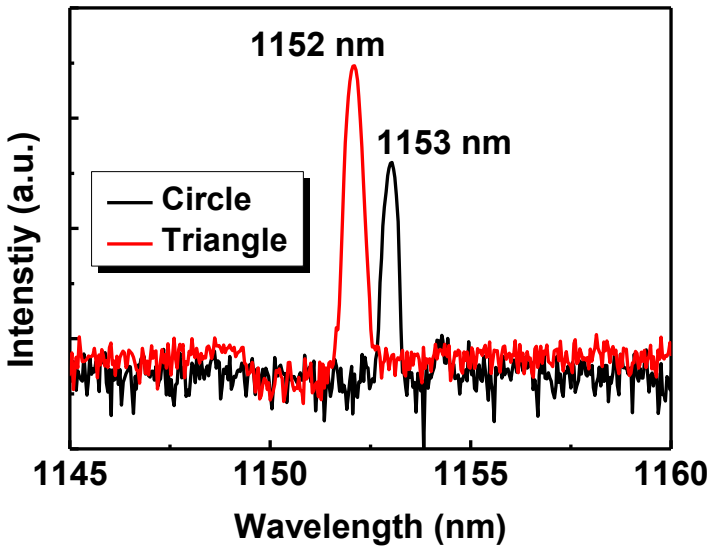

Figure 5.19 : Lasing spectra of two atom shapes devices at 2A. Both are obtained under quasi-CW conditions at room temperature.

5.5.4 Effect of Photonic Crystal Atom Crystal Orientation

The change in the symmetry of the air holes can control the coupling coefficient and the in-plane electric and magnetic field distribution [57]. The symmetry of the PC can be changed by changing the atom shape or the rotation/orientation of the atom shape. In this section, the orientation of the circle and triangle atom shape will be considered.

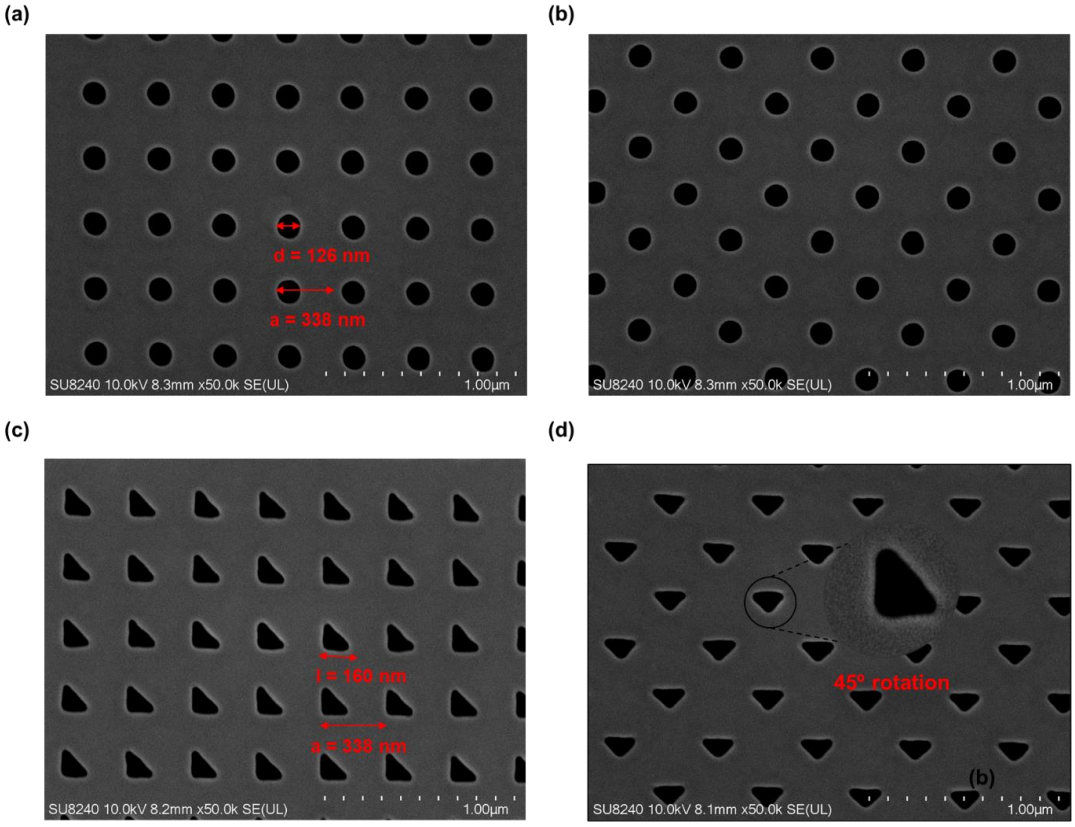

Figure 5.20: Plan view SEM images of (a) 90-degree circular atom (b) 45-degree circular atom (c) 90-degree triangular atom (d) 45-degree triangular atom.

Table 5-4: PC design parameters of fabricated devices

Device No.	Atom shape and Orientation	Etch depth	Fabricated r/a or l/a	Fabricated Diameter or length	Fabricated Lattice period
Device G	Circle (90 and 45-degree)	~ 400 nm	~ 0.2 r/a	~124 nm	~338 nm
Device H	Triangle (90 and 45-degree)	~ 400 nm	~ 0.5 l/a	~140 nm	~338 nm

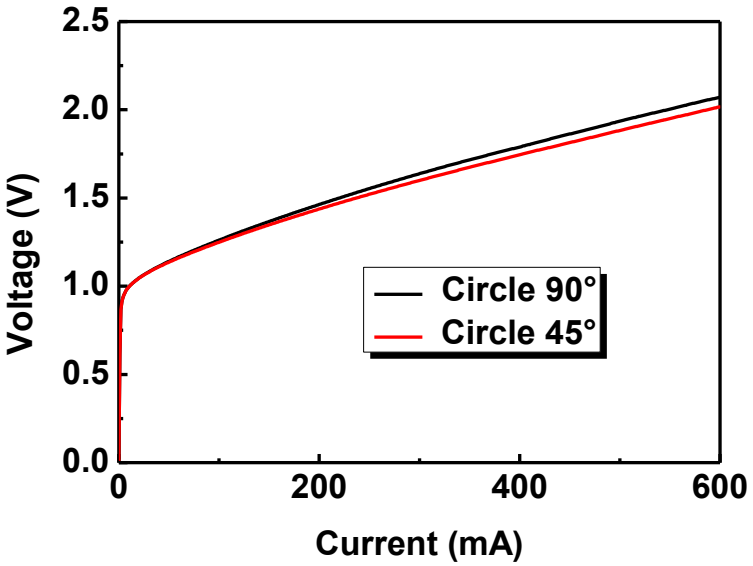

Figure 5.21 : Current-voltage relationship of circular atom with 90 and 45-degree orientation devices.

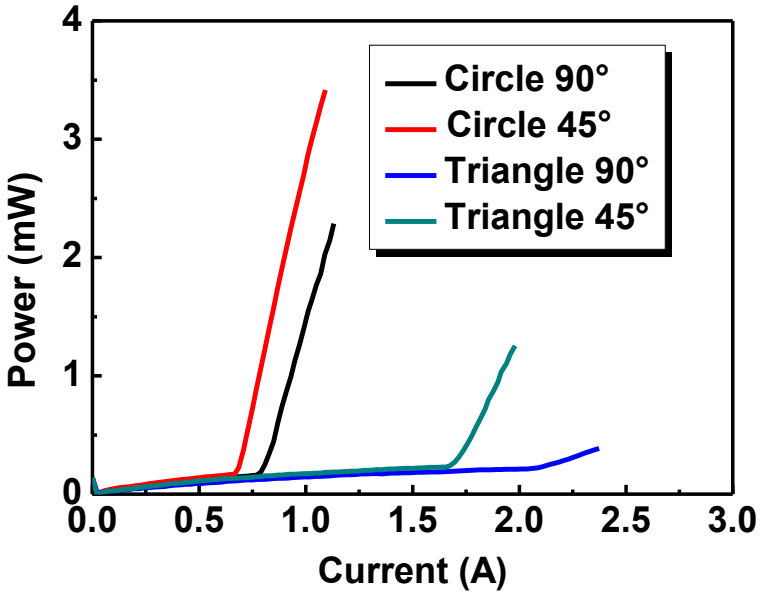

Figure 5.22 : Current-light output power relationship of circular and triangular atom with 90 and 45-degree orientation devices.

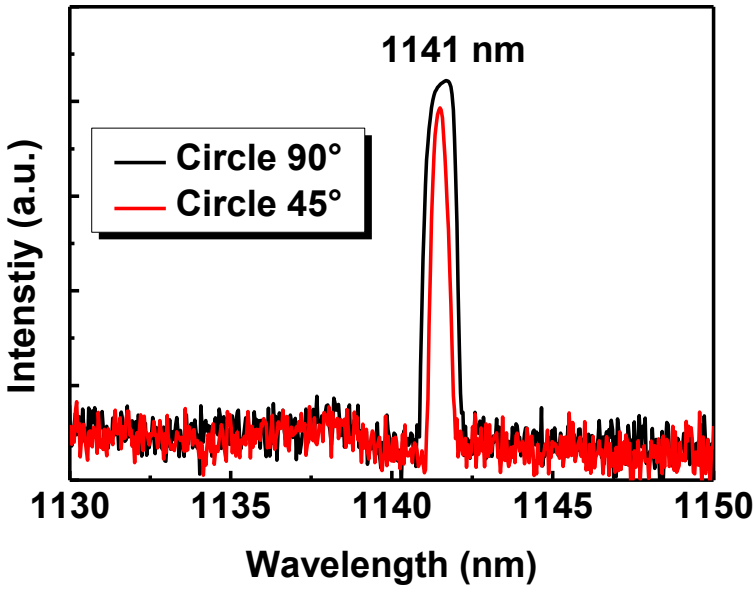

Figure 5.23 : Lasing spectra of circular atom with 90 and 45-degree orientation devices at 2A. Both are obtained under quasi-CW conditions at room temperature.

The PC patterns are circular and triangular air holes with square lattices and the PC etch depth 400 nm. The air holes are aligned to the substrate crystallographic orientation and rotated by 45 degrees. After the regrowth, a mesa size of is 600 μm x 600 μm is etched to a mesa etch depth of 1000 nm. Square lattice periods of ~ 334 nm with circular atom shapes are patterned to emit the lasing wavelength around the gain peak ES (~1140 nm) of QD. The r/a is ~ 0.2 r/a for circular atom and l/a is ~ 0.5 l/a for triangular atom. Plan view SEM images of the PC before regrowth are shown in Figure 5.20. TEM micrograph has not yet been obtained for these structures. The details of the fabricated device parameters are shown in Table 5-4.

The current-voltage relation of the circular atom shape orientation is shown in Figure 5.21. The same turn-on voltage of 1 V with a series resistance of ~ 1.5 Ω for both devices I_1 and I_2. The current-light output power relationship of the circle and triangular atom with 45 and 0-degree rotation is shown in Figure 5.22. The threshold current of devices I_1 and I_2 are 0.8 and 0.6 A with slope efficiency of 6.5 mW/A and 8 mW/A, respectively. For devices J_1 and J_2, the threshold currents are 2 A and 1.6 A with a slope efficiency of 0.57 mW/A and 3.77 mW/A, respectively. In both atom shapes, the 45-degree orientation devices have a slightly lower threshold current.

The lasing spectrum of the circular atom shape with two different orientations is shown in Figure 5.23. The peak lasing wavelengths are 1141 nm for both devices. The lasing spectra is measured at 2 A. The TEM/SEM images of the 45-degree rotation are not carried out and therefore the void shape cannot be compared. However, since the peak lasing wavelengths are the same, the effective refractive index for both devices maybe the same, and hence the void shape and size maybe the same for both orientations. Further work to analyse the structure of the PC, and the band-structure and macroscopic scattering properties of these structures is required.

5.5.5 Varying Area of Photonic Crystal Surface Emitting Lasers

In this section, the effect of PC region mesa area variation on the electrical and optical characteristics will be discussed. The PC patterns are circular and triangular air holes with square lattices and the PC etch depth 400 nm. Square lattice periods of ~ 340 nm with circular atom shapes are patterned to emit the lasing wavelength around the gain peak ES (~1150 nm) of QD. The r/a is 0.19 r/a for circular atom and l/a is 0.47 l/a for triangular atom. After the regrowth, a mesa size ranging from 200 μm^2 to 800 μm^2 with a step of 200 μm is etched with a mesa etch depth of 1000 nm.

Figure 5.24 and Figure 5.25 presents the IV characteristics for different devices size of PCSELs for circular and triangular atom shapes, respectively. A slight increase in turn-on voltage and the series resistance is observed with decreasing the device size. This behaviour occurs in both circular and triangular atom shapes. The contact resistance, which is main factor for series resistance of the device, is a measure of the ease with which current can flow across the metal-semiconductor interface (and the area of semiconductor). Therefore, reducing the contact area can increase the resistance value. The resistance value is decreased with increasing the area of the PCSEL.

The LI characteristics of the devices are presented for circular and triangular PC shapes in Figure 5.26 and Figure 5.27, respectively. The threshold current density is decreased when the device size increase. This may be attributed to the effect in small devices as the slightly higher resistance or the thermal effect may not be easily extracted compared to the devices with a larger area. Moreover, the scattering losses related to mesa sidewall roughness may be serious in the smaller area devices. Lasing occurs when the gain overcomes these losses such as scattering loss. These losses in the small area are higher and therefore higher current density is needed to overcome the total loss and consequently the threshold current density is higher.

The lasing spectrum of the various device size is shown in Figure 5.28 and Figure 5.29 for circular and triangular shape respectively. The peak wavelength for the circular atom shape for various device size is 1151 nm and for the triangular atom shape is 1152 nm.

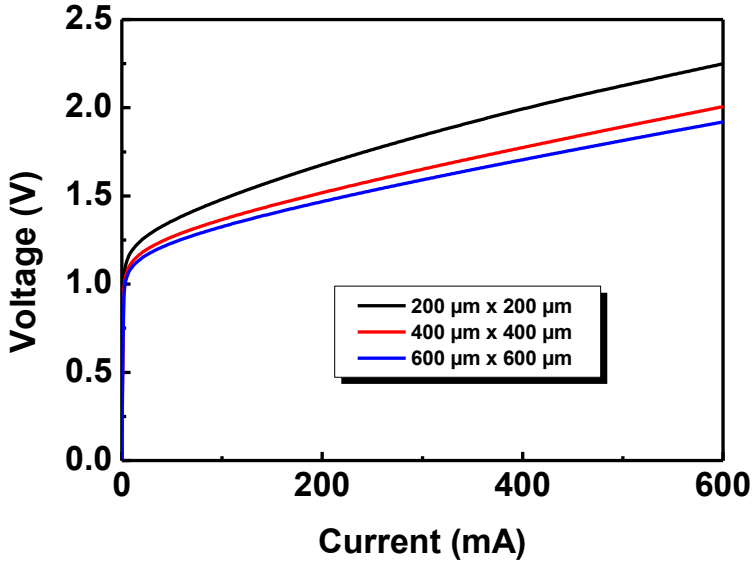

Figure 5.24 : Current-voltage relationship of vary mesa area of circular atom shape PCSEL.

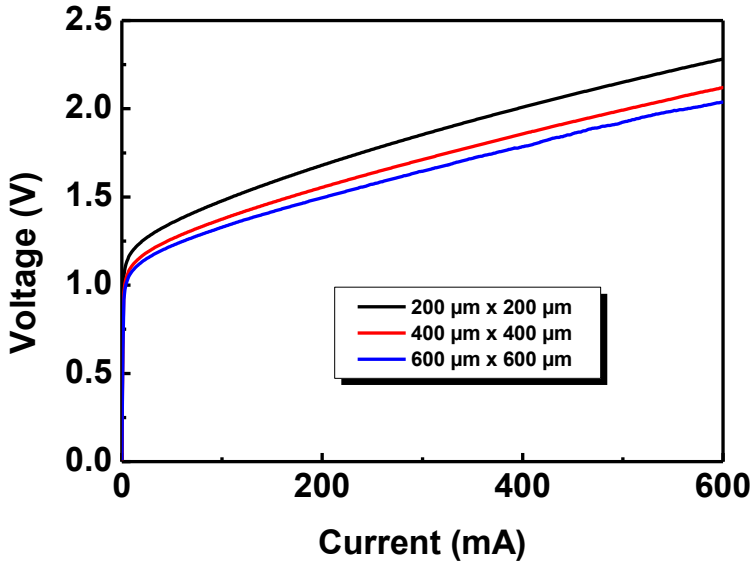

Figure 5.25 : Current-light output power relationship of vary mesa area of triangular atom shape PCSEL.

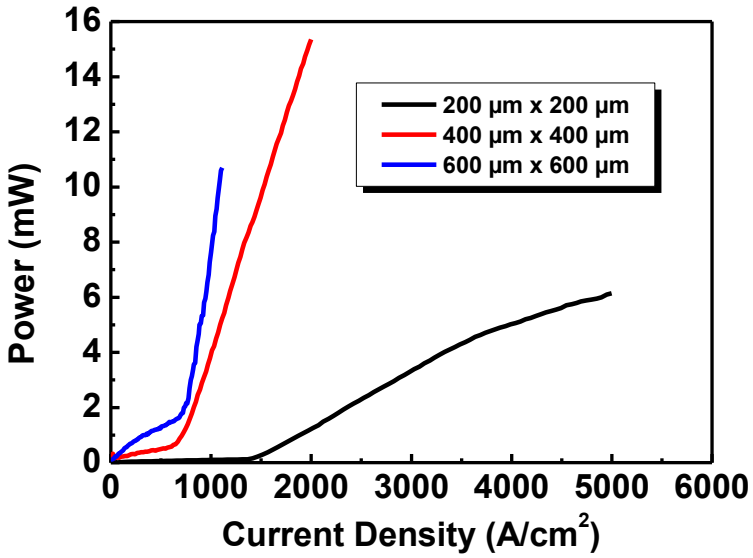

Figure 5.26: Current-light output power relationship of vary mesa area of circular atom shape PCSEL.

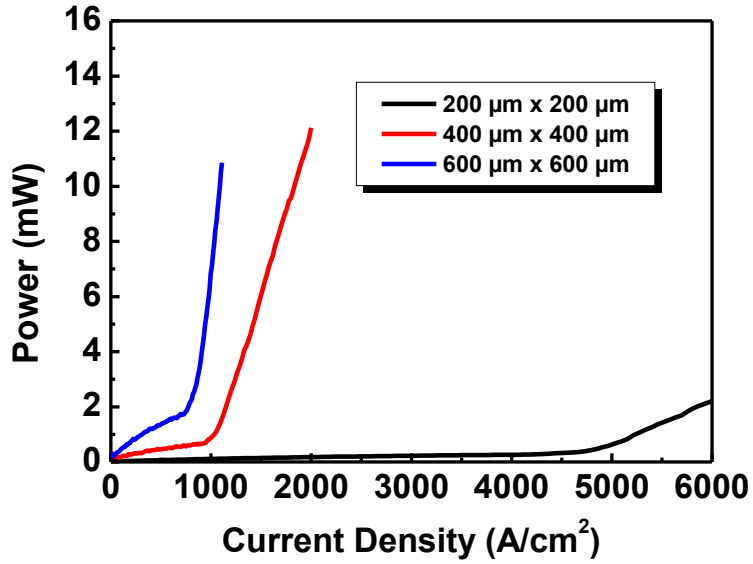

Figure 5.27: Current-light output power relationship of vary mesa area of triangular atom shape PCSEL.

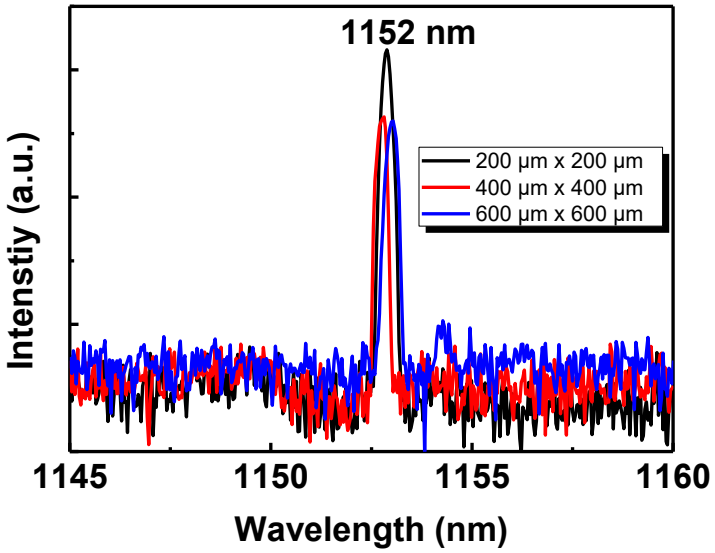

Figure 5.28 : Spectral power of vary mesa area of circular atom shape PCSEL, obtained under quasi-CW conditions and with a 0.1 nm bandwidth resolution. Spectra obtained at 2A.

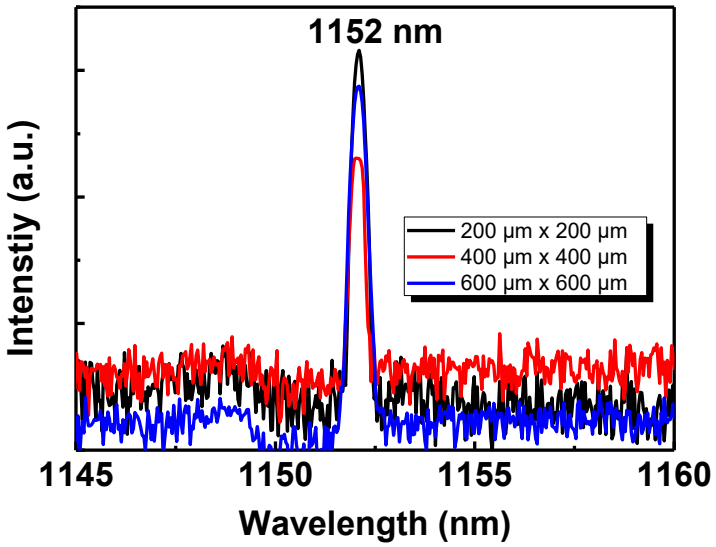

Figure 5.29: Spectral power of vary mesa area of triangular atom shape PCSEL, obtained under quasi-CW conditions and with a 0.1 nm bandwidth resolution. Spectra obtained at 2A.

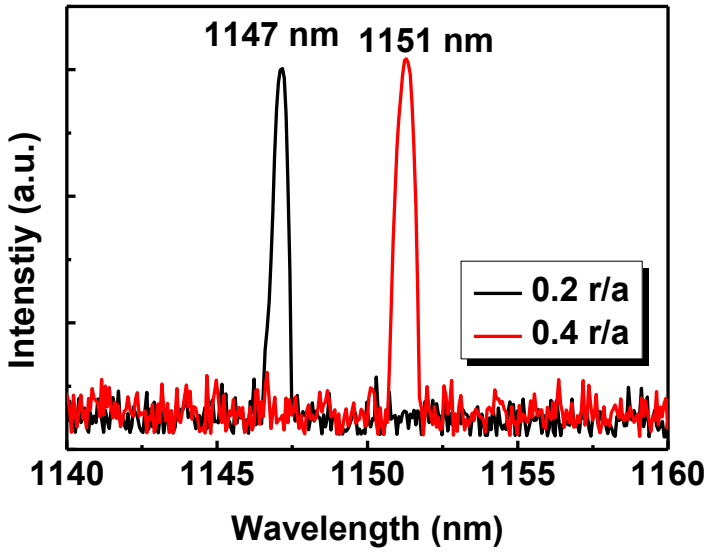

Figure 5.30 : Spectral power of two r/a devices, obtained under quasi-CW conditions and with a 0.1 nm bandwidth resolution. Spectra obtained at 2 A.

5.6 Conclusion

In this chapter the characterisation of PCSEL with varying PC structures has been discussed. Since the lasing wavelength in a PCSEL is defined by the grating period of PC and careful design of these grating periods allows lasing from neighbouring devices at the GS (~1230 nm) or ES (~1140 nm) of the QD, 90 nm apart in wavelength with threshold current of 1.1 A and 1.6 A, respectively. The effect of PC structure including atom radius, etch depth, atom shape and orientation on lasing performance was studied. The smaller r/a value have higher slope efficiency than that of larger r/a which may be attributed to the different void shape and size. Two PC etch depth of 300 nm and 400 nm were compared and the deeper etch depth has higher output power which is attributed to higher in-plane PC coupling and higher slope efficiencies due to a more suitable PC height and minimal distance to the active region. It was known that changing the PC atom air hole (shape or orientation) can improve the lasing performances as it can break in-plane symmetry and increase out-of-plane (surface) emission. Two atom shapes (circular and triangular) are compared. The triangular atom shape has lower output power due to the limitation of current but a slightly higher slope efficiency. The increase in the current injection area and high current may give higher output power compared to a circular atom. At last, PC mesa area variation was studied, and it has been observed that $\alpha_{//}$ is decreased with increasing device size, where for an infinitely large PCSEL these would be zero. In line with expectations, the lower threshold current density

is achieved with increasing device size which is attributed to low $\alpha_{//}$ with higher slope efficiencies.

5.7 Future Work

The effect of PC structure on performance of PCSEL optical characteristics (LI and spectrum) was studied in this chapter. The far-field and near-fields of each device could provide interesting information on the effect of coupling strength on the 2D feedback device. To fully understand the effect of atom radius on lasing performance, it would be worthwhile to further investigate the band-structure measurement to identify the zone centre frequencies to determine the PC coupling coefficient. In order to fully understand the effect of PC atom shape on lasing characteristic requires significant further work in terms of determining microscopic in-plane scattering coefficients [58] and associated macroscopic device loss parameters. It would be great to examine the far-field and near-field of varying area of PCSEL to determine the coherence lasing oscillation. To summarise, it would be beneficial to characterise the far-field images as well as the band structure of PC atom shape as it allows to understand more of coupling strength and so on.

Bibliography

[1] M. Imada, S. Noda, A. Chutinan, T. Tokuda, M. Murata, and G. Sasaki., "Coherent two-dimensional lasing action in surface-emitting laser with triangular-lattice photonic crystal structure," *Applied physics letters*, vol. 75, no. 3, p. 316–318, 1999.

[2] Y. Kurosaka, S. Iwahashi, Y. Liang, K. Sakai, E. Miyai, W. Kunishi, D. Ohnishi and S. Noda., "On-chip beam-steering photonic-crystal lasers," *Nature Photonics*, vol. 4, no. 7, p. 447–450, 2010.

[3] M. Imada, A. Chutinan, S. Noda, and M. Mochizuki., "Multidirectionally distributed feedback photonic crystal lasers," *Physical Review B*, vol. 65, no. 19, p. 195306, 2002.

[4] G. P. A. Agrawal, N. K. Dutta, and D. Renner., "Long-Wavelength Semiconductor Lasers," *IEEE journal of quantum electronics*, vol. 23, no. 5, p. 641, 1987.

[5] Q. Wang, H. Wang, B. Zhang, X. Wang, W. Liu, J. Wang, J. Wang, J. Fan, Y. Zou, X. Ma., "Integrated fabrication of a high strain InGaAs/GaAs quantum well structure under variable temperature and improvement of properties using MOCVD technology," *Optical Materials Express*, vol. 11, no. 8, p. 2378–2388, 2021.

[6] K. Mukai, Y. Nakata, K. Otsubo, M. Sugawara, N. Yokoyama, and H. Ishikawa, "High characteristic temperature of near-1.3- μm InGaAs/GaAs quantum-dot lasers at room temperature," *Applied Physics Letters*, vol. 76, no. 23, p. 3349-3351, 2000.

[7] H. Shoji, Y. Nakata, K. Mukai, Y. Sugiyama, M. Sugawara, N. Yokoyama, and H. Ishikawa., "Temperature dependent lasing characteristics of multi-stacked quantum dot lasers," *Applied Physics Letters*, vol. 71, no. 2, p. 193–195, 1997,

[8] D. L. Huffaker, G. Park, Z. Zou, O. B. Shchekin, and D. G. Deppe, "1.3 μm room-temperature GaAs-based quantum-dot laser," *Applied Physics Letters*, vol. 73, no. 18, p 2546-2566, 1998.

[9] N. Kirstatedter, N.N. Ledentsov, M. Grundmann, D. Bimberg, V. M. Ustinov, S. S. Ruvimov, M. V. Maximov, P. S. Kop'ev, Zh. I. Alferov, U. Richter, P. Werner, U. Gosele and J. Heydenreich., "Low threshold, large T_0 injection laser emission from (InGa) As quantum dots," *Electronics Letters* 30, no. 17, p. 1416-1417, 1994.

[10] K. Otsubo, N. Hatori, M. Ishida, S. Okamura, T. Akiyama, Y. Naka, H. Ebe, M. Sugawara, and Y. Arakwa "Temperature-Insensitive Eye-Opening under 10-Gb/s Modulation of 1.3μm p-doped Quantum-Dot Lasers without Current Adjustments," Japanese Journal of Applied Physics, vol. 43, no. 8B, p. 1124, 2004.

[11] O. B. Shchekin and D. G. Deppe., “Low-threshold high-T_0 1.3-μm InAs quantum-dot lasers due to p-type modulation doping of the active region,” *EEE Photonics Technology Letters*, vol. 14, no. 9, p. 1231–1233, 2002.

[12] D. G. Deppe, K. Shavritranuruk, G. Ozgur, H. Chen, and S. Freisem., “Quantum dot laser diode with low threshold and low internal loss,” *Electronics Letters*, vol. 45, no. 1, p. 54-56, 2009.

[13] C. Y. Jin, T. J. Badcock, H. Y. Liu, K. M. Groom, R. J. Royce, D. J. Mowbray and M. Hopkinson., “Observation and modeling of a room-temperature negative characteristic temperature 1.3-μm p-type modulation-doped quantum-dot laser,” *IEEE journal of quantum electronics*, vol. 42, no. 12, p. 1259–1265, 2006.

[14] T. Kageyama, K. Takada, K. Nishi, M. Yamaguchi, R. Mochida, Y. Maeda, H. Kondo, K. Takemasa, Y. Tanaka, T. Yamamoto, M. Sugawara, Y. Arakawa., “Long-wavelength quantum dot FP and DFB lasers for high temperature applications,” In *Novel In-Plane Semiconductor Lasers XI SPIE*, vol. 8277, p. 73-80, 2012.

[15] Y. Tanaka, M. Ishida, K. Takada, T. Yamamoto, H. -Z. Song, Y. Nakata, M. Yamaguchi, K. Nishi, M. Sugawara, and Y. Arakawa., “25 Gbps direct modulation in 1.3μm InAs/GaAs high-density quantum dot lasers,” *CLEO/QELS: 2010 Laser Science to Photonic Applications*, p. 1–2, 2010.

[16] N. N. Ledentsov, F. Hopfer, and D. Bimberg, “High-speed quantum-dot vertical-cavity surface-emitting lasers,” *Proceedings of the IEEE*, vol. 95, no. 9, p. 1741–1756, 2007.

[17] Y. H. Chang, P. C. Peng, W. K. Tsai, Gray Lin, FangI Lai, R. S. Hsiao, H. P. Yang, H. C. Yu, K. F. Lin, J. Y. Chi, S. C. Wang, and H. C. Kuo., “Single-mode monolithic quantum-dot VCSEL in 1.3 μm with sidemode suppression ratio over 30 dB,” *IEEE Photonics Technology Letters*, vol. 18, no. 7, p. 847–849, 2006.

[18] V. M. Ustinov, N. A. Maleev, A. R. Kovsh, and A. E. Zhukov, “Quantum dot VCSELs,” in *Physica Status Solidi (A)*, vol. 202, no. 3, p. 396–402, 2005.

[19] J. D. Joannopoulos, S. G. Johnson, J. N. Winn, R. D. Meade., “Photonic Crystals: Molding of Light (Second Edition),” Princeton University Press, 2007.

[20] S. Noda, K. Kitamura, T. Okino, D. Yasuda, and Y. Tanaka, “Photonic-crystal surface-emitting lasers: Review and introduction of modulated-photonic crystals,” *IEEE Journal of Selected Topics in Quantum Electronics*, vol. 23, no. 6, Nov. 2017.

[21] M. Meier, A. Mekis, A. Dodabalapur, A. Timko, R. E. Slusher, J. D. Joannopoulos, O. Nalamasu., "Laser action from two-dimensional distributed feedback in photonic crystals," *Applied Physics Letters*, vol. 74, no. 1, p. 7–9, 1999.

[22] "Coherent two-dimensional lasing action in surface-emitting laser with triangular-lattice photonic crystal structure," *Applied physics letters*, vol. 75, no. 3, p. 316-318, 1999.

[23] Y. Liang, C. Peng, K. Sakai, S. Iwahashi, and S. Noda., "Three-dimensional coupled-wave model for square-lattice photonic crystal lasers with transverse electric polarization: A general approach," *Physical Review B*, vol. 84, no. 19, p. 1–11, 2011.

[24] S. Noda, M. Yokoyama, M. Imada, A. Chutinan, and M. Mochizuki, "Polarization Mode Control of Two-Dimensional Photonic Crystal Laser by Unit Cell Structure Design," *Science, vol.293, no. 5532, p. 1123-1125, 2001.*

[25] H. Matsubara, S. Yoshimoto, H. Saito, Y. Tanaka and S. Noda., "GaN Photonic-Crystal Surface-Emitting Laser at Blue-Violet Wavelengths," *Science*, vol. 319, no. 5862, p. 445–447, 2008.

[26] D. Ohnishi, T. Okano, M. Imada, and S. Noda., "Room temperature continuous wave operation of a surface-emitting two-dimensional photonic crystal diode laser," *optics express*, vol. 12, no. 8, p. 1562-1568, 2004.

[27] S. Iwahashi, K. Sakai, Y. Kurosaka, and S. Noda., "Air-hole design in a vertical direction for high-power two-dimensional photonic-crystal surface-emitting lasers," *Journal of the Optical Society of America B*, vol. 27, no. 6, p. 1204-1297, 2010.

[28] K. bin Hong, C. C. Yang, and T. C. Lu., "Optical characteristics of GaAs-based high index contrast photonic crystal lasers with deeply-etched air holes," *International Semiconductor Laser Conference (ISLC)*. IEEE, p. 1-2, 2016.

[29] H. Y. Lu, S, C. Tian, C. Z. Tong, L. J. Wang, J. M. Rong, C. Y. Liu, H. Wang, S. L. Shu, and L. J. Wang., "Extracting more light for vertical emission: high power continuous wave operation of 1.3-μm quantum-dot photonic-crystal surface-emitting laser based on a flat band," *Light: Science & Applications*, vol. 8, no. 1, p. 1-6, 2019.

[30] M. Y. Hsu, G. Lin, and C. H. Pan., "Electrically injected 1.3- μ m quantum-dot photonic-crystal surface-emitting lasers," *Optics Express*, vol. 25, no. 26, p. 32697–32704, 2017.

[31] J. Bin, K. Feng, W. Shen, M. Meng, and Q. Liu, “Investigation on GaN-Based Membrane Photonic Crystal Surface Emitting Lasers,” *Materials*, vol. 15, no. 4, p. 1479, 2022.

[32] K. Emoto, T. Koizumi, M. Hirose, Masahiro Jutori, T. Inoue, K. Ishizaki, M. Dezoysa, H. Togawa, and S. Noda., “Wide-bandgap GaN-based watt-class photonic-crystal lasers,” *Communications Materials*, vol. 3, no. 1, p. 1-8, 2022.

[33] T. C. Lu, S. W. Chen, L. F. Lin, T. T. Kao, C. C. Kao, P. Yu, H. C. Kuo, and S. C. Wang., “GaN-based two-dimensional surface-emitting photonic crystal lasers with AlNGaN distributed Bragg reflector,” *Applied Physics Letters*, vol. 92, no. 1, p. 011129 2008.

[34] S. Kawashima, T. Kawashima, Y. Nagatomo, Y. Hori, H. Iwase, T. Uchida, K. Hoshino, A. Numata, and M. Uchida., “GaN-based surface-emitting laser with two-dimensional photonic crystal acting as distributed-feedback grating and optical cladding,” *Applied Physics Letters*, vol. 97, no. 25, p. 251112, 2010.

[35] D. M. Williams, K. M. Groom, B. J. Steven, D. T. D. Childs, R. J. E. Taylor, S. Khamas, R. A. Hogg, N. Ikeda, and Y Sugimoto., “Epitaxially regrown GaAs-based photonic crystal surface-emitting laser,” *IEEE Photonics Technology Letters*, vol. 24, no. 11, p. 966–968, 2012.

[36] S. C. Huang, K. B. Hong, H. L. Chiu, S. W. Lan, T.C. Chang, H. Li and T. C. Lu,“Design of photonic crystal surface emitting lasers with indium-tin-oxide top claddings,” *Applied Physics Letters*, vol. 112, no. 6, p. 061105, 2018.

[37] Z. Bian, K. J. Rae, A. F. McKenzie, B. C. King, N. Babazaeh, G. Li, J. R. Orchard, N. D. Gerrad, S. Thoms, D. A. MaccLaren, R. J. E. Taylor, D. T. D. Childs, R. A. Hogg., “1.5 μm Epitaxially Regrown PCSEL Diode,” *IEEE Photonics Technology Letter*, vol. 34, no. 24, p. 1531–1534, 2020.

[38] Z. L. Li, B. H. Chang, C. H. Lin, and C. P. Lee, “Dual-wavelength GaSb-based mid infrared photonic crystal surface emitting lasers,” *Journal of Applied Physics*, vol. 223, no. 9, p. 093102, 2018.

[39] Z. L. Li, S. C. Lin, G. Lin, H. W. Cheng, K. W. Sun, and C. P. Lee, “Effect of etching depth on threshold characteristics of GaSb-based middle infrared photonic-crystal surface-emitting lasers,” *Micromachines*, vol. 10, no. 3, p. 188, 2019.

[40] B. C. King, K. J. Rae, A. F. McKenzie, A. Boldin, D. Kim, N. D. Gerrard, G. Li, K.Nishi, K. Takemasa, M. Sugawara, R. J. E. Taylor, D. T. D. Childs, and R. A. Hogg.,

"Coherent power scaling in photonic crystal surface emitting laser arrays," *AIP Advances* vol.11, no. 1 p. 015017, 2021.

[41] M. Imada, S. Noda, A. Chutinan, M. Murata, and G. Sasaki, "Semiconductor lasers with one- and two-dimensional air/semiconductor gratings embedded by wafer fusion technique," *IEEE Journal on Selected Topics in Quantum Electronics*, vol. 5, no. 3, p. 658–663, May 1999,

[42] M. Y. Hsu, G. Lin, Z. L. Li, and P. C. Pan, "Threshold current temperature dependence of quantum-dot photonic crystal surface-emitting lasers with respect to gain-cavity detuning," *Optics express*, vol. 26, no. 10, p. 13483-13488, 2018.

[43] D. M. Williams, K. M. Groom, B. J. Stevens, D. T. D. Childs, R. J. E. Taylor, S. Khamas, R. A. Hogg, N. Ikeda and Y. Sugimoto., "Optimisation of coupling between photonic crystal and active elements in an epitaxially regrown GaAs based photonic crystal surface-emitting laser," *Japanese Journal of Applied Physics*, vol. 51, no. 2, 2012.

[44] K. Hirose, Y. Liang, Y. Kurosaka, A. Watanabe, T. Sugiyama, and S. Noda, "Watt-class high-power, high-beam-quality photonic-crystal lasers," *Nature photonics*, vol. 8, no. 5, p. 406–411, 2014.

[45] K. Ishizaki, M. D. Zoysa, and S. Noda, "Progress in Photonic-Crystal Surface-Emitting Lasers † ," *Photonics*, vol.6, no. 3, p. 96, 2019.

[46] G. Park, O. B. Shchekin, D. L. Huffaker, and D. G. Deppe., "Low-threshold oxide-confined 1.3-μm quantum-dot laser," *IEEE Photonics Technology Letters*, vol. 12, no. 3, p. 230-232, 2000.

[47] R. R. Alexander, D. Childs, and H. Agarwal, "Growth, Fabrication, and Operating Characteristics of Ultra-Low Threshold Current Density 1.3 Quantum Dot Lasers," *Japanese Journal of Applied Physics To*, vol. 44, p. 2520, 2005,

[48] D. O'Brien, S. P. Hegarty, G. Huyet, J. G. McInerney, T. Kettler, M. Laemmlin, D. Bimberg, V. M. Ustinov, A. E. Zhukov, S. S. Mikhrin and A. R. Kovsh., "Feedback sensitivity of 1.3 μm InAs/GaAs quantum dot lasers," *Electron Letter*, vol. 39, no. 25, p. 1819-1820, 2003.

[49] C. Shang, Y. Wan, J. Selvidge, E. Hughes, R. Herrick, K. Mukherjee, J. Duan, F. Grillot, W. W. Chow, and J. E. Bowers., "Perspectives on advances in quantum dot lasers and integration with Si photonic integrated circuits," *ACS photonics*, vol. 8, no. 9. p. 2555-2566, 2021.

[50] A. Markus, J. X. Chen, C. Paranthoen, A. Fiore, C. Platz, and O. Gauthier-Lafaye., "Simultaneous two-state lasing in quantum-dot lasers," *Applied Physics Letters*, vol. 82, no. 12, p. 1818-1820, 2003.

[51] B. J. Stephens, D. T. D. Childs, H. Shahid and R. A. Hogg., "Direct modulation of excited state quantum dot lasers," *Applied Physics Letters,* vol. 95, no. 6, p. 061101, 2009.

[52] R. J. E. Taylor, P. Ivanov, G. Li, D. T. D. Childs, and R. A. Hogg, "Optimisation of photonic crystal coupling through waveguide design," *Optical and Quantum Electronics*, vol. 49, no. 2, p. 1-26, 2017.

[53] B. C. King, "Gallium Arsenide Based Photonic Crystal Surface Emitting Lasers," *PhD Thesis,* 2021.

[54] K. Sakai, E. Miyai, T. Sakaguchi, D. Ohnishi, T. Okano, and S. Noda, "Lasing Band-Edge Identification for a Surface-Emitting Photonic Crystal Laser," *EEE Journal on Selected Areas in Communications,* vol. 23, no. 7, p. 1335–1340, 2005.

[55] T. Inoue, R. Morita, M. Yoshida, M. de Zoysa, Y. Tanaka, and S. Noda, "Comprehensive analysis of photonic-crystal surface-emitting lasers via time-dependent three-dimensional coupled-wave theory," *Physical Review B,* vol. 99, no. 3, p. 035308, 2019.

[56] J. Liu, D. Kim, J. Feng, Y. Gao, and R. A. Hogg., "Monte Carlo modelling of photonic crystal surface emitting laser," *SPIE,* 2023.

[57] Y. Kurosaka, S. Iwahashi, K. Sakai, E. Miyai, W. Kunishi, D. Ohnishi, and S. Noda., "Band structure observation of 2D photonic crystal with various V-shaped air-hole arrangements," *EICE Electronics express,* vol. 6, no. 13, p. 966–971, 2009.

[58] Z. Bian, K. J. Rae, B. C. King, D. Kim, G. Li, S. Thoms, D. T. D. Childs, N. D. Gerrard, N. Babazadeh, P. Reynolds, J. Grant, A. F. McKenzie, J. R. Orchard, R. J. E. Taylor and R. A. Hogg., "Comparative analysis of void-containing and all-semiconductor 1.5 μm InP-based photonic crystal surface-emitting laser diodes," *AIP Advances,* vol. 11, no. 6, p. 065315, 2021.

Chapter 6: Conclusion

The purpose of this thesis is to investigate the characterization of quantum-dot based photonic devices, with a specific focus on superluminescent diodes (SLDs) and photonic crystals surface-emitting lasers (PCSELs). SLDs have emerged as a valuable light source for medical imaging, particularly in the application of optical coherence tomography for skin tissues. To effectively achieve high resolution and deep penetration depth in skin tissue imaging, SLDs require a broad bandwidth and moderate output power. Utilising the inhomogeneous properties of QD, QD-SLDs are capable of providing the necessary broad bandwidth for this application. PCSELs, on the other hand, are new types of semiconductor laser that has in-plane gain and feedback orthogonal to the out-of-plane emission. The integration of QDs into PCSEL allows multiple emission wavelengths from one heterostructure. Through this research, we aim to gain a comprehensive understanding of the properties and performance of these QD-based photonic devices, with a view toward identifying potential applications and areas for further research.

In chapter 3, the impact of ridge etch depth on SLD performance (power and bandwidth) was examined. Prior studies on QD-based SLD have primarily focused on optimizing the materials and device structures of SLD to achieve broad bandwidth and high output power [1],[2] but the importance of considering fabrication parameters such as etch depth of ridge is lacking. An investigation was undertaken to evaluate the losses, modal gain, output power, spectral bandwidth and current confinement with extreme variations in etch depth. Additionally, the impact of thermal effects on SLDs for both etch depth was examined. In a deep-ridge device, an increase in FWHM of SLD emission from 118 nm to 167 nm occurs with increasing temperature due to the broadening of the FWHM of the states. However, the output power is low in these deep-ridge devices because of the large scattering loss and self-heating effects in the ridge. In contrast, shallow etched devices exhibit moderate output power even at high operating temperatures. The benefit of the carrier thermalization into the higher states of the dots (ES_2) make the FWHM of SLD emission increases from 50 nm to 250 nm because of the combined contribution of ES_1 and ES_2 with increasing temperature. It should be noted that this FWHM was achieved using standard QD laser epitaxial structures without the need for any specialised layer structures or growth techniques but solely through the use of extreme operating temperature.

In chapter 4, the concept of hybrid QW/QD structure for SLD was introduced. The proposed structures feature a high dot density with the aim of achieving a higher modal gain value which is important for achieving high output power. Due to the high dot density, the use of

lower number of dot layer (QW/5 layers of QDs) results in higher modal gain value of 25 cm^{-1} modal gain value and a broader gain spectrum spanning ~350 nm compared to previous studies [3]. The number of layers of dots on modal gain was also studied. An increase in modal gain value was observed with an increased number of dot layers. Furthermore, the comparison of "unchirped" and "chirped" in terms of modal gain and spectral bandwidth was presented. The "chirped" of the QD leads to improved gain "flatness" and enhancement of FWHM of SLD emission. This chapter highlights the potential of proposed hybrid QW/QD structure in achieving broad spectral bandwidth and high modal gain (high output power) in SLDs.

In chapter 5, the study presented epitaxially regrown GaAs-based PCSELs utilising self-assembled InAs QD, exhibiting lasing at room temperature. The ability to utilise both the ground-state (GS) and excited-state (ES) of the QDs allows multiple emission wavelengths from one heterostructure. The choice of the grating periods allows lasing at the ground state (GS) or excited state (ES) of the QD, 90 nm apart in wavelength. The effect of the device mesa area, photonic crystal (PC) structure (square, circle, height) and crystallographic orientation of the PC on device performance was also studied. This chapter highlights the potential of utilising epitaxially regrown QDs-based PCSELs and the impact of PC designs on lasing performances.

Bibliography

[1] M. Rossetti, L. H. Li, A. Fiore, L. Occhi, and C. Velez., "Quantum dot superluminescent diodes," In *Handbook of Self Assembled Semiconductor Nanostructures for Novel Devices in Photonics and Electronics*, p. 565-567, 2008.

[2] Z. Y. Zhang, Z. G. Wang, B. Xu, P. Jin, Z. Z. Sun, and F. Q. Liu., "High-Performance Quantum-Dot Superluminescent Diodes," *IEEE Photonics Technology Letters*, vol. 16, no. 1, p. 27-29, 2004.

[3] S. M. Chen, K. J. Zhou, Z. Y. Yang, D. T. D. Childs, M. Hugues, A. J. Ramsay, and R. A. Hogg., "Ultra-broad spontaneous emission and modal gain spectrum from a hybrid quantum well/quantum dot laser structure," *Applied Physics Letters*, vol. 100, no.4, p. 41118, 2012.